radovan bast   quantum chemistry beyond the charge density

Radovan Bast

Quantum chemistry beyond the charge density

Soutenue publiquement le 7 janvier 2008

moji rodině
meiner familie

Acknowledgments

First and foremost, I would like to thank my supervisor Trond Saue for his multi-level support over the last three years, which have been filled with group seminars, lunches, scientific discussions, and many scientific "aha" effects.

I am grateful for the generous financial support from the Fonds der Chemischen Industrie through the Kekulé scholarship, by the Conseil Régional d'Alsace through the Bourse Régionale, and by the Agence Nationale de la Recherche.

I would like to thank

– the members du Laboratoire de Chimie Quantique, past and present: David Ambrosek, Michiko Atsumi, Nadia Ben Amor, Marc Bénard, Hélène Bolvin, Chantal Daniel, Alain Dedieu, Sébastien Dubillard, Sylvie Fersing, Carole Fevrier, Thomas Fleurentdidier, André Severo Pereira Gomes, Miroslav Iliaš, Emmanuelle Jablonski, Ali Kachmar, Pierre Labeguerie, Xavier Lopez, Roberto Marquardt, Antonio Mota, Aziz Ndoye, François-Paul Notter, Lilyane Padel, Marie-Madeleine Rohmer, Alain Strich, Elisabeth Vaccaro, and Sébastien Villaume for many nice moments and for giving me the feeling to be at home,

– Kenneth Ruud for inviting me to work in Tromsø, and Jonas Jusélius, Luca Frediani, Dmitry Shcherbin, Harald Solheim, and Andreas Thorvaldsen for making my stay in Tromsø special,

– Patrick Norman for inviting me to Linköping and teaching me quadratic response, and Ulf Ekström and Johan Henriksson for a very nice stay in Linköping,

– my scientific co-authors,

– the DIRAC family for enthusiasm, fun, and patience with my past, present, and future bugs,

– the NCPMOL team,

– Romaric David for having a solution for every problem,

– Ulf Ekström for cool visualization tricks,

– Johan Henriksson and Paweł Sałek for insights into the DFT response machinery,

– Johan Henriksson for lots of help with the implementation of the spin density contribution to quadratic response,

– Ajith Perera for nice discussions,

– the PyNGL team at the National Center for Atmospheric Research in Boulder, for help with streamline plots,

– the Marburg hurricane/southside gang for lots of fun and good memories,

– Hans Jørgen Aagaard Jensen for comments on the manuscript,

– Hélène Bolvin for help and support,

– Gernot Frenking for his kind support,

– Roberto Marquardt for many useful comments and for correcting my confusing use of atomic units,

– Roberto Marquardt for nice discussions,

Contents

Sommaire

Au cours des dix dernières années, la théorie de la fonctionnelle de la densité (DFT) a complètement changé le paysage de la chimie théorique. Elle est la méthode la plus populaire aujourd'hui.[1] La DFT a permis aux chimistes théoriciens de s'attaquer à des problèmes chimiques réels. Son succès réside dans sa capacité à inclure la corrélation électronique pour un coût de calcul réduit, elle peut donc fournir des résultats de haute précision pour une grande gamme de problèmes. Le fondement rigoureux de la DFT est fourni par le théorème de Hohenberg-Kohn qui énonce que l'énergie s'exprime comme une fonctionnelle de la densité de charge de telle sorte que le calcul de la fonction d'onde complète n'est pas nécessaire. Un aspect clef des calculs DFT modernes est l'utilisation de la méthode Kohn-Sham (KS) dans laquelle la densité de l'état fondamental du système réel est obtenue à partir d'un système de référence déterminé par un potentiel effectif local où les particules n'interagissent pas entre elles. Cependant, la forme précise de ce potentiel dit d'échange et de corrélation (XC) est inconnue. L'utilisation et l'amélioration continuelle de la DFT dépend donc de façon critique du développement de fonctionnelles approximatives. L'approximation locale (LDA), puis l'introduction de l'approximation du gradient généralisé (GGA) et, plus récemment, les fonctionnelles hybrides ont constitué un progrès spectaculaire.

On peut dire que dans la chimie quantique d'aujourd'hui la densité de charge est la variable fondamentale. En revanche, les théories généralisées de la fonctionnelle de la densité étendent la DFT approximative conventionnelle en incluant d'autres variables, comme par exemple la densité de spin (théorie de la fonctionnelle de la densité de spin, SDFT) et la densité de courant (théorie de la fonctionnelle de la densité de courant, CDFT). La raison pour laquelle la SDFT et d'autres DFT généralisées sont utilisées et developpées est le fait que les densités généralisées supplémentaires permettent d'agrandir l'espace fonctionnel et donnent plus de flexibilité dans

la procédure variationnelle. Ceci est essentiel pour l'étude des propriétés magnétiques et des systèmes à couche ouverte pour lesquels les fonctionnelles approximatives de la seule densité de charge, qui sont actuellement disponibles, échouent. D'autres exemples où la DFT généralisée est susceptible d'améliorer les résultats de la DFT approximative conventionnelle est le traitement des états dégénérés des systèmes atomiques, des états excités et de la corrélation non-locale (par exemple, polarisabilité dipolaire des chaînes moléculaires).

Notre développement dans la domaine de la DFT généralisée est guidé par des arguments physiques et non par ajustement d'un nombre important de paramètres. Pour atteindre ce but, il est préférable de se placer dans un cadre relativiste, car les interactions fondamentales qui interviennent en chimie, les interactions électromagnétiques, sont intrinsèquement relativistes. Cette thèse constitue les premiers pas vers le développement de la CDFT dans un cadre relativiste. Nous nous concentrons sur la mise en œuvre de la TD-SDFT (time-dependent SDFT) non-colinéaire qui fournira la structure du code nécessaire pour la TD-CDFT, grâce à la structure similaire entre les operateurs de la densité de spin et de courant de charge et entre les matrices XC et leurs transformées correspondantes. Nous avons presenté et discuté la mise en œuvre des réponses linéaire et quadratique dans les systèmes à couche fermée dans le cadre de la théorie adiabatique de la fonctionnelle de la densité dépendant du temps avec la contribution de la densité de spin (TD-SDFT) non-colinéaire. Les contributions XC aux réponses linéaire et quadratique ont étés dérivées par un développement perturbatif du gradient électronique XC par rapport au champ extérieur. Trois autres implémentations de la réponse linéaire relativiste dans la théorie TD-SDFT fondée sur le noyau XC non-colinéaires ont été rapportées jusqu'à aujourd'hui, deux d'entre elles en utilisant l'hamiltonien ZORA à deux composantes—par le groupe de Ziegler[2] et par Liu et collaborateurs[3]— et une implémentation en utilisant l'hamiltonien à quatre composantes par Liu et collaborateurs.[4] Jusqu'à présent, les noyaux XC non-colinéaires ont été limités au noyau LDA. L'implémentation présentée dans ce mémoire permet également d'employer le noyau XC adiabatique dépendant du gradient de la densité de spin. Ce travail constitue à notre connaissance la première implémentation relativiste de la réponse quadratique dans le cadre TD-SDFT. La dérivation étant répétitive et récursive mais aussi sensible aux erreurs en raison du nombre important de termes, cela nous a motivé pour développer des logiciels permettant une dérivation et une simplification automatiques.

Dans l'avenir, cela nous permettera de progresser vers les ordres élevés du développement.

Pour valider la mise en œuvre de la réponse linéaire dans la théorie TD-SDFT non-colinéaire, nous avons calculé les énergies d'excitations de Zn, Cd, Hg, AuH et UO_2^{2+}. Ces ensembles ont été choisis pour deux aspects : (i) ils contiennnent des éléments lourds, y compris le métal post-transitionnel U, et (ii) il nous était possible de comparer nos énergies d'excitation avec les résultats publiés par d'autres groupes. En outre, nous avons complété l'étude des spectres électroniques de Zn, Cd, Hg et AuH, en étudiant la performance des autres fonctionnelles, notamment des fonctionnelles dépendant du gradient de la densité en utilisant leurs propres noyaux XC.

Dans la théorie de la réponse basée sur la quasi-énergie moyennée dans le temps, les propriétés moléculaires dépendant de la fréquence, les énergies d'excitation et les éléments de matrice de transition peuvent être associées à des fonctions de réponse, à leurs singularités et à leurs résidus. Nous avons montré comment les dérivés des densités analytiques et numériques peuvent être utilisées pour calculer et visualiser les propriétés moléculaires statiques et dépendant de la fréquence et comment des densités de propriétés peuvent être définies de façon très générale. Les densités du premier ordre, statiques et dépendant de la fréquence, qui correspondent aux propriétés du second ordre, ont été obtenues en appliquant la théorie de la réponse sur des déterminants Hartree-Fock (HF) ou KS. D'autres perturbations (statiques) peuvent être imposées en utilisant la méthode des perturbations finies. En outre, il est possible d'isoler et de tracer les contributions orbitalaires individuelles en utilisant seulement certains éléments du vecteur de réponse correspondant pour la construction des matrices de la densité modifiée. Les densités de propriétés "paramagnétiques" et "diamagnétiques" peuvent être définies de la même façon que les fonctions de réponse linéaire "paramagnétiques" et "diamagnétiques" sont calculées : en considérant seulement les amplitudes d'excitation vers les orbitales d'énergie positive ou vers les orbitales d'énergie négative. Ainsi les effets relativistes scalaires et les effets du couplage spin–orbite peuvent être visualisés de la même façon qu'ils sont soit calculés soit éliminés des calculs de réponse linéaire. Le potentiel de cette approche visuelle des propriétés moléculaires dans l'espace physique à trois dimensions est illustrée pour plusieurs des exemples discutés ci-dessus.

Nous avons par example étudié la densité induite par un champ électrique statique pour l'atome Ne et la molécule HF. Les graphiques montrent effectivement les zones de l'espace contribuant le plus à la propriété. Par exemple, les graphiques présentés dans ce mémoire soulignent que la polarisabilité dipolaire et la première hyperpolarisabilité sont des propriétés de la région de valence extérieure. Cela peut être utile pour démontrer les exigences sur un jeu de base pour une propriété spécifique. L'interprétation des propriétés non-linéaires peut être difficile et les isosurfaces de densité induites à différents ordres qui sont présentées dans ce travail donnent un aperçu supplémentaire pour le problème au-delà des chiffres, par exemple pour discuter des tendances des propriétés dans une classe de molécules.

Nous avons démontré comment la polarisabilité dipolaire linéaire dépendante de la fréquence peut être visualisée en utilisant soit la densité de charge induite, soit la densité de courant induite. La représentation de l'équation de continuité dans une base finie a été étudiée. Pour une séquence de bases, nous avons démontré comment la représentation de l'équation de continuité peut être améliorée.

Inspirés par l'approche générale et quantitative de Jusélius, Sundholm et Gauss[5] dans le cadre non-relativiste, nous avons appliqué notre réalisation relativiste à quatre composantes pour l'étude de la densité de courant induite dans les composés hétéro-aromatiques du groupe 15, C_5H_5E (E = N, P, As, Sb, Bi). Nous avons présenté et qualitativement discuté les graphiques des densités de courant de probabilité induites. Les contributions "paramagnétiques" et "diamagnétiques" ont été examinées séparément. Pour une analyse plus quantitative, nous avons discuté les susceptibilités du courant dans le cycle aromatique.

Nous avons tracé les densités de couplage nucléaire spin–spin pour la molécule CO. Nous avons démontré comment les contributions non-relativistes habituelles—i.e. la contribution paramagnétique spin–orbite (PSO), la contribution spin-dipôle (SD) plus l'interaction Fermi-contact (FC), et l'interaction diamagnétique spin–orbite (DSO)—peuvent être également visualisées dans le cadre relativiste. Bien que l'approche de la visualisation de la densité de couplage nucléaire spin–spin soit déjà connue dans le cadre non-relativiste, l'avantage de l'approche présentée ici est la possibilité de traiter les systèmes avec des éléments lourds avec une méthodologie appropriée.

Puis, nous avons examiné la différence d'énergie entre les deux énantiomères de CHFClBr causée par la violation de la parité en introduisant la densité γ^5

$$\gamma^5(\mathbf{r}) = \psi^\dagger \begin{bmatrix} 0_{2\times2} & 1_{2\times2} \\ 1_{2\times2} & 0_{2\times2} \end{bmatrix} \psi \tag{0.1}$$

qui est soumise à une distorsion géométrique le long d'un mode vibrationnel. Le but de cette discussion est que l'étude de la densité γ^5 peut donner une autre vue sur la différence d'énergie causée par la violation de la parité. Si on arrivait à faire la connection entre la différence d'énergie et la structure spatiale de la densité γ^5 et sa variation avec une distorsion géométrique, cela permettrait peut-être de faciliter la conception de la molécule candidate telle que l'effet minuscule soit maximisée et, espérons-le, à la portée de la résolution expérimentale.

Nous avons aussi rapporté la première étude relativiste à quatre composantes de la contribution de non-conservation de la parité (NCP) aux constantes d'écran RMN isotropiques pour les molécules chirales. Nous avons étudié ici les P-énantiomères de la série H_2X_2 ($X = {}^{17}O$, ${}^{33}S$, ${}^{77}Se$, ${}^{125}Te$, ${}^{209}Po$). Les contributions NCP sont obtenues dans une approche de réponse linéaire au niveau Hartree-Fock. Les résultats relativistes à quatre composantes basés sur l'hamiltonien Dirac-Coulomb sont comparés avec les résultats Lévy-Leblond (non-relativistes) et ceux obtenus par l'équation de Dirac modifiée spin-free. Les calculs montrent que le couplage spin–orbite joue un rôle substantiel même pour un traitement qualitatif de $H_2{}^{77}Se_2$ et de ses homologues plus lourds, avec un effet opposé aux effets relativistes scalaires. Le formalisme présenté sera utile pour la future recherche de molécules candidates pour la première détermination expérimentale des effets NCP dans les spectres RMN.

Ainsi nous avons examiné le calcul des contributions électrofaibles NCP dans les paramètres spectraux de RMN du point de vue méthodologique. Nous avons calculé les paramètres d'écran RMN et les constantes de couplage spin–spin indirectes pour trois molécules chirales, H_2O_2, H_2S_2 et H_2Se_2. Les effets de base et de traitement de la corrélation électronique ainsi que les effets de la relativité restreinte ont été étudiés. Tous les effets sont importants. La dépendance par rapport à la base est très prononcée, particulièrement pour les méthodes corrélées. Les résultats coupled-cluster et DFT pour les contributions NCP diffèrent de manière significative des résultats HF. La DFT surestime les effets NCP, en particulier avec les fonctionnelles XC non-hybrides. La relativité restreinte est importante pour les propriétés NCP de RMN, ce qui est mis

en évidence ici en comparant les résultats obtenus par le traitement perturbatif à une composante avec divers calculs à quatre composantes. Contrairement aux paramètres d'ecran RMN, le choix du modèle pour représenter la distribution de la charge nucléaire—charge ponctuelle ou modèle gaussien—a un impact significatif sur la contribution NCP aux constantes de couplage spin–spin indirectes.

Indépendamment, nous avons présenté des calculs relativistes à quatre composantes HF et DFT de polarisabilité électrique dipôle-dipôle statique et dépendant de la fréquence pour tous les atomes à couche fermée jusqu'à Ra. Pour cette étude, douze fonctionnelles non-relativistes y compris trois fonctionnelles asymptotiquement corrigées ont été considérées. La meilleure performance a été obtenue en utilisant les fonctionnelles hybrides et leurs versions asymptotiquement corrigées (GRAC). La performance de la fonctionnelle SAOP est parmi les meilleures pour des fonctionnelles non-hybrides pour des atomes du groupe 18 mais sa précision se dégrade quand on considère l'ensemble complet les atomes étudiés. Pour ces systèmes CAMB3LYP représente seulement une amélioration légère par rapport à B3LYP. En outre, nous avons démontré que les potentiels effectifs de cœur ne devraient pas être utilisés en combinaison avec l'interpolation de GRAC. Nous avons constaté que les gaz rares ne sont pas entièrement représentatifs pour l'étalonnage des nouvelles fonctionnelles pour le calcul des polarisabilités.

C'est un plaisir de conclure ce travail en voyant plusieurs projets former des connections qui convergent vers la thématique centrale de cette thèse : la chimie quantique au-delà de la densité de charge.

Motivation and overview

*You think quantum physics has the answer? I mean, what purpose
does it serve for me that time and space are exactly the same thing?
I ask a guy what time it is, he tells me six miles? What the hell is
that?*

Woody Allen in *Anything Else* (2003)

This thesis focuses on the calculation and visualization of molecular properties within the 4-component relativistic framework. Response theory together with density functional theory (DFT) within the Kohn-Sham (KS) approach are the main tools. In the following I will explain why the 4-component relativistic framework, response theory, and DFT form a good team for the calculation and visualization of molecular properties and why the development of these methods is worthwhile.

The speed of light is finite and our world is relativistic—with all their fascinating consequences on our understanding of nature. Relativistic effects in chemistry and molecular physics are important and have been recognized as early (or as late) as in the 1970's[6-8] (see also Refs. 9 and 10 and the bibliography therein). The increasing interest for relativistic effects visible in more and more calculations correlates with a very active development of appropriate tools for their computational treatment, which are now available in several quantum-chemical codes (BDF,[11,12] BERTHA,[13-15] DIRAC,[16] DREAMS,[17,18] MOLFDIR,[19] REL4D,[20-22] and several 2-component implementations). Whether it is necessary to include relativistic effects in quantum-chemical calculations depends in the end on "your attitude"[23] since the motivations for treating these effects can be very different: (i) for heavy-element systems there is no alternative to a relativistic treatment in order to obtain even a qualitative description of the electronic structure, (ii) today calculations can reach the accuracy where relativistic effects begin to count even for light elements, and finally, (iii) the relativistic theory offers the natural framework to describe the interaction of particles with electromagnetic fields, especially magnetic properties—they are inherently *relativistic* phenomena. Magnetic interactions can be described

in a nonrelativistic (NR) formalism. However, the 4-component relativistic framework usually offers "nicer" expressions on paper and a more consistent theory,[24] often (but not always!) at the cost of more sophisticated coding and more expensive calculations. Numerous excellent textbooks[25–29] and review volumes[30–34] on relativistic effects in chemistry and relativistic quantum theory exist and it would be redundant to make a lengthy general introduction to this theory in this thesis. Relativity will therefore not appear in a separate chapter, it will rather constitute the point of view and it will be interwoven in the notation and the discussion of expressions and results.

DFT is today's most popular method in computational chemistry[1] and the preferred method in this thesis. Based on the proofs of Hohenberg and Kohn[35] (HK), the ground state electron density is a sufficient variable for the description of the electronic many-body quantum system. This variable is intuitive and observable, in contrast to the many-body wave function in wave functional theory. In principle not only the ground state energy, but all observables of the system are functionals of the ground state density. The theory is exact and rigorous. Unfortunately for practical applications, DFT, in the spirit of HK, does not offer explicit expressions.

Practical, explicit DFT, which is almost exclusively used in the formulation of Kohn and Sham[36] (KS), relies on many approximations and presently many different functionals, which are obtained based on various motivations, are on the market. Given the wealth of available functionals, part of them designed using several semi-empirical parameters, DFT often meets the critique of being too much *cuisine*. In strong disagreement to this critique, the design and selection of density functional approximations can be and should be systematic, following the method of "constraint satisfaction" along the "Jacob's Ladder to heaven of chemical accuracy" nicely discussed in Ref. 37, without fitting to data sets. The present difficulty and challenge for the future is however the fact, that although a systematic hierarchy of physical sophistication exists for density functional approximations (rungs of the "Jacob's Ladder"), for today's approximate functionals this series does not guarantee convergence towards exact solutions *in every case*. This is in contrast to wave function based methods with a limit that is known (full configuration interaction) but is for most practical purposes computationally (not conceptually) out of reach.

The huge driving force behind the development of new functionals and the popularity of DFT is the favorable cost/performance ratio and scaling with the size of the system, together with relatively modest basis set requirements. A large number of quantum mechanical studies of interesting systems whose size disqualifies wave function based methods would not be possible without DFT.

DFT becomes all the more interesting in the relativistic community due to the typically larger number of electrons to correlate in the treatment of heavier elements. As in NR DFT, one has to distinguish between a firm theoretical basis, laid down by Rajagopal and Callaway[38] with the 4-current density being the fundamental variable, and the practical side where such functionals are not yet available and one therefore usually resorts to the use of NR functionals in combination with 2- and 4-component Hamiltonians.

The generalization of the time-independent HK theorem to the time-dependent domain (TD-DFT) by Runge and Gross[39] with the formulation of a corresponding time-dependent KS scheme made a large number of time-dependent molecular properties accessible within DFT. The usually addressed electronic excitation spectrum is only one of many possible applications. Some of the difficulties of stationary DFT mentioned above apply also in TD-DFT. New problems arise, e.g. the so-called ultra-nonlocality[40] or the memory of the exchange-correlation kernel.[41]

The calculation of static and frequency-dependent molecular properties within TD-DFT, formulated in the language of response theory, and employing the time-averaged quasienergy formalism will be the core of this thesis. Within the time-averaged quasienergy response theory, frequency-dependent molecular properties, excitation energies, and transition matrix elements can be associated with response functions, their poles, and residues, respectively. The implementation of closed-shell linear and quadratic response functions within TD-DFT in the 4-component relativistic framework will be presented with extensions that include contributions from spin density. It will be argued why these extensions can be necessary for the treatment magnetic and time-dependent electric molecular properties using approximate functionals despite the fact that these additional variables do not appear in the original HK theorems. Especially for the study of magnetic molecular properties, the employed 4-component formalism will be shown to offer a convenient and transparent framework.

Finally, several components from response theory will be put together to produce a visualization tool for various densities which will be used as a valuable alternative for the demonstration, rationalization, and discussion of some basic concepts response theory and relativistic quantum chemistry and offer a real-space approach to molecular properties within the 4-component relativistic framework. It will be demonstrated how scalar relativistic effects and effects due to spin–orbit coupling can be visualized separately. Numbers will be given colors and properties will be given shapes, which may open up new views on well-known models and concepts.

Layout of this thesis

The thesis is divided into three parts:

I The first part gives an introduction to the methodology, starting from the molecular electronic energy (Section 1), then introducing response theory for approximate variational wave functions (Section 2), followed by a detailed discussion of the noncollinear TD-SDFT implementation for linear and quadratic response (Section 3). Section 4 tests the TD-SDFT implementation for excitation energies. Finally, Section 5 discusses a real-space approach to molecular properties within the 4-component relativistic framework.

II In the second part three papers are presented.

III It is a good tradition of the T. Saue research group to prepare notes for problems and for solutions. In this spirit, several notes are included which relate to Parts I and II. These might be useful when more insight into the implementations and more technical details are needed.

Notation, conventions, and units

SI-based atomic units[42,43] are used throughout unless explicitly noted. The electron mass* m and the elementary charge e are written out explicitly for compatibility with the literature. The Einstein implicit summation convention is used where it is clear from the context, recalled where it is less clear from the context, and avoided where it is not expected.

The Dirac identity[44]

$$(\boldsymbol{\sigma} \cdot \mathbf{A})(\boldsymbol{\sigma} \cdot \mathbf{B}) = \mathbf{A} \cdot \mathbf{B} + \mathrm{i}\boldsymbol{\sigma} \cdot (\mathbf{A} \times \mathbf{B}) \tag{0.2}$$

will be repeatedly used. Here $\boldsymbol{\sigma}$ is the vector of Pauli spin matrices in the standard representation (defined in Section 1.3, p. 30), $\mathbf{A}$ and $\mathbf{B}$ are arbitrary vectors.

Orbital indices $i, j, \ldots$ will be reserved of occupied (or inactive) orbitals, indices $a, b, \ldots$ for virtual (or secondary) orbitals, and $p, q, \ldots$ will be general orbital indices.

LDA calculations will always employ the parametrization VWN5 of Vosko *et al.* [45] (SVWN5). The acronym LSDA will not be used for LDA within spin density functional theory because for other functionals this distinction is not made either. The acronym ALDA will not be used for the adiabatic LDA kernel to keep a consistent notation with other adiabatic kernels where the prefix "A" is typically not used.

Electromagnetic properties will be discussed using the (electron) charge density ρ, and the (electron) charge current density $\mathbf{j}$. However, it will actually minimize the confusion by making two exceptions:

(i) The DFT and TD-SDFT implementation will be presented using the probability (or number) density n. The charge and number densities are related by the factor $-e$, which is the charge q of the electron.

$$\rho = qn = -en \tag{0.3}$$

The reason is that density functionals are typically formulated and programmed using the number density n.

(ii) Induced currents will be visualized using the probability current density, denoted by the calligraphic $\mathcal{J}$. Again, the charge current density $\mathbf{j}$ and the probability current density $\mathcal{J}$ are related by the electron charge $q = -e$.

$$\mathbf{j} = q\mathcal{J} = -e\mathcal{J} \tag{0.4}$$

The reason is that it is more intuitive to rationalize induced $\mathcal{J}$ with the familiar right hand rules than induced $\mathbf{j}$ which points opposite to the electron velocity vector, combined with possibly unfamiliar left-hand rules.

---

* For compatibility with the literature on relativistic electronic structure theory the electron mass is written as m instead of m_e.

Part I

Methodology

Molecular electronic energy

Dr. Brackish Menzies, who works at the Mount Wilson Observatory, or else is under observation at the Mount Wilson Mental Hospital (the letter is not clear), claims that travelers moving at close to the speed of light would require many millions of years to get here, even from the nearest solar system, and, judging from the shows on Broadway, the trip would hardly be worth it.

Woody Allen, *The UFO Menace* in *Side Effects*

1.1   Dirac equation and the molecular electronic energy

Books about programming languages typically start with a very easy example: the "hello world". From there more difficult and more sophisticated models are introduced. Quantum chemical dissertations and articles go in the opposite direction and start typically with probably their most difficult example, the time-dependent Dirac equation:

$$ i\frac{\partial}{\partial t}|\psi(t)\rangle = [\hat{H} + \hat{P}(t)]|\psi(t)\rangle. \tag{1.1} $$

This equation describes the time evolution of the quantum states of motion $|\psi(t)\rangle$ (wave functions), from which all observables may be extracted. The total Hamiltonian* $[\hat{H} + \hat{P}(t)]$ is partitioned here into a time-independent term $\hat{H}$ and an explicitly time-dependent perturbation $\hat{P}(t)$.

---

* Before giving the Hamiltonian in its explicit relativistic form (see Section 1.2, p. 28) the time-dependent Dirac equation can be understood here as a synonym for the time-dependent Schrödinger equation.

For an isolated system ($\hat{P}(t)$ = 0) the Hamiltonian and the total energy are constants of motion, and the time-dependent Dirac equation (Eq. 1.1) reduces to its well-known time-independent version:

$$\hat{H}|\psi_m\rangle = E_m|\psi_m\rangle. \tag{1.2}$$

The stationary states $|\psi_m\rangle$ are eigenvectors of the Hamiltonian that correspond to the eigenvalues E_m. Among $|\psi_m\rangle$ is the ground state $|\psi_0\rangle$ obtained as a solution of

$$\hat{H}|\psi_0\rangle = E_0|\psi_0\rangle. \tag{1.3}$$

We are interested in the electronic problem and invoke the Born-Oppenheimer approximation. In the second-quantization representation the electronic Hamiltonian is given by

$$\hat{H} = h_{pq}\hat{a}_p^\dagger\hat{a}_q + \frac{1}{2}g_{pqrs}\hat{a}_p^\dagger\hat{a}_r^\dagger\hat{a}_s\hat{a}_q \tag{1.4}$$
$$= h_{pq}\hat{x}_{pq} + \frac{1}{2}g_{pqrs}\hat{x}_{pqrs},$$

and consists of one- and two-electron excitation operators $\hat{x}_{pq}$ and $\hat{x}_{pqrs}$ and the associated probability amplitudes h_{pq} and g_{pqrs}. To keep the form of the Hamiltonian as generic as possible at this stage, the terms h_{pq} and g_{pqrs} are not further specified. The explicit one- and two-electron integrals h_{pq} and g_{pqrs} will be detailed later in the discussion (Section 1.2, p. 29). Having solved the time-independent Dirac equation (Eq. 1.3), the ground state wave function $|\psi_0\rangle$ or any other state is obtained, and the ground state molecular electronic energy E_0 is given as the expectation value expression

$$E_0 = \langle\psi_0|\hat{H}|\psi_0\rangle = h_{pq}\langle\psi_0|\hat{x}_{pq}|\psi_0\rangle + \frac{1}{2}g_{pqrs}\langle\psi_0|\hat{x}_{pqrs}|\psi_0\rangle \tag{1.5}$$
$$= h_{pq}D_{pq} + \frac{1}{2}g_{pqrs}d_{pqrs},$$

where D_{pq} and d_{pqrs} are the one- and two-electron (reduced) density matrices, respectively. Other observables are expectation values of their corresponding operators. In principle, it is possible to approximate $|\psi_0\rangle$ to any desired accuracy using the full configuration interaction by representing the electronic state in the N-particle basis, i.e. in the basis of so-called occupation number (ON) vectors (or Slater determinants = antisymmetrized products of orbitals).

A useful quantum-chemical calculation is then a balanced choice of at least the following three approximations: (i) choice of the Hamiltonian, this is the choice of h_{pq} and g_{pqrs}, to obtain a useful approximation for the physical problem under study, (ii) approximation of the N-particle wave function represented in the basis of Slater determinants (usually called *the method*), and (iii) choice of the one-particle basis in which the orbitals are represented. The three axes which define a quantum chemical model for the molecular energy are depicted in
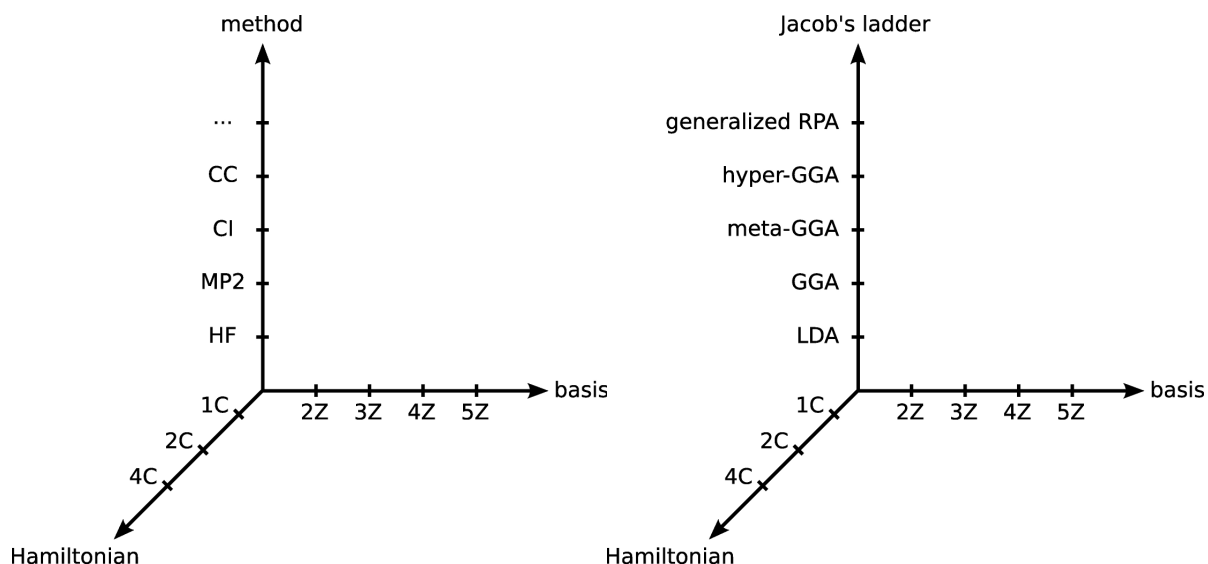
Figure 1.1: The three axes which define a quantum chemical model for the molecular energy as a wave functional (left) or as a KS density functional (right).

Fig. 1.1, one (left) as a wave functional and the other (right) as a KS density functional. The ticks along the axes represent steps along a systematic improvement of the approximation towards the exact solution (actually towards other approximations[46]). In the following the two axes, Hamiltonian and method/functional, will be highlighted separately. The Hamiltonian axis will be discussed "backwards", starting from the 4-component form, and the discussion of the method/functional axis will put more emphasis on the KS DFT approach since this is the approach studied in this thesis. A nice discussion of the choice of the basis set can be found in for instance in Ref. 47.

1.2   4-component relativistic Hamiltonian

Within the Born-Oppenheimer approximation the electronic Hamiltonian—whether being relativistic or not—has the generic form given in Eq. 1.4, with the one- and two-electron integrals,

$$h_{pq} = \langle \phi_p | \hat{h} | \phi_q \rangle \tag{1.6}$$

and

$$g_{pqrs} = \langle \phi_p \phi_r | \hat{g} | \phi_q \phi_s \rangle, \tag{1.7}$$

respectively, in which appears the one-electron operator $\hat{h}$ and the two-electron interaction operator $\hat{g}$. The specification of these operators for 4-component relativistic molecular calculations will be the subject of the present section. We will assume an orthogonal basis $\{\phi_p\}$.

The starting point in 4-component relativistic theory is the free-particle Dirac operator

$$\hat{h}_0 = \beta' mc^2 + c(\boldsymbol{\alpha} \cdot \mathbf{p}). \tag{1.8}$$

The relativistic orbitals, also called 4-spinors, have four components, and the free-particle Dirac operator is a 4×4 matrix. As done here, it is common to replace the matrix βmc^2 by

$$\beta' mc^2 = (\beta - 1_{4\times4}) mc^2 = \begin{bmatrix} 0 & 0 & 0 & 0 \\ 0 & 0 & 0 & 0 \\ 0 & 0 & -2mc^2 & 0 \\ 0 & 0 & 0 & -2mc^2 \end{bmatrix} \tag{1.9}$$

to align relativistic and NR energy scales. Here $1_{4\times4}$ is the 4×4 identity matrix. The particle mass is given as m, c is the speed of light, $\mathbf{p}$ the (canonical) linear momentum operator, and the 4×4 matrix $\boldsymbol{\alpha}$ contains in the off-diagonal blocks the vector of Pauli spin matrices in the standard representation (see also Section 1.3, p. 30):

$$\boldsymbol{\alpha} = \begin{bmatrix} 0_{2\times2} & \boldsymbol{\sigma} \\ \boldsymbol{\sigma} & 0_{2\times2} \end{bmatrix}. \tag{1.10}$$

At this stage the Hamiltonian describes not only the electron, but also its antiparticle, the positron. The one-particle Hamiltonian in the presence of external scalar (ϕ) and vector ($\mathbf{A}$) potentials can be obtained from its free-particle counterpart by the Gell-Mann minimal electromagnetic substitution prescription[48]

$$\mathbf{p} \to \mathbf{p} - q\mathbf{A} \quad \text{and} \quad E \to E + q\phi, \tag{1.11}$$

where q is the charge of the particle:

$$\hat{h} = \beta' mc^2 + c(\boldsymbol{\alpha} \cdot \mathbf{p}) - qc(\boldsymbol{\alpha} \cdot \mathbf{A}) + q\phi. \tag{1.12}$$

The minimal electromagnetic coupling requires the specification of the particle charge q. The charge of an electron is $q = -e$. This gives the one-electron Hamiltonian

$$\hat{h} = \beta' mc^2 + c(\boldsymbol{\alpha} \cdot \mathbf{p}) + ec(\boldsymbol{\alpha} \cdot \mathbf{A}) - e\phi. \tag{1.13}$$

The relativistic two-electron interaction operator $\hat{g}$ is considerably more involved since it describes all effects of retardation and magnetic interactions due to the finite speed of light. In the Coulomb gauge

$$\nabla \cdot \mathbf{A} = 0 \tag{1.14}$$

the operator $\hat{g}$ can be conveniently expanded in powers of c^{-2}. One typically considers only the zeroth-order term, the instantaneous Coulomb interaction

$$\hat{g}^{\text{Coulomb}} = \frac{\left(1_{4\times4} \otimes 1_{4\times4}\right)}{r_{12}}, \tag{1.15}$$

where the 4×4 identity matrices ($1_{4\times4}$) emphasize the 4-component structure of this operator. This operator provides spin-same, but not spin-other orbit interaction.[24] Together with the Dirac one-electron operator it constitutes the Dirac-Coulomb (DC) Hamiltonian. The first-order term is the Breit term which is usually expressed as the sum of the Gaunt term $\hat{g}^{\text{Gaunt}}$ and a gauge-dependent term $\hat{g}^{\text{gauge}}$ according to

$$\hat{g}^{\text{Breit}} = \hat{g}^{\text{Gaunt}} + \hat{g}^{\text{gauge}} \tag{1.16}$$

$$= -\frac{(c\boldsymbol{\alpha}_1) \cdot (c\boldsymbol{\alpha}_2)}{c^2 r_{12}} - \frac{(c\boldsymbol{\alpha}_1 \cdot \nabla_1)(c\boldsymbol{\alpha}_2 \cdot \nabla_2)r_{12}}{2c^2}.$$

In the NR limit $\hat{g}$ reduces to the instantaneous Coulomb interaction. All contributions beyond the zeroth-order term are neglected in this thesis. This specific choice of a Hamiltonian fixes h_{pq} and g_{pqrs}. In the second-quantization representation and the Born-Oppenheimer approximation and in the absence of external fields other than the scalar potential v^{ext} created by the nuclei, h_{pq} and g_{pqrs} are given by

$$h_{pq} = \langle \phi_p | \hat{h} | \phi_q \rangle \tag{1.17}$$

$$= \beta' mc^2 \delta_{pq} + c \langle \phi_p | (\boldsymbol{\alpha} \cdot \mathbf{p}) | \phi_q \rangle + \langle \phi_p | v^{\text{ext}} | \phi_q \rangle$$

$$= \beta' mc^2 \delta_{pq} + c \langle \phi_p | (\boldsymbol{\alpha} \cdot \mathbf{p}) | \phi_q \rangle - \sum_K Z_K \int d\mathbf{r} \, \frac{\Omega_{pq}(\mathbf{r})}{|\mathbf{R}_K - \mathbf{r}|}$$

$$g_{pqrs} = \iint d\mathbf{r}_1 d\mathbf{r}_2 \, \frac{\Omega_{pq}(\mathbf{r}_1)\Omega_{rs}(\mathbf{r}_2)}{|\mathbf{r}_2 - \mathbf{r}_1|}. \tag{1.18}$$

Here $\mathbf{R}_K$ and Z_K are the position and charge of nucleus K, respectively, and Ω_{pq} is the orbital overlap distribution $\phi_p^\dagger \phi_q$.

It is important to note that the DC Hamiltonian is not the last tick on the Hamiltonian-axis in Fig. 1.1: all two-electron interactions beyond the instantaneous Coulomb interaction (retardation and magnetic interactions) are neglected and the frequently used term "fully relativistic calculation" in combination with the DC Hamiltonian is therefore misleading.

1.3   Dirac matrices

The following brief discussion of the Dirac matrices, their explicit form and physical content will be rewarding because a knowledge of their transformation properties under symmetry operations can save a substantial amount of computation time and programming effort.

Start from the following four 2×2 matrices σ_i (with $i = 0, 1, 2, 3$)

$$\sigma_0 = \begin{bmatrix} 1 & 0 \\ 0 & 1 \end{bmatrix} = 1_{2\times2} \qquad \sigma_1 = \begin{bmatrix} 0 & 1 \\ 1 & 0 \end{bmatrix} \qquad \sigma_2 = \begin{bmatrix} 0 & -i \\ i & 0 \end{bmatrix} \qquad \sigma_3 = \begin{bmatrix} 1 & 0 \\ 0 & -1 \end{bmatrix}, \qquad (1.19)$$

where $\sigma_{1,2,3}$ are the well-known Pauli spin matrices $\sigma_{x,y,z}$ in the standard representation. For later reference it is worth to note the useful mapping between the Pauli spin matrices times imaginary i and the quaternion units[*] ǐ, ǰ, and ǩ:

$$i\sigma_z \leftrightarrow \check{i}, \quad i\sigma_y \leftrightarrow \check{j}, \quad i\sigma_x \leftrightarrow \check{k} \qquad (1.20)$$

As pointed out by Jordan,[50] they have the same algebra. Next, form the 4×4 matrices A_i and B_i defined by

$$A_i = 1_{2\times2} \otimes \sigma_i \qquad \text{and} \qquad B_i = \sigma_i \otimes 1_{2\times2}. \qquad (1.21)$$

The products $M_{ij} = A_i B_j$ are the 16 Dirac matrices.[51,52] In a compact notation they are given in Tab. 1.1 or explicitly in Tab. 1.2. These 16 Dirac matrices have many interesting properties,[28,51] i.e. they are Hermitian, 15 of them are traceless, and most notably they form a complete set for any 4×4 matrix. This means that the perturbation operators in Section 2 can be defined by a linear combination of these 16 Dirac matrices. Apart from being esthetically appealing they have physical content (see Tab. 1.3) and possess transformation properties under spatial and time-reversal symmetry operations which will be explored in the following and which can be exploited in calculations and programming.

---

[*] A quaternion number q is given by $q = a + b\check{j} = \text{Re}(a) + \text{Im}(a)\check{i} + \text{Re}(b)\check{j} + \text{Im}(b)\check{k}$, with $\check{i}^2 = \check{j}^2 = \check{k}^2 = -1$, $\check{i}\check{j} = \check{k}$, $\check{j}\check{k} = \check{i}$, and $\check{k}\check{i} = \check{j}$. The quaternion units $\check{i}$, $\check{j}$, and $\check{k}$ anticommute. Quaternion numbers do not commute under multiplication.[49]

Table 1.1: 16 Dirac matrices M_{ij} in compact notation.

$$M_{00} = 1_{4\times4} \qquad M_{01} = \Sigma_x \qquad M_{02} = \Sigma_y \qquad M_{03} = \Sigma_z$$

$$M_{10} = \gamma^5 \qquad M_{11} = \alpha_x \qquad M_{12} = \alpha_y \qquad M_{13} = \alpha_z$$

$$M_{20} = -i\beta\gamma^5 \qquad M_{21} = -i\beta\alpha_x \qquad M_{22} = -i\beta\alpha_y \qquad M_{23} = -i\beta\alpha_z$$

$$M_{30} = \beta \qquad M_{31} = \beta\Sigma_x \qquad M_{32} = \beta\Sigma_y \qquad M_{33} = \beta\Sigma_z$$

Table 1.2: Explicit Dirac matrices M_{ij}.

$$1_{4\times4} = \begin{bmatrix} 1 & 0 & 0 & 0 \\ 0 & 1 & 0 & 0 \\ 0 & 0 & 1 & 0 \\ 0 & 0 & 0 & 1 \end{bmatrix} \qquad \Sigma_x = \begin{bmatrix} 0 & 1 & 0 & 0 \\ 1 & 0 & 0 & 0 \\ 0 & 0 & 0 & 1 \\ 0 & 0 & 1 & 0 \end{bmatrix} \qquad \Sigma_y = \begin{bmatrix} 0 & -i & 0 & 0 \\ i & 0 & 0 & 0 \\ 0 & 0 & 0 & -i \\ 0 & 0 & i & 0 \end{bmatrix} \qquad \Sigma_z = \begin{bmatrix} 1 & 0 & 0 & 0 \\ 0 & -1 & 0 & 0 \\ 0 & 0 & 1 & 0 \\ 0 & 0 & 0 & -1 \end{bmatrix}$$

$$\gamma^5 = \begin{bmatrix} 0 & 0 & 1 & 0 \\ 0 & 0 & 0 & 1 \\ 1 & 0 & 0 & 0 \\ 0 & 1 & 0 & 0 \end{bmatrix} \qquad \alpha_x = \begin{bmatrix} 0 & 0 & 0 & 1 \\ 0 & 0 & 1 & 0 \\ 0 & 1 & 0 & 0 \\ 1 & 0 & 0 & 0 \end{bmatrix} \qquad \alpha_y = \begin{bmatrix} 0 & 0 & 0 & -i \\ 0 & 0 & i & 0 \\ 0 & -i & 0 & 0 \\ i & 0 & 0 & 0 \end{bmatrix} \qquad \alpha_z = \begin{bmatrix} 0 & 0 & 1 & 0 \\ 0 & 0 & 0 & -1 \\ 1 & 0 & 0 & 0 \\ 0 & -1 & 0 & 0 \end{bmatrix}$$

$$-i\beta\gamma^5 = \begin{bmatrix} 0 & 0 & -i & 0 \\ 0 & 0 & 0 & -i \\ i & 0 & 0 & 0 \\ 0 & i & 0 & 0 \end{bmatrix} \qquad -i\beta\alpha_x = \begin{bmatrix} 0 & 0 & 0 & -i \\ 0 & 0 & -i & 0 \\ 0 & i & 0 & 0 \\ i & 0 & 0 & 0 \end{bmatrix} \qquad -i\beta\alpha_y = \begin{bmatrix} 0 & 0 & 0 & -1 \\ 0 & 0 & 1 & 0 \\ 0 & 1 & 0 & 0 \\ -1 & 0 & 0 & 0 \end{bmatrix} \qquad -i\beta\alpha_z = \begin{bmatrix} 0 & 0 & -i & 0 \\ 0 & 0 & 0 & i \\ i & 0 & 0 & 0 \\ 0 & -i & 0 & 0 \end{bmatrix}$$

$$\beta = \begin{bmatrix} 1 & 0 & 0 & 0 \\ 0 & 1 & 0 & 0 \\ 0 & 0 & -1 & 0 \\ 0 & 0 & 0 & -1 \end{bmatrix} \qquad \beta\Sigma_x = \begin{bmatrix} 0 & 1 & 0 & 0 \\ 1 & 0 & 0 & 0 \\ 0 & 0 & 0 & -1 \\ 0 & 0 & -1 & 0 \end{bmatrix} \qquad \beta\Sigma_y = \begin{bmatrix} 0 & -i & 0 & 0 \\ i & 0 & 0 & 0 \\ 0 & 0 & 0 & i \\ 0 & 0 & -i & 0 \end{bmatrix} \qquad \beta\Sigma_z = \begin{bmatrix} 1 & 0 & 0 & 0 \\ 0 & -1 & 0 & 0 \\ 0 & 0 & -1 & 0 \\ 0 & 0 & 0 & 1 \end{bmatrix}$$

Table 1.3: Dirac matrices M_{ij} and the physical meaning of the corresponding generalized densities $\psi^\dagger M_{ij}\psi$. This table points to sections where these densities are further explored/used. The evaluation of these densities is described in Note B, p. 185.

M_{ij}	$\psi^\dagger M_{ij}\psi$	
$1_{4\times4}$	number density	see Section 5.2, p. 95 and Section 5.3, p. 102
$\Sigma_{x,y,z}$	spin density in x, y, z-direction	see Section 3.1, p. 63
γ^5	γ^5 density or chirality density	see Section 5.6, p. 124
$\alpha_{x,y,z}$	$(1/c)\times$ velocity density in x, y, z-direction	see Section 5.3, p. 102 and Section 5.4, p. 110

Time reversal

The antilinear time reversal operator $\hat{K}$ reverses the time arrow

$$\hat{K}\psi(t) = \bar{\psi}(-t), \tag{1.22}$$

reverses all vectors that describe the *movement* at a specific time

$$\hat{K}\mathbf{v}\hat{K}^{-1} = -\mathbf{v}, \tag{1.23}$$

flips the spin, but keeps positions and orientations unchanged. In the 4-component relativistic framework it is given by

$$\hat{K} = -i\Sigma_y\hat{K}_o, \tag{1.24}$$

with Σ_y defined previously (Tab. 1.2) and $\hat{K}_o$ being the complex conjugation operator. The latter is the time reversal operator for scalar wave functions. In the case of systems with fermion symmetry a double time reversal operating on the corresponding wave function yields

$$\hat{K}^2\psi(t) = -\psi(t). \tag{1.25}$$

The operation of $\hat{K}$ on fermion basis functions $\{\phi\}$ generates their complementary partners (Kramers partners) $\{\bar{\phi}\}$. The union of both sets is the Kramers restricted basis.

Table 1.4: Time reversal symmetry of the 16 Dirac matrices M_{ij}.

$1_{4\times4} : t = +1$	$\Sigma_x : t = -1$	$\Sigma_y : t = -1$	$\Sigma_z : t = -1$
$\gamma^5 : t = +1$	$\alpha_x : t = -1$	$\alpha_y : t = -1$	$\alpha_z : t = -1$
$-i\beta\gamma^5 : t = -1$	$-i\beta\alpha_x : t = +1$	$-i\beta\alpha_y : t = +1$	$-i\beta\alpha_z : t = +1$
$\beta : t = +1$	$\beta\Sigma_x : t = -1$	$\beta\Sigma_y : t = -1$	$\beta\Sigma_z : t = -1$

It can be easily verified[28] that a Hermitian time reversal symmetric ($t = +1$) or antisymmetric ($t = -1$) operator $\hat{\Omega}$ represented in the Kramers restricted basis

$$\Omega = \begin{bmatrix} \langle\phi_p|\hat{\Omega}|\phi_q\rangle & \langle\phi_p|\hat{\Omega}|\bar{\phi}_q\rangle \\ \langle\bar{\phi}_p|\hat{\Omega}|\phi_q\rangle & \langle\bar{\phi}_p|\hat{\Omega}|\bar{\phi}_q\rangle \end{bmatrix} = \begin{bmatrix} \Omega_{pq} & \Omega_{p\bar{q}} \\ \Omega_{\bar{p}q} & \Omega_{\bar{p}\bar{q}} \end{bmatrix} \tag{1.26}$$

has the structure*

$$\Omega = \begin{bmatrix} \Omega_{pq} & \Omega_{p\bar{q}} \\ -t\Omega^{\star}_{p\bar{q}} & t\Omega^{\star}_{pq} \end{bmatrix}. \tag{1.27}$$

This means that for $t = +1$, time reversal symmetry allows to block diagonalize Ω and to reduce the computational effort (and memory requirement) by a factor of two, however at the price of introducing quaternion algebra. This strategy is not restricted to Hermitian ($h = +1$) time reversal symmetric ($t = +1$) operators since $h = +1$, $t = -1$ operators can be incorporated in the symmetry scheme by extracting a purely imaginary phase, which makes them $h = -1$, $t = +1$. Operators general with respect to time reversal symmetry can always be decomposed in to a $t = +1$ and $t = -1$ part. To some extent time reversal symmetry recovers spin symmetry lost in the relativistic framework.

It is a good exercise to verify the time reversal symmetry of the 16 Dirac matrices M_{ij} (Tabs. 1.1 and 1.2) by checking t in

$$\hat{K}M_{ij}\hat{K}^{-1} = tM_{ij}, \tag{1.28}$$

with the result listed in Tab. 1.4.

---

* In this context t does not represent the time.

Spatial symmetry

The use of time reversal symmetry allows to reduce the dimension of the problem by a factor of two at the price of introducing quaternion algebra. Additional symmetry savings can be achieved by the use of spatial symmetry which enables in some cases to reduce the algebra from quaternion to complex or even real algebra (see for instance Ref. 53).

A good starting point for studying the spatial symmetry of the Dirac matrices M_{ij} is again the free-particle Dirac Hamiltonian

$$\hat{h}_o = \beta' mc^2 + c(\boldsymbol{\alpha} \cdot \mathbf{p}), \tag{1.29}$$

which transforms as the totally symmetric irreducible representation Γ_o. This means that β', the unprimed β, and $(\boldsymbol{\alpha} \cdot \mathbf{p})$, all transform as Γ_o. The momentum operator that transforms like the coordinates $(\Gamma_\mathbf{r})$ implies together with a totally symmetric $(\boldsymbol{\alpha}{\cdot}\mathbf{p})$ that also the three matrices α_x, α_y, and α_z transform as the corresponding coordinates Γ_x, Γ_y, and Γ_z. The transformation of the chirality matrix γ^5 as the parity inversion Γ_{xyz} can be deduced by writing γ^5 as

$$\gamma^5 = \alpha_x \alpha_y \alpha_z. \tag{1.30}$$

This is also in line with the requirement that the inversion of parity implies a switch of chirality. Finally, remembering that

$$\boldsymbol{\Sigma} = \left(M_{01}, M_{02}, M_{03}\right) = \gamma^5 \boldsymbol{\alpha} \tag{1.31}$$

means that $\boldsymbol{\Sigma}$ has to transform like the vector of rotations ($\Gamma_\mathbf{R}$).

1.4   Eliminating relativistic effects

Relativistic effects can be defined as the differences between the physics at a finite speed of light ($c \approx 137.0359998\, a_{\mathrm{o}} E_{\mathrm{h}}/\hbar$) and the NR situation at $c = \infty$.[9] Relativistic effects are usually divided into scalar relativistic and spin–orbit effects. Scalar relativistic effects are related to the change in kinematics of electrons moving at significant fractions of the finite speed of light. The effect of spin–orbit coupling can be regarded as magnetic induction, the coupling of the electron spin to the induced magnetic field due to the moving charges of nuclei and other charged particles (e.g. electrons) in the rest frame of the electron. In NR theory the spin and spatial degrees of freedom are completely decoupled, and spin and—in the case of atoms—orbital angular momenta have good quantum numbers. With spin–orbit coupling, this NR symmetry is lost.

The differences between the physics at a finite speed of light and the NR situation at $c = \infty$ can not be measured in experiment. Nevertheless, the assessment of relativistic effects is more than just a hypothetical discussion. If they are negligible, the computationally advantageous NR approximation is a good approximation. However, especially for heavy elements where core electrons obtain considerable velocities due to the significant nuclear charge, relativistic corrections have to be accounted for. Corrections due to scalar relativity can be included in standard NR quantum chemical codes at almost no additional computational cost through the use of relativistic pseudopotentials[54] or approximate scalar relativistic Hamiltonians.[55–59] This is not true in the case of spin–orbit coupling which requires a 2-component description and complex algebra.

Having a 4-component code at hand it is possible to go in the other direction and start, for instance, from a DC Hamiltonian and subsequently eliminate relativistic effects. Coming back to the definition of relativistic effects, the obvious ansatz is to increase the speed of light. This will approach the NR limit and eventually eliminate all relativistic effects. Instead of eliminating all relativistic effects it is possible to separate out the spin–orbit interaction by keeping scalar relativity and a 4-component framework.[24,60] The problem of separating out the spin-dependent terms from the Dirac equation

$$
\begin{bmatrix} \hat{V} & c(\boldsymbol{\sigma} \cdot \mathbf{p}) \\ c(\boldsymbol{\sigma} \cdot \mathbf{p}) & \hat{V} - 2mc^2 \end{bmatrix} \begin{bmatrix} \psi^{\mathrm{L}} \\ \psi^{\mathrm{S}} \end{bmatrix} = E \begin{bmatrix} \psi^{\mathrm{L}} \\ \psi^{\mathrm{S}} \end{bmatrix},
\tag{1.32}
$$

given here in the 2-spinor form, is that the spin appears in the kinetic energy operator $c(\boldsymbol{\sigma} \cdot \mathbf{p})$. The ansatz independently proposed by Dyall[61] and Kutzelnigg[62] is the nonunitary transformation

$$
\begin{bmatrix} \psi^{\mathrm{L}} \\ \psi^{\mathrm{S}} \end{bmatrix} = \begin{bmatrix} 1_{2\times2} & 0_{2\times2} \\ 0_{2\times2} & \frac{1}{2mc^2}(\boldsymbol{\sigma} \cdot \mathbf{p}) \end{bmatrix} \begin{bmatrix} \psi^{\mathrm{L}} \\ \phi^{\mathrm{S}} \end{bmatrix},
\tag{1.33}
$$

leading to the so-called modified Dirac equation

$$\begin{bmatrix} \hat{V} & \hat{T} \\ \hat{T} & \frac{1}{4m^2c^2}(\boldsymbol{\sigma}\cdot\mathbf{p})\hat{V}(\boldsymbol{\sigma}\cdot\mathbf{p})-\hat{T} \end{bmatrix}\begin{bmatrix} \psi^{\mathrm{L}} \\ \phi^{\mathrm{S}} \end{bmatrix} = E\begin{bmatrix} 1_{2\times2} & 0_{2\times2} \\ 0_{2\times2} & \frac{1}{2mc^2}\hat{T} \end{bmatrix}\begin{bmatrix} \psi^{\mathrm{L}} \\ \phi^{\mathrm{S}} \end{bmatrix},\qquad(1.34)$$

where the NR kinetic energy operator

$$\frac{1}{2m}(\boldsymbol{\sigma}\cdot\mathbf{p})(\boldsymbol{\sigma}\cdot\mathbf{p}) = \frac{\mathbf{p}\cdot\mathbf{p}}{2m} = \hat{T}\qquad(1.35)$$

has been used. Spin-dependence can now be separated out using the Dirac identity (Eq. 0.2)

$$(\boldsymbol{\sigma}\cdot\mathbf{p})\hat{V}(\boldsymbol{\sigma}\cdot\mathbf{p}) = \mathbf{p}\hat{V}\cdot\mathbf{p} + i\boldsymbol{\sigma}\cdot\mathbf{p}\hat{V}\times\mathbf{p},\qquad(1.36)$$

and the modified Dirac Hamiltonian $\tilde{\hat{H}}$ can be given by a sum of a spin-free and a spin-dependent term

$$\tilde{\hat{H}} = \begin{bmatrix} \hat{V} & \hat{T} \\ \hat{T} & \frac{1}{4m^2c^2}\{\mathbf{p}\hat{V}\cdot\mathbf{p}-\hat{T}\} \end{bmatrix} + \begin{bmatrix} 0_{2\times2} & 0_{2\times2} \\ 0_{2\times2} & \frac{1}{4m^2c^2}\{i\boldsymbol{\sigma}\cdot\mathbf{p}\hat{V}\times\mathbf{p}\} \end{bmatrix}.\qquad(1.37)$$

This equation can be cast in quaternion formulation in a very simple form.[60] The contribution due to spin–orbit coupling can then be eliminated by deleting the quaternion imaginary parts.

Another nonunitary transformation

$$\begin{bmatrix} \psi^{\mathrm{L}} \\ \psi^{\mathrm{S}} \end{bmatrix} = \begin{bmatrix} 1_{2\times2} & 0_{2\times2} \\ 0_{2\times2} & \frac{1}{c}1_{2\times2} \end{bmatrix}\begin{bmatrix} \psi^{\mathrm{L}} \\ \phi^{\mathrm{S}} \end{bmatrix}\qquad(1.38)$$

in the NR limit $(c\to\infty)^*$ yields the 4-component NR equation

$$\begin{bmatrix} \hat{V} & (\boldsymbol{\sigma}\cdot\mathbf{p}) \\ (\boldsymbol{\sigma}\cdot\mathbf{p}) & -2m \end{bmatrix}\begin{bmatrix} \psi^{\mathrm{L}} \\ \phi^{\mathrm{S}} \end{bmatrix} = E\begin{bmatrix} 1_{2\times2} & 0_{2\times2} \\ 0_{2\times2} & 0_{2\times2} \end{bmatrix}\begin{bmatrix} \psi^{\mathrm{L}} \\ \phi^{\mathrm{S}} \end{bmatrix}\qquad(1.39)$$

proposed by Lévy-Leblond.[65] This equation is equivalent to the Schrödinger equation.[64] Note that both nonunitary transformations change the small-small block of the metric.[28] Both the spin-free modified Dirac Hamiltonian and the Lévy-Leblond Hamiltonian will be frequently used for the isolation and discussion of scalar relativistic and spin–orbit effects.

---

* With the restrictions: $|E| \ll c^2$ and a nonsingular scalar potential ϕ. In practice this means that attention is restricted to the positive-energy solutions (a separate limit exists for negative-energy solutions[63]), and the NR limit is only valid for extended nuclei.[64]

1.5 Nonrelativistic vs. relativistic charge and charge current density

In Section 1.2, p. 28, external fields have been introduced through the external vector and scalar potential, $\mathbf{A}$ and ϕ, respectively, invoking the Gell-Mann minimal electromagnetic substitution prescription (Eq. 1.11) which gave the relativistic one-electron Hamiltonian (Eq. 1.13)

$$\hat{h}_{\mathrm{R}} = \beta' mc^2 + c(\boldsymbol{\alpha} \cdot \mathbf{p}) + ec(\boldsymbol{\alpha} \cdot \mathbf{A}) - e\phi. \tag{1.40}$$

Starting from this 4-component relativistic (subscript "R") one-electron Hamiltonian the 4-component relativistic expressions for the central quantities in this thesis, the charge and charge current density, will be identified closely following Refs. 24 and 66. This analysis will be performed in parallel starting from the NR one-electron Hamiltonian in order to compare the NR and relativistic final expressions. It will be convenient to write the NR free-particle Hamiltonian in the form

$$\hat{h}_{\mathrm{NR,o}} = \frac{p^2}{2m} = \frac{1}{2m}(\boldsymbol{\sigma} \cdot \mathbf{p})(\boldsymbol{\sigma} \cdot \mathbf{p}), \tag{1.41}$$

where the Dirac identity (Eq. 0.2) has been used "backwards". Without an external vector potential to interact with, the spin remains "hidden". The external potentials can be introduced again using Eq. 1.11 which yields the NR one-electron Hamiltonian in the presence of external fields

$$\hat{h}_{\mathrm{NR}} = \frac{p^2}{2m} + \frac{e}{2m}(\boldsymbol{\sigma} \cdot \mathbf{p})(\boldsymbol{\sigma} \cdot \mathbf{A}) + \frac{e}{2m}(\boldsymbol{\sigma} \cdot \mathbf{A})(\boldsymbol{\sigma} \cdot \mathbf{p}) + \frac{e^2}{2m}(\boldsymbol{\sigma} \cdot \mathbf{A})(\boldsymbol{\sigma} \cdot \mathbf{A}) - e\phi. \tag{1.42}$$

From now on attention will be restricted to the interaction parts of the corresponding Hamiltonians

$$\hat{h}_{\mathrm{NR}}^{\mathrm{int}} = \frac{e}{2m}(\boldsymbol{\sigma} \cdot \mathbf{p})(\boldsymbol{\sigma} \cdot \mathbf{A}) + \frac{e}{2m}(\boldsymbol{\sigma} \cdot \mathbf{A})(\boldsymbol{\sigma} \cdot \mathbf{p}) + \frac{e^2}{2m}(\boldsymbol{\sigma} \cdot \mathbf{A})(\boldsymbol{\sigma} \cdot \mathbf{A}) - e\phi \tag{1.43}$$

$$= \frac{e}{2m}[\mathbf{p}, \mathbf{A}]_+ + \frac{e}{2m}(\boldsymbol{\sigma} \cdot \mathbf{B}) + \frac{e^2}{2m}(\boldsymbol{\sigma} \cdot \mathbf{A})(\boldsymbol{\sigma} \cdot \mathbf{A}) - e\phi$$

$$\hat{h}_{\mathrm{R}}^{\mathrm{int}} = ec(\boldsymbol{\alpha} \cdot \mathbf{A}) - e\phi, \tag{1.44}$$

and the corresponding interaction energies are

$$E_{\mathrm{NR}}^{\mathrm{int}} = -e\langle\psi| \left[\phi - \frac{1}{2m}[\mathbf{p}, \mathbf{A}]_+ - \frac{1}{2m}(\boldsymbol{\sigma} \cdot \mathbf{B}) - \frac{e}{2m}A^2 \right] |\psi\rangle \tag{1.45}$$

$$E_{\mathrm{R}}^{\mathrm{int}} = -e\langle\psi| \left[\phi - c(\boldsymbol{\alpha} \cdot \mathbf{A}) \right] |\psi\rangle. \tag{1.46}$$

Note that the NR Hamiltonian (or the corresponding energy) contains the so-called paramagnetic term, which is linear in the vector potential $\mathbf{A}$, and the so-called diamagnetic term, which is quadratic in $\mathbf{A}$. The simpler relativistic expression lacks this quadratic term and a distinction in paramagnetic and diamagnetic contributions can not be made at this stage.

Using the *relativistic* interaction functional introduced by Schwarzschild[67]

$$E_{\mathrm{R}}^{\mathrm{int}} = \int \mathrm{d}\mathbf{r} \left[\phi\rho - \mathbf{A} \cdot \mathbf{j} \right], \tag{1.47}$$

the charge and charge current densities can be identified as the functional derivatives

$$\rho = \frac{\delta E^{\mathrm{int}}}{\delta \phi} \qquad \text{and} \qquad \mathbf{j} = -\frac{\delta E^{\mathrm{int}}}{\delta \mathbf{A}}. \tag{1.48}$$

Using Eqs. 1.45 and 1.46, the corresponding charge and current densities are given by*

$$\rho_{\mathrm{NR}} = -e\psi^{\dagger}\psi \tag{1.49}$$

$$\rho_{\mathrm{R}} = -e\psi^{\dagger}\psi \tag{1.50}$$

and

$$\mathbf{j}_{\mathrm{NR}} = -\frac{e}{2m}\left(\psi^{\dagger}\mathbf{p}\psi - \psi^{T}\mathbf{p}\psi^{\star}\right) - \frac{e}{2m}\nabla \times \psi^{\dagger}\boldsymbol{\sigma}\psi - \frac{e^{2}}{m}\psi^{\dagger}\mathbf{A}\psi \tag{1.51}$$

$$\mathbf{j}_{\mathrm{R}} = -e\psi^{\dagger}c\boldsymbol{\alpha}\psi. \tag{1.52}$$

The first two right-hand side terms in Eq. 1.51 arise from the paramagnetic interaction contribution, which has been separated into the spin-free orbital term and a spin-dependent (spin-current density) term using the Dirac identity. The latter is the curl of the spin density. The third right-hand side term in Eq. 1.51 is the diamagnetic current density. The situation is again considerably simpler in the relativistic case (Eq. 1.52).

A very similar expression to Eq. 1.51 can be achieved by the Gordon decomposition[27,68] of the 4-component relativistic current density $\mathbf{j}_{\mathrm{R}}$ (here given for the time-independent case)

$$\mathbf{j}_{\mathrm{R}} = -\frac{e}{2m}\left(\psi^{\dagger}\beta\mathbf{p}\psi - \psi^{T}\beta\mathbf{p}\psi^{\star}\right) - \frac{e}{2m}\nabla \times \psi^{\dagger}\beta\boldsymbol{\Sigma}\psi - \frac{e^{2}}{m}\psi^{\dagger}\beta\mathbf{A}\psi. \tag{1.53}$$

The corresponding Dirac matrices are defined in Tab. 1.2.

---

* Subscripts "NR" and "R" imply "NR" and "R" wave functions.

More insight into the NR and relativistic current density expressions can be obtained when remembering that for classical point charges q the charge current density is given by $\mathbf{j} = nq\mathbf{v} = \rho\mathbf{v}$, with n being the particle density and $\mathbf{v}$ the average velocity. The NR and relativistic velocity operators can be obtained from Heisenberg equation of motion

$$\frac{d\mathbf{r}}{dt} = -i[\mathbf{r}, \hat{h}] \begin{cases} -i[\mathbf{r}, \hat{h}_{\mathrm{NR}}] &= \frac{\mathbf{p}}{m} \\ \\ -i[\mathbf{r}, \hat{h}_{\mathrm{R}}] &= c\boldsymbol{\alpha} = c\boldsymbol{\sigma}^{\mathrm{LS}} + c\boldsymbol{\sigma}^{\mathrm{SL}} \end{cases} \tag{1.54}$$

The correspondence between the relativistic velocity operator, which has been further split up into the large-small (LS) and small-large (SL) sub-blocks, and the corresponding current density operator is evident. It is however less clear how the second and third right-hand side terms in Eq. 1.51 relate to the NR velocity operator.

Finally, the correspondence between the NR and relativistic velocity operators in Eq. 1.54 can be rationalized by recalling the NR limit of the coupling between the large and small component (see for instance Ref. 64)

$$\lim_{c\to\infty} 2mc\,\psi^{\mathrm{S}} = (\boldsymbol{\sigma}\cdot\mathbf{p})\psi^{\mathrm{L}}. \tag{1.55}$$

1.6   Infinite-order 2-component relativistic Hamiltonian

The presently most rigorous treatment of relativistic effects is based on 4-component relativistic Hamiltonians which are accurate to various orders in powers of c^{-2}. The relatively high computational effort of 4-component relativistic calculations (albeit not the scaling with system size) has motivated the development of less expensive 2-component relativistic Hamiltonians, e.g. the Barysz-Sadlej-Snijders[69,70] (BSS) Hamiltonian and the popular Douglas-Kroll-Hess[55–57] (DKH) and zeroth-order regular approximation[58,59] (ZORA) Hamiltonians.

Within the finite basis approximation, the provocative "four-components good, two-components bad!" attitude[*] is today superseded by 2-component schemes performed at the matrix level, which offer an arbitrary (including infinite) order 2-component (IOTC) relativistic Hamiltonians and completely avoid the so-called picture change error discussed for instance in Ref. 66.

The one-step IOTC Hamiltonian, employed in this thesis especially for development and testing but also for production (Section 4, p. 77), has been developed by Jensen and Iliaš,[71] and by Iliaš and Saue.[72] A similar scheme for obtaining an infinite-order 2-component relativistic Hamiltonian at the matrix level has been reported by Liu and Peng[73] and by Kutzelnigg and Liu[74,75] under the name of exact quasi-relativistic (XQR) theory.

The decoupling of the positive and negative eigensolutions which leads to the IOTC Hamiltonian can be achieved either by elimination of the small components or by a unitary decoupling Foldy-Wouthuysen (FW) transformation[76,77]

$$\hat{U}^\dagger \hat{h}_\mathrm{R} \hat{U} = \begin{bmatrix} \hat{h}_+ & 0 \\ 0 & \hat{h}_- \end{bmatrix}. \tag{1.56}$$

It is useful[63] to write the transformation matrix $\hat{U}$ as the product of two transformations

$$\hat{U} = \hat{W}_1 \hat{W}_2 = \begin{bmatrix} 1 & -\hat{R}^\dagger \\ \hat{R} & 1 \end{bmatrix} \begin{bmatrix} \hat{N}_+^{-1} & 0 \\ 0 & \hat{N}_-^{-1} \end{bmatrix}, \tag{1.57}$$

with $\hat{N}_+ = \sqrt{1 + \hat{R}^\dagger \hat{R}}$ and $\hat{N}_- = \sqrt{1 + \hat{R}\hat{R}^\dagger}$. The first transformation $\hat{W}_1$ provides decoupling, whereas the second, $\hat{W}_2$ ensures renormalization of the eigenvectors.

The exact (state-specific) decoupling operator

$$\hat{R} = \frac{1}{2mc} B(E)(\boldsymbol{\sigma} \cdot \mathbf{p}), \quad \text{with} \quad B(E) = \left[1 + \frac{E-V}{2mc^2} \right]^{-1}, \tag{1.58}$$

is energy dependent[72] and known only *a posteriori*.[†] However, in the finite basis approximation the exact decoupling matrix can be obtained by a solution of the one-electron Dirac equation in

---

[*] This is part of the title of Ref. 14.   [†] Iliaš and Saue[72] use the state-universal coupling operator after Heully *et al.*[77]

a molecular field.[72] This is usually a modest investment compared to the computational savings (see Ref. 72 for more details).

The contribution of the 2-electron spin–orbit coupling can be introduced in a mean-field fashion,[78] for instance using the AMFI[79] code.

1.7   Jacob's ladder: DFT vs. WFT

Returning to Fig. 1.1, this section will discuss the so-called Jacob's ladder in DFT[37,80] (right panel in Fig. 1.1) by a comparative contrasting with a corresponding "WFT Jacob's ladder" (left panel in Fig. 1.1).

Within KS ground state DFT the system is assumed to be a noninteracting ensemble. For a noninteracting system one occupation number (ON) vector is sufficient. The clever idea of Kohn and Sham was however to define this ON vector $|o\rangle$ such that the density of the KS system equals the exact density of the interacting system

$$\langle o|\hat{n}|o\rangle = n^{\mathrm{KS}} = n = \langle \psi_o|\hat{n}|\psi_o\rangle. \tag{1.59}$$

All effects due to exchange and correlation are cast in the ground state exchange-correlation (XC) energy E_{XC} which can be proved[35] to be a functional of the total electron density n. In the KS formalism, the exact energy is expressed as

$$E_o = h_{ii} + \frac{1}{2}g_{iijj} + E_{\mathrm{XC}}[n], \tag{1.60}$$

with the orbital indices defined on p. 21. This equation will be adapted later for hybrid functionals. The challenge is however that this XC energy functional is known neither exactly nor as a systematic series of approximations converging in every case to the exact answer.[37] This is probably the major practical difference between DFT and WFT. The latter offers several systematic series (CC or CI) that converge to the exact answer in every case. This does not mean that this series can actually be followed all the way in practice but in contrast to DFT the challenge in going one step further along the series is purely technical. In the absence of the exact XC energy functional, practical KS DFT approximates the XC energy by an integral over an approximate XC energy density F

$$E_{\mathrm{XC}} = \int \mathrm{d}\mathbf{r}\, \varepsilon_{\mathrm{XC}}[n] \approx \int \mathrm{d}\mathbf{r}\, F(\{U\}), \tag{1.61}$$

where F depends on set of local arguments $\{U\}$. Depending on the actual set $\{U\}$, the approximate XC functionals can be organized into the rungs of the Jacob's ladder in DFT[37,80] (right

panel in Fig. 1.1), which separates the Hartree world from the "heaven of chemical accuracy". The first four rungs are the local density approximation (LDA)[36]

$$F^{\mathrm{LDA}} = F^{\mathrm{LDA}}(n_\uparrow, n_\downarrow),$$

the generalized gradient approximation (GGA)[81]

$$F^{\mathrm{GGA}} = F^{\mathrm{GGA}}(n_\uparrow, n_\downarrow, \nabla n_\uparrow, \nabla n_\downarrow),$$

the meta-GGA[82]

$$F^{\mathrm{m\text{-}GGA}} = F^{\mathrm{m\text{-}GGA}}(n_\uparrow, n_\downarrow, \nabla n_\uparrow, \nabla n_\downarrow, \tau_\uparrow, \tau_\downarrow),$$

and the hyper-GGA[80]

$$F^{\mathrm{h\text{-}GGA}} = F^{\mathrm{h\text{-}GGA}}(n_\uparrow, n_\downarrow, \nabla n_\uparrow, \nabla n_\downarrow, \tau_\uparrow, \tau_\downarrow, \varepsilon_{\mathrm{X}\uparrow}, \varepsilon_{\mathrm{X}\downarrow}).$$

Here $\uparrow$ ($\downarrow$) represents the spin-up (-down) portion of the density (n), density gradient (∇n), kinetic energy density (τ), and exact exchange energy density (ε_X). The ground state energy of semi-empirical global hyper-GGAs

$$E_0 = h_{ii} + \frac{1}{2}\big[g_{iijj} - \lambda g_{ijji}\big] + \int \mathrm{d}\mathbf{r}\ F \tag{1.62}$$

(such as the popular functionals B3LYP[83,84] and PBE0[85]), contains a fraction of orbital exchange g_{ijji}, scaled by λ. Neglecting the XC contribution altogether and setting $\lambda = 1$ yields as a self-consistent solution the HF energy. Finally, the fifth rung (generalized random phase approximation) utilizes all of the KS orbitals.[37]

An increasing number of ingredients is expected to enable the use of less and less empirical fit parameters and to satisfy an increasing number of exact constraints by providing more flexibility, however at the cost of an increasing computational effort and more involved programming, especially in the case of nonlinear response which is also addressed in this thesis.

One axis has been completely omitted in the right panel in Fig. 1.1: that is the integration grid. A DFT user often simply trusts that the error from numerical integration is insignificant. For DFT programmers, a clever design of the numerical grid for the problem under study is an important part of the work and can be decisive for the scaling with respect to the system size. This scaling is one of few differences between the two panels of Fig. 1.1. Especially at the lower rungs of the Jacob's ladder DFT offers a scaling which makes DFT very attractive compared to correlated WFT methods. This also holds for DFT's rather modest basis set requirements.

1.8   Generalized density functional theories

In the previous section, spin density has been tacitly and implicitly introduced as an additional local ingredient to the XC functional together with other generalized (number) density-like variables. To make this more clear, consider again the LDA XC energy per particle, with

$$F^{\mathrm{LDA}} = F^{\mathrm{LDA}}(n_\uparrow, n_\downarrow),$$

where $n_\uparrow$ and $n_\downarrow$ are two such generalized densities. Equivalently, F^{LDA} can be expressed using other complementary variables like for instance the combinations

$$n_\uparrow + n_\downarrow = n \tag{1.63}$$

and

$$n_\uparrow - n_\downarrow = s. \tag{1.64}$$

The first (Eq. 1.63) may be recognized as the (total) number density n. The second expression (Eq. 1.64) defines the spin density s which was already introduced as an additional variable in the seminal paper of Kohn and Sham.[36] In their paper it is used as an extension to the theory of Hohenberg-Kohn[35] (HK) to obtain self-consistent equations for the treatment of the spin susceptibility of an electron gas subject to an external magnetic field which led to the spin density functional theory[86,87] (SDFT). In NR theory the spin and spatial degrees of freedom are completely decoupled and a quantization axis for the spin angular momentum can be freely chosen, independently of the molecular orientation in space, for instance—as done conventionally today and as done in the original formulation of KS—along the z-axis. With this choice the spin density can be expressed as

$$s = \phi_i^\dagger \sigma_z \phi_i, \tag{1.65}$$

where σ_z is one of the Pauli spin matrices (Section 1.3, p. 30) and ϕ_i are the KS orbitals. Spin density is an important ingredient in this thesis and Section 3.1, p. 63, will elaborate on this variable in more detail and discuss its adaptation to the 4-component relativistic theory.

The set of basic variables has been later enlarged* by the curl of the velocity (vorticity) which led to the current density functional theory[89,90] (CDFT). Another extension of DFT[91] enabled the treatment of superconducting systems in terms of the Cooper pair condensate density.†

---

* The remaining part of this section follows the very nice discussion in Ref. 88, pp. 346–348.   † Gradients, Laplacians, …, of (generalized) densities are not to be considered as additional generalized densities.

Typically, generalized DFTs (or multi-density functional theories) consider the following Hamiltonian[87, 88, 92]

$$\hat{H} = \hat{T} + \hat{U} + \hat{V}, \tag{1.66}$$

where $\hat{T}$ and $\hat{U}$ are the operators for the kinetic energy (or, more generally, the free-particle energy) and the Coulomb interaction between the electrons, respectively, and where

$$\hat{V} = \sum_i \int \mathrm{d}\mathbf{r}\, \hat{n}_i V_i, \tag{1.67}$$

with the generalized density operators $\hat{n}_i$ which couple linearly to their conjugate fields V_i. In the case of F^{LDA} the conjugate fields of the basic variables n and s (defined as in Eq. 1.65), are the scalar potential and the z-component of the magnetic field, respectively. Note that in the NR domain CDFT does not quite fit into this scheme due to the presence of the diamagnetic term which is quadratic in the external vector potential (Eq. 1.45).[88]

Generalized DFTs extend the HK universal functional $G[n]$ to a generalized universal functional $G[n_1, n_2, \ldots]$ which is defined analogously[93] as

$$G[n_1, n_2, \ldots] = \min \langle \psi | \hat{T} + \hat{U} | \psi \rangle, \tag{1.68}$$

where the minimum is taken over all normalized antisymmetric wave functions ψ which give rise to the generalized densities $n_1, n_2, \ldots$. Making the assumption that the generalized densities n_i can be varied independently[88] and applying the variational principle leads to the stationarity conditions

$$\frac{\delta G[n_1, n_2, \ldots]}{\delta n_i} = -V_i, \tag{1.69}$$

and the corresponding XC parts of KS potentials—one for each variable—which read as

$$v_{\mathrm{XC},i} = \frac{\delta E_{\mathrm{XC}}[n_1, n_2, \ldots]}{\delta n_i}. \tag{1.70}$$

The extension to generalized DFTs is for many reasons not straightforward, for instance, the question of nonuniqueness of the external potentials in generalized DFTs has been raised.[94, 95]

Spin density is an additional variable in most present-day time-dependent DFT (TD-(S)DFT) and almost all open-shell ground state DFT calculations—nonrelativistic and relativistic—and the question is: why do we need and use SDFT and other generalized DFTs?

It is indeed possible to incorporate external fields in the conventional (number density-only) DFT, since the ground state wave function of the generalized Hamiltonian (Eq. 1.66) can still be proved to be a functional of the conventional number density. This would enable to introduce a nonuniversal functional $G[n; V_2, V_3, \ldots]$, which depends on n and *parametrically* on the external fields $V_2, V_3, \ldots$, analogously to the scalar potential created by the nuclei within

the Born-Oppenheimer approximation. The advantage of the corresponding generalized *universal* functional* $G[n, n_2, \ldots]$ is that it allows the existence of (and computational access to) nontrivial self-consistent solutions $n_i \neq 0$ even in the absence of the conjugate fields thanks to the presence of the corresponding self-consistent XC potentials. However, in the absence of the corresponding "driving field" one may then question the definition of the generalized densities n_i. Returning to the example of SDFT, the spin-up (-down) portions of the number density are no longer well-defined when there is no external magnetic field and therefore no logical spin quantization axis. In order to use n_i also when the magnetic field is absent, it is argued that an infinitesimal magnetic field can be introduced to stabilize the direction, along which $n_\uparrow$ and $n_\downarrow$ can be measured.[87,96]

The second reason for using SDFT and other generalized DFTs is the fact that additional generalized density variables enlarge the functional space and give more flexibility in the variational procedure. This is, for instance, vital for the study of open-shell systems for which presently available (approximate) density-only functionals fail.[96] In these systems, different states that arise from the same electron configuration can have very similar number densities, for a density-only functional these states "look" very similar. In contrast, SDFT obtains additional information by sampling the spin density as an additional variable and can thus correctly distinguish these states by assigning more exchange energy to the state having the higher multiplicity. Note however that in the presence of an external magnetic field, spin density functionals which are constructed to depend on the square of the spin polarization

$$\zeta = \frac{s}{n},\tag{1.71}$$

yield the same value for the state M_S and $-M_S$ as pointed out by Savin.[96] The discussion of spin density will be resumed in Section 3.1, p. 63, where it will be introduced as an additional variable to the XC response formalism.

Another example for the success of generalized DFT is the solution of the long-standing fundamental problem in density-functional theory for the treatment of degenerate states in atomic systems.[96] Consider for instance an atom with a p^1 configuration.[†] All three possible ways of populating the real orbitals p_x, p_y, and p_z will generate densities with different orientations, but with equivalent shapes. DFT will therefore correctly assign equal energies to the three degenerate occupations. The complex orbitals $p_{\pm 1}$, however, have toroidal densities that are not equivalent to the densities obtained from real orbitals. The approximate density functionals that we are bound to use, have the difficult task to generate the same energy from the different densities.[96] The open d-shells of transition elements are even more problematic, as not even all real d-type orbitals produce equivalent densities. Becke has shown[97–99] that using

---

* In this case $n_1 \equiv n$.   † In the following a scalar relativistic situation is assumed for simplicity.

CDFT, which samples as an additional variable the nonzero current density present in nonzero M_L states, degeneracy is nearly restored for all single-determinantal angular momentum eigen-states.

A success-story for TD-CDFT applied to molecular systems is the static electric dipole linear polarizability of quasi-one-dimensional conjugated polymers, which is largely overestimated by presently available approximate local functionals. The inclusion of the curl and the divergence of the velocity as additional variables using the VK functional[100] yields results in excellent agreement with the best available correlated methods (see Ref. 101 for a review).

1.9 Orbital rotations by exponential parametrization

During the optimization of variational parameters leading to a stationary HF or KS electronic state or to obtain the response of such reference state to external perturbations it is necessary to perform transformations between different sets of orthonormal orbitals,[47] which in the second quantization formalism corresponds to unitary transformations of creation and annihilation operators. The variational exponential parametrization of the unitary transformation matrix*

$$U = \exp\left[-\hat{\kappa}\right] \tag{1.72}$$

in terms of an anti-Hermitian matrix κ turns out to be extremely useful.[47,102] This choice of parametrization offers an independent set of variational parameters (orbital rotation amplitudes) κ_{pq}, appearing in

$$\hat{\kappa} = \kappa_{pq}\hat{a}_p^\dagger\hat{a}_q = \kappa_{pq}\hat{x}_{pq}. \tag{1.73}$$

Here $\hat{a}_p^\dagger$ and $\hat{a}_q$ are the creation and annihilation operators, respectively, together they form the excitation operator $\hat{x}_{pq}$ introduced in Section 1.1, p. 26, p and q are general orbital indices. This set of orbital rotation amplitudes conserves orthonormality by construction, with *a priori* no restrictions on the allowed values of κ_{pq}. Such a parametrization allows to optimize the variational parameters using unconstrained optimization techniques. It is nevertheless useful in several situations to impose restrictions on certain orbital blocks of κ_{pq}, for instance to restrict attention to certain symmetry blocks or to identify and eliminate redundant parameters. Rotations among occupied or among virtual orbitals do not contribute to the electronic gradient and are therefore redundant for energy optimizations. The remaining nonredundant set contains in the closed-shell case only rotations between occupied and virtual orbitals, with the indices for orbital classes defined previously (p. 21)

$$\hat{\kappa} = \kappa_{ai}\hat{x}_{ai} - \kappa_{ai}^\star\hat{x}_{ia}. \tag{1.74}$$

In the 4-component relativistic framework there is a natural division between rotations with positive energy virtuals and rotations with negative energy virtuals which can be associated with "paramagnetic" and "diamagnetic" contributions familiar from NR theory.[103,104]

---

* The minus sign is conventional.

Response theory for approximate variational wave functions

Whenever you write, strive for originality, but if you have to steal, steal from the best.

Woody Allen in *Anything Else* (2003)

In this section molecular properties will be defined in the framework of response theory for approximate variational wave functions, that is HF and KS. In the time-independent limit, molecular properties can be obtained by differentiation of the total energy. However, finite perturbation methods cannot handle time-dependent perturbations, and there is no well-defined energy in time-dependent theory on which a variational condition could be based. In addition, it may be difficult to obtain the desired numerical precision especially for larger systems and for higher order properties.

If one restricts the perturbations of the Hamiltonian to be periodic, a variational so-called time-averaged quasienergy framework can be formulated. Within the time-averaged quasi-energy response theory, frequency-dependent molecular properties, excitation energies, and transition matrix elements can be associated with response functions, their poles, and residues, respectively. The quasienergy reduces to the usual energy in the limit of a static perturbation. Time-independent molecular properties can then be treated as a special case.

For this, the time-averaged quasienergy will be defined in the following and associated with response functions. Based on response equations, the derivation of response functions becomes then "a matter of straightforward differentiation after the quasienergy Lagrangian".[105] The notation will be kept as general as possible to accommodate both HF and KS theories. Explicit implementation details of the XC contribution to response functions will be discussed separately in Section 3.

2.1   Kubo relation

The starting point is again the time-dependent Dirac equation

$$i\frac{\partial}{\partial t}|\psi(t)\rangle = [\hat{H} + \hat{P}(t)]|\psi(t)\rangle. \tag{2.1}$$

The explicitly time-dependent perturbation $\hat{P}(t)$ which has been set to zero in Section 1.1 to obtain the stationary molecular electronic energy, is now included. By imposing the perturbation $\hat{P}(t)$ to be periodic

$$\hat{P}(t) = \hat{P}(t + T), \tag{2.2}$$

with T being the period, the perturbation can be written as a sum of monochromatic perturbations:

$$\hat{P}(t) = \sum_{k=-N}^{N} \exp[-i\omega_k t] \sum_{X} f_X(\omega_k)\hat{X}. \tag{2.3}$$

Each of these is associated to a linear 4×4 matrix operator $\hat{X}$ (see Section 1.3) and a corresponding field amplitude f_X. All frequencies ω_k can be expressed as integer multiples of the fundamental frequency $\omega_T = 2\pi/T$ and the solutions of the Hamiltonian $[\hat{H} + \hat{P}(t)]$ are then restricted to so-called Floquet states.[106,107] One of the $2N + 1$ frequencies is zero which means that static perturbations may be included.

With a time-dependent Hamiltonian a system observable, such as an expectation value $\langle\hat{A}\rangle$ associated with the operator $\hat{A}$, becomes time-dependent

$$\langle\psi(t)|\hat{A}|\psi(t)\rangle = \langle\psi(t)|\hat{A}|\psi(t)\rangle^{(0)} + \langle\psi(t)|\hat{A}|\psi(t)\rangle^{(1)} + \langle\psi(t)|\hat{A}|\psi(t)\rangle^{(2)} + \cdots \tag{2.4}$$

and its time-dependence is typically described in a perturbation expansion in orders of the perturbing field. This is the Kubo relation,[108] with

$$\langle\psi(t)|\hat{A}|\psi(t)\rangle^{(0)} = \langle 0|\hat{A}|0\rangle \tag{2.5}$$

$$\langle\psi(t)|\hat{A}|\psi(t)\rangle^{(1)} = \sum_{k} \exp[-i\omega_k t] \sum_{B} \langle\langle\hat{A};\hat{B}\rangle\rangle_{\omega_k} f_B(\omega_k) \tag{2.6}$$

$$\langle\psi(t)|\hat{A}|\psi(t)\rangle^{(2)} = \frac{1}{2} \sum_{kl} \exp[-i(\omega_k + \omega_l)t] \sum_{BC} \langle\langle\hat{A};\hat{B},\hat{C}\rangle\rangle_{\omega_k,\omega_l} f_B(\omega_k) f_C(\omega_l) \tag{2.7}$$

$$\langle\psi(t)|\hat{A}|\psi(t)\rangle^{(3)} = \cdots$$

The zeroth-order term corresponds to the unperturbed expectation value. The expansion co-
efficients of the Fourier components denoted as $\langle\langle\hat{A};\hat{B}\rangle\rangle_{\omega_k}$, $\langle\langle\hat{A};\hat{B},\hat{C}\rangle\rangle_{\omega_k,\omega_l}$, ..., are the linear-,
quadratic-, ..., response functions, respectively, and can be associated with frequency-depend-
ent molecular properties. If one restricts the frequencies to one single zero frequency the static
limit is recovered with the static response functions being the expansion coefficients of the Tay-
lor series which can be associated with static molecular properties.

It can be shown[105] that switching the sign of all frequencies implies a complex conjugation
of the response function (Eq. 2.8) in order to preserve Hermiticity of the Hamiltonian.

$$\langle\langle\hat{A};\hat{B},\hat{C},\cdots\rangle\rangle_{\omega_k,\omega_l,\cdots} = \langle\langle\hat{A};\hat{B},\hat{C},\cdots\rangle\rangle^{\star}_{-\omega_k,-\omega_l,\cdots} \qquad (2.8)$$

This also implies that all static response functions have to be real. The response functions are
the quantities of interest in this thesis.

2.2   Quasienergy

The time-dependent wave function $|\psi(t)\rangle$ may be written in the phase isolated form

$$|\psi(t)\rangle = \exp[-iF(t)]|\tilde{t}\rangle \qquad (2.9)$$

where F is a real function of time. Also the phase isolated wave function $|\tilde{t}\rangle$ is in general still a function of time.

The following requirements can be imposed[105]: In the unperturbed limit $|\tilde{t}\rangle$ has to reduce to the unperturbed wave function

$$|\tilde{t}\rangle \xrightarrow{\hat{P}(t)\to 0} |0\rangle, \qquad (2.10)$$

and Eq. 2.9 has to reduce to the usual separation into a time-dependent phase and the time-independent wave function, i.e.

$$\exp[-iF(t)]|\tilde{t}\rangle \xrightarrow{\hat{P}(t)\to 0} \exp[-iE_0 t]|0\rangle. \qquad (2.11)$$

It is now clear that the time derivative of $F(t)$ which is called quasienergy $Q(t)$ reduces to the stationary energy in the unperturbed limit according to

$$\frac{\partial F(t)}{\partial t} = \langle\tilde{t}|[\hat{H} + \hat{P}(t) - i\frac{\partial}{\partial t}]|\tilde{t}\rangle \equiv Q(t) \xrightarrow{\hat{P}(t)\to 0} E_0 \qquad (2.12)$$

and it is tempting to regard the quasienergy $Q(t)$ as the time-dependent analogue to the stationary energy. There are however at least two good reasons for not doing this[105]: these are the time-dependent variational condition

$$\delta\langle\tilde{t}|[\hat{H} + \hat{P}(t) - i\frac{\partial}{\partial t}]|\tilde{t}\rangle + i\frac{\partial}{\partial t}\langle\tilde{t}|\delta\tilde{t}\rangle = 0 \qquad (2.13)$$

and the time-dependent Hellmann-Feynman theorem

$$\frac{dQ(t)}{df_A(\omega)} = \langle\tilde{t}|\hat{A}|\tilde{t}\rangle\exp[-i\omega t] - i\frac{\partial}{\partial t}\langle\tilde{t}|\frac{d\tilde{t}}{df_A(\omega)}\rangle. \qquad (2.14)$$

The last terms in Eqs. 2.13 and 2.14 show that $Q(t)$ does not take over the role of energy in time-dependent theory. These terms vanish, however, if the time-average over the period T is taken.[109] The wanted analogue is therefore the time-averaged quasienergy Q defined by

$$Q \equiv \{Q(t)\}_T = T^{-1}\int_{-T/2}^{T/2} dt\, Q(t). \qquad (2.15)$$

2.3 Molecular properties from quasienergy derivatives

The link between response functions and the quasienergy is established by expanding the time-averaged quasienergy derivative

$$\frac{dQ}{df_A(\omega)}$$

in orders of the perturbing field:

$$
\begin{aligned}
\frac{dQ}{df_A(\omega)} ={}& \langle \hat{A} \rangle \\
&+ \sum_k \sum_B \langle\langle \hat{A}; \hat{B} \rangle\rangle_{\omega_k} f_B(\omega_k) \delta(\omega + \omega_k) \\
&+ \frac{1}{2} \sum_{kl} \sum_{BC} \langle\langle \hat{A}; \hat{B}, \hat{C} \rangle\rangle_{\omega_k, \omega_l} f_B(\omega_k) f_C(\omega_l) \delta(\omega + \omega_k + \omega_l) \\
&+ \cdots
\end{aligned}
\tag{2.16}
$$

Frequency-dependent molecular properties can therefore be defined as derivatives of the time-averaged quasienergy at zero field. To third-order these read

$$\langle \hat{A} \rangle = \frac{dQ}{df_A(0)} \tag{2.17}$$

$$\langle\langle \hat{A}; \hat{B} \rangle\rangle_{\omega_k} = \frac{d^2 Q}{df_A(-\omega_k) df_B(\omega_k)} \tag{2.18}$$

$$\langle\langle \hat{A}; \hat{B}, \hat{C} \rangle\rangle_{\omega_k, \omega_l} = \frac{d^3 Q}{df_A(-\omega_k - \omega_l) df_B(\omega_k) df_C(\omega_l)}. \tag{2.19}$$

The frequency of the measured response is minus the sum of external perturbations[105]

$$\langle\langle \hat{A}(-\omega_k - \omega_l - \cdots); \hat{B}, \hat{C}, \cdots \rangle\rangle_{\omega_k, \omega_l, \cdots}. \tag{2.20}$$

Furthermore, any pair of operators can be swapped ($\hat{A}$ with $\hat{B}$, $\hat{B}$ with $\hat{C}$, ...) if also the corresponding frequencies are interchanged ($-\omega_k - \omega_l - \cdots$ with ω_k, ω_k with ω_l, ...) and the same response function is obtained.[105]

2.4   Response functions

In this section we seek explicit expressions for the response functions, that is, for derivatives of the time-averaged quasienergy $Q = \{Q(t)\}_T$ with respect to the field amplitudes f_X at zero field ($f = 0$). The time-averaged quasienergy Q defined in Section 2.2 can be written as

$$Q = Q_0 + \sum_{k=-N}^{N} \sum_X f_X(\omega_k) X(\omega_k), \tag{2.21}$$

having introduced the short-hand notation

$$Q_0 = E_0(0) - S \tag{2.22}$$

$$S = \left\{ \langle \tilde{t} | \mathrm{i} \frac{\partial}{\partial t} | \tilde{t} \rangle \right\}_T \tag{2.23}$$

$$X(\omega_k) = \left\{ \langle \tilde{t} | \hat{X} | \tilde{t} \rangle \exp[-\mathrm{i}\omega_k t] \right\}_T. \tag{2.24}$$

Using this notation first-order properties may be written as

$$\left. \frac{\mathrm{d}Q}{\mathrm{d}f_A(\omega_A)} \right|_{f=0} = \left[\frac{\mathrm{d}Q_0}{\mathrm{d}f_A(\omega_A)} + A(\omega_A) \right.$$
$$\overbrace{ + \sum_{k=-N}^{N} \sum_X f_X(\omega_k) \frac{\mathrm{d}X(\omega_k)}{\mathrm{d}f_A(\omega_A)} }^{=0 \text{ since } f=0} \left. \vphantom{\sum} \right]_{f=0} \tag{2.25}$$

which for a variational wave function reduces to the expectation value expression

$$\left. \frac{\mathrm{d}Q}{\mathrm{d}f_A(\omega_A)} \right|_{f=0} = A^{(0)} \delta(\omega_A). \tag{2.26}$$

Second-order properties may be written accordingly as

$$\left. \frac{\mathrm{d}^2 Q}{\mathrm{d}f_A(\omega_A)\mathrm{d}f_B(\omega_B)} \right|_{f=0} = \left[\frac{\mathrm{d}^2 Q_0}{\mathrm{d}f_A(\omega_A)\mathrm{d}f_B(\omega_B)} + \frac{\mathrm{d}A(\omega_A)}{\mathrm{d}f_B(\omega_B)} + \frac{\mathrm{d}B(\omega_B)}{\mathrm{d}f_A(\omega_A)} \right.$$
$$\overbrace{ + \sum_{k=-N}^{N} \sum_X f_X(\omega_k) \frac{\mathrm{d}^2 X(\omega_k)}{\mathrm{d}f_A(\omega_A)\mathrm{d}f_B(\omega_B)} }^{=0 \text{ since } f=0} \left. \vphantom{\sum} \right]_{f=0}, \tag{2.27}$$

and third-order properties

$$\frac{d^3 Q}{df_A(\omega_A)df_B(\omega_B)df_C(\omega_C)}\bigg|_{f=0} = \Bigg[\frac{d^3 Q_0}{df_A(\omega_A)df_B(\omega_B)df_C(\omega_C)} \tag{2.28}$$

$$+ \underbrace{\frac{d^2 A(\omega_A)}{df_B(\omega_B)df_C(\omega_C)} + \frac{d^2 B(\omega_B)}{df_A(\omega_A)df_C(\omega_C)} + \frac{d^2 C(\omega_C)}{df_A(\omega_A)df_B(\omega_B)}}_{=0 \text{ since } f=0}$$

$$+ \overbrace{\sum_{k=-N}^{N} \sum_X f_X(\omega_k) \frac{d^3 X(\omega_k)}{df_A(\omega_A)df_B(\omega_B)df_C(\omega_C)}} \Bigg]_{f=0},$$

et cetera. The over-braced terms vanish because the derivatives are taken at zero field ($f = 0$).

The response of the exponentially parametrized HF or KS determinant (see Section 1.9)

$$|\tilde{t}\rangle = \exp[-\hat{\kappa}(t)]|0\rangle \tag{2.29}$$

is carried by the nonredundant orbital rotation parameters which can be collected in the vector

$$\mathbf{K}(\omega_k) = \begin{bmatrix} \mathbf{p} \\ \mathbf{q}^\star \end{bmatrix} \quad \text{with} \quad \begin{aligned} p_{ai} &= \kappa_{ai}(\omega_k) \\ q_{ai} &= \kappa_{ai}(-\omega_k) \end{aligned} \tag{2.30}$$

The expectation values Q_0 and $X(\omega_k)$ may be Baker-Campbell-Hausdorff expanded using the vector $\mathbf{K}(\omega_k)$, which in turn may be expanded in the perturbing field amplitudes. This step is detailed for instance in Refs. 53 and 66.

Explicit expressions for the response functions can be found from the variational condition

$$\frac{\partial Q}{\partial \mathbf{K}(\omega_k)} = 0 \tag{2.31}$$

which should also hold true for any choice of field amplitudes. After some manipulations the response functions can be identified. Again, only the final result shall be given here for the linear response function[53,66,105]

$$\langle\langle \hat{A}; \hat{B} \rangle\rangle_\omega = -\mathbf{A}^{(1)\dagger}(E_0^{(2)} - \omega S^{(2)})^{-1}\mathbf{B}^{(1)} \tag{2.32}$$

and the quadratic response function[66,105,110–112]

$$\begin{aligned} \langle\langle \hat{A}; \hat{B}, \hat{C} \rangle\rangle_{\omega_B,\omega_C} &= \mathbf{N}^{(A)\dagger}(\omega_B + \omega_C)E_0^{(3)}\mathbf{N}^{(B)}(-\omega_B)\mathbf{N}^{(C)}(-\omega_C) \\ &+ \mathbf{N}^{(A)\dagger}(\omega_B + \omega_C)B^{(2)}\mathbf{N}^{(C)}(-\omega_C) \\ &+ \mathbf{N}^{(A)\dagger}(\omega_B + \omega_C)C^{(2)}\mathbf{N}^{(B)}(-\omega_B) \\ &+ \mathbf{N}^{(B)\dagger}(-\omega_B)A^{(2)}\mathbf{N}^{(C)}(-\omega_C) \end{aligned} \tag{2.33}$$

in which appear the property gradients $\mathbf{A}^{(1)}$ and $\mathbf{B}^{(1)}$ with the structure

$$\mathbf{X}^{(1)} = \begin{bmatrix} \mathbf{g} \\ \mathbf{g}^\star \end{bmatrix}; \qquad g_{ai} = \langle o|[-\hat{x}_{ia}, \hat{X}]|o\rangle \quad \text{with} \quad \hat{X} = \hat{A}, \hat{B}, \tag{2.34}$$

the electronic Hessian $E_o^{(2)}$ and the property Hessians $A^{(2)}$, $B^{(2)}$, and $C^{(2)}$ with the structure

$$X^{(2)} = \begin{bmatrix} \mathbf{A} & \mathbf{B} \\ \mathbf{B}^\star & \mathbf{A}^\star \end{bmatrix}; \qquad \begin{aligned} A_{ai,bj} &= \langle o|[-\hat{x}_{ia}, [\hat{x}_{bj}, \hat{X}]]|o\rangle \\ B_{ai,bj} &= \langle o|[\hat{x}_{ia}, [\hat{x}_{jb}, \hat{X}]]|o\rangle \end{aligned} \quad \text{with} \quad \hat{X} = \hat{H}, \hat{A}, \hat{B}, \hat{C}, \tag{2.35}$$

the generalized metric

$$S^{(2)} = \begin{bmatrix} \mathbf{\Sigma} & \mathbf{\Delta} \\ -\mathbf{\Delta}^\star & -\mathbf{\Sigma}^\star \end{bmatrix}; \qquad \begin{aligned} \Sigma_{ai,bj} &= \langle o|[-\hat{x}_{ia}, \hat{x}_{bj}]|o\rangle \\ \Delta_{ai,bj} &= \langle o|[\hat{x}_{ia}, \hat{x}_{jb}]|o\rangle, \end{aligned} \tag{2.36}$$

and the electronic third derivative tensor $E_o^{(3)}$. The response vectors $\mathbf{N}^{(A)}$, $\mathbf{N}^{(B)}$, and $\mathbf{N}^{(C)}$ are obtained by solving the linear response equations

$$\mathbf{N}^{(X)}(\omega_X) = \left[E_o^{(2)} - \omega_X S^{(2)}\right]^{-1} \mathbf{X}^{(1)} \quad \text{with} \quad \hat{X} = \hat{A}, \hat{B}, \hat{C}. \tag{2.37}$$

2.5 Solution of linear response equations

The dimensionality of the electronic Hessian $E_\mathrm{o}^{(2)}$ which appears in the linear response function

$$\langle\langle\hat{A};\hat{B}\rangle\rangle_\omega = -\mathbf{A}^{(1)\dagger}(E_\mathrm{o}^{(2)} - \omega S^{(2)})^{-1}\mathbf{B}^{(1)} \tag{2.38}$$

is generally too large to allow its explicit construction. Therefore, the linear response function is rather obtained by an iterative solution of the response equation

$$(E_\mathrm{o}^{(2)} - \omega S^{(2)})\mathbf{N}^{(B)}(\omega) = \mathbf{B}^{(1)}, \tag{2.39}$$

followed by the contraction of the response vector $\mathbf{N}^{(B)}(\omega)$ with the property gradient $\mathbf{A}^{(1)}$ to form

$$\langle\langle\hat{A};\hat{B}\rangle\rangle_\omega = -\mathbf{A}^{(1)\dagger}\mathbf{N}^{(B)}(\omega). \tag{2.40}$$

The linear response is carried by the first-order orbital rotation amplitudes that form the response vector according to

$$\mathbf{N}^{(B)}(\omega) = \begin{bmatrix} \mathbf{z} \\ \mathbf{y}^\star \end{bmatrix} \quad \text{with} \quad \begin{matrix} z_{ai} &= \kappa_{ai}^{(B)}(\omega) \\ y_{ai} &= \kappa_{ai}^{(B)}(-\omega), \end{matrix} \tag{2.41}$$

and it can be shown[53] that a second solution exists

$$\mathbf{N}^{(B)}(-\omega) = \begin{bmatrix} \mathbf{y} \\ \mathbf{z}^\star \end{bmatrix}, \tag{2.42}$$

obtained from the linear response equation of opposite frequency

$$(E_\mathrm{o}^{(2)} + \omega S^{(2)})\mathbf{N}^{(B)}(-\omega) = \mathbf{B}^{(1)}. \tag{2.43}$$

In general, $\mathbf{z}$ and $\mathbf{y}^\star$ (or $\mathbf{y}$ and $\mathbf{z}^\star$) constitute elements of a general matrix with respect to Hermiticity, in contrast to the upper and lower blocks of the property gradients $\mathbf{A}^{(1)}$ and $\mathbf{B}^{(1)}$, which are related by the Hermiticity of the corresponding property matrix. However, a general matrix can always be decomposed into a Hermitian and an anti-Hermitian matrix. Therefore also the response vector which contains elements of a general matrix may be written as a sum of a Hermitian and anti-Hermitian contribution:

$$\mathbf{N}^{(B)}(\omega) = \mathbf{N}^{+(B)}(\omega) + \mathbf{N}^{-(B)}(\omega) \tag{2.44}$$

An analogous decomposition of vectors is also possible in terms of time reversal symmetry of the generating matrix. Returning to the linear response equation (Eq. 2.39), consider a property

gradient $\mathbf{B}^{(1)}$ which is Hermitian and has a well-defined time reversal symmetry indicated by the parameter $t = \pm 1$.* Note that in order to take full advantage of time reversal symmetry in quaternion formulation (Section 1.3), in practice all property gradients are required to be time reversal symmetric. For time reversal antisymmetric operators this can be achieved by the extraction of an imaginary phase (thus making them anti-Hermitian). The imaginary phase is reintroduced in the final construction of the linear response function.[53] The end result is that $\mathbf{B}^{(1)}$ is well-defined with respect to both time reversal symmetry ($t = \pm 1$) and Hermiticity ($h = \pm 1$).

The linear response equation (Eq. 2.39) is solved by expanding the response vector $\mathbf{N}^{(B)}(\omega)$ in a set of N trial vectors $\mathbf{w}_i$

$$\mathbf{N}^{(B)}(\omega) = \sum_{i=1}^{N} \mathbf{w}_i a_i^{(B)}(\omega) \tag{2.45}$$

followed by the solution of the N-dimensional reduced equation

$$(\tilde{E}_o^{(2)} - \omega \tilde{S}^{(2)})\mathbf{a}^{(B)}(\omega) = \tilde{\mathbf{B}}^{(1)} \tag{2.46}$$

in which appear the reduced quantities

$$\tilde{E}_o^{(2)} = \mathbf{W}^\dagger E_o^{(2)} \mathbf{W} \tag{2.47}$$

$$\tilde{S}^{(2)} = \mathbf{W}^\dagger S^{(2)} \mathbf{W} \tag{2.48}$$

$$\tilde{\mathbf{B}}^{(1)} = \mathbf{W}^\dagger \mathbf{B}^{(1)} \tag{2.49}$$

with $\mathbf{W}^T = \begin{bmatrix} \mathbf{w}_1 & \mathbf{w}_2 & \cdots & \mathbf{w}_N \end{bmatrix}$. The explicit construction of the Hessian is now bypassed by instead calculating the so-called sigma vector $\sigma_i = E_o^{(2)} \mathbf{w}_i$, which can be expressed in terms of modified Fock-, or KS matrices.[53,113] Similarly, the generalized metric $S^{(2)}$ is contracted with trial vectors. One finds that both $E_o^{(2)}$ and $S^{(2)}$ conserve the time reversal symmetry t of the trial vector, however, the Hermiticity h is conserved only by $E_o^{(2)}$, but reversed by $S^{(2)}$.[53] This implies that in the static case the response vector $\mathbf{N}^{(B)}(0)$ has well-defined Hermiticity h which is inherited from the property gradient along with the time reversal symmetry. In the frequency-dependent case $\mathbf{N}^{(B)}(\omega)$ keeps t, but has mixed Hermiticity and may be decomposed following Eq. 2.44. Next, consider the implications for a linear response function obtained by a contraction of the property gradient with the response vector, both with well-defined Hermiticities h_A, h_N and time reversal symmetries t_A, t_N.

---

* +1: symmetric; −1: antisymmetric.

The property gradient has the structure[53, 66]

$$\mathbf{A}^{(1)\dagger} = \begin{bmatrix} \mathbf{a}^\dagger & \mathbf{b}^\dagger & t_A \mathbf{a}^T & -t_A \mathbf{b}^T & h_A \mathbf{a}^T & h_A \mathbf{b}^T & h_A t_A \mathbf{a}^\dagger & -h_A t_A \mathbf{b}^\dagger \end{bmatrix}. \qquad (2.50)$$

Similarly, the response vector has the structure[53, 66]

$$\mathbf{N}^{h_N(B)T}(\omega) = \begin{bmatrix} \mathbf{c}^T & \mathbf{d}^T & t_N \mathbf{c}^\dagger & -t_N \mathbf{d}^\dagger & h_N \mathbf{c}^\dagger & h_N \mathbf{d}^\dagger & h_N t_N \mathbf{c}^T & -h_N t_N \mathbf{d}^T \end{bmatrix}, \qquad (2.51)$$

and the linear response function is given by[66]

$$\langle\langle \hat{A}; \hat{B} \rangle\rangle_\omega = -(1 + h_A h_N t_A t_N)(z + h_A h_N z^\star), \qquad (2.52)$$

where $z = (\mathbf{a}^\dagger \mathbf{c} + \mathbf{b}^\dagger \mathbf{d})$.

Three situations may be distinguished:

(i) $h_A h_N = t_A t_N = +1$
     The property operators $\hat{A}$ and $\hat{B}$ have the same symmetry under time reversal.
     $\langle\langle \hat{A}; \hat{B} \rangle\rangle_\omega$ has contributions only from $\mathbf{N}^{+(B)}(\omega)$.
     $\langle\langle \hat{A}; \hat{B} \rangle\rangle_\omega = -4\mathrm{Re}(z)$

(ii) $h_A h_N = t_A t_N = -1$
      The property operators $\hat{A}$ and $\hat{B}$ have the opposite symmetry under time reversal.
      $\langle\langle \hat{A}; \hat{B} \rangle\rangle_\omega$ has contributions only from $\mathbf{N}^{-(B)}(\omega)$.
      $\langle\langle \hat{A}; \hat{B} \rangle\rangle_\omega = -4i\mathrm{Im}(z)$

(iii) $h_A h_N = -t_A t_N$
       The property operators $\hat{A}$ and $\hat{B}$ have the opposite symmetry under time reversal.
       There are no contributions from $\mathbf{N}^{-(B)}(\omega)$ at $\omega = 0$.
       $\langle\langle \hat{A}; \hat{B} \rangle\rangle_0 = 0$

   In the static case trial vectors can be restricted to the Hermiticity of the property gradient $\mathbf{B}^{(1)}$. For the construction of the sigma vector, however, it is advantageous to select trial vectors with well-defined Hermiticity also in the frequency-dependent case where the response vector has mixed Hermiticity as this facilitates an efficient implementation of the response code. For instance, the XC contribution to linear and quadratic response has been implemented such that contributions that are zero by Hermiticity of the trial vector, are not calculated (Section 3, p. 61). This separation also favors a more efficient evaluation of perturbed density gradients within TD-SDFT. With the same arguments, the separate manipulation of response vectors with well-defined Hermiticity facilities the visualization of induced densities within the real-space approach to molecular properties (Section 5, p. 89).

Response theory within TD-SDFT

And Nietzsche, with his theory of eternal recurrence. He said that the life we lived we're gonna live over again the exact same way for eternity. Great. That means I'll have to sit through the Ice Capades again.

Woody Allen in *Hannah and Her Sisters* (1986)

The aim of this chapter is to document and to discuss the implementation of the closed-shell linear and quadratic response theory within the adiabatic time-dependent spin density functional theory (TD-SDFT), in which the density of electron spin angular momentum, *spin density*, is considered an additional variable of the XC energy functional.

The XC contributions to linear and quadratic response are derived by expanding the XC electronic gradient in perturbing field amplitudes. Most of the notation and working equations are contained in the collinear part (Section 3.2). In Section 3.3 the noncollinear formulation will be introduced by a rather simple modification of the collinear approximation.

This approach closely follows the 4-component relativistic implementation of KS theory reported by Saue and Helgaker[114] and the implementation of linear response at the 4-component relativistic density functional level reported by Sałek *et al.* [113] This work is based on the 4-component relativistic HF quadratic response implementation of Norman and Jensen[115] and has substantially benefited from the implementation of the XC contribution to electrostatic quadratic response by Henriksson.[116] Three other linear response implementations of relativistic TD-SDFT based on the noncollinear XC kernel have been reported, two of them using the 2-component ZORA Hamiltonian—by the Ziegler group[2] and by Liu and coworkers[3]—and one 4-component relativistic implementation by Liu and coworkers.[4] However, so far the XC kernel has been restricted to the LDA kernel. The presented implementation also enables to employ

adiabatic density gradient-dependent kernels. It is to our knowledge also the first relativistic implementation of quadratic response within TD-SDFT. On the NR side, see for instance Ref. 117 for quadratic response and also the cubic response implementation within TD-DFT by Jansik *et al.* [118]

The presented implementation is in principle straightforward as it is highly repetitive and recursive but it can also become very tedious and error-prone due to the increasing number of terms when going to higher orders in the perturbation expansion. For the derivation of quadratic response, the repetitiveness and recursion have been turned into an advantage: the working equations and expressions have been obtained and simplified by extensive use of PYTHON-driven[119] MAXIMA[120] scripts that have been developed during this work. At least for the XC contribution to the response, these scripts make it possible to implement any desired order in the future.

The fundamental problem in quasienergy KS theory—that the time-periodic density of a quasienergy steady-state does not uniquely determine the time-periodic potential (as pointed out by Maitra and Burke[121, 122])—is bypassed in the approximate finite basis methodology adopted here.[122]

3.1 Spin density in the relativistic framework

The motivation for including spin density in the relativistic domain is very similar to the NR situation (see Section 1.8, p. 43). While there is in principle no need to introduce additional variables in the absence of external vector potentials other than density alone, in practice, additional variables like spin or current density improve relativistic density functional calculations of open-shell systems.[123,124] Because genuine relativistic XC functionals that depend on the 4-current are presently not available and because relativistic corrections to XC functionals have been found to have only little effect on calculated valence properties,[123–125] it is common practice to use NR functionals even in 4-component codes, as done in this work. The difficulty then is in porting NR spin density functionals to the relativistic domain, since there is a fundamental reason why they should not be used the same way they are being used in NR DFT implementations. In NR theory the spin and spatial degrees of freedom are completely decoupled and a quantization axis for the spin angular momentum can be freely chosen, independently of the molecular orientation in space—conventionally the quantization axis is chosen along the z-axis. A simple adaptation of the NR spin density (Section 1.8, p. 43)

$$s_{\mathrm{NR}} = \phi_i^\dagger \sigma_z \phi_i, \tag{3.1}$$

to the 4-component relativistic framework would be, for instance, to use the 4×4 operator

$$\Sigma_z = \begin{bmatrix} \sigma_z & 0_{2\times2} \\ 0_{2\times2} & \sigma_z \end{bmatrix} \tag{3.2}$$

and define spin density as

$$s = m_z = \phi_i^\dagger \Sigma_z \phi_i, \tag{3.3}$$

which corresponds to the z-component of the spin magnetization vector

$$\mathbf{m} = \phi_i^\dagger \mathbf{\Sigma} \phi_i. \tag{3.4}$$

It should be mentioned that this is not the only definition found in the literature. Other authors[4,126,127] use the operator $\beta\mathbf{\Sigma}$ and define the spin magnetization vector accordingly as

$$\tilde{\mathbf{m}} = \phi_i^\dagger \beta\mathbf{\Sigma} \phi_i. \tag{3.5}$$

This is justified by the Gordon decomposition of the 4-component relativistic charge current density[27,68] (compare Eqs. 1.51 and 1.53), but it is equally clear that $\mathbf{\Sigma}$ is the spin operator in the 4-component relativistic framework, not $\beta\mathbf{\Sigma}$. In the following derivations and applications the definition in Eq. 3.4 will be used. This choice will affect neither the following discussion, nor the results in Section 4, p. 77.*

---

* We have implemented and tested both definitions—with no significant effect on excitation energies reported in Section 4, p. 77. A distinction may be expected when core excitations are considered.

The definition in Eq. 3.3 is called the collinear approach, which is a valid assumption if the spin magnetization vector is collinear with the external magnetic field ($|\mathbf{m}| = m_z$; $\mathbf{B}$ chosen along z). However, with spin–orbit coupling, this is in general not the case. If spin–orbit coupling is included, the collinear approach breaks the rotational invariance of the energy, which is of course a very undesirable feature when performing a molecular DFT calculation. This has been demonstrated by van Wüllen[128] together with the defect that the collinear approach is in general not able to recover full spin polarization ζ (Eq. 1.71) of a relativistic one-electron or quasi one-electron system where the spin density should be equal to the number density.* As a solution, the so-called noncollinear approach is invoked where one considers a more general definition of the spin density and the corresponding spin polarization by using the norm of the spin magnetization vector,

$$s = |\mathbf{m}|; \qquad \zeta = \frac{|\mathbf{m}|}{n} \tag{3.6}$$

which is invariant under rotations in real space.

In this work only closed-shell systems are considered, for which spin density does not enter in either formulation for the energy and for electrostatic properties. However, as soon as vector potentials or time-dependent scalar potentials are included as perturbations, first- and higher-order spin densities will be induced. The same distinction between collinear and noncollinear approach and the same problems associated to the collinear approximation apply to the kernel and its derivatives. This is for instance the case when calculating excitation energies within TD-SDFT. The failure of the collinear XC kernel has been demonstrated by Gao *et al.* [4] The example taken from their work are the $6s^2 \rightarrow 6s^16p^1$ excitation energies of Hg obtained with collinear and noncollinear forms of the adiabatic XC kernel (Tab. 3.1).† The performance of the XC potentials and kernels compared to experimental values will be discussed in Section 4.2, p. 79. The important message at this point is that for atoms in the collinear approximation the different M_J components of an excited J state are not degenerate. This is at odds with the fact that for atoms the total angular momentum J is a good quantum number. The collinear XC kernel does not commute with the J^2 operator[4] because like the collinear XC potential it is not isotropic in spin space. This can again be corrected by using the corresponding noncollinear forms (see Tab. 3.1). The defect of the collinear approach is not limited to the relativistic framework as the degeneracy is also broken for different M_S states in the NR domain. This degeneracy is restored using the noncollinear XC kernel (results not given here).

Finally, it should be warned that although we have a noncollinear definition of the spin density based on the norm of the vector defined in Eq. 3.4 (or in Eq. 3.5), for the problem of

---

* With the definition in Eq. 3.5 a relativistic (quasi) one-electron system cannot be fully spin polarized by construction.   † The LDA numbers presented have been calculated in this work and supplemented by BLYP numbers. For computational details see Section 4.1, p. 78.

Table 3.1: DC and IOTC $6s^2 \rightarrow 6s^1 6p^1$ excitation energies (in eV) of Hg obtained with collinear (c-) and noncollinear (nc-) forms of the LDA and BLYP kernels together with the corresponding XC potentials. M_J is the sum of Kramers projections.

	c-LDA			nc-LDA		c-BLYP			nc-BLYP		exp.[a]
Hamiltonian	DC			DC	IOTC	DC			DC	IOTC	
$\lvert M_J \rvert$	0	1	2	all	all	0	1	2	all	all	
J											
0	5.13			4.87	4.85	4.99			4.74	4.73	4.67
1	5.56	5.23		5.08	5.06	5.38	5.08		4.94	4.93	4.89
2	5.90	5.98	6.12	5.67	5.65	5.68	5.74	5.86	5.47	5.46	5.46
1	6.55	6.54		6.53	6.51	6.31	6.30		6.30	6.28	6.70

[a] Ref. 129.

reconstructing the magnetization in a crystal from magnetic neutron-diffraction data or from band-theoretical calculations, the definition of the magnetization* is not unique.[130,131] Landau and Lifshitz[132] define magnetization in terms of the charge current density **j** and require that **m** satisfies the differential equation

$$\nabla \times \mathbf{m} = \mathbf{j} \tag{3.7}$$

together with the requirement that **m** integrated over the volume of a sample gives its magnetic moment and should vanish outside the sample. This definition is not unique since a gauge transformation

$$\mathbf{m} \rightarrow \mathbf{m}' = \mathbf{m} + \nabla \chi \tag{3.8}$$

where χ is a continuous and differentiable function that is constant at the boundaries and beyond, will not affect the requirements given above. Stated differently, any magnetization can be identified as a density of *effective* magnetic dipole moments if it generates the correct transverse charge current density by Eq. 3.8.[130] And although this magnetic dipole moment density is in principle observable, the contributions of the individual moments—spin angular moments or orbital angular moments—cannot be distinguished.

A nice synthesis is given by Hirst in Ref. 130: "magnetization is only a device for encoding information about the current density, and clarification of this encoding can have no impact on quantities that could be discussed in terms of the current density itself". It is also clear that in relativistic DFT, magnetization will be replaced by the 4-current as soon as such functionals become available (see also Ref. 133 for a connection between SDFT and CDFT functionals).

---

* Magnetization is already a density, the term "magnetization density" should be avoided.[130]

3.2   Collinear formulation

Recall that in the collinear SDFT formalism the LDA XC energy has been written as

$$E_{\text{XC}}^{\text{LDA}} = \int d\mathbf{r} \, F(n_\uparrow, n_\downarrow), \tag{3.9}$$

and the XC energy of GGA functionals can be typically written as

$$E_{\text{XC}}^{\text{GGA}} = \int d\mathbf{r} \, F(n_\uparrow, n_\downarrow, |\nabla n_\uparrow|, (\nabla n_\uparrow \cdot \nabla n_\downarrow), |\nabla n_\downarrow|), \tag{3.10}$$

in both cases using an appropriate analytic function F as an approximation to the XC energy density. The scalar variable $(\nabla n_\uparrow \cdot \nabla n_\downarrow)$ appears in some GGA correlation functionals, for instance in the LYP[134,135] functional. Deep inside the DFT evaluator modules of the DIRAC[16,113] code and certainly also in other programs, the analytic functions F are programmed exactly as suggested by the authors of the respective functionals. The DFT evaluator modules receive the input parameters ($n_\uparrow$ and $n_\downarrow$, in the case of GGA functionals also $|\nabla n_\uparrow|$, $(\nabla n_\uparrow \cdot \nabla n_\downarrow)$, and $|\nabla n_\downarrow|$) and return F, which is then numerically integrated to give E_{XC}, and—if needed—return also derivatives of F which contribute to the XC potential, kernel, and higher-order kernels. The working equation for linear and nonlinear response could be expressed using this variable set $\{n_\uparrow, n_\downarrow, |\nabla n_\uparrow|, (\nabla n_\uparrow \cdot \nabla n_\downarrow), |\nabla n_\downarrow|)\}$. This can be found for instance in Refs. 117 and 136.

It is an important point for the following derivations to recognize that the program can work with another, but equivalent set of variables outside the DFT evaluator modules, for instance, with the now familiar number and spin density n and s, instead of $n_\uparrow$ and $n_\downarrow$, and the three scalar products,

$$Z = \nabla n \cdot \nabla n \tag{3.11}$$

$$Y = \nabla n \cdot \nabla s \tag{3.12}$$

$$X = \nabla s \cdot \nabla s, \tag{3.13}$$

instead of $\{|\nabla n_\uparrow|, (\nabla n_\uparrow \cdot \nabla n_\downarrow), |\nabla n_\downarrow|)\}$. This has several advantages. The use of scalar products of gradients instead of their norm facilitates the derivation of the working equations and also the distribution of functional derivatives in the Fock-type matrices and their transforms in the code. A major advantage when using a closed-shell reference—which is always imposed in this thesis—is the fact that using the variable set $\{n, s, Z, Y, X\}$ makes it easier to recognize when terms become zero due to the symmetry of the perturbation (or trial vector). This facilitates the programing of a more structured and efficient code. As an example, in the electrostatic case all spin-dependence vanishes. The vanishing terms can easily be skipped by ignoring all terms that contain s or Y or X. However, this choice comes at a price and the price we have to pay

is to transform derivatives of F with respect to $\{n_\uparrow, n_\downarrow, |\nabla n_\uparrow|, (\nabla n_\uparrow \cdot \nabla n_\downarrow), |\nabla n_\downarrow|)\}$, which are delivered by the DFT evaluator modules, to derivatives of F with respect to $\{n, s, Z, Y, X\}$. For higher order derivatives this can rapidly become cumbersome since the restriction to closed-shell may only be imposed at the end. This transformation of expressions is described separately in Note D, p. 193.

Passing on to the derivation of the working expressions, the starting point is the variational condition of collinear SDFT

$$\left.\frac{\mathrm{d}E_{\mathrm{XC}}}{\mathrm{d}\kappa_{ai}}\right|_{\kappa=0} = \int \mathrm{d}\mathbf{r}\, K_{ia} = \int \mathrm{d}\mathbf{r}\, \frac{\delta E_{\mathrm{XC}}}{\delta n}\frac{\mathrm{d}n}{\mathrm{d}\kappa_{ai}}\Bigg|_{\kappa=0} + \int \mathrm{d}\mathbf{r}\, \frac{\delta E_{\mathrm{XC}}}{\delta s}\frac{\mathrm{d}s}{\mathrm{d}\kappa_{ai}}\Bigg|_{\kappa=0}. \tag{3.14}$$

In DIRAC,[16,113] the gradient elements $\frac{\mathrm{d}E_{\mathrm{XC}}}{\mathrm{d}\kappa_{ai}}$ are elements of a generally quaternion matrix. The integrands K_{ia} therefore split into generally four real contributions $K_{ia,\mu}$ ($\mu = 0, x, y, z$). In collinear SDFT (with the quantization axis along z) only $K_{ia,0}$ and $K_{ia,z}$ need to be considered. However, for gradient-corrected functionals it is computationally not advantageous to express $K_{ia,0}$ and $K_{ia,z}$ using the explicit XC potentials as done in Eq. 3.14, since the explicit integration may require the calculation of the Laplacian or the full Hessian of the density and spin density at each quadrature point.[114] The computationally useful forms for the variable set $\{n, s, Z, Y, X\}$ may be obtained based on a nonredundant exponential parametrization of the KS energy by expanding the XC energy density and the functional variables in the orbital rotation elements[114] or by partial integration of Eq. 3.14. The computationally advantageous forms of $K_{ia,0}$ and $K_{ia,z}$ can be shown to have the general form of a scalar prefactor r_μ times a generalized overlap distribution $\Omega_{ia,\mu}$, with

$$\Omega_{ia,0} = \phi_i^\dagger \phi_a \quad \text{and} \quad \Omega_{ia,k} = \phi_i^\dagger \Sigma_k \phi_a; \quad (k = x, y, z) \tag{3.15}$$

and a vector prefactor $\mathbf{q}_\mu$ times the gradient $\nabla\Omega_{ia,\mu}$, and are given by*

$$K_{ia,\mu} = r_\mu \Omega_{ia,\mu} + \mathbf{q}_\mu \cdot \nabla\Omega_{ia,\mu} \tag{3.16}$$

using the scalar prefactors

$$r_0 = F_n \tag{3.17}$$

$$r_z = F_s, \tag{3.18}$$

and the vector prefactors

$$\mathbf{q}_0 = \left(2F_Z \nabla n + F_Y \nabla s\right) \tag{3.19}$$

$$\mathbf{q}_z = \left(2F_X \nabla s + F_Y \nabla n\right). \tag{3.20}$$

---

* We adopt the useful notation of Refs. 112 and 118.

From here on out, the symbols $F_U, F_{UV}, F_{UVW}, \ldots$, will be used as a short-hand notation for

$$\frac{\partial F}{\partial U}, \quad \frac{\partial^2 F}{\partial U \partial V}, \quad \frac{\partial^3 F}{\partial U \partial V \partial W}, \quad \ldots,$$

evaluated using n and $|\nabla n|$ of the unperturbed closed-shell reference system. The scalar and vector prefactors simplify for a closed-shell reference to

$$r_0 = F_n \tag{3.21}$$

$$r_z = 0 \tag{3.22}$$

$$\mathbf{q}_0 = 2F_Z \nabla n \tag{3.23}$$

$$\mathbf{q}_z = 0 \tag{3.24}$$

because in this case ∇s, F_s, and F_Y vanish. For closed-shell systems spin density does not contribute to the electronic gradient.

For linear and quadratic response, the perturbed integrands $K_{ia,\mu}^{(B)}$ and $K_{ia,\mu}^{(BC)}$ are required. In the second-quantization formalism these can be evaluated using commutators of the generalized orbital overlap distribution with the orbital rotation operators $\hat{\kappa}$ carrying the response,

$$\Omega_{ia,\mu}^{[B]} = \left[\hat{\kappa}^{(B)}, \Omega_{ia,\mu}\right] \tag{3.25}$$

$$\Omega_{ia,\mu}^{[BC]} = \left[\hat{\kappa}^{(BC)}, \Omega_{ia,\mu}\right] + \frac{1}{2}\left(\left[\hat{\kappa}^{(B)}, \left[\hat{\kappa}^{(C)}, \Omega_{ia,\mu}\right]\right] + \left[\hat{\kappa}^{(C)}, \left[\hat{\kappa}^{(B)}, \Omega_{ia,\mu}\right]\right]\right), \tag{3.26}$$

together with densities of modified matrices, scaled with functional derivatives and collected into perturbed scalar and vector prefactors.

The XC contribution to the linear response can be expressed in terms of 4 matrices,

$$\begin{aligned} K_{ia,\mu}^{(B)} = r_\mu \Omega_{ia,\mu}^{[B]} \quad &+ \mathbf{q}_\mu \cdot \nabla \Omega_{ia,\mu}^{[B]} \\ &+ r_\mu^{(B)} \Omega_{ia,\mu} + \mathbf{q}_\mu^{(B)} \cdot \nabla \Omega_{ia,\mu}. \end{aligned} \tag{3.27}$$

Correspondingly, one can see that the XC quadratic response contribution may be written compactly as

$$\begin{aligned} K_{ia,\mu}^{(BC)} = r_\mu \Omega_{ia,\mu}^{[BC]} \quad &+ \mathbf{q}_\mu \cdot \nabla \Omega_{ia,\mu}^{[BC]} \\ &+ r_\mu^{[B]} \Omega_{ia,\mu}^{[C]} \quad + \mathbf{q}_\mu^{[B]} \cdot \nabla \Omega_{ia,\mu}^{[C]} \\ &+ r_\mu^{[C]} \Omega_{ia,\mu}^{[B]} \quad + \mathbf{q}_\mu^{[C]} \cdot \nabla \Omega_{ia,\mu}^{[B]} \\ &+ r_\mu^{[BC]} \Omega_{ia,\mu} + \mathbf{q}_\mu^{[BC]} \cdot \nabla \Omega_{ia,\mu} \\ &+ r_\mu^{(BC)} \Omega_{ia,\mu} + \mathbf{q}_\mu^{(BC)} \cdot \nabla \Omega_{ia,\mu}. \end{aligned} \tag{3.28}$$

Before giving the explicit perturbed prefactors it is important to realize that the terms containing superscripts in square brackets, i.e. $r_\mu \Omega_{ia,\mu}^{[B]}$, $(\mathbf{q}_\mu \cdot \nabla \Omega_{ia,\mu}^{[B]})$, $r_\mu \Omega_{ia,\mu}^{[BC]}$, $(\mathbf{q}_\mu \cdot \nabla \Omega_{ia,\mu}^{[BC]})$, $r_\mu^{[B]} \Omega_{ia,\mu}^{[C]}$,

$(\mathbf{q}_\mu^{[B]} \cdot \nabla \Omega_{ia,\mu}^{[C]})$, $r_\mu^{[C]} \Omega_{ia,\mu}^{[B]}$, $(\mathbf{q}_\mu^{[C]} \cdot \nabla \Omega_{ia,\mu}^{[B]})$, $r_\mu^{[BC]} \Omega_{ia,\mu}$, and $(\mathbf{q}_\mu^{[BC]} \cdot \nabla \Omega_{ia,\mu})$ need not be coded explicitly. With the exception of the last two terms these contain 1-index and 2-index transforms of the molecular orbital overlap. These terms can be evaluated using $K_{ia,\mu}$ (first 4 terms) and $K_{ia,\mu}^{(B)}$ (last 6 terms) when provided with the appropriate density matrices. The challenge is now to find explicit expressions for the remaining perturbed parameters $r_\mu^{(B)}$, $\mathbf{q}_\mu^{(B)}$, $r_\mu^{(BC)}$, and $\mathbf{q}_\mu^{(BC)}$.

The first-order prefactors $r_o^{(B)}$ and $r_z^{(B)}$ read as

$$r_o^{(B)} = F_{nn} n^{(B)} + F_{ns} s^{(B)} + F_{nZ} Z^{(B)} + F_{nY} Y^{(B)} + F_{nX} X^{(B)} \tag{3.29}$$

and

$$r_z^{(B)} = F_{sn} n^{(B)} + F_{ss} s^{(B)} + F_{sZ} Z^{(B)} + F_{sY} Y^{(B)} + F_{sX} X^{(B)}. \tag{3.30}$$

For a closed-shell reference these reduce to

$$r_o^{(B)} = F_{nn} n^{(B)} + F_{nZ} Z^{(B)} \tag{3.31}$$

and

$$r_z^{(B)} = F_{ss} s^{(B)} + F_{sY} Y^{(B)} \tag{3.32}$$

because F_{ns}, F_{nY}, F_{sZ}, and $X^{(B)}$ vanish.[*]

The first-order prefactors $\mathbf{q}_o^{(B)}$ and $\mathbf{q}_z^{(B)}$ are given by

$$
\begin{aligned}
\mathbf{q}_o^{(B)} = {}& 2F_{Zn}(\nabla n)\, n^{(B)} && + F_{Yn}(\nabla s)\, n^{(B)} \\
& + 2F_{Zs}(\nabla n)\, s^{(B)} && + F_{Ys}(\nabla s)\, s^{(B)} \\
& + 2F_{ZZ}(\nabla n)\, Z^{(B)} && + F_{YZ}(\nabla s)\, Z^{(B)} \\
& + 2F_{ZY}(\nabla n)\, Y^{(B)} && + F_{YY}(\nabla s)\, Y^{(B)} \\
& + 2F_{ZX}(\nabla n)\, X^{(B)} && + F_{YX}(\nabla s)\, X^{(B)} \\
& + 2F_Z \nabla n^{(B)} && + F_Y \nabla s^{(B)}
\end{aligned}
\tag{3.33}
$$

and

$$
\begin{aligned}
\mathbf{q}_z^{(B)} = {}& 2F_{Xn}(\nabla s)\, n^{(B)} && + F_{Yn}(\nabla n)\, n^{(B)} \\
& + 2F_{Xs}(\nabla s)\, s^{(B)} && + F_{Ys}(\nabla n)\, s^{(B)} \\
& + 2F_{XZ}(\nabla s)\, Z^{(B)} && + F_{YZ}(\nabla n)\, Z^{(B)} \\
& + 2F_{XY}(\nabla s)\, Y^{(B)} && + F_{YY}(\nabla n)\, Y^{(B)} \\
& + 2F_{XX}(\nabla s)\, X^{(B)} && + F_{YX}(\nabla n)\, X^{(B)} \\
& + 2F_X \nabla s^{(B)} && + F_Y \nabla n^{(B)}
\end{aligned}
\tag{3.34}
$$

---

[*] The functional derivatives are symmetric.

For a closed-shell reference these reduce to

$$\mathbf{q}_0^{(B)} = 2F_{Zn}(\nabla n)\, n^{(B)} \tag{3.35}$$
$$+ 2F_{ZZ}(\nabla n)\, Z^{(B)}$$
$$+ 2F_Z \nabla n^{(B)}$$

and

$$\mathbf{q}_z^{(B)} = F_{Ys}(\nabla n)\, s^{(B)} \tag{3.36}$$
$$+ F_{YY}(\nabla n)\, Y^{(B)}$$
$$+ 2F_X \nabla s^{(B)}$$

since ∇s, F_{nY}, F_{sZ}, F_{ZY}, F_Y, and $X^{(B)}$ vanish.

The second-order prefactors can be obtained analogously. Only the final closed-shell result shall be given here:

$$
\begin{aligned}
r_0^{(BC)} = 2\bigg[&F_{nnn}n^{(B)}n^{(C)} &+ F_{nss}s^{(B)}s^{(C)} \\
&+F_{nnZ}\big(n^{(B)}Z^{(C)} + Z^{(B)}n^{(C)}\big) + F_{nsY}\big(s^{(B)}Y^{(C)} + Y^{(B)}s^{(C)}\big) \\
&+F_{nZZ}Z^{(B)}Z^{(C)} &+ F_{nYY}Y^{(B)}Y^{(C)} \\
&+F_{nZ}Z^{(BC)} &+ F_{nX}X^{(BC)} \bigg]
\end{aligned}
\tag{3.37}
$$

$$
\begin{aligned}
r_z^{(BC)} = 2\bigg[&F_{sns}\big(n^{(B)}s^{(C)} + s^{(B)}n^{(C)}\big) \\
&+F_{snY}\big(n^{(B)}Y^{(C)} + Y^{(B)}n^{(C)}\big) \\
&+F_{sZs}\big(Z^{(B)}s^{(C)} + s^{(B)}Z^{(C)}\big) \\
&+F_{sZY}\big(Z^{(B)}Y^{(C)} + Y^{(B)}Z^{(C)}\big) \\
&+F_{sY}Y^{(BC)} \bigg]
\end{aligned}
\tag{3.38}
$$

$$\mathbf{q}_0^{(BC)} = 4\big(\nabla n^{(B)}\big)\, a_Z^{(C)} + 4\big(\nabla n^{(C)}\big)\, a_Z^{(B)} + 4(\nabla n)\, a_Z^{(BC)} \tag{3.39}$$
$$+ 2\big(\nabla s^{(B)}\big)\, a_Y^{(C)} + 2\big(\nabla s^{(C)}\big)\, a_Y^{(B)}$$

$$\mathbf{q}_z^{(BC)} = 2\big(\nabla n^{(B)}\big)\, a_Y^{(C)} + 2\big(\nabla n^{(C)}\big)\, a_Y^{(B)} + 2(\nabla n)\, a_Y^{(BC)} \tag{3.40}$$
$$+ 4\big(\nabla s^{(B)}\big)\, a_X^{(C)} + 4\big(\nabla s^{(C)}\big)\, a_X^{(B)}$$

with the auxiliary parameters

$$
\begin{aligned}
a_Z^{(BC)} =\, & F_{ZZZ} Z^{(B)} Z^{(C)} && + F_{ZYY} Y^{(B)} Y^{(C)} \\
& + F_{ZnZ}\big(n^{(B)} Z^{(C)} + Z^{(B)} n^{(C)}\big) + F_{ZsY}\big(s^{(B)} Y^{(C)} + Y^{(B)} s^{(C)}\big) \\
& + F_{Znn} n^{(B)} n^{(C)} && + F_{Zss} s^{(B)} s^{(C)} \\
& + F_{ZZ} Z^{(BC)}
\end{aligned}
\tag{3.41}
$$

$$
a_Z^{(P)} = F_{Zn} n^{(P)} + F_{ZZ} Z^{(P)} \quad \text{with} \quad P = B, C \tag{3.42}
$$

$$
a_Y^{(P)} = F_{Ys} s^{(P)} + F_{YY} Y^{(P)} \tag{3.43}
$$

$$
a_X^{(P)} = F_{Xn} n^{(P)} + F_{XZ} Z^{(P)} \tag{3.44}
$$

$$
\begin{aligned}
a_Y^{(BC)} = \, & F_{Yns}\big(n^{(B)} s^{(C)} + s^{(B)} n^{(C)}\big) \\
& + F_{YnY}\big(n^{(B)} Y^{(C)} + Y^{(B)} n^{(C)}\big) \\
& + F_{YZs}\big(Z^{(B)} s^{(C)} + s^{(B)} Z^{(C)}\big) \\
& + F_{YZY}\big(Z^{(B)} Y^{(C)} + Y^{(B)} Z^{(C)}\big) \\
& + F_{YY} Y^{(BC)}
\end{aligned}
\tag{3.45}
$$

We have introduced the following perturbed variables

$$
Z^{(B)} = 2\big(\nabla n^{(B)} \cdot \nabla n\big) \tag{3.46}
$$

$$
Z^{(C)} = 2\big(\nabla n^{(C)} \cdot \nabla n\big) \tag{3.47}
$$

$$
Z^{(BC)} = 2\big(\nabla n^{(B)} \cdot \nabla n^{(C)}\big) \tag{3.48}
$$

$$
Y^{(B)} = \big(\nabla n^{(B)} \cdot \nabla s\big) + \big(\nabla n \cdot \nabla s^{(B)}\big) \tag{3.49}
$$

$$
Y^{(C)} = \big(\nabla n^{(C)} \cdot \nabla s\big) + \big(\nabla n \cdot \nabla s^{(C)}\big) \tag{3.50}
$$

$$
Y^{(BC)} = \big(\nabla n^{(C)} \cdot \nabla s^{(B)}\big) + \big(\nabla n^{(B)} \cdot \nabla s^{(C)}\big) \tag{3.51}
$$

$$
X^{(B)} = 2\big(\nabla s^{(B)} \cdot \nabla s\big) \tag{3.52}
$$

$$
X^{(C)} = 2\big(\nabla s^{(C)} \cdot \nabla s\big) \tag{3.53}
$$

$$
X^{(BC)} = 2\big(\nabla s^{(B)} \cdot \nabla s^{(C)}\big). \tag{3.54}
$$

Note that the remaining terms in $Z^{(BC)}$, $Y^{(BC)}$, and $X^{(BC)}$, which arise by differentiation of Z, Y, and X, are already cast in the terms $r_\mu^{[BC]}\Omega_{ia,\mu}$ and $(\mathbf{q}_\mu^{[BC]} \cdot \nabla\Omega_{ia,\mu})$ and therefore do not appear here explicitly. The first-order number and spin densities $n^{(B)}$, $n^{(C)}$, $s^{(B)}$, and $s^{(C)}$, and their respective gradients are evaluated using the first-order density matrices $\langle o|[\kappa^{(B)}, \hat{x}_{pq}]|o\rangle$ and $\langle o|[\kappa^{(C)}, \hat{x}_{pq}]|o\rangle$, respectively (see Note B, p. 185).

Before turning to the discussion of the noncollinear implementation a few comments on the structure of the code are pertinent. Consider for instance the closed-shell first-order prefactors $r_o^{(B)}$ (Eq. 3.31), $r_z^{(B)}$ (Eq. 3.32), $\mathbf{q}_o^{(B)}$ (Eq. 3.35), and $\mathbf{q}_z^{(B)}$ (Eq. 3.36). The first two and last two contributions have very similar structures, not only on paper. With only minor modifications an existing $K_o^{(B)}$ code can be adapted to evaluate $K_z^{(B)}$. All first-order densities $n^{(B)}$ (and their gradients) have to be replaced by first-order spin densities $s^{(B)}$ (gradients). The modifications of the corresponding derivatives are minute (see Note D, p. 193).

The analogy between these contributions was expected. In the NR regime $K_o^{(B)}$ and $K_z^{(B)}$ appear in the XC parts of the singlet and triplet coupled perturbed equations, respectively. These singlet and triplet XC parts can be solved using a generic code where only the functional derivatives are modified.

At first glance the computational effort seems doubled when including spin polarization. This is not true in the static case since then the first-order density matrix, from which first-order densities are extracted (see Note B, p. 185), is either Hermitian or anti-Hermitian and corresponds to trial vectors of well-defined Hermiticity (Section 2.5, p. 58). Therefore only either $(r_o^{(B)}, \mathbf{q}_o^{(B)})$ or $(r_z^{(B)}, \mathbf{q}_z^{(B)})$ can be nonzero and the remaining terms are in practice skipped. The blocking due to time reversal symmetry corresponds to some extent to the generalized singlet/triplet blocking known from NR theory.

From the structure of the second-order prefactors Eqs. 3.37 to 3.45 it can be seen that in the static case many terms become zero which can be exploited in the implementation of KS quadratic response.

3.3 Noncollinear formulation

The ansatz for a noncollinear formulation of SDFT is to use the noncollinear definition of spin density, $s = |\mathbf{m}|$, and in this case we will require all four integrands $K_{ia,\mu}$ ($\mu = o, x, y, z$), and for simplicity start with LDA, for which we can use the SDFT variational condition (Eq. 3.14) directly and obtain

$$K_{ia,\mu} = r_\mu \Omega_{ia,\mu}. \tag{3.55}$$

The prefactor r_o is unchanged, and the remaining prefactors r_k ($k = x, y, z$) become

$$r_k = F_s \frac{1}{s} m_k = F_{ss} m_k, \tag{3.56}$$

where we have used the closed-shell relation

$$F_s \frac{1}{s} = F_{ss}. \tag{3.57}$$

Consequently, $r_k = 0$ for a closed-shell system. Note that if one component of **m** equals s, Eq. 3.56 reduces to the collinear case. The noncollinear derivation of nonzero closed-shell prefactors $r_\mu^{(B)}$ and $r_\mu^{(BC)}$ runs in parallel to the collinear derivation, with the first-order prefactors given by

$$r_o^{(B)} = F_{nn} n^{(B)} \tag{3.58}$$

$$r_k^{(B)} = F_{ss} m_k^{(B)}, \tag{3.59}$$

and the second-order prefactors given by

$$r_o^{(BC)} = 2F_{nnn} n^{(B)} n^{(C)} + 2F_{nss} \big(m_x^{(B)} m_x^{(C)} + m_y^{(B)} m_y^{(C)} + m_z^{(B)} m_z^{(C)} \big) \tag{3.60}$$

$$r_k^{(BC)} = 2F_{nss} \big(n^{(B)} m_k^{(C)} + m_k^{(B)} n^{(C)} \big). \tag{3.61}$$

Again, all expressions reduce to their collinear versions if only one component of **m** is nonzero, as they should.

At this point it is worthwhile to realize that although we have arrived at the final noncollinear closed-shell LDA working equations starting from the definition $s = |\mathbf{m}|$, we could have well developed starting from the final collinear equations by repeating all spin-dependent operations also for the remaining two components of **m**. This observation is important for the noncollinear GGA response. The explicit XC potentials that appear in the SDFT variational condition (Eq. 3.14) may not be computationally useful for an efficient GGA implementation, however Eq. 3.14 can be used as an argument to adapt the collinear gradient-dependent parts of spin density response to the noncollinear case analogously to LDA, i.e. by repeating all spin-dependent operations also for the remaining two components of **m**.[*] This is particularly simple when working with generally quaternion matrices. Each operation on one of the imaginary parts is repeated for the remaining two quaternion imaginary parts—the modification of the collinear code is minimal. The additional computational effort is a factor three in the evaluation of perturbed spin-dependent densities and a factor of three in the accumulation of $K_{ia,k}^{(B)}$ and $K_{ia,k}^{(BC)}$, and certain intermediates that contribute to $K_{ia,o}^{(B)}$ and $K_{ia,o}^{(BC)}$. The evaluation of functional derivatives is not modified.

---

[*] We are currently checking the validity of this simple approach.

3.4   Testing the implementation

The implementation of the XC contribution to quadratic response is a nontrivial task because it implies coding of many terms. At some stage the correct implementation has to be checked. For the static case an obvious option is to check the quadratic response functions

$$\beta_{ijk}(0, 0) = \langle\langle \hat{\mu}_i; \hat{\mu}_j(0), \hat{\mu}_k(0) \rangle\rangle \tag{3.62}$$

which are the elements of the first-order hyperpolarizability tensor, against finite perturbation results: these can be the third-order energy derivatives, the second-order derivatives of the electric dipole moment expectation value, or most conveniently, the first-order derivatives of the linear polarizability obtained within static linear response. The latter can be checked accordingly. The problem is that the finite perturbation test, if properly set up, can only give information indicating if everything is correct or if something is wrong but will not indicate where the error is being made. We have therefore first obtained an automatically generated noddy code that matches the finite perturbation result. In parallel, we have written a more structured code and have compared the two implementations by screening selected combinations of variables. An additional difficulty is given by the fact that the static finite perturbation approach tests only terms containing exclusively the variables n and/or Z. Other contributions are zero in the static case. In order to check the spin-polarization contribution to the quadratic response it is possible to test the frequency-dependent

$$\beta_{ijk}(\omega, 0) = \langle\langle \hat{\mu}_i; \hat{\mu}_j(\omega), \hat{\mu}_k(0) \rangle\rangle \tag{3.63}$$

where spin density contributes, against finite perturbation results using the spin-polarized frequency-dependent linear response functions $\langle\langle \hat{\mu}_i; \hat{\mu}_j(\omega) \rangle\rangle$. The frequency-dependent linear response functions without spin-polarization are documented in Ref. 113. In this case one has to rely on a correct implementation of the spin density contribution to linear response, which we believe we can, based on excitation energies (Section 4, p. 77) and the nuclear spin–spin coupling constants (Section 5.5, p. 119) obtained in this work.

The chosen test case for the above described spin-polarized KS quadratic response implementation is the frequency-dependent $\beta_{zzz}(\omega, 0)$ in HCl compared to finite perturbation results obtained from the first derivative of $\alpha_{zz}(\omega)$. The results are listed in Tab. 3.2. We have tested the contribution of spin density at various places in the implementation. This gives three approximations to the full response found in the rightmost column of Tab. 3.2. The agreement between the quadratic response and the finite perturbation results, respectively, suggests that the implementation is correct, both in the LDA and the GGA case. In addition, the results in

Table 3.2: Frequency-dependent first-order hyperpolarizability component $\beta_{zzz}(\omega, 0)$ in HCl, calculated by quadratic response (QR) and by finite perturbation (FP) using $\alpha_{zz}(\omega)$ with $\omega = 0.22\ E_h/\hbar$. SDFT-LR means that we have included (1) or not included (0) the spin density contribution in the solution of the linear response equations. [SDFT-QR] means that we have included (1) or not included (0) the spin density contribution to the terms $r_\mu^{[B]}\Omega_{ia,\mu}^{[C]}$, $(\mathbf{q}_\mu^{[B]} \cdot \nabla\Omega_{ia,\mu}^{[C]})$, $r_\mu^{[C]}\Omega_{ia,\mu}^{[B]}$, $(\mathbf{q}_\mu^{[C]} \cdot \nabla\Omega_{ia,\mu}^{[B]})$, $r_\mu^{[BC]}\Omega_{ia,\mu}$, and $(\mathbf{q}_\mu^{[BC]} \cdot \nabla\Omega_{ia,\mu})$, where linear response code is being used. SDFT-QR means that we have included (1) or not included (0) the spin density contribution to the genuine QR terms $r_\mu^{(BC)}\Omega_{ia,\mu}$ and $(\mathbf{q}_\mu^{(BC)} \cdot \nabla\Omega_{ia,\mu})$. All values are in $e^3 a_0^3/E_h^2$.[a]

spin density	SDFT-LR	0	1	1	1
included in	[SDFT-QR]	0	0	1	1
	SDFT-QR	0	0	0	1
LDA	QR	32.125849	32.282680	32.287046	32.286544
	FP	32.125853			32.286557
BLYP	QR	30.265355	30.914573	30.931585	30.931218
	FP	30.265351			30.931240

[a] The field strengths are ±0.000005 E_h/ea_0 using the uncontracted t-aug-cc-pVTZ[137,138] basis set for two functionals: LDA (SVWN5)[45,139] and the generalized gradient correction functional BLYP.[134,135,140] The molecule is oriented along the z-axis, with $z_{Cl} = 0.0675$ and $z_H = -2.3412\ a_0$. We have used the IOTC Hamiltonian[72] with very tight convergence thresholds for the self-consistent field and the response, no integral screening and a fine integration grid (DIRAC[16] keywords: ANGINT = 65; RADINT = 1.0×10^{-15}).

Tab. 3.2 show that for this example it is a good approximation to include spin density only in the solution of the linear response equations (second column). We also note that the results indicate that it seems to be a very good approximation to exclude spin density from the genuine quadratic response terms $r_\mu^{(BC)}\Omega_{ia,\mu}$ and $(\mathbf{q}_\mu^{(BC)} \cdot \nabla\Omega_{ia,\mu})$ altogether, since they bring in only a minute correction in this case. From the programmer's point of view it is of course discouraging to see the inverse proportionality between the contributions and the programming effort but this situation can completely change for other properties with strong contributions from spin density.

Another useful sanity check* is to verify the quadratic response function symmetry

$$\beta_{ijk}(\omega, 0) = \beta_{jik}(\omega, 0). \tag{3.64}$$

The results of this test for $\beta_{zxx}(\omega, 0)$ and $\beta_{xzx}(\omega, 0)$ in HCl for the BLYP functional are summarized in Tab. 3.3. We have introduced errors on purpose and checked whether the above symmetry can be reproduced. The results show that this test is only a necessary condition. A "symmetric" error (like the error B in Tab. 3.3) remains undetected.†

Table 3.3: Frequency-dependent first-order hyperpolarizability components $\beta_{zxx}(\omega, 0)$ and $\beta_{xzx}(\omega, 0)$ in HCl, calculated with the BLYP functional under the same conditions as detailed in Tab. 3.2. Error A means that the first four right-hand side lines in Eq. 3.45 have been set to zero. Error B means that the spin density contribution to the second-order parameters $r_\mu^{(BC)} \Omega_{ia,\mu}$ and $(\mathbf{q}_\mu^{(BC)} \cdot \nabla \Omega_{ia,\mu})$ has been neglected (corresponds to third column in Tab. 3.2). All values are in $e^3 a_0^3 / E_h^2$.

	$\beta_{zxx}(\omega, 0)$	$\beta_{xzx}(\omega, 0)$	difference
implementation	24.34579659	24.34579726	−0.00000067
error A	24.32761315	24.32747057	0.00014258
error B	24.34569631	24.34569699	−0.00000068

---

* With thanks to J. Henriksson and P. Norman for pointing this out.   † First observed by J. Henriksson.

<div align="right">Chapter 4</div>

TD-SDFT at work: excitation energies

> *I awoke on Friday, and because the universe is expanding it took*
> *me longer than usual to find my robe.*
>
> Woody Allen, *Strung Out* in *Mere Anarchy*

In this chapter we wish to validate our noncollinear 4-component relativistic implementation of the spin density contribution to the closed-shell KS linear response (as detailed in Section 3, p. 61 and following) by calculating electronic excitation energies of Zn, Cd, Hg, AuH, and UO_2^{2+}. This test set has been selected because it fulfills two aspects: (i) it contains heavy elements, including the post-transition metal U, and (ii) TD-SDFT results based on the non-collinear XC kernel which have been published by other groups for this test set, can be used as reference. These are 2-component relativistic studies using the ZORA Hamiltonian by Wang *et al.* [2] (Zn, Cd, Hg), by Peng *et al.* [3] (AuH), and by Pierloot *et al.* [141] (UO_2^{2+}), and a 4-component relativistic study by Gao *et al.* [4] (Zn, Cd, Hg, AuH). So far the XC kernel has been restricted to the LDA kernel. The presented implementation also enables us to employ adiabatic density gradient-dependent kernels. Therefore, we can extend the study of the electronic spectrum of Zn, Cd, Hg, and AuH, reported by Gao *et al.* [4] and test the performance of other functionals, also employing their corresponding gradient-dependent kernels.

4.1   Computational details

The excitation energies have been obtained as all-electron calculations using a development version of the DIRAC[16] code, as solutions of the eigenvalue equation[142]

$$(E_0^{(2)} - \omega S^{(2)})\mathbf{N}(\omega) = \mathbf{0}, \tag{4.1}$$

in which appears the electronic Hessian $E_0^{(2)}$ and the generalized metric $S^{(2)}$ (see Section 2.5, p. 57 for further details). The calculations have been carried out using the functionals LDA (SVWN5),[45,139] GLLBsaopLBα (SAOP),[143] LB94,[144] BLYP,[134,135,140] B3LYP,[83,84] CAMB3LYP,[145] PBE,[146] PBE0,[85] and BP86.[140,147] LDA, SAOP, and LB94 have been used together with the noncollinear LDA kernel. Other functionals are used with their corresponding noncollinear kernel. The integration procedure has been tested and the reported values can be considered free of errors due to numerical quadrature. We have used the 4-component Dirac-Coulomb (DC) and the infinite-order 2-component (IOTC) Hamiltonians[72] (see Section 1.6, p. 40), the latter with the contribution of the 2-electron spin same-orbit coupling modeled in a mean-field fashion[78] using the AMFI[79] code. This mean field contribution modifies only the original KS matrix and its index-transforms in the response formalism and no additional explicit contributions to the response are considered. To obtain scalar relativistic excitation energies, effects due to spin–orbit coupling have been eliminated as described in Refs. 24 and 60.

The two-electron Coulomb integrals (SS|SS), involving only the small components, have been eliminated in both the SCF and the TD-SDFT part. Rotations between positive and negative energy solutions have been suppressed within the TD-SDFT module. A Gaussian charge distribution has been chosen as the nuclear model using the recommended values of Ref. 148.

In order to allow a direct comparison to the results reported in Refs. 4 and 141, the same Au–H (2.8913 a_0) and U–O (3.2277 a_0) distances have been used.

4.2   Basis sets

The comparison of excitation energies calculated within this work with the Zn, Cd, Hg, and AuH excitation spectra calculated by Gao *et al.* ,[4] and with the UO_2^{2+} excitation spectrum reported by Pierloot *et al.* [141] is hampered by the fact that both groups have used Slater-type basis set expansions. Therefore, a thorough validation of the here employed Gaussian-type basis set deserves special attention in the following discussion of results.

In this project we can benefit from extensive basis sets studies performed during previous work on static and frequency-dependent electric dipole linear polarizabilities (see Paper III, p. 167) and start out with the same basis sets for Zn, Cd, and Hg. Also the basis sets for the remaining atoms Au and U have been constructed in a similar fashion. These are aug-cc-pVTZ-DK[149] for Zn, triple-zeta and quadruple-zeta relativistic all-electron basis sets of Dyall[150] for Cd, Hg, Au, and U, including valence correlating and valence polarization functions. The H basis set is d-aug-cc-pVTZ.[151] For O we have used cc-pVTZ and cc-pVQZ.[152] Additional diffuse functions are not needed for UO_2^{2+}. The Zn basis set has been further augmented by *1s1p1d1f* and the Cd, Hg, and Au basis sets by *2s2p2d2f* diffuse exponents using the outermost quotient of each angular momentum. The small component basis set for the 4-component relativistic calculations has been generated using unrestricted kinetic balance with restricted kinetic balance imposed in the canonical orthonormalization step.[60] All basis sets are used in the uncontracted form.

4.3   Electronic spectrum of Zn, Cd, and Hg

The $ns^2 \rightarrow ns^1np^1$ excitation energies (in eV) of group 12 atoms (n = 4 − 6 for Zn, Cd, and Hg) calculated with various XC functional/kernel pairs and the DC Hamiltonian are listed in Tab. 4.1. To test the performance of the various XC functional/kernel pairs and compare with experimental values[129] is only the secondary target of this study. Before turning to this performance test, it must be the primary target to compare our LDA results with those reported by Gao *et al.* [4] in order to check the validity of our implementation. At first sight this comparison is disappointing (compare columns LDA and LDA^b in Tab. 4.1).

The first three excitation energies of Zn are 0.05 eV smaller than the reference values, the fourth (scalar relativistically ^1P) is 0.31 eV smaller than the reference. The differences are less pronounced for Cd and Hg, 0.02–0.04 eV, but again the fourth excitation energies deviate by 0.16 eV for Cd and 0.13 eV for Hg.

The authors of Ref. 4 have used numerical atomic bispinors in combination with kinetically balanced triple-zeta Slater-type functions, including two sets of polarization and one set of diffuse functions. Unfortunately we can not employ such basis sets in our calculations and it was necessary to carefully check the quality of our Gaussian-type basis set which has been done for Cd and Hg (see Tab. 4.2). Our final basis set choice which is the basis set used for the results listed in Tab. 4.1, is designated d-aug-TZ+pol. in Tab. 4.2. We have tested the effect of subsequently removing the valence polarization functions and the diffuse functions. This changes the fourth excitation energy of Cd considerably and actually brings the Cd excitation energies in very good agreement.

Table 4.1: The $ns^2 \rightarrow ns^1np^1$ excitation energies (in eV) of group 12 atoms ($n = 4 - 6$ for Zn, Cd, and Hg) calculated with various functionals and the DC Hamiltonian. The lower section of the table compares the deviations of the calculated TD-SDFT excitation energies with the corresponding experimental values from Ref. 129 (MAE: mean absolute error; MRE: mean relative error; ME: maximum error).

	J	exp.[a]	LDA	LDA[b]	SAOP	LB94	BLYP	B3LYP	CAMB3LYP	PBE	PBE0	BP86
Zn	0	4.01	4.32	4.37	4.68	4.92	4.22	4.02	3.89	3.76	3.42	4.02
	1	4.03	4.35	4.40	4.71	4.95	4.25	4.04	3.92	3.78	3.44	4.04
	2	4.08	4.40	4.45	4.77	5.03	4.30	4.09	3.97	3.83	3.50	4.09
	1	5.80	5.76	6.07	6.37	6.76	5.61	5.58	5.60	5.58	5.49	5.67
Cd	0	3.73	3.95	3.97	4.27	4.57	3.85	3.66	3.48	3.47	3.15	3.66
	1	3.80	4.02	4.04	4.35	4.67	3.92	3.73	3.56	3.54	3.22	3.73
	2	3.95	4.17	4.19	4.53	4.88	4.06	3.88	3.72	3.69	3.39	3.88
	1	5.42	5.34	5.50	5.89	6.34	5.18	5.14	5.12	5.14	5.05	5.22
Hg	0	4.67	4.87	4.89	5.19	5.40	4.74	4.51	4.27	4.45	4.09	4.63
	1	4.89	5.08	5.12	5.43	5.67	4.94	4.73	4.51	4.66	4.33	4.84
	2	5.46	5.67	5.69	6.14	6.48	5.47	5.31	5.14	5.21	4.94	5.42
	1	6.70	6.53	6.66	7.16	7.56	6.30	6.27	6.21	6.32	6.25	6.42
MAE			0.16	0.23	0.58	0.89	0.02	−0.13	−0.26	−0.26	−0.52	−0.08
MRE (%)			4.0	5.4	12.8	19.5	1.2	−2.5	−5.5	−5.6	−11.7	−1.5
ME			0.32	0.37	0.69	1.02	−0.40	−0.43	−0.49	−0.38	−0.45	−0.28

[a] Ref. 129. [b] Ref. 4.

However, this behavior is probably fortuitous as it is not paralleled for Hg. The test in the other direction consists of improving the basis set from d-aug-TZ+pol. to d-aug-QZ+pol. Going from triple- to the rather extensive quadruple-zeta basis sets is found to have no effect on the calculated excitation energies in the reported significant digits (Tab. 4.2).

A comparison of LDA, SAOP, and LB94 excitation energies for Zn, Cd, and Hg with 2-component ZORA results reported by Wang *et al.* [a] is summarized in Tab. 4.3. The differences are smaller than 0.02 eV which is an excellent agreement given the fact that we compare two different noncollinear implementations. Therefore, we conclude with confidence in our choice of the basis set and in the here reported excitation energies. The excitation energies reported by Gao *et al.* [4] are probably not fully converged with respect to the basis set.

Table 4.2: LDA $ns^2 \to ns^1 np^1$ excitation energies of Cd ($n = 5$) and Hg ($n = 5$) using the DC Hamiltonian and different basis sets. Comparison with results reported by Gao *et al.* [4] (all values in eV).

	J	d-aug-QZ+pol.[a]	d-aug-TZ+pol.[b]	d-aug-TZ[c]	TZ[d]	Gao *et al.* [e]
Cd	0	3.95	3.95	3.96	3.96	3.97
	1	4.02	4.02	4.03	4.03	4.04
	2	4.17	4.17	4.18	4.18	4.19
	1	5.34	5.34	5.47	5.50	5.50
Hg	0	4.87	4.87	4.88	4.88	4.89
	1	5.08	5.08	5.09	5.09	5.12
	2	5.67	5.67	5.68	5.67	5.69
	1	6.53	6.53	6.55	6.56	6.66

[a] Quadruple-zeta,[150] augmented by *2s2p2d2f* diffuse exponents.
[b] Triple-zeta,[150] augmented by *2s2p2d2f* diffuse exponents (identical to the basis set detailed in Section 4.2, p. 79).
[c] Triple-zeta,[150] without valence polarization functions augmented by *2s2p2d* diffuse exponents.
[d] Triple-zeta,[150] without valence polarization functions and without additional diffuse exponents.
[e] Ref. 4.

Returning to Tab. 4.1, the slight discrepancy between our LDA excitation energies and those reported by Gao *et al.* [4] does not affect the overall performance which is measured by the mean absolute error (MAE), the mean relative error (MRE), and the maximum error (ME) with respect to experimental values.[129] LDA overestimates the excitation energies with the exception of the fourth states (scalar relativistically ^1P). The deviations are largest for Zn with 0.32 eV and relatively small for Cd and Hg. The rather good performance of LDA for excitation energies of Cd and Hg goes hand in hand with the good performance in frequency-dependent electric dipole linear polarizability calculations as observed in Ref. 113 and in Paper III, p. 167. In terms of statistics, LDA is rivaled only by two functionals with good accuracy: BLYP and BP86, the latter with excellent performance for Zn. Admixture of exact exchange (compare BLYP with

B3LYP and PBE with PBE0 in Tab. 4.1) lowers the excitation energies, overshooting in the case of B3LYP and moving PBE results further away from experimental reference data. The asymptotically correct LB94 overestimates all studied excitation energies with a MRE of 19.5%. This behavior is inherited by the interpolating SAOP potential with a MRE of 12.8%. This observation is again in agreement with underestimated frequency-dependent electric dipole linear polarizabilities of these functionals found in Paper III, p. 167. For this atomic test set CAMB3LYP gives no improvement over the B3LYP numbers.

Table 4.3: The $ns^2 \rightarrow ns^1np^1$ excitation energies of group 12 atoms ($n = 4 - 6$ for Zn, Cd, and Hg) calculated with LDA, SAOP, and LB94 and the d-aug-TZ+pol[b] basis set. Comparison of the DC results obtained within this work with 2-component ZORA results reported by Wang *et al.* [a] (all values in eV).

	J	LDA		SAOP		LB94	
		this work	Wang *et al.* [a]	this work	Wang *et al.* [a]	this work	Wang *et al.* [a]
Zn	0	4.32	4.33	4.68	4.69	4.92	4.94
	1	4.35	4.35	4.71	4.72	4.95	4.97
	2	4.40	4.41	4.77	4.78	5.03	5.05
	1	5.76	5.76	6.37	6.37	6.76	6.76
Cd	0	3.95	3.95	4.27	4.27	4.57	4.57
	1	4.02	4.02	4.35	4.36	4.67	4.67
	2	4.17	4.17	4.53	4.53	4.88	4.88
	1	5.34	5.35	5.89	5.89	6.34	6.34
Hg	0	4.87	4.87	5.19	5.20	5.40	5.41
	1	5.08	5.09	5.43	5.44	5.67	5.67
	2	5.67	5.67	6.14	6.14	6.48	6.47
	1	6.53	6.53	7.16	7.16	7.56	7.55

[a] Ref. 2. [b] Triple-zeta,[150] augmented by *2s2p2d2f* diffuse exponents (identical to the basis set detailed in Section 4.2, p. 79).

4.4 Electronic spectrum of AuH

To the best of our knowledge, five theoretical investigations on low-lying excited states of AuH have been published.[2–4,153,154] Among them are three TD-SDFT studies: 2-component relativistic calculations based on the zeroth-order regular approximation performed by Wang *et al.* [2] and by Peng *et al.* ,[3] and a 4-component study reported by Gao *et al.* [4] Using the LDA and SAOP results that are presented in Ref. 4 as reference values, the first 15 LDA and SAOP vertical excitation energies of AuH are listed in Tab. 4.4. The agreement of the vertical excitation energies calculated within this work with the 4-component relativistic results reported by Gao *et al.* [4] is quite good. Nevertheless, some excitation energies differ from the reference values by as much as 0.06 eV. Having achieved a very good agreement with reference values for the TD-SDFT calculations on Zn, Cd, and Hg (Tab. 4.3), the slight disagreements in the case of AuH might again be a basis set effect or differences in the precision of the numerical integration procedure. The difference between the 2-component relativistic results based on the IOTC Hamiltonian and the 4-component relativistic results based on the DC Hamiltonian are at most 0.02 eV and—as expected—independent of the functional (Tab. 4.4).

To complete the TD-SDFT studies of other groups[2–4,153,154] on low-lying excited states of AuH, we have employed the same set of XC functional/kernel pairs as for the TD-SDFT calculations on Zn, Cd, and Hg. The results are summarized in Tab. 4.5 and compared to MRPT2 results obtained by Gao *et al.* [4] It can be seen that both SAOP and its asymptotic limit, LB94, perform remarkably well with a mean relative error of less than 2%. Also the maximum errors of SAOP and LB94 are the smallest among the studied set of functionals. For all other employed functionals the statistics (measured by the mean absolute error, mean relative error, and maximum error) improve when taking higher-lying excitation into account. Note that all employed XC functionals reverse the ordering of the excited states $(II)0^+$ and $(II)2$ with respect to the MRPT2 ordering. Other changes in the ordering also appear: LDA and SAOP reverse $(III)1$ and $(II)0^-$, in addition B3LYP, CAMB3LYP, PBE, PBE0, and BP86 reverse $(III)0^+$ and $(III)1$. Other rearrangements appear for B3LYP, CAMB3LYP, PBE, and PBE0. It is interesting to note that the calculated excitation energies are generally underestimated compared to MRPT2 results with generally comparable statistics—the only exceptions are SAOP and LB94 excitation energies. It has been found that for this system GGA-type and hybrid functionals bring no improvement to excitation energies obtained by LDA.

Table 4.4: LDA and SAOP vertical excitation energies (in eV) of AuH, obtained using the DC and IOTC Hamiltonians and compared with 4-component relativistic results reported by Gao *et al.* [4] The three lower sections of the table compare the deviations of the first 6, 12, and all calculated 15 TD-SDFT excitation energies with the corresponding MRPT2 values from Ref. 4 (MAE: mean absolute error; MRE: mean relative error; ME: maximum error).

Ω	MRPT2[a]	LDA			SAOP			transition
		DC^a	DC^b	$IOTC^b$	DC^a	DC^b	$IOTC^b$	
0^-	3.07	2.83	2.83	2.83	3.03	3.02	3.02	$2\sigma_{1/2}{\to}3\sigma_{1/2}$
1	3.09	2.85	2.85	2.85	3.05	3.04	3.04	$2\sigma_{1/2}{\to}3\sigma_{1/2}$
3	3.79	3.04	3.09	3.10	3.61	3.64	3.65	$\delta_{5/2}{\to}3\sigma_{1/2}$
2	3.81	3.10	3.15	3.16	3.67	3.70	3.71	$\delta_{5/2}{\to}3\sigma_{1/2}$
(II)2	3.89	3.46	3.44	3.45	3.98	3.95	3.95	$\delta_{3/2}{\to}3\sigma_{1/2}$
(II)0^+	3.46	3.39	3.36	3.37	3.70	3.65	3.65	$2\sigma_{1/2}{\to}3\sigma_{1/2}$
(II)1	3.97	3.56	3.54	3.55	4.08	4.04	4.05	$\delta_{3/2}{\to}3\sigma_{1/2}$
(II)0^-	4.81	4.50	4.45	4.46	4.91	4.85	4.86	$\pi_{1/2}{\to}3\sigma_{1/2}$
(III)1	5.04	4.64	4.62	4.64	5.09	5.05	5.06	$\pi_{1/2}{\to}3\sigma_{1/2}$
(III)0^+	4.91	4.66	4.61	4.63	5.10	5.04	5.06	$\pi_{1/2}{\to}3\sigma_{1/2}$
(III)2	5.36	4.79	4.82	4.84	5.30	5.32	5.34	$\pi_{3/2}{\to}3\sigma_{1/2}$
(IV)1	5.33	4.96	4.95	4.97	5.45	5.43	5.45	$\pi_{3/2}{\to}3\sigma_{1/2}$
(III)0^-	5.15	5.09	5.08	5.08	5.72	5.66	5.66	$2\sigma_{1/2}{\to}2\pi_{1/2}$
(IV)0^+	5.35	5.13	5.12	5.12	5.75	5.70	5.70	$2\sigma_{1/2}{\to}2\pi_{1/2}$
(V)1	5.44	5.24	5.23	5.23	5.90	5.84	5.84	$2\sigma_{1/2}{\to}2\pi_{1/2}, 2\pi_{3/2}$
MAE		−0.41	−0.40	−0.39	−0.01	−0.02	−0.01	
MRE (%)	first 6	−13.2	−12.8	−12.5	−0.4	−0.6	−0.5	
ME		−0.75	−0.70	−0.69	0.24	0.19	0.19	
MAE		−0.40	−0.40	−0.39	0.04	0.02	0.03	
MRE (%)	first 12	−10.9	−10.9	−10.6	0.7	0.2	0.4	
ME		−0.75	−0.70	−0.69	0.24	0.19	0.19	
MAE		−0.35	−0.36	−0.35	0.12	0.10	0.10	
MRE (%)	all 15	−9.3	−9.4	−9.2	2.2	1.7	1.8	
ME		−0.75	−0.70	−0.69	0.57	0.51	0.51	

[a] Ref. 4. [b] This work.

Table 4.5: Vertical excitation energies (in eV) of AuH, calculated with various functionals and the DC Hamiltonian. The three lower sections of the table compare the deviations of the first 6, 12, and all calculated 15 TD-SDFT excitation energies with the corresponding MRPT2 values from Ref. 4 (MAE: mean absolute error; MRE: mean relative error; ME: maximum error).

Ω	MRPT2[a]	LDA	SAOP	LB94	BLYP	B3LYP	CAMB3LYP	PBE	PBE0	BP86
0^-	3.07	2.83	3.02	3.02	2.66	2.63	2.50	2.65	2.58	2.74
1	3.09	2.85	3.04	3.04	2.68	2.65	2.52	2.67	2.60	2.76
3	3.79	3.09	3.64	3.52	2.91	3.15	3.06	3.03	3.33	3.07
2	3.81	3.15	3.70	3.59	2.98	3.22	3.13	3.10	3.37	3.14
(II)2	3.89	3.44	3.95	3.87	3.21	3.40	3.30	3.29	3.51	3.34
(II)0^+	3.46	3.36	3.65	3.65	3.20	3.23	3.11	3.29	3.32	3.33
(II)1	3.97	3.54	4.04	3.97	3.33	3.51	3.42	3.40	3.60	3.46
(II)0^-	4.81	4.45	4.85	4.82	4.22	4.34	4.25	4.21	4.31	4.32
(III)1	5.04	4.62	5.05	5.02	4.40	4.56	4.47	4.45	4.61	4.52
(III)0^+	4.91	4.61	5.04	5.07	4.41	4.53	4.42	4.39	4.46	4.49
(III)2	5.36	4.82	5.32	5.31	4.62	4.86	4.76	4.70	4.91	4.76
(IV)1	5.33	4.95	5.43	5.42	4.75	4.96	4.87	4.84	4.93	4.91
(III)0^-	5.15	5.08	5.66	5.85	4.91	4.95	4.86	4.77	4.79	4.92
(IV)0^+	5.35	5.12	5.70	5.89	4.95	4.99	4.91	4.85	4.91	4.98
(V)1	5.44	5.23	5.84	6.05	5.05	5.11	5.04	4.92	5.15	5.06
MAE		−0.40	−0.02	−0.07	−0.58	−0.47	−0.58	−0.51	−0.40	−0.46
MRE (%)	first 6	−12.8	−0.6	−2.1	−19.7	−15.6	−20.0	−17.2	−13.3	−14.9
ME		−0.70	0.19	−0.27	−0.88	−0.64	−0.73	−0.76	−0.49	−0.72
MAE		−0.40	0.02	−0.02	−0.60	−0.46	−0.56	−0.54	−0.42	−0.47
MRE (%)	first 12	−10.9	0.2	−0.7	−17.1	−12.8	−16.3	−15.3	−11.5	−13.1
ME		−0.70	0.19	−0.27	−0.88	−0.64	−0.73	−0.76	−0.50	−0.72
MAE		−0.36	0.10	0.11	−0.55	−0.43	−0.52	−0.53	−0.41	−0.44
MRE (%)	all 15	−9.4	1.7	1.5	−15.1	−11.5	−14.5	−14.1	−10.7	−11.8
ME		−0.70	0.51	0.70	−0.88	−0.64	−0.73	−0.76	−0.50	−0.72

[a] Ref. 4.

4.5   Electronic spectrum of UO_2^{2+}

With their recent TD-SDFT study of the electronic spectrum of UO_2^{2+} and $[UO_2Cl_4]^{2-}$, Pierloot *et al.* [141] have presented the first application of relativistic TD-SDFT on compounds containing an element heavier than a transition metal. In their study, spin–orbit coupling is included by means of the 2-component relativistic ZORA Hamiltonian. They have obtained convincing results for the SAOP functional, closely corresponding to both experiment and to CASPT2. This is a very positive message for future research on spectroscopic properties of heavy element compounds.

Our primary aim is to test our implementation and to compare our TD-SDFT excitation energies with the results reported by Pierloot *et al.* [141]* For simplicity we consider only UO_2^{2+} and focus on the vertical excitation energies exclusively. For maximum overlap with the work of Pierloot *et al.* ,[141] we choose the same U–O bond distance and calculate all excitations out of the bonding σ_u^+ orbitals (formed by O2p and U6d orbitals) into the nonbonding δ_u or ϕ_u orbitals (pure U5f orbitals). For compatibility with the work of Pierloot *et al.* [141] and with experimental work, we maintain the $D_{\infty h}$ single-group notation ($\Sigma, \Pi, \Delta, \ldots$) also for results including spin–orbit coupling. For details on the electronic structure and on previous experimental and theoretical work on this fascinating molecule the reader is referred to Refs. 141 and 155 and the bibliography therein.

The AMFI[79] code—as presently implemented in DIRAC[16]—does not allow h- and i-functions which are present in the U basis set. For consistency we have therefore chosen to carry out all calculations using the DC Hamiltonian.† Based on previous studies (Section 4.4, p. 83) we can expect differences of 0.01 or 0.02 eV between our 4-component results and the 2-component reference values.

The calculated LDA and SAOP vertical excitation energies of UO_2^{2+} are listed in Tab. 4.6 and compared to 2-component relativistic TD-SDFT and CASPT2 results reported by Pierloot *et al.* [141] While the agreement is quite good for SAOP excitation energies including spin–orbit coupling (SO), our scalar relativistic (SR) results agree less consistently with the reference values—especially for LDA and especially for the singlet excitations. The SAOP singlet excitation energies differ by 0.08 and 0.17 eV. The SR LDA numbers are throughout higher by 0.08–0.23 eV. Also among the SO SAOP excitation energies we find a discrepancy of 0.08 eV for $c\,\Delta_g$, which in terms of the SR states[141] is composed by 56% of $^1\Delta_g$, which in turn deviates by 0.17 eV. The discrepancy between the SR and SO numbers—especially the disagreement between the LDA results—is surprising since LDA is the "easier" functional. It should be mentioned that

LDA yields a smaller HOMO–LUMO gap (2.33 eV) than SAOP (3.24 eV; both SR). The LDA HOMO–LUMO gap agrees well with the HOMO–LUMO gap obtained by Pierloot *et al.* [141] who kindly made this unpublished information available.

Although we are not able to use the same basis set as Pierloot *et al.* ,[141] which is a Slater-type quadruple-zeta all electron basis set with four polarization functions, we can be confident in our triple-zeta results as the rather extensive quadruple-zeta basis set ($37s34p27d20f8g5h2i$ on U) yields practically the same results for LDA and same performance can be expected for SAOP. We can exclude doubts about a different (wrong) reference state. In addition, we have pulled out all the stops to verify the convergence of the SCF and TD-SDFT parts and of the numerical integration procedure.

Summing up, although we reproduce the SAOP excitation energies including SO quite well, the conclusion of this test case leaves unfortunately a small question mark. Additional studies—possibly using both implementations—may be necessary. We decided not to employ other functionals until this point is clarified.

Table 4.6: LDA and SAOP vertical excitation energies of UO_2^{2+} calculated with the DC Hamiltonian and compared to 2-component relativistic TD-SDFT and CASPT2 results reported by Pierloot *et al.* [141] (all values in eV; SR: scalar relativistic; SO: including spin–orbit coupling).

		LDA			SAOP		CASPT2[b]
		QZ[a]	TZ[a]	Ref.[b]	TZ[a]	Ref.[b]	
SR	$^3\Phi_g$	2.04	2.04	1.92	3.01	2.98	2.84
	$^3\Delta_g$	2.38	2.38	2.29	3.24	3.21	2.79
	$^1\Phi_g$	2.54	2.54	2.36	3.50	3.42	3.37
	$^1\Delta_g$	3.22	3.22	2.99	4.10	3.93	3.76
SO	$a\,\Delta_g$	1.49	1.49		2.49	2.52	2.38
	$a\,\Phi_g$	1.65	1.64		2.63	2.66	2.51
	$a\,\Pi_g$	2.04	2.04		2.92	2.95	2.49
	$b\,\Delta_g$	2.26	2.26		3.14	3.15	2.76
	$a\,\Gamma_g$	2.39	2.39		3.32	3.36	3.26
	$b\,\Phi_g$	2.63	2.62		3.51	3.53	3.15
	$c\,\Phi_g$	2.75	2.75		3.65	3.65	3.61
	$b\,\Pi_g$	2.81	2.81		3.78		
	$b\,\Gamma_g$	2.92	2.92		3.87		
	$c\,\Delta_g$	3.14	3.14		4.05	3.97	3.88
	$d\,\Phi_g$	3.15	3.15		4.10		

[a] This work. [b] Ref. 141.

Chapter 5

Real-space approach to molecular properties

*This ... this, I think, has a kind of wonderful otherness to it, you
know.—A marvelous negative capability. Kind of wonderful energy
to it, don't you think?*

Woody Allen in *Manhattan* (1979)

Consider a molecule in the presence of perturbations, which could be potentials generated by external electric or magnetic fields, or potentials generated by the nuclear magnetic moments for instance, or geometrical distortions. As a start, these perturbations can be restricted to static external electric or magnetic fields. In the time-independent limit, the molecular energy is well-defined and will change upon perturbation. One can monitor the energy change to specific perturbation amplitudes and define (and obtain) static molecular properties as energy derivatives with respect to specific perturbation amplitudes at zero field.

Depending on the perturbation, changes in the charge-, spin-, or charge current density or other densities can be induced. This chapter will demonstrate how the corresponding density derivatives can be used to calculate and visualize molecular properties and how to define molecular property densities. Frequency-dependent properties can be visualized employing the quasienergy formalism.

The static and frequency-dependent first-order densities and densities corresponding to second-order properties are obtained from the linear response of the HF or KS determinant. Further (static) perturbations may be imposed by using the finite perturbation method, which is described in Note C, p. 189. The only limit is then the numerical precision.

After a methodological section the potential of the real-space approach to molecular properties will be illustrated in five examples: (i) charge density of Ne and the HF molecule induced

by a static electric field, (ii) the static and frequency-dependent polarizability of Ne from the induced charge and current density, (iii) the induced current density in the group 15 heteroaromatic compounds (pyridine to bismabenzene), (iv) the nuclear spin–spin coupling density in CO, and finally (v), the parity-violating energy difference between the two enantiomers of CHF-ClBr subject to a geometrical distortion along a vibrational mode, studied via the γ^5 density.

5.1   Analytical first-order densities and property densities

The frequency-dependent linear HF or KS response to the perturbation P is carried by the first-order orbital rotation amplitudes that form the response vector according to (see Section 2.5, p. 57 for more details)

$$\mathbf{N}^{(P)}(\omega) = \begin{bmatrix} \mathbf{z} \\ \mathbf{y}^\star \end{bmatrix} \quad \text{with} \quad \begin{aligned} z_{ai} &= \kappa_{ai}^{(P)}(\omega) \\ y_{ai} &= \kappa_{ai}^{(P)}(-\omega) \end{aligned}. \tag{5.1}$$

The vector elements are the nonredundant elements of a MO matrix and so properties of the matrix are transferred to vector elements, e.g. Hermiticity and time reversal symmetry as discussed in Section 2.5, p. 57. The response vector is accordingly expressed as a sum of a Hermitian and anti-Hermitian contribution

$$\mathbf{N}^{(P)}(\omega) = \mathbf{N}^{+(P)}(\omega) + \mathbf{N}^{-(P)}(\omega) \tag{5.2}$$

with well-defined time reversal symmetry ($t = \pm 1$). In the 4-component relativistic framework there is a natural division between rotations with positive energy virtuals and rotations with negative energy virtuals and it is useful to distinguish between contributions to the response vector that contain only rotations with positive energy virtuals (positive-positive; pp) and contributions that contain only rotations with negative energy virtuals (positive-negative; pn)

$$\mathbf{N}^{(P)}(\omega) = \mathbf{N}_{\mathrm{pp}}^{+(P)}(\omega) + \mathbf{N}_{\mathrm{pn}}^{+(P)}(\omega) + \mathbf{N}_{\mathrm{pp}}^{-(P)}(\omega) + \mathbf{N}_{\mathrm{pn}}^{-(P)}(\omega). \tag{5.3}$$

For a static time reversal symmetric perturbation only the Hermitian part is nonzero

$$\mathbf{N}^{(P)}(0) = \mathbf{N}_{\mathrm{pp}}^{+(P)}(0) + \mathbf{N}_{\mathrm{pn}}^{+(P)}(0), \tag{5.4}$$

whereas for a static time reversal antisymmetric perturbation* the response vector reduces to its anti-Hermitian part

$$\mathbf{N}^{(P)}(0) = \mathbf{N}_{\mathrm{pp}}^{-(P)}(0) + \mathbf{N}_{\mathrm{pn}}^{-(P)}(0). \tag{5.5}$$

---

* Recall that in order to take full advantage of time reversal symmetry in quaternion formulation, t and h have been reversed in this case by the extraction of an imaginary phase which is later reintroduced.

From the elements of the Hermitian and anti-Hermitian part of the response vector $\mathbf{N}^{+(P)}$ and $\mathbf{N}^{-(P)}$, we construct the first-order (AO) density matrices

$$D_{\lambda\kappa}^{h(P)} = c_{\lambda p} W_{pq} c_{\kappa q}^{\star} \tag{5.6}$$

of well-defined Hermiticity ($D_{\lambda\kappa}^{h(P)\dagger} = h D_{\kappa\lambda}^{h(P)}$), using the symmetric auxiliary matrix:

$$W_{ii} = 0; \qquad W_{aa} = 0; \qquad W_{ai} = N_{ai}^{h(P)}; \qquad W_{ia} = W_{ai}. \tag{5.7}$$

In the static case there will be only one first-order $h = +1$ ($h = -1$) density matrix, corresponding to a $t = +1$ ($t = -1$) perturbation. By considering only the pp (pn) part of the response vector it is possible to construct a density matrix that describes—in NR terms—the "paramagnetic" ("diamagnetic") response (see also Section 1.9, p. 47).

Having a first-order density matrix $D_{\lambda\kappa}^{h(P)}$ of well-defined Hermiticity $h = \pm 1$ enables us to calculate various (analytical) first-order densities $\psi^{\dagger} M_t \psi$ (Note B, p. 185), where M_t is one of the Dirac matrices with well-defined time reversal symmetry $t = \pm 1$ (Tab. 1.4). This possibility will be explored further below in several examples. Combining Tabs. 1.4 and B.1, it is now understood that only the combinations

$$M_+ \quad \text{and} \quad D_{\lambda\kappa}^{+(P)}$$

and

$$M_- \quad \text{and} \quad D_{\lambda\kappa}^{-(P)}$$

can give a nonzero density $\psi^{\dagger} M_t \psi$.

Before turning to actual examples of induced first-order densities, it is possible to go one step further and define linear response property densities. For this start from the linear response function $\langle\langle \hat{A}; \hat{P} \rangle\rangle_{\omega}$ written as a linear variation of the expectation value $A = \langle \hat{A} \rangle$ under the perturbation P,

$$\langle\langle \hat{A}; \hat{P} \rangle\rangle_{\omega} = \frac{dA}{df_B(\omega)} = \frac{\partial A}{\partial \mathbf{K}(\omega)} \frac{\partial \mathbf{K}(\omega)}{\partial f_B(\omega)} = -\mathbf{A}^{(1)\dagger} \mathbf{N}^{h(P)}(\omega) \tag{5.8}$$

with the property gradient

$$\mathbf{A}^{(1)} = \begin{bmatrix} \mathbf{g} \\ \mathbf{g}^{\star} \end{bmatrix} \tag{5.9}$$

which is always Hermitian and contains the elements

$$g_{ai} = -\langle \phi_a | \hat{A} | \phi_i \rangle, \tag{5.10}$$

and a response vector of well-defined Hermiticity

$$\mathbf{N}^{h(P)}(\omega) = \begin{bmatrix} \mathbf{v} \\ h\mathbf{v}^\star \end{bmatrix}. \tag{5.11}$$

The linear response function can be therefore written as

$$\langle\langle \hat{A}; \hat{P} \rangle\rangle_\omega = \sum_{ai} \left[\langle \phi_a | \hat{A} | \phi_i^{(P)} \rangle + \langle \phi_i^{(P)} | \hat{A} | \phi_a \rangle \right] \tag{5.12}$$

$$= -\sum_{ai} \int d\mathbf{r} \left[\phi_a^\dagger \hat{A} \phi_i v_{ai} + h\phi_i^\dagger v_{ai}^\star \hat{A} \phi_a \right].$$

For $\hat{A}$ choose for instance the operator of a uniform electric field $\mathbf{F}$,

$$\hat{A} = e\mathbf{r}. \tag{5.13}$$

With this specific choice Eq. 5.12 becomes

$$\langle\langle \hat{A}; \hat{P} \rangle\rangle_\omega = -\int d\mathbf{r}\, e\mathbf{r}\, \Omega_{\kappa\lambda} D_{\lambda\kappa}^{h(P)}, \tag{5.14}$$

using Eq. 5.6 and the structure of the auxiliary matrix W in Eq. 5.7. Here $\Omega_{\kappa\lambda} = \chi_\kappa \chi_\lambda$ is the AO overlap distribution. The term $\Omega_{\kappa\lambda} D_{\lambda\kappa}^{h(P)}$ can be identified with the induced first-order number density $n^{(P)}$ which enables us to reexpress the linear response function with $\hat{A} = e\mathbf{r}$ as

$$\langle\langle \hat{A}; \hat{P} \rangle\rangle_\omega = -e \int d\mathbf{r}\, \mathbf{r} n^{(P)} = \int d\mathbf{r}\, \mathbf{r} \rho^{(P)} \tag{5.15}$$

and to obtain, for instance, a specific component $\alpha_{ij}(\omega)$ of the frequency-dependent electric dipole linear polarizability tensor by

$$\alpha_{ij}(\omega) = \langle\langle \hat{A}_i; \hat{A}_j \rangle\rangle_\omega = \int d\mathbf{r}\, r_i \rho^{(j)}(\omega) = \int d\mathbf{r}\, \alpha_{ij}(\mathbf{r}; \omega) \tag{5.16}$$

The above exercise can be repeated for other responding operators $\hat{A}$, e.g. the uniform magnetic field $\mathbf{B}$

$$\hat{A} = -\frac{1}{2}(\mathbf{r}_G \times \hat{\mathbf{j}}), \tag{5.17}$$

to give

$$\langle\langle \hat{A}; \hat{P} \rangle\rangle_\omega = -\frac{1}{2} \int d\mathbf{r}\, (\mathbf{r}_G \times \mathbf{j}^{(P)}), \tag{5.18}$$

or for the nuclear magnetic dipole moment $\mathbf{M}_K$

$$\hat{A}^K = -\frac{1}{c^2 r_K^3}(\mathbf{r}_K \times \hat{\mathbf{j}}), \tag{5.19}$$

to give

$$\langle\langle \hat{A}^K; \hat{P} \rangle\rangle_\omega = -\frac{1}{c^2} \int d\mathbf{r}\, \frac{1}{r_K^3}(\mathbf{r}_K \times \mathbf{j}^{(P)}). \tag{5.20}$$

In the above two examples $\mathbf{r}_G$ is the distance vector from the gauge origin, $\mathbf{r}_K$ the distance vector from the center of the nucleus K, and $\mathbf{j}^{(P)}$ is the induced charge current density. These examples (Eqs. 5.15, 5.18, and 5.20) are the first-order terms of the corresponding multipole expansions (see Ref. 66).

The approach outlined above enables us to visualize real-space property densities that correspond to linear response functions. This idea is however not new. The concept of property densities has already been introduced 1979 by Jameson and Buckingham[156, 157] with nuclear magnetic shielding density function and later enhanced by several groups[158–167] to enable the visualization of nuclear spin–spin coupling densities with different methodological flavors.

The formulation presented here suggests that it should be possible and relatively easy to define property densities for arbitrary linear response functions. In contrast to NR realizations of other implementations[156–161, 163–167] this 4-component relativistic approach to property densities allows for the extension of the scope to heavy-element systems including spin–orbit coupling effects.

Some general observations can already be made at this stage and will be outlined before turning to a discussion of some examples:

(i) Property densities as defined in the above examples are in general not unique. The integral over all space (the linear response function) has the symmetry

$$\langle\langle \hat{A}(-\omega); \hat{P}(\omega) \rangle\rangle = \langle\langle \hat{P}(\omega); \hat{A}(-\omega) \rangle\rangle, \tag{5.21}$$

however, this symmetry is in general not given for the linear response function density distribution in space.

(ii) Property densities in the present implementation are not gauge origin including, which implies an ambiguity in the choice of gauge origin for magnetic property densities. Note, for instance, that a change of origin $r_i \rightarrow r_i + d$ will not affect the induced electric dipole moment

$$\mu_i^{(P)} = \int d\mathbf{r}\, r_i \rho^{(P)} \tag{5.22}$$

$$\mu_i'^{(P)} = \int d\mathbf{r}\, (r_i + d) \rho^{(P)} \tag{5.23}$$

$$= \int d\mathbf{r}\, r_i \rho^{(P)} + d \int d\mathbf{r}\, \rho^{(P)} = \mu_i^{(P)},$$

since the integral over $\rho^{(P)}$ must be zero (see next section). The nuclear spin–spin coupling density which will be discussed below is not affected by the choice of gauge origin since it contains only reference to (well-defined) nuclear centers.

(iii) It is a trivial task to isolate (and plot) individual orbital contributions by using particular elements of the corresponding response vectors for the construction of modified density matrices.

(iv) "Paramagnetic" and "diamagnetic" property densities can be defined exactly as the "paramagnetic" and "diamagnetic" parts of linear response functions are calculated, by considering only the pp or pn parts of the corresponding response vectors.

(v) Scalar relativistic effects and spin–orbit coupling effects to property densities can be visualized exactly as they are calculated/eliminated in linear response calculations.

5.2   Densities induced by a static electric field

This section focuses on the first- and second-order charge density induced by a static external uniform electric field $\mathbf{F}$ for which the total energy $E(\mathbf{F})$ can be expanded in different orders of field strengths along the Cartesian directions $i, j, k, l, \ldots$

$$E(\mathbf{F}) = E(0) - \mu_i(0)F_i - \frac{1}{2!}\alpha_{ij}F_iF_j - \frac{1}{3!}\beta_{ijk}F_iF_jF_k - \frac{1}{4!}\gamma_{ijkl}F_iF_jF_kF_l - \cdots. \tag{5.24}$$

The total electric dipole moment is given by

$$\mu_i = -\frac{\partial E}{\partial F_i} = \mu_i(0) + \alpha_{ij}F_j + \frac{1}{2!}\beta_{ijk}F_jF_k + \frac{1}{3!}\gamma_{ijkl}F_jF_kF_l + \cdots. \tag{5.25}$$

Here $\mu_i(0)$ is one component of the permanent electric dipole moment, and $\alpha_{ij}, \beta_{ijk}, \gamma_{ijkl}, \ldots,$ are the components of the electric dipole linear polarizability and the first-, second-, $\ldots$, hyper-polarizability tensor, respectively. These tensors are symmetric under permutation of indices, e.g.

$$\alpha_{ij} = \alpha_{ji} \tag{5.26}$$

$$\beta_{ijk} = \beta_{ikj} = \beta_{jik} = \beta_{jki} = \beta_{kij} = \beta_{kji} \tag{5.27}$$

$$\cdots = \cdots$$

The electric dipole moment component μ_i can be evaluated using the charge density

$$\mu_i = -e\langle 0|\hat{r}_i|0\rangle = \int d\mathbf{r}\, r_i\rho. \tag{5.28}$$

This is the general expression which can be expanded in the orders of field strengths and enables us to write

$$\mu_i = \int d\mathbf{r}\, r_i\rho(0) + \int d\mathbf{r}\, r_i\rho^{(j)}F_j + \frac{1}{2!}\int d\mathbf{r}\, r_i\rho^{(jk)}F_jF_k + \frac{1}{3!}\int d\mathbf{r}\, r_i\rho^{(jkl)}F_jF_kF_l + \cdots, \tag{5.29}$$

introducing the first-, second-, third-, $\ldots$, order induced charge densities $\rho^{(j)}, \rho^{(jk)}, \rho^{(jkl)}, \ldots$. A comparison of Eq. 5.25 to Eq. 5.25 allows one to identify

$$\alpha_{ij} = \int d\mathbf{r}\, r_i\rho^{(j)} \tag{5.30}$$

$$\beta_{ijk} = \int d\mathbf{r}\, r_i\rho^{(jk)} \tag{5.31}$$

$$\cdots = \cdots$$

Interchanging the Cartesian directions will not change the value of these integrals. However, the full permutational symmetry does not hold for the integrands. Permutational symmetry holds,
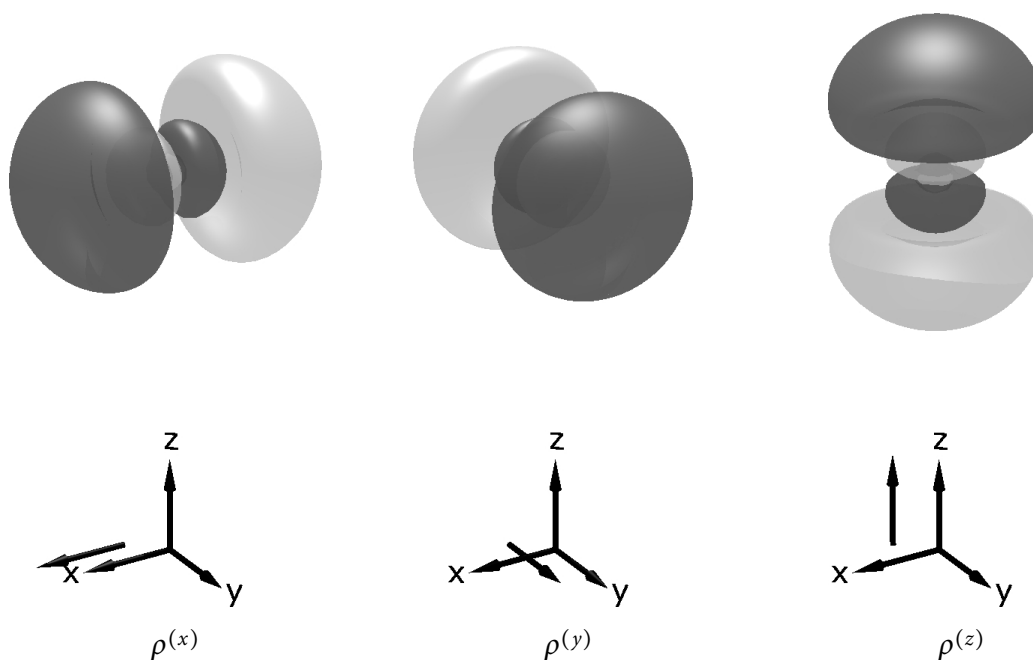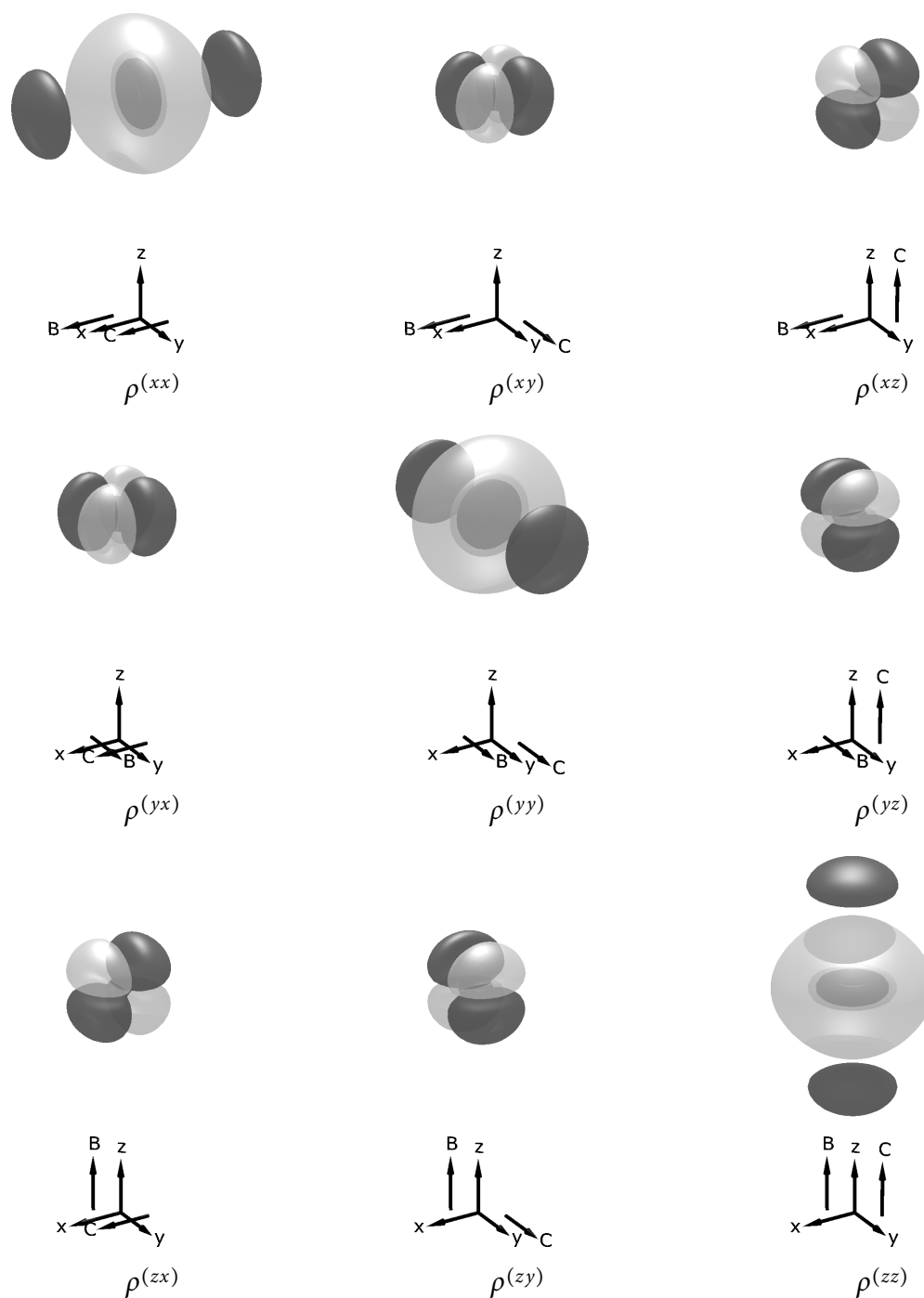
Figure 5.1: First-order charge density $\rho^{(j)}$ of Ne (LDA, uncontracted t-aug-cc-pVTZ). Dark (light) iso-surface corresponds to +0.05 (−0.05) $e^2/a_o^2 E_h$. The plots use the same scaling as in Fig. 5.3. The additional arrow indicates the orientations of the perturbing electric dipole operator.

though, for the induced charge densities which are independent of the ordering of derivatives, e.g.

$$\rho^{(jk)} = \rho^{(kj)} \tag{5.32}$$

$$\rho^{(jkl)} = \rho^{(jlk)} = \rho^{(klj)} = \rho^{(kjl)} = \rho^{(ljk)} = \rho^{(lkj)} \tag{5.33}$$

$$\cdots = \cdots$$

In Fig. 5.1 the three first-order charge densities $\rho^{(j)}$ are plotted as isosurfaces for Ne, corresponding to the three Cartesian orientation of the perturbing electric dipole. These densities have been obtained analytically from linear response (Section 5.1, p. 90) using the LDA (SVWN5)[45,139] functional together with the uncontracted t-aug-cc-pVTZ[168] basis set. This specific choice of functional is not important for the following qualitative discussion. The perturbing electric field cannot generate but only redistribute charge, which implies that $\rho^{(j)}$ and all higher-order charge densities beyond the zeroth-order integrate to zero charge, order by order, and therefore the plots always contain isosurfaces of both signs. Fig. 5.1 also demonstrates the shell structure of the induced first-order charge densities. In the example of Ne three shells are visible, although the inner isosurface (arising from *1s* charge density) is small. The first-order

charge densities $\rho^{(j)}$ can be weighted with the three directions r_i and integrated "visually" to α_{ij}. Doing this with the first-order charge densities in Fig. 5.1 confirms the expectation that all diagonal elements α_{ii} are equal and that all off-diagonal elements vanish for Ne.

All elements β_{ijk} must vanish for Ne, and this fact can be used to double-check the nine second-order charge densities depicted in Fig. 5.2. The first perturbation (operator B) has been introduced within linear response whereas the response to the second (operator C) has been obtained by finite perturbation (Note C, p. 189). The orientations of operators B and C are represented by arrows in Fig. 5.2. Indeed, all "visually" integrated

$$\beta_{ijk} = \int \mathrm{d}\mathbf{r}\, r_i \rho^{(jk)} \tag{5.34}$$

vanish since, as expected, $\rho^{(jk)}$ are symmetric with respect to the plane normal to the Cartesian direction i. It can also be verified that the ordering of operators B and C does not matter such that $\rho^{(jk)} = \rho^{(kj)}$.

To obtain nonzero β_{ijk}, the second-order charge densities $\rho^{(jk)}$ have been plotted for the HF molecule (Fig. 5.4), using the experimental bond length $R = 0.9171$ Å.[169] These densities are obtained by finite perturbation differentiation from the analytical first-order charge densities depicted in Fig. 5.3.

Again, "visual" integration of β_{ijk} in Fig. 5.4 identifies $\beta_{xxz}, \beta_{xzx}, \beta_{zxx}, \beta_{xxy}, \beta_{xyx}, \beta_{yxx}$, and β_{zzz} as the only nonzero components. For LDA (SVWN5)[45,139] with the uncontracted t-aug-cc-pVTZ[168] basis set they are $\beta_{xxz} = \beta_{xzx} = \beta_{zxx} = \beta_{xxy} = \beta_{xyx} = \beta_{yxx} = 2.29\ e^3 a_o^3 / E_h^2$ and $\beta_{zzz} = 10.65\ e^3 a_o^3 / E_h^2$.

Figure 5.2: Second-order charge density $\rho^{(jk)}$ of Ne (LDA, uncontracted t-aug-cc-pVTZ). Dark (light) isosurface corresponds to $+0.1$ (-0.1) $e^3/a_\mathrm{o}E_\mathrm{h}^2$. The plots use the same scaling as in Fig. 5.4. The arrows indicate the orientation of the perturbing electric dipole operators B and C.

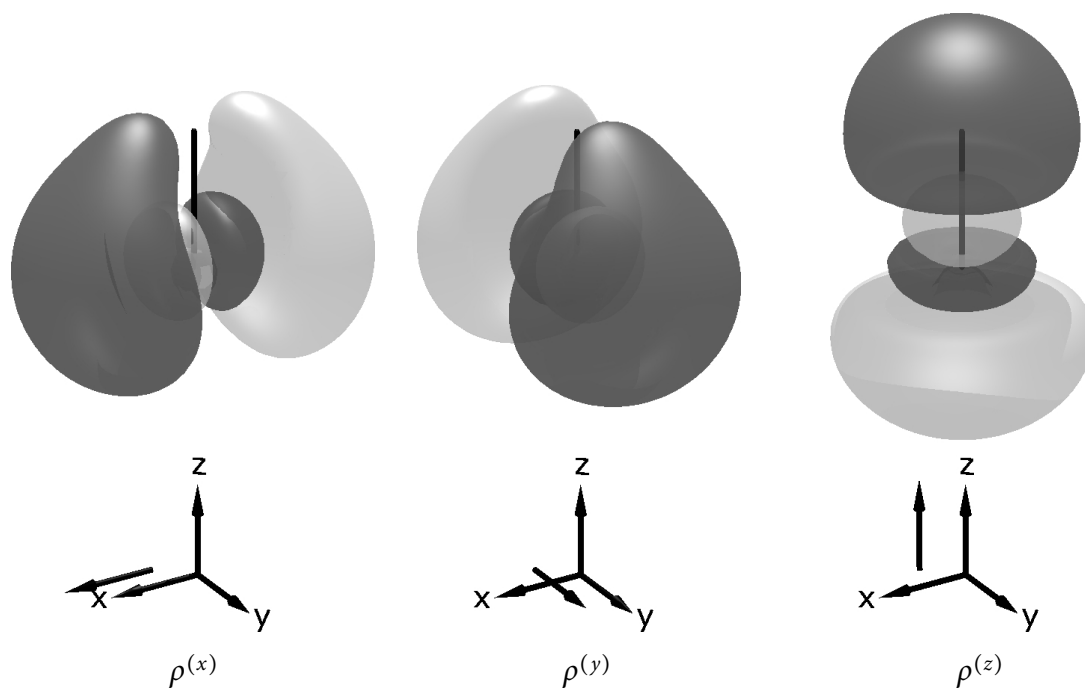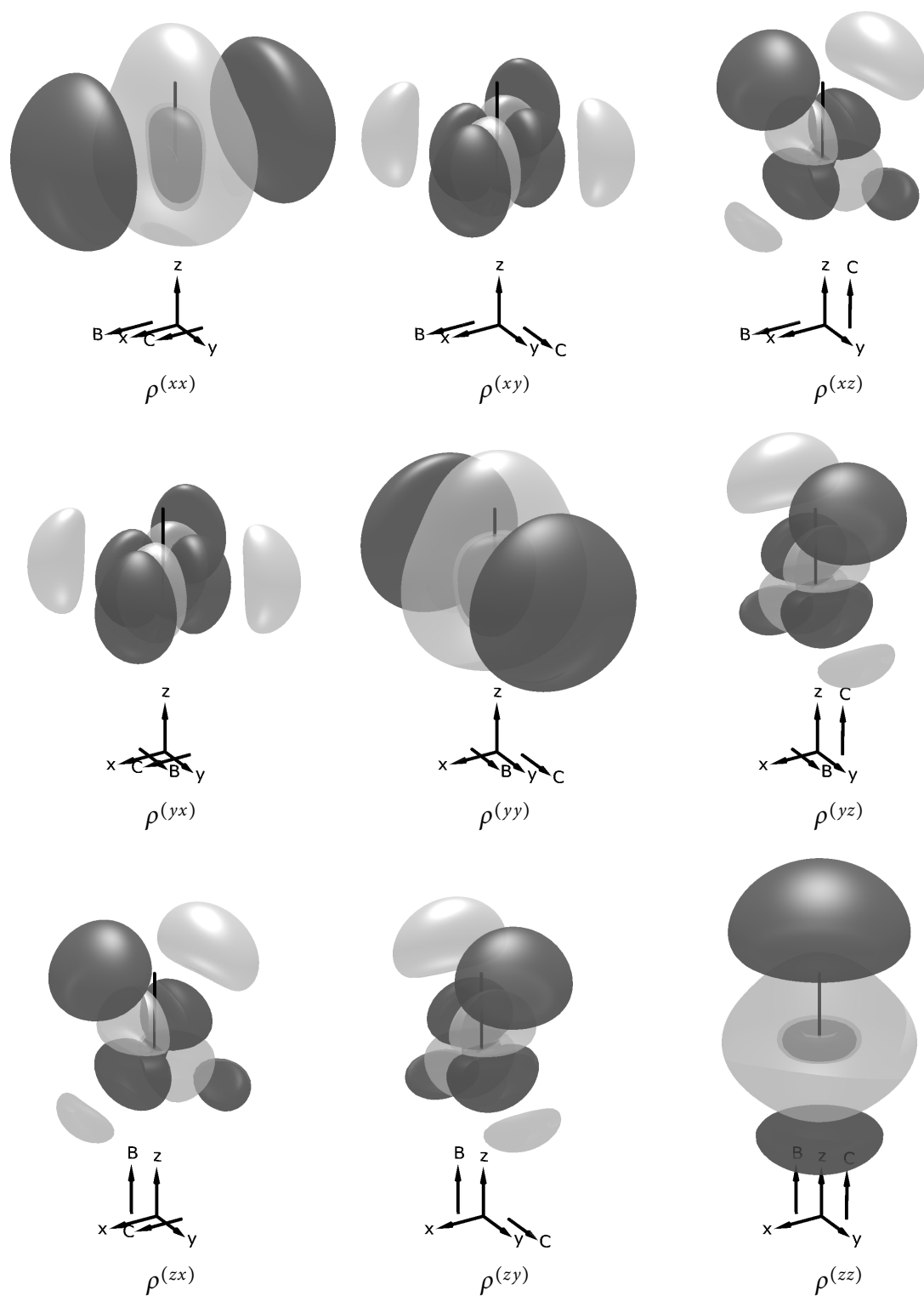**Figure 5.3:** First-order charge density $\rho^{(j)}$ of the HF molecule (LDA, uncontracted t-aug-cc-pVTZ). Dark (light) isosurface corresponds to $+0.05$ (-0.05) $e^2/a_o^2 E_h$. The molecule (dark stick representation) is oriented along the z-axis (top atom: H; bottom atom: F). The additional arrow indicates the orientations of the perturbing electric dipole operator.

$\rho^{(xx)}$　　　　　　$\rho^{(xy)}$　　　　　　$\rho^{(xz)}$

$\rho^{(yx)}$　　　　　　$\rho^{(yy)}$　　　　　　$\rho^{(yz)}$

$\rho^{(zx)}$　　　　　　$\rho^{(zy)}$　　　　　　$\rho^{(zz)}$

Figure 5.4: Second-order charge density $\rho^{(jk)}$ of the HF molecule (LDA, uncontracted t-aug-cc-pVTZ). Dark (light) isosurface corresponds to $+0.1$ (-0.1) $e^3/a_0 E_h^2$. The molecule (dark stick representation) is oriented along the z-axis (top atom: H; bottom atom: F). The arrows indicate the orientation of the perturbing electric dipole operators B and C.

As a conclusion, the plots in Figs. 5.1 to 5.4 are without doubt nice, but can they also be useful?

(i) The real-space plots actually show where in space the response has been sampled. For instance the presented plots underline that the linear polarizability and the first nonlinear hyperpolarizability are valence properties sampled in the outer valence region. This can be useful at least to demonstrate the basis set requirements of a specific property.

(ii) Interpretations of nonlinear properties can be elusive and the induced density isosurface plots presented here may give additional insight to the problem up and above just the numbers, for instance to discuss trends of properties among a class of molecules.

5.3 Densities induced by a frequency-dependent electric field

This section will demonstrate how the frequency-dependent electric dipole linear polarizability can be visualized (and evaluated) using the induced charge density or alternatively using the induced charge current density.

The charge density ρ and the charge current density $\mathbf{j}$ obey the continuity relation

$$-\frac{\partial \rho}{\partial t} = \nabla \cdot \mathbf{j} \tag{5.35}$$

which in the frequency domain becomes

$$\rho(\omega) = -\frac{i}{\omega} \nabla \cdot \mathbf{j}(\omega) \tag{5.36}$$

with the frequency ω. As described in the previous section, the frequency-dependent electric dipole linear polarizability component $\alpha_{ij}(\omega)$ may be evaluated from the first-order charge density $\rho^{(j)}(\omega)$ induced by the component F_j of an external electric field according to

$$\alpha_{ij}(\omega) = \int d\mathbf{r}\, r_i \rho^{(j)}(\omega), \tag{5.37}$$

or alternatively, using Eq. 5.36, from the divergence of the first-order charge current density $\nabla \cdot \mathbf{j}^{(j)}(\omega)$ according to

$$\alpha_{ij}(\omega) = -\frac{i}{\omega} \int d\mathbf{r}\, r_i \nabla \cdot \mathbf{j}^{(j)}(\omega). \tag{5.38}$$

Next, using integration by parts

$$\alpha_{ij}(\omega) = \frac{i}{\omega} \int_V d\mathbf{r}\, \mathbf{j}^{(j)}(\omega) \cdot \nabla r_i - \frac{i}{\omega} \oint_S r_i\, \mathbf{j}^{(j)}(\omega) \cdot d\mathbf{s}, \tag{5.39}$$

Eq. 5.38 reduces to

$$\alpha_{ij}(\omega) = \frac{i}{\omega} \int d\mathbf{r}\, j_i^{(j)}(\omega), \tag{5.40}$$

assuming that $\mathbf{j}$ vanishes at infinity. The frequency-dependent electric dipole linear polarizability component $\alpha_{ij}(\omega)$ may now be obtained by integrating the first-order induced $j_i^{(j)}(\omega)$. This argument is also used by van Faassen *et al.* to calculate static $\alpha_{ij}(0)$ within current density functional theory by extrapolating to zero frequency (see for instance Ref. 101 and references therein). This assumption is certainly valid for finite systems within the finite basis approximation. An interesting test case turns out be the representation of the continuity relation (Eq. 5.36) in a finite basis. To demonstrate this, we have calculated $\alpha_{zz}(\omega)$ of Ne with $\omega = 0.1\, E_{\mathrm{h}}/\hbar$, using the s- and d-aug-cc-pVNZ (N = D, T, Q, 5, 6) series of basis sets[170,171] in the uncontracted form. In addition a family-type basis set has been generated where the even-tempered parent set consists of 50 exponents

$$\eta_k = \alpha \beta^{(50-k)}; \qquad k = 1, \dots, 50 \tag{5.41}$$

with $\alpha = 0.0005$ and $\beta = 1.6$. The respective exponent subsets $\{k_s\}$, $\{k_p\}$, $\{k_d\}$, and $\{k_f\}$ are 7–42, 12–42, 29–39, and 30–38. This basis set will be denoted ET (for even-tempered). We have chosen the LDA (SVWN5)[45,139] functional together with the DC Hamiltonian, although this specific choice of functional and Hamiltonian is not important for the following discussion. The induced charge and charge current density are obtained analytically following the outline in Section 5.1, p. 90 using the Hermitian and anti-Hermitian parts of the response vector, respectively (Eq. 5.2).

The results are listed in Tab. 5.1. Starting from (uncontracted) d-aug-cc-pVQZ, the frequency-dependent polarizability can be considered converged to three significant digits ($3.10\ e^2 a_o^2/E_h$). The agreement—using the s-aug-cc-pVDZ basis set—between the results obtained using Eq. 5.37 and Eq. 5.38, respectively, is rather poor (2.14 vs. 1.99 $e^2 a_o^2/E_h$). Again, it requires to employ at least d-aug-cc-pVQZ to get good agreement between these two approaches, which are related by the continuity.

Table 5.1: LDA frequency-dependent ($\omega = 0.1\ E_h/\hbar$) polarizability of Ne (in $e^2 a_o^2/E_h$) obtained by numerical integration from the induced charge density and from the induced charge current density. All basis sets are uncontracted.

basis	$\int d\mathbf{r}\ r_z \rho^{(z)}(\omega)$	$-\frac{i}{\omega} \int d\mathbf{r}\ r_z \nabla \cdot \mathbf{j}^{(z)}(\omega)$
s-aug-cc-pVDZ	2.1407	1.9892
d-aug-cc-pVDZ	3.0485	3.0549
d-aug-cc-pVTZ	3.0913	3.0940
d-aug-cc-pVQZ	3.1016	3.1022
d-aug-cc-pV5Z	3.1017	3.1018
d-aug-cc-pV6Z	3.1015	3.1016
ET[a]	3.1014	3.1012

[a] See p. 103.

Figs. 5.5 and 5.6 show cuts through $\rho^{(z)}(\omega)$ and $-\frac{\mathrm{i}}{\omega}\nabla \cdot \mathbf{j}^{(z)}(\omega)$ for several basis sets. The left-hand panels of Figs. 5.5 and 5.6 correspond to cuts though the right panel of Fig. 5.1. They look identical, the minute modifications when improving the basis set (compare with Tab. 5.1) are not visible. The situation is different for $-\frac{\mathrm{i}}{\omega}\nabla \cdot \mathbf{j}^{(z)}(\omega)$ (right-hand panels). Especially in the core region, the disagreement with $\rho^{(z)}(\omega)$ and a slow convergence with respect to the basis set cardinal number is clearly visible. Although the overall topology of the contour plots and the nodal structure are reasonably represented in the induced $-\frac{\mathrm{i}}{\omega}\nabla \cdot \mathbf{j}^{(z)}(\omega)$, additional nodal surfaces appear and only by using d-aug-cc-pV6Z or the dedicated ET basis set a visually qualitative agreement is reached.

This comparison is not meant to disqualify moderately sized basis sets for obtaining frequency-dependent electric dipole linear polarizabilities from the induced charge current density. The position component r_i which appears for instance in Eq. 5.38 favors the outer valence and therefore a disagreement in the core region is less important for this *valence* property (Tab. 5.1).

The aim is to show that a systematic improvement of the basis set improves the representation of the continuity relation which holds only in a complete basis. The chosen basis set series d-aug-cc-pVNZ may not be the ideal choice being only slowly convergent and certainly not designed for the property under study. The most convincing plots have been obtained using the ET basis set which shows that flexibility in the core region is needed rather than high angular momentum exponents in this situation.
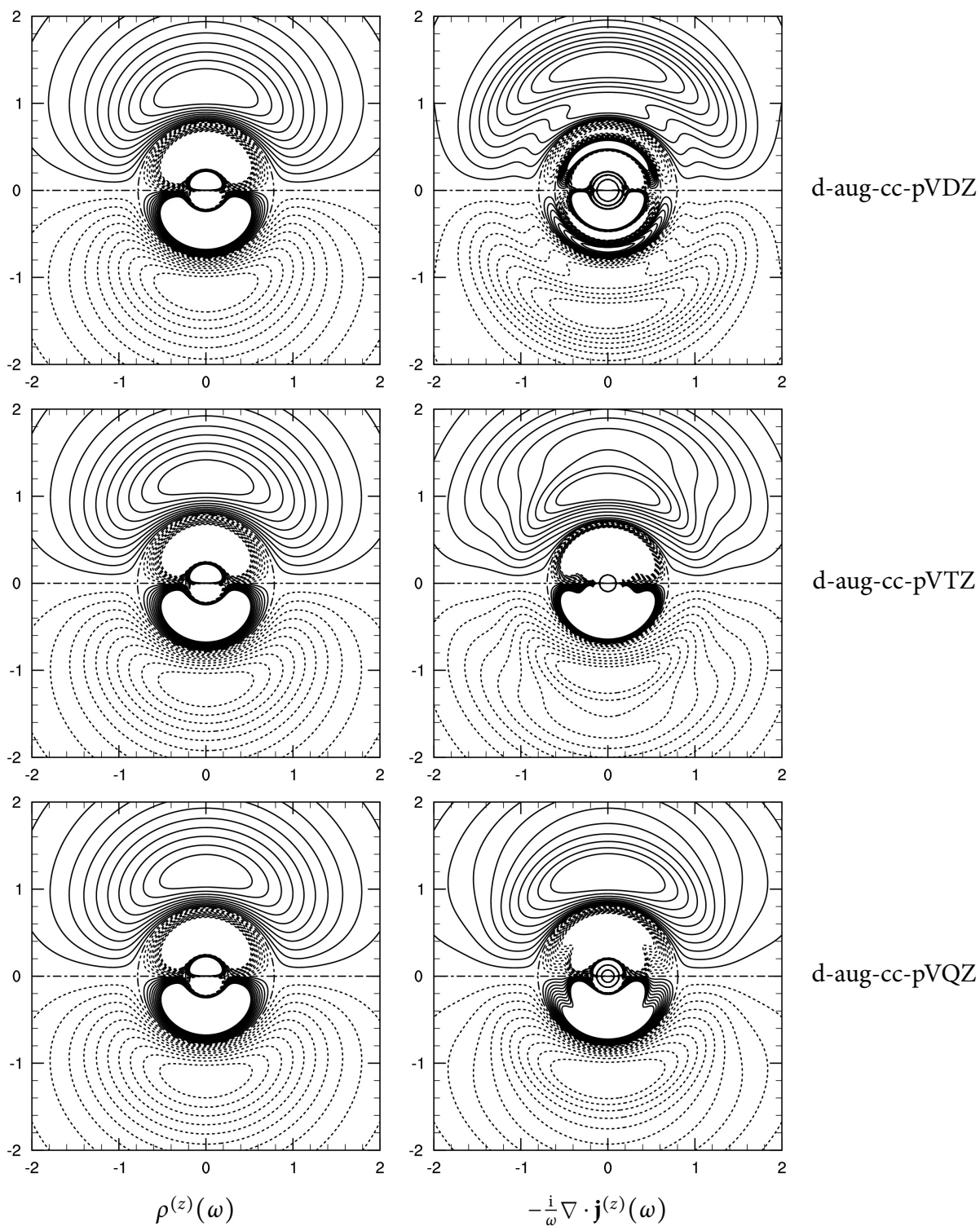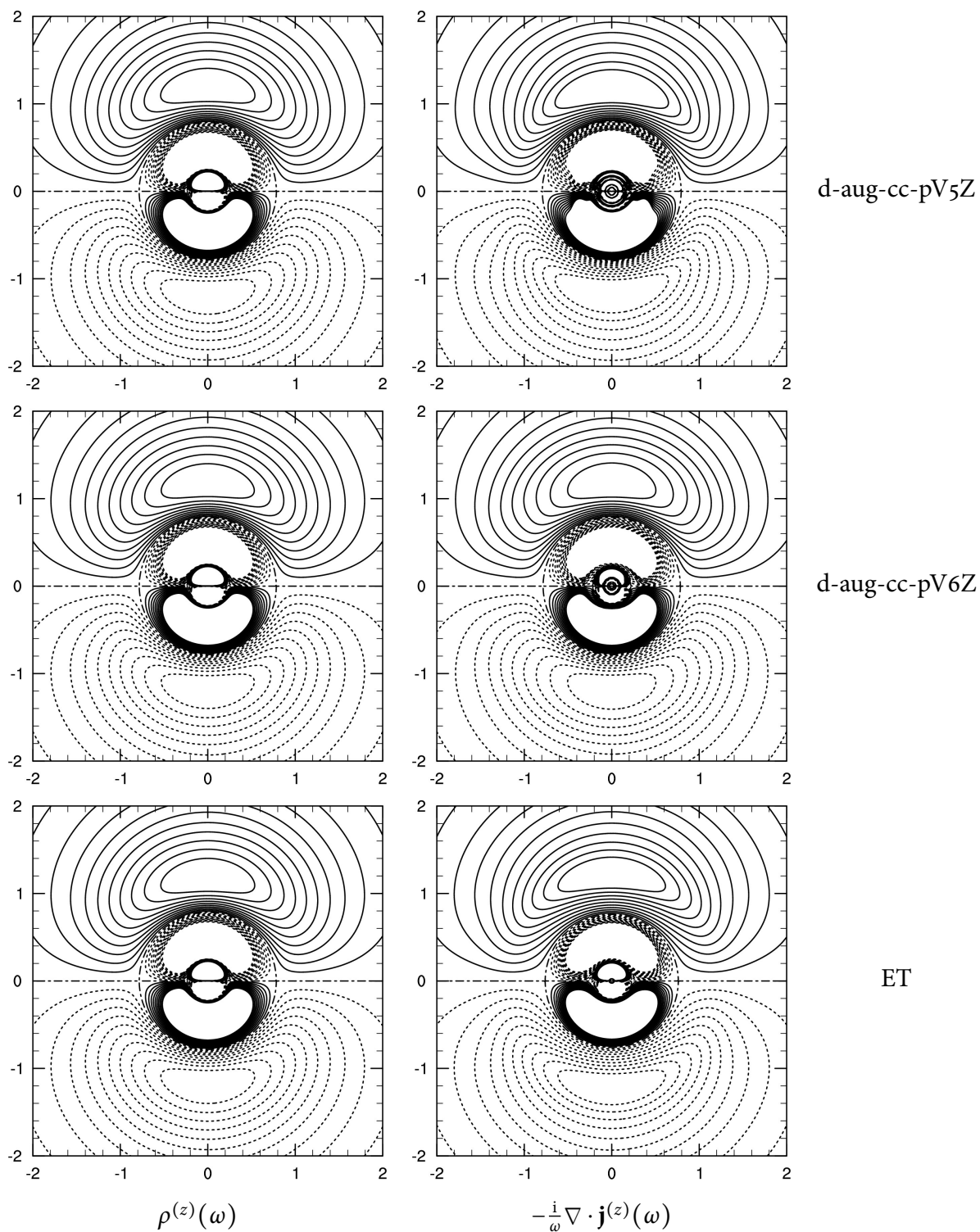
Figure 5.5: LDA first-order charge density and divergence of the first-order charge current density of Ne induced by a frequency-dependent ($\omega = 0.1\ E_\mathrm{h}/\hbar$) electric field, using different basis sets (from top to bottom: d-aug-cc-pVDZ, d-aug-cc-pVTZ, d-aug-cc-pVQZ; all uncontracted). Solid (dotted) contour lines are plotted in the range from $+0.01$ to $+0.1$ (-0.01 to -0.1) $e^2/a_\mathrm{o}^2 E_\mathrm{h}$ in intervals of $0.01\ e^2/a_\mathrm{o}^2 E_\mathrm{h}$. The dash-dotted contour line represents $0\ e^2/a_\mathrm{o}^2 E_\mathrm{h}$. The dimensions of the plots are $4 \times 4\ a_\mathrm{o}$.

$$\rho^{(z)}(\omega) \qquad\qquad -\tfrac{\mathrm{i}}{\omega}\nabla\cdot\mathbf{j}^{(z)}(\omega)$$

Figure 5.6: LDA first-order charge density and divergence of the first-order charge current density of Ne induced by a frequency-dependent ($\omega = 0.1\ E_\mathrm{h}/\hbar$) electric field, using different basis sets (from top to bottom: d-aug-cc-pV5Z, d-aug-cc-pV6Z, ET; all uncontracted). Solid (dotted) contour lines are plotted in the range from $+0.01$ to $+0.1$ (-0.01 to -0.1) $e^2/a_\mathrm{o}^2 E_\mathrm{h}$ in intervals of $0.01\ e^2/a_\mathrm{o}^2 E_\mathrm{h}$. The dash-dotted contour line represents $0\ e^2/a_\mathrm{o}^2 E_\mathrm{h}$. The dimensions of the plots are $4 \times 4\ a_\mathrm{o}$.
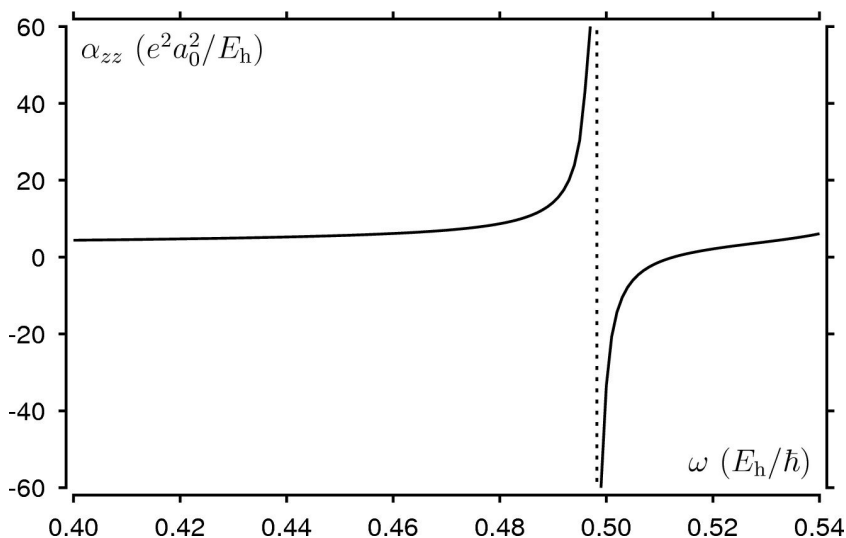
Figure 5.7: Scalar relativistic LDA electric dipole linear polarizability α_{zz} of Ne as a function of frequency using the ET basis set (see p. 103). The dotted line represents the $2p^6 \rightarrow 2p^5 3s^1$ excitation energy (0.498 E_h; 13.56 eV).

Without the introduction of finite lifetimes,[172] the frequency-dependent electric dipole linear polarizability has singularities at frequencies that correspond to excitation energies (Fig. 5.7). We have plotted the first-order charge and probability current density of Ne when approaching and passing beyond the $2p^6 \rightarrow 2p^5 3s^1$ resonance energy (0.498 E_h; 13.56 eV) which is depicted in Fig. 5.7. Spin–orbit coupling has been eliminated to prevent close-lying excitation energies due to small spin–orbit splitting of the p orbitals. The resulting plots for the LDA functional with the so far best-performing ET basis set are depicted in Figs. 5.8 and 5.9 for the frequencies 0.40, 0.47, 0.48, 0.49, 0.50, and 0.51 (all in $E_\mathrm{h}/\hbar$). The first-order charge and probability current density are plotted side by side. With increasing frequency the charge density contour plots "blow up". Correspondingly, the line intensity of the probability current density streamline plots increases. The current density field has sources and drains (fading of the streamline intensity) and these correspond to the induced charge density plots on the left panels of Figs. 5.8 and 5.9 (recall Figs. 5.5 and 5.6). The probability current density streamline plots contain vortices in the core region, as well as in the valence region, which are moving closer together, as the frequency approaches resonance and represent a toroidal vector field around the axis of the perturbing electric dipole. When passing beyond resonance, the switching of phase is nicely observed by the sign change of both first-order charge density and first-order probability current density.
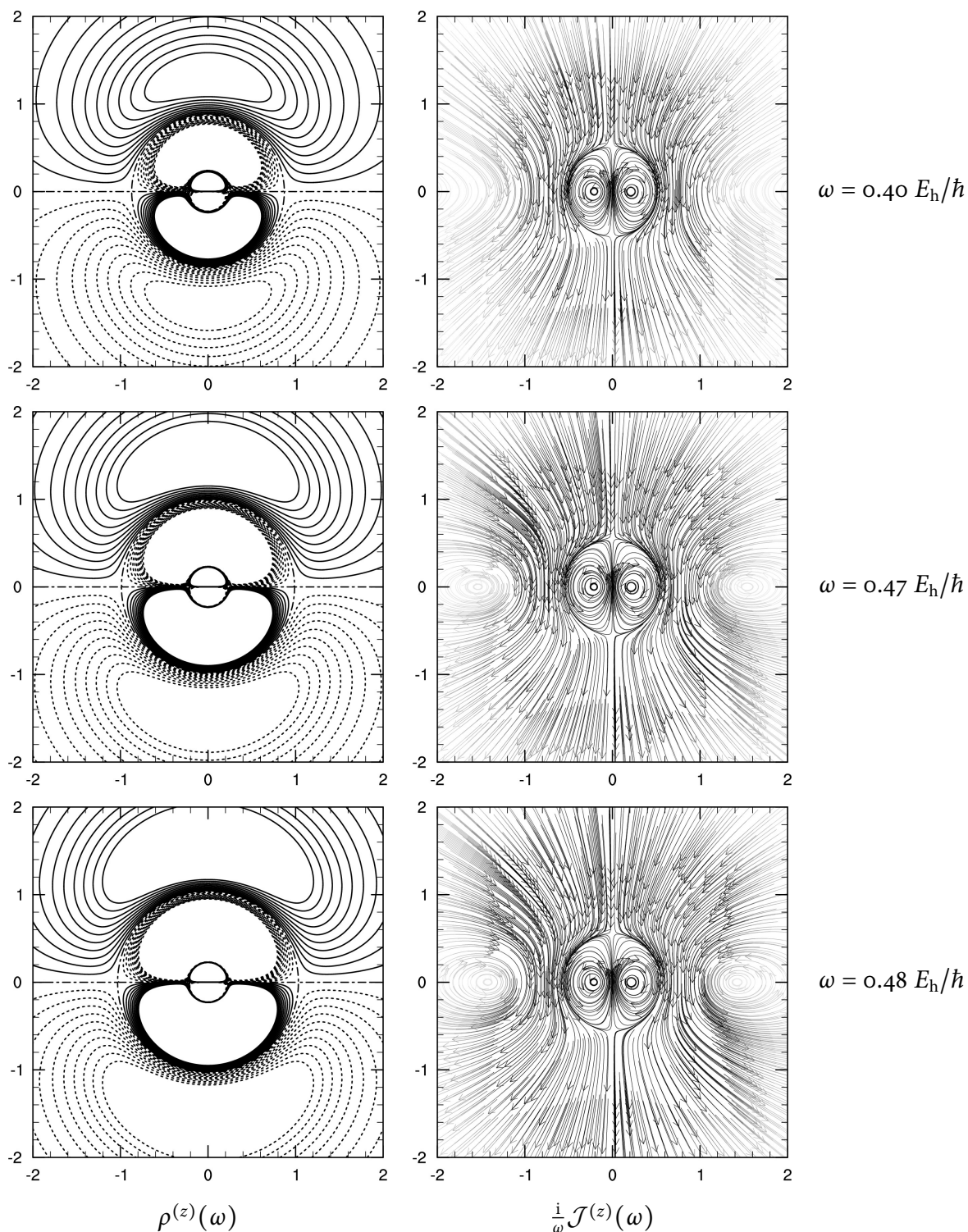
$\rho^{(z)}(\omega)$ 　　　　　 $\frac{\mathrm{i}}{\omega}\mathcal{J}^{(z)}(\omega)$

$\omega = 0.40\ E_\mathrm{h}/\hbar$

$\omega = 0.47\ E_\mathrm{h}/\hbar$

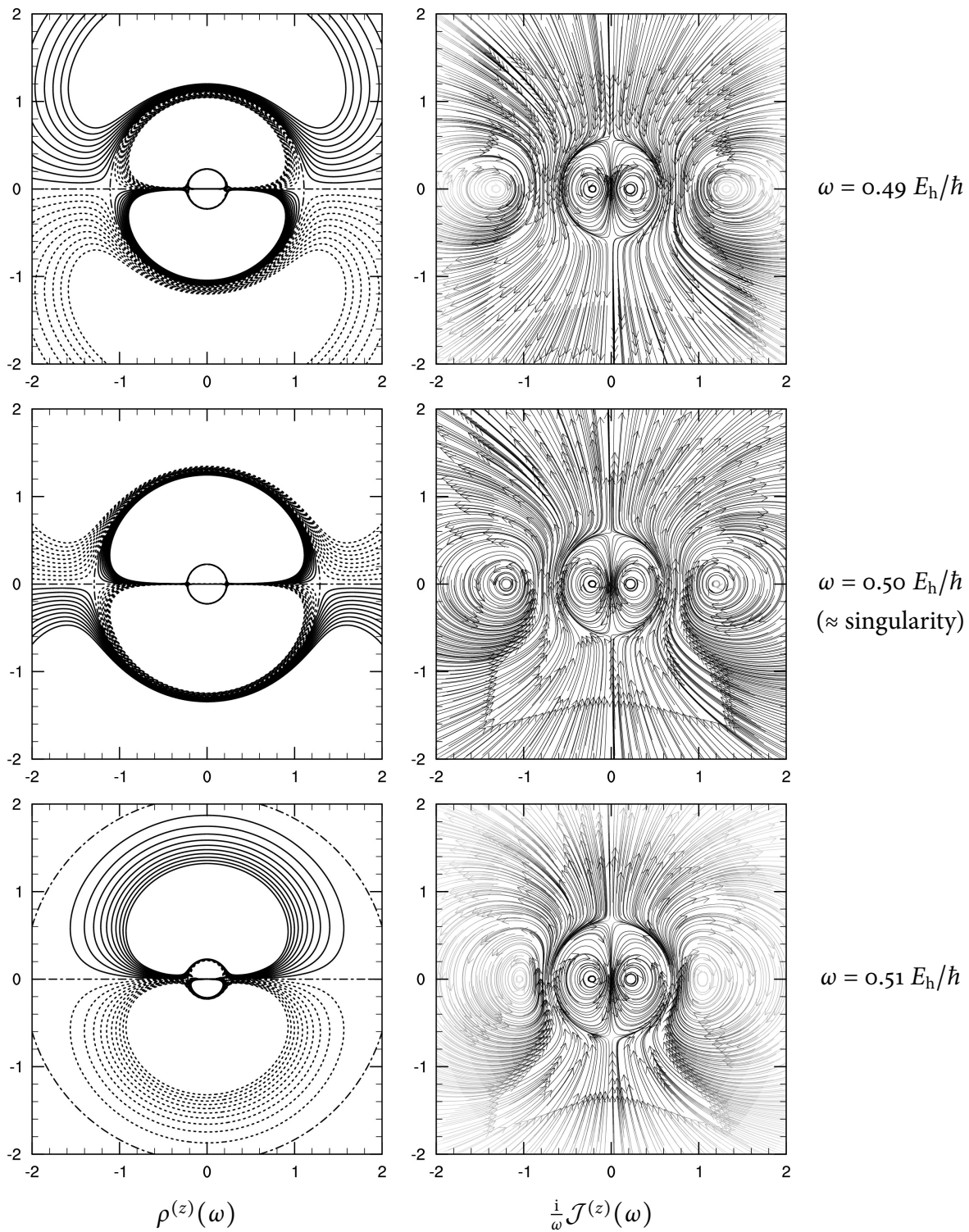$\omega = 0.48\ E_\mathrm{h}/\hbar$

Figure 5.8: Scalar relativistic LDA first-order charge density and first-order probability current density of Ne induced by a frequency-dependent electric field (ω from top to bottom: 0.40, 0.47, and 0.48 $E_\mathrm{h}/\hbar$). Left panels: solid (dotted) contour lines are plotted in the range from +0.01 to +0.1 (−0.01 to −0.1) $e^2/a_\mathrm{o}^2 E_\mathrm{h}$ in intervals of 0.01 $e^2/a_\mathrm{o}^2 E_\mathrm{h}$. The dash-dotted contour line represents 0 $e^2/a_\mathrm{o}^2 E_\mathrm{h}$. Right panels: line intensity is proportional to i$|\mathcal{J}^{(z)}(\omega)|$. The dimensions of the plots are $4 \times 4\ a_\mathrm{o}$.

$$\rho^{(z)}(\omega) \qquad\qquad \frac{\mathrm{i}}{\omega}\mathcal{J}^{(z)}(\omega)$$

Figure 5.9: Scalar relativistic LDA first-order charge density and first-order probability current density of Ne induced by a frequency-dependent electric field (ω from top to bottom: 0.49, 0.50, and 0.51 $E_\mathrm{h}/\hbar$). Left panels: solid (dotted) contour lines are plotted in the range from $+0.01$ to $+0.1$ (-0.01 to -0.1) $e^2/a_\mathrm{o}^2 E_\mathrm{h}$ in intervals of 0.01 $e^2/a_\mathrm{o}^2 E_\mathrm{h}$. The dash-dotted contour line represents 0 $e^2/a_\mathrm{o}^2 E_\mathrm{h}$. Right panels: line intensity is proportional to $\mathrm{i}|\mathcal{J}^{(z)}(\omega)|$. The dimensions of the plots are $4 \times 4\ a_\mathrm{o}$.

5.4   Induced current density in the group 15 heteroaromatic compounds

The concept of aromaticity keeps fascinating chemists ever since the first isolation and characterization of benzene by Michael Faraday in 1825.[173] To a certain degree it remains to be an elusive concept and Frenking calls it aptly "a typical example for a unicorn of the chemical bonding models, because everybody seems to know what it means although it is not an observable quantity".[174,175] Many criteria have been introduced in the past. Some became obsolete or not general enough. Table 2 of Ref. 176 lists 61 important aromaticity criteria and key developments 1825–2005. They can be grouped into four classes: structural, energetic, reactivity, and magnetic criteria. Being devoted to review the extensively used nucleus-independent chemical shift (NICS) aromaticity criterion Ref. 176 gives also a beautiful overview over the history of aromaticity and is certainly an ideal entry point into the subject with a rich bibliography.

The last entry in Table 2 of Ref. 176 is the criterion of integrated magnetically induced currents as aromaticity index, introduced by Jusélius, Sundholm, and Gauss.[5] The aromatic ring current theory has already been established in 1936 by Pauling and others (see review[177]). *Ab initio* current density plots have been pioneered by Lazzeretti and Zanasi[178,179] and widely applied by several groups to closed-shell systems (see reviews[180,181]) and recently also to open-shell molecules.[182,183] To the best of our knowledge, no 4-component relativistic *ab initio* current density plots have appeared so far. Inspired by the quantitative and general approach of Jusélius, Sundholm, and Gauss[5] in the NR framework, we wish here to fill this gap and to apply our 4-component relativistic implementation for the study of the induced current density in the group 15 heteroaromatic compounds C_5H_5E ($E = N$, P, As, Sb, Bi). This series of heteroaromatic compounds has been recently studied by Fernández and Frenking[174] by means of energy decomposition analysis. In an elegant approach, based on an energy decomposition analysis,[184–188] the authors have estimated the aromatic stabilization energy (ASE) and found a larger π stabilization in pyridine (45.7 kcal mol^{-1}) than in benzene (42.5 kcal mol^{-1}). Other heterobenzenes were found less stabilized (ASE descending to 29.4 kcal mol^{-1} in C_5H_5Bi), but still rather large. In another study, on the basis of hydrogenation energies, NICS values, and lack of bond alternation, Shobe[189] concluded that the entire series appears to be aromatic and to a roughly equal degree. A study of Salcedo[190] based on NICS values and homodesmic reaction energies, concludes with C_5H_5P being the most aromatic member of the series, again with roughly equal NICS values.

Computational details

The C_5H_5E (E = N, P, As, Sb, Bi) and C_6H_6 structures have been optimized using the GAUS-SIAN[191] program package. We have employed the B3LYP functional[83,84,134] and the basis sets aug-cc-pVTZ for H,[151] C,[151] N,[151] P,[192] and As,[193] and the basis sets aug-cc-pVTZ-PP[194] with effective core potentials[195] for Sb and Bi.

The induced current densities have been obtained and plotted using a development version of the DIRAC[16] program package. The calculations have been carried out at the HF level of theory and also using the density functionals B3LYP[83,84] and PBE.[146] We have used the 4-component Dirac-Coulomb (DC) and the 4-component nonrelativistic Lévy-Leblond[65] Hamiltonians. The same basis sets have been used for H, C, N, and P, however in uncontracted form. For As, Sb, and Bi, uncontracted all-electron TZ basis sets of Dyall[196] have been used, including the core and valence correlating and diffuse exponents. The small component basis set for the calculations based on the DC Hamiltonian has been generated using restricted kinetic balance. The calculations proceed in two steps. First we obtain the linear response of the HF or KS determinant to the perturbing magnetic dipole operator. In a second calculation we use the response vector to construct the first-order density matrix and to obtain the first-order induced current density following the procedure outlined in Section 5.1, p. 90. The response calculations employ a common gauge origin, placed at the center of mass with the perturbing magnetic dipole operator oriented perpendicular to the molecular plane. The integration of the induced current density has been carried out using the two-dimensional Gaussian or Lobatto quadrature detailed in Ref. 5. The integration plane has been chosen perpendicular to the molecular plane, extending from the ring center 10 a_0 above, below and outward, perpendicular to the C_2 symmetry axis (dashed lines in Figs. 5.10 to 5.13). The ring center has been defined as $\mathbf{R}_{center} = (\mathbf{R}_E + \mathbf{R}_C)/2$ where $\mathbf{R}_E$ and $\mathbf{R}_C$ are the position vectors of E and its opposing C atom, respectively. The integration grid density has been increased and monitored until reaching convergence in the significant digits reported later in the discussion.

Discussion

We will proceed in two steps: we will start with a qualitative discussion of the induced probability current density plots and later turn to a quantitative analysis of the integrated ring current susceptibilities.

First, consider the induced 4-component relativistic HF probability current streamline plots for C_5H_5N in Fig. 5.10. The induced "paramagnetic" and "diamagnetic" probability current densities are plotted separately—both are obtained in the molecular plane. The line intensity is chosen proportional to the norm of the probability current density vector, and the magnetic

field vector points towards the reader. The paratropic response (top panel) and the diatropic response (bottom panel) are nicely seen. The streamlines of the induced "diamagnetic" probability current are concentric around the gauge origin whereas the induced "paramagnetic" probability current streamlines follow hexagonal patterns—one inside the carbon ring and one outside the carbon ring shifted by 60 degrees. The corresponding benzene streamline plots are very similar (not given here). When summing up the "paramagnetic" and "diamagnetic" parts to the total probability current densities, we arrive at Fig. 5.11 (top panel). Situated still in the molecular plane, a diatropic probability current outside the carbon ring and the opposite paratropic probability current inside the carbon ring are nicely seen. Between atoms one can observe diatropic vortices. We can also "visually" integrate the induced ring current from the ring center outward, following the dashed line in Fig. 5.11 and verify—as expected—that the diatropic and paratropic contributions nearly cancel. This is different above and below the molecular plane (Fig. 5.11; bottom panel), where the diatropic ring current of the π-system dominates the streamline plot. This characteristic aromatic diatropic response is present also when examining the heavier homologues C_5H_5P to C_5H_5Bi (Figs. 5.12 and 5.13). Starting with C_5H_5As, the diamagnetic atomic contributions of the heteroatoms are increasingly visible in the streamline plots. Also the pattern of the vortex domains inside the carbon ring changes for the heavier homologues. The induced DFT probability current streamline plots and also the NR probability currents are qualitatively quite similar and therefore not given here.

For a more quantitative analysis we now turn to the discussion of the integrated induced ring current susceptibilities listed in Tab. 5.2. With the exception of the B3LYP induced ring current susceptibilities of C_5H_5Sb and C_5H_5Bi at the 4-component relativistic level, we obtain a consistent picture. The largest induced ring current susceptibilities are obtained for the prototypical aromatic molecule C_6H_6. Slightly smaller are the numbers for C_5H_5N which then slowly decrease to C_5H_5Sb, but keep the order of magnitude. The values for C_5H_5Bi are slightly above the C_5H_5Sb induced ring current susceptibilities. The only exception is the DC HF value. Although the B3LYP numbers are significantly larger than HF and PBE, the qualitative trend for the homologue series is quite comparable, again except the DC B3LYP numbers which drop abruptly between C_5H_5As and C_5H_5Sb. Disregarding these two values for the moment, the differences between the 4-component relativistic and the NR treatment are quite small. When comparing the DC and NR values in Tab. 5.2, the relativistic effect seems minimized for C_5H_5As. In order to elucidate this effect we have examined the "paramagnetic" and "diamagnetic" contributions separately (Tab. 5.2).* The differences between DC and NR values for C_6H_6, C_5H_5N, and C_5H_5P are exclusively between the "diamagnetic" DC and NR contributions and can be interpreted as a

---

* Note that the "paramagnetic" and "diamagnetic" contributions should not be compared between different compounds since the gauge origin is placed at the center of mass which is then different.
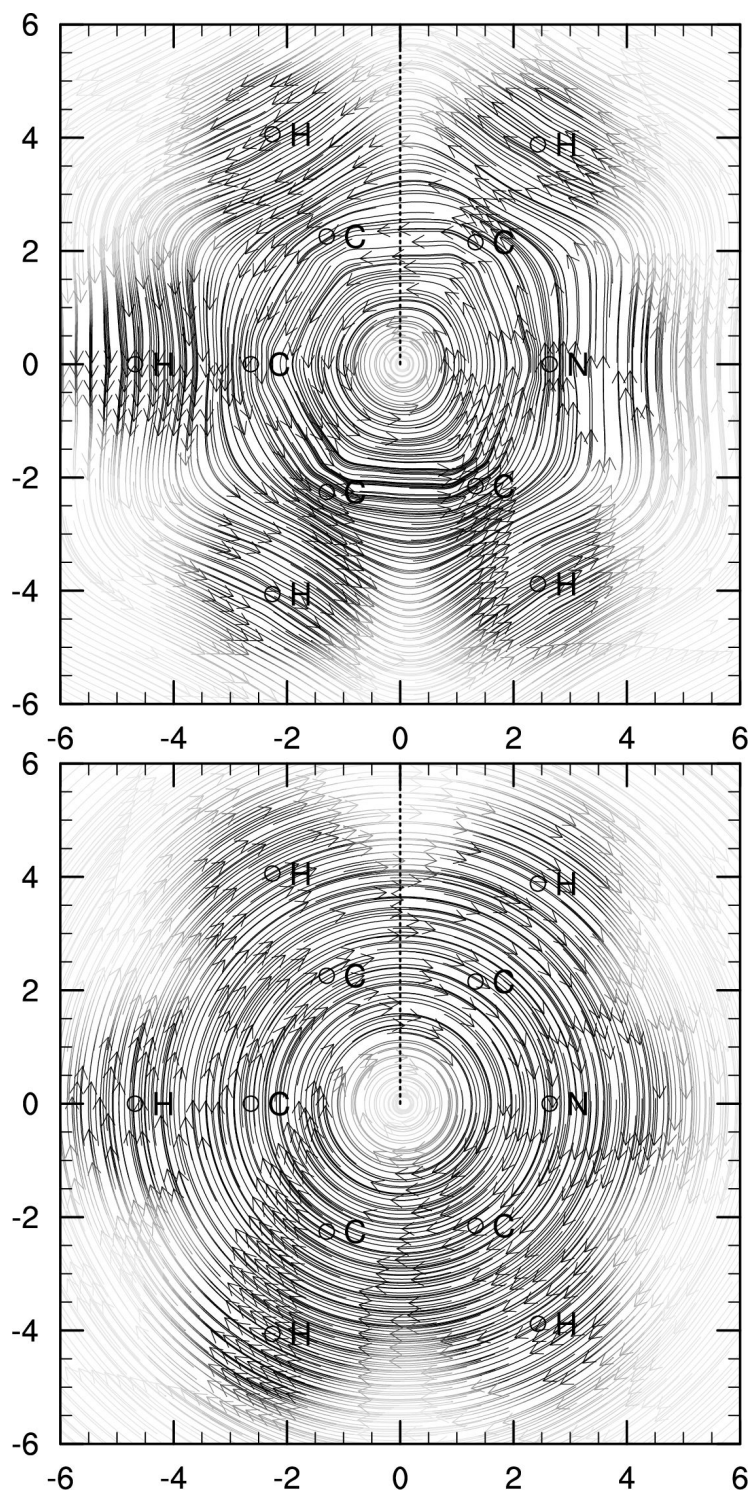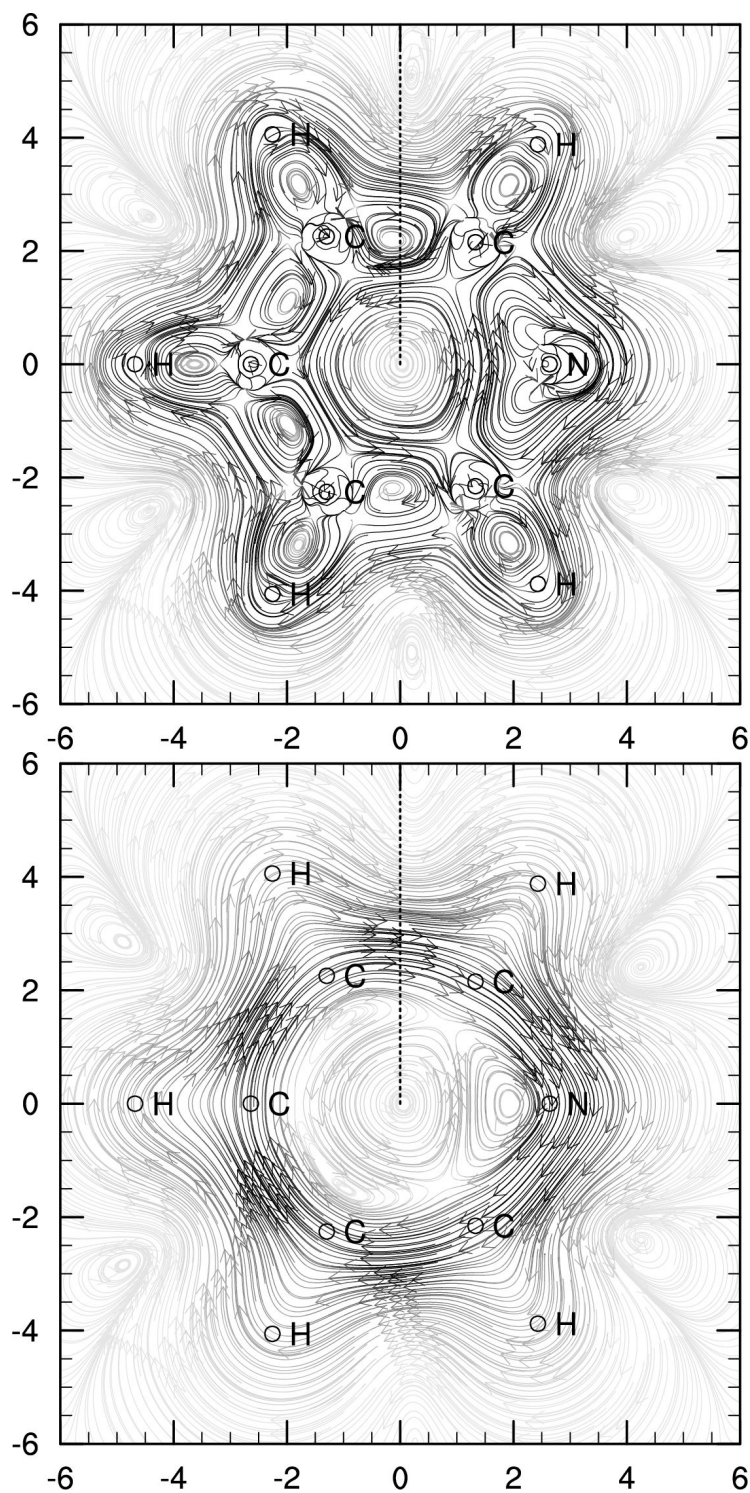
Figure 5.10: Induced HF "paramagnetic" (top panel) and "diamagnetic" (bottom panel) probability current density $\mathcal{J}$ in C_5H_5N, plotted in the molecular plane (dimensions: $12 \times 12\ a_0$). The magnetic field vector points towards the reader. Line intensity is proportional to the norm of $\mathcal{J}$. Small circles represent the atomic centers. Dashed line represents the intersection with the integration plane.
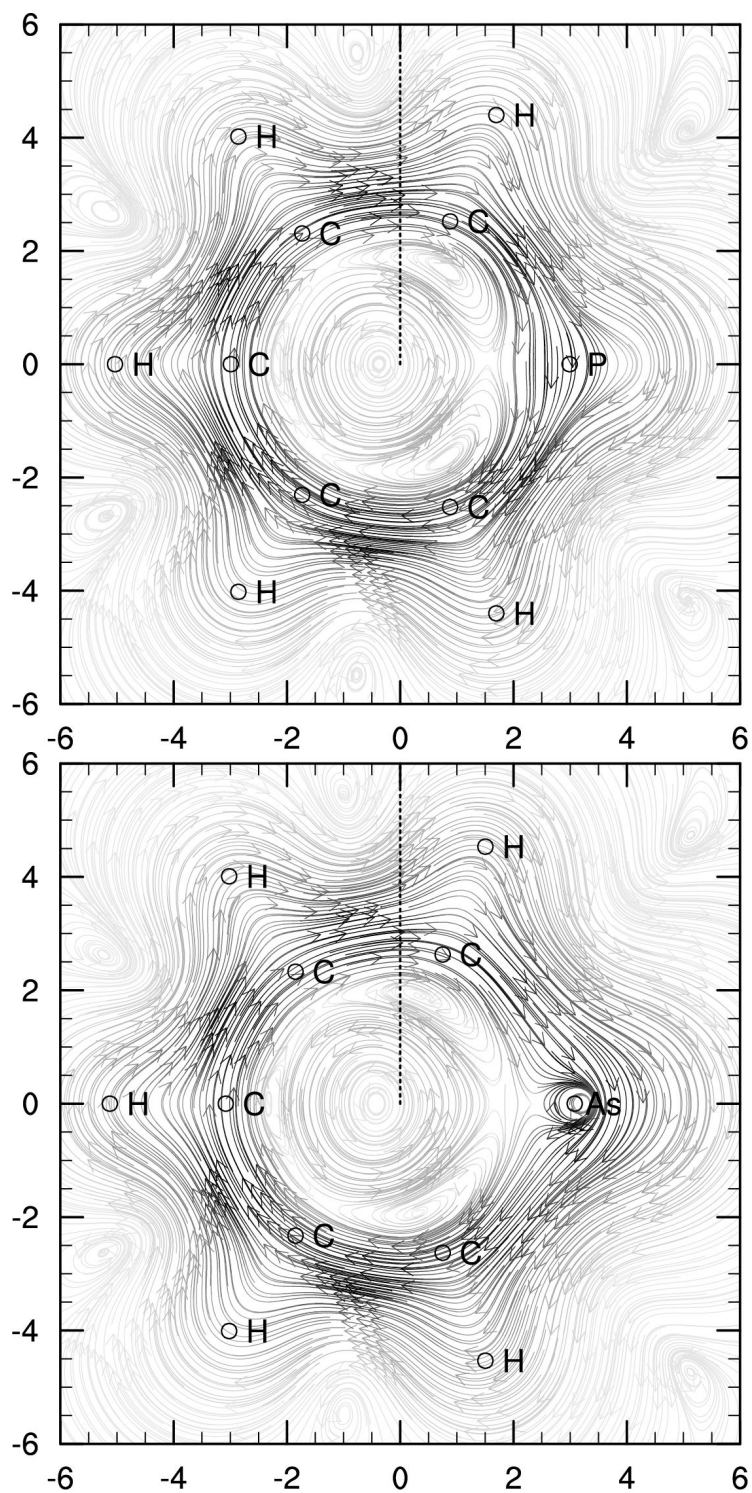
Figure 5.11: Induced HF total probability current density $\mathcal{J}$ in C_5H_5N, plotted in the molecular plane (top panel) and $1\ a_0$ above (or below) the molecular plane (bottom panel; dimensions: 12×12 a_0). The magnetic field vector points towards the reader. Line intensity is proportional to the norm of $\mathcal{J}$. Small circles represent the atomic centers. Dashed line represents the intersection with the integration plane.

Figure 5.12: Induced HF total probability current density $\mathcal{J}$ in C_5H_5P (top panel) and C_5H_5As (bottom panel), plotted 1 a_0 above (or below) the molecular plane (dimensions: 12 × 12 a_0). The magnetic field vector points towards the reader. Line intensity is proportional to the norm of $\mathcal{J}$. Small circles represent the atomic centers. Dashed line represents the intersection with the integration plane.

Figure 5.13: Induced HF total probability current density $\mathcal{J}$ in C_5H_5Sb (top panel) and C_5H_5Bi (bottom panel), plotted 1 a_0 above (or below) the molecular plane (dimensions: 12×12 a_0). The magnetic field vector points towards the reader. Line intensity is proportional to the norm of $\mathcal{J}$. Small circles represent the atomic centers. Dashed line represents the intersection with the integration plane.
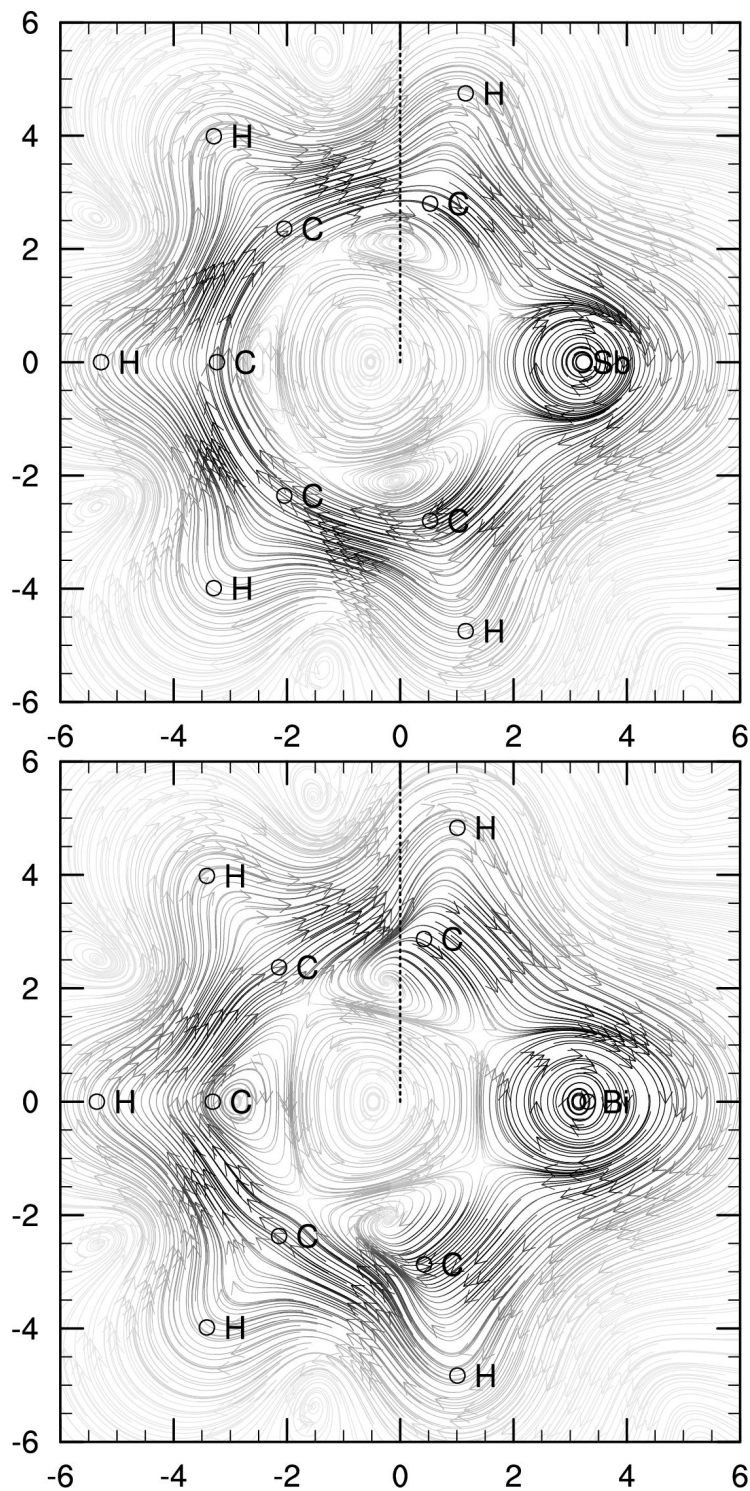
defect of the basis sets for C, N, and P. These basis sets seem not to provide sufficient magnetic balance for the resolution of identity which appears in the Sternheim approximation.[24,103,197] This seems not to be a problem for the heavier homologues, and for C_5H_5Sb and C_5H_5Bi the rather small differences between DC and NR values are dominated by the "paramagnetic" contributions. The quite substantial differences when using the B3LYP functional are surprising. We can exclude doubts about a different (wrong) reference state. It can also be stated that the differences are not possible artifacts of the numerical integration procedure as this abrupt trend is also obtained in the calculated component χ_{zz} of the magnetizability tensor (results not given here).* However, for the HF and B3LYP response calculations on C_5H_5Sb and C_5H_5Bi we have detected a possible instability in the solution of the reduced response equations which can signal a triplet instability of the reduced electronic Hessian. This interpretation is also consistent with the fact that B3LYP contains a fraction of orbital exchange in contrast to the nonhybrid PBE functional where such an instability is not signaled. The calculated HF and B3LYP induced ring current susceptibilities of C_5H_5Sb and C_5H_5Bi clearly call for a closer analysis and must be considered with reservation at this stage.

---

* The magnetic field vector is oriented along the z-coordinate. The component χ_{zz} of the magnetizability tensor is obtained "for free" by contracting the response vector with the appropriate property gradient.

Table 5.2: Induced ring current susceptibility (in nA/T) in benzene and the group 15 heteroaromatic compounds C_5H_5E (E = N, P, As, Sb, Bi; DC: Dirac-Coulomb Hamiltonian; NR: nonrelativistic).

method	Hamiltonian		C_6H_6	C_5H_5N	C_5H_5P	C_5H_5As	C_5H_5Sb	C_5H_5Bi
HF	DC	total	13.35	12.69	12.25	11.66	10.48	10.41
		para	−33.20	−32.33	−43.44	−50.10	−66.19	−78.95
		dia	46.55	45.02	55.69	61.76	76.67	89.36
	NR	total	13.82	13.14	12.40	11.70	10.59	11.17
		para	−33.20	−32.33	−43.44	−50.07	−66.16	−78.49
		dia	47.03	45.48	55.84	61.78	76.75	89.66
	DC – NR	total	−0.47	−0.45	−0.15	−0.04	−0.11	−0.75
		para	0.01	0.01	−0.00	−0.02	−0.02	−0.46
		dia	−0.48	−0.45	−0.15	−0.02	−0.08	−0.29
B3LYP	DC	total	17.05	16.45	16.36	16.08	9.13	9.40
		para	−28.26	−27.38	−38.63	−45.40	−68.13	−81.12
		dia	45.31	43.83	55.00	61.48	77.26	90.52
	NR	total	17.55	16.92	16.49	16.06	15.92	17.31
		para	−28.27	−27.39	−38.63	−45.38	−61.36	−73.35
		dia	45.82	44.31	55.12	61.44	77.27	90.66
	DC – NR	total	−0.50	−0.47	−0.13	0.01	−6.79	−7.91
		para	0.01	0.01	−0.00	−0.02	−6.78	−7.77
		dia	−0.51	−0.48	−0.13	0.03	−0.01	−0.14
PBE	DC	total	12.12	11.58	10.78	10.06	8.86	9.09
		para	−33.13	−32.19	−44.22	−51.48	−68.55	−81.64
		dia	45.25	43.78	55.00	61.54	77.41	90.73
	NR	total	12.62	12.05	10.91	10.06	8.92	9.62
		para	−33.14	−32.20	−44.22	−51.44	−68.48	−81.21
		dia	45.75	44.25	55.12	61.50	77.41	90.83
	DC – NR	total	−0.50	−0.47	−0.13	0.00	−0.07	−0.53
		para	0.01	0.01	−0.00	−0.03	−0.07	−0.43
		dia	−0.51	−0.48	−0.12	0.04	0.00	−0.10

5.5 Nuclear spin–spin coupling density in CO

To illustrate the real-space approach to the nuclear spin–spin coupling using our new implementation, we have chosen CO as a test example since it is a small molecule for which the Fermi-contact (FC) contribution is not dominating and is on the order of the paramagnetic spin–orbit (PSO) and the spin-dipole (SD) interactions.[198,199]

First, we wish to validate the calculated reduced isotropic indirect nuclear spin–spin coupling constant (NSSCC) of CO, obtained within the spin-polarized KS approach using the BLYP[134,135,140] functional, before turning to a discussion of the nuclear spin–spin coupling density itself. The reduced isotropic indirect NSSCC between the nuclear spins of C and O, corresponds to the static linear response function

$$K(\mathrm{C},\mathrm{O}) = \frac{1}{3}\sum_i \langle\langle \hat{A}_i^{\mathrm{C}}; \hat{A}_i^{\mathrm{O}}\rangle\rangle_0 \tag{5.42}$$

where the sum over i runs over the three principal axes, with $\hat{A}^K$ being the nuclear magnetic dipole operator for nucleus K defined in Eq. 5.19. For implementation details of 4-component relativistic calculations of isotropic indirect NSSCC the reader is referred to Ref. 200. The 4-component relativistic implementation of KS linear response is documented in Ref. 113. In contrast to Ref. 113, spin density contribution (Section 3, p. 61) is now included in the construction of the sigma vector (Section 2.5, p. 58).

In order to compare the 4-component results with NR results reported by other groups,[198,199] it is possible to eliminate either all relativistic effects,[65] or exclusively the spin–orbit interaction[24,60] within the 4-component framework (see also Section 1.4, p. 35). The calculated $K(\mathrm{C},\mathrm{O})$ are summarized in Tab. 5.3 and compared to results reported by Sychrovský *et al.*,[198] employing the same basis set H-III of Huzinaga[201] modified by Kutzelnigg *et al.*,[202] and the same C–O distance of 2.1316 a_0. While in the NR framework $K(\mathrm{C},\mathrm{O})$ is obtained as a sum of four contributions, which correspond to the first-order perturbation operators PSO, FC, SD, and the second-order diamagnetic spin–orbit (DSO) operator, this separation is absent in relativistic theory—for the description of NSSCC there is only one perturbation operator (Eq. 5.19; see also Ref. 66 for a comparison of relativistic and NR one-electron perturbation operators). The isolation of the "paramagnetic" and "diamagnetic" contributions is on the other hand possible in relativistic theory[103,104] (see Section 5.1, p. 90). Removing subsequently spin–orbit coupling and scalar relativity and reintroducing the basis set contraction scheme brings our values reasonably close to the results of Sychrovský *et al.*,[198] −55.13 vs. −55.17 SI units (Tab. 5.3). Note that the NR diamagnetic contribution to the NSSCC (DSO term) is obtained as an expectation value. The effects due to scalar relativity and spin–orbit coupling are small, as expected for this test case (compare values for the uncontracted basis set).

Table 5.3: Reduced nuclear spin–spin coupling constants of CO, calculated with BLYP and the H-III basis set (in SI units: 10^{19} m^{-2} kg s^{-2} A^{-2}; NR: nonrelativistic Lévy-Leblond Hamiltonian; SR: scalar relativistic; DC: Dirac-Coulomb Hamiltonian).

	basis set contracted	spin-dependent contributions deleted	total	para	PSO	FC	SD	FC+SD	dia
Sychrovský et al. [a]	yes	no	−55.17	−54.95	−35.51	−33.41	13.97	−19.44	−0.22
NR	yes	no	−55.13	−54.90					−0.23
NR	no	no	−53.73	−53.51					−0.23
SR	no	no	−54.90	−54.66					−0.24
DC	no	no	−55.02	−54.78					−0.24
NR	yes	yes	−35.70	−35.47				−19.43	−0.23
NR	no	yes	−35.58	−35.36				−18.15	−0.23
SR	no	yes	−35.79	−35.48				−19.18	−0.30

[a] Ref. 198.

Saue has demonstrated[24] how spin-dependence can be selectively removed and thereby the PSO term recovered. Indeed, this separation applied on the paramagnetic contribution (lower part of Tab. 5.3) yields −35.47 SI units compared to the reference PSO value of −35.51 SI units. The remaining part is the sum FC+SD with −19.43 SI units (the reference value is −19.44 SI units).

Having validated our results, we are now ready to visualize the three contributions: PSO, FC+SD, and DSO. For this we solve six linear response equations (Eq. 2.39) which correspond to three principal components of both perturbations $\hat{A}^{\mathrm{C}}$ and $\hat{A}^{\mathrm{O}}$, and obtain six response vectors: $\mathbf{N}_i^{(\mathrm{C})}$ and $\mathbf{N}_i^{(\mathrm{O})}$ (Einstein summation over i). From these response vectors corresponding first-order density matrices (Eq. 5.6) are constructed, from which the induced charge current densities are calculated as described in Note B, p. 185. Having obtained the induced charge current densities, $K(\mathrm{C}, \mathrm{O})$ may be calculated by

$$K(\mathrm{C}, \mathrm{O}) = \int \mathrm{d}\mathbf{r}\, \frac{-1}{3c^2 r_{\mathrm{C}}^3} \sum_i (\mathbf{r}_{\mathrm{C}} \times \mathbf{j}^{(\mathrm{O}_i)})_i \tag{5.43}$$

$$= \int \mathrm{d}\mathbf{r}\, k_{\mathrm{CO}}(\mathbf{r})$$

and consequently,

$$K(\mathrm{O}, \mathrm{C}) = \int \mathrm{d}\mathbf{r}\, k_{\mathrm{OC}}(\mathbf{r}) \tag{5.44}$$

by interchanging the perturbing with the responding nucleus. Eqs. 5.43 and 5.44 define the reduced isotropic indirect NSSCC densities $k_{\mathrm{CO}}(\mathbf{r})$ and $k_{\mathrm{OC}}(\mathbf{r})$ which are the target quantities

here. The paramagnetic and diamagnetic contributions to $k(\mathbf{r})$ can be obtained by considering only the pp or pn parts of the response vectors, respectively (Section 5.1, p. 90). In addition, the corresponding PSO and FC+SD contributions can be recovered by selectively removing spin-dependence[24] as done in Tab. 5.3. We check all plotted densities $k(\mathbf{r})$ by comparing the numerically integrated values with the numbers listed in Tab. 5.3.

Contour plots representing cuts through the densities $k_{\mathrm{CO}}(\mathbf{r})$ and $k_{\mathrm{OC}}(\mathbf{r})$ are depicted in Fig. 5.14. These densities possess cylindrical symmetry around the C–O bond axis. Compare the top and bottom panels in Fig. 5.14 and observe that the density distributions depend on the choice of the perturbing and responding nuclear spins. Independent of this choice are the integrated values which correspond to numbers listed in the last line of Tab. 5.3. The DSO contributions $k_{\mathrm{CO}}^{\mathrm{DSO}}(\mathbf{r})$ and $k_{\mathrm{OC}}^{\mathrm{DSO}}(\mathbf{r})$ are very similar (right panels in Fig. 5.14). Indeed, in the NR limit these contributions are obtained as expectation values and are therefore independent of this choice. The $k_{AB}^{\mathrm{DSO}}(\mathbf{r}) = 0$ isosurfaces are almost spherical (remember cylindrical symmetry). It is a nice exercise to show that in the NR limit the isosurfaces are perfect spheres with the diameter r_{AB}, with a negative (positive) $k_{AB}^{\mathrm{DSO}}(\mathbf{r})$ inside (outside) this spherical isosurface. The sign of $k_{AB}^{\mathrm{DSO}}(\mathbf{r})$—obtained as an expectation value—is determined by the scalar product $\mathbf{r}_{iA}\cdot\mathbf{r}_{iB}$. All points $\mathbf{r}_i$ for which $\mathbf{r}_{iA}\cdot\mathbf{r}_{iB} = 0$, form a sphere centered at $(\mathbf{r}_A + \mathbf{r}_B)/2$ with the diameter r_{AB}. This is Thales' theorem (already pointed out in Ref. 198, see also Refs. 203, 204, and 205). The $k_{AB}^{\mathrm{DSO}}(\mathbf{r})$ plots in Fig. 5.14 are not obtained as an expectation value and the deformation of the otherwise spherical isosurfaces is a basis set effect. The DSO term scans the charge anisotropy around each of the coupling nuclei[167] and although sizable $k^{\mathrm{DSO}}(\mathbf{r})$ values are reached along the C–O bond axis, the integral is two orders of magnitude smaller than the integral over $k^{\mathrm{PSO}}(\mathbf{r})$ or $k^{\mathrm{FC+SD}}(\mathbf{r})$. A large DSO contribution may be anticipated for instance in certain transition metal atoms featuring stronger charge anisotropy, as pointed out by Cremer and Gräfenstein.[167] Passing on to the middle panels in Fig. 5.14, $k^{\mathrm{FC+SD}}(\mathbf{r})$ contour plots nicely show the structure of the dipole field with its shell structure, generated by the perturbing nuclear moment and the double-cone structure at the responding nucleus which monitors the SD spin polarization with a quadrupolar potential (see Ref. 167 for a nice discussion of these features along with a separate visualization of the FC coupling density and for explicit NR expressions). The remaining densities $k^{\mathrm{PSO}}(\mathbf{r})$ are depicted in the left panels in Fig. 5.14. They are complementary to $k^{\mathrm{FC+SD}}(\mathbf{r})$ in the sense that they probe the induced orbital current in contrast to the FC and SD mechanisms mediated by the spin-dependent part of the induced paramagnetic current. The densities $k^{\mathrm{PSO}}(\mathbf{r})$ provide also complementary information to $k^{\mathrm{DSO}}(\mathbf{r})$ as they probe not only the density anisotropy but also the orbital structure close to the coupling nuclei.[167] The integral is with –35.48 SI units slightly larger than the FC contribution with –33.41 SI units.
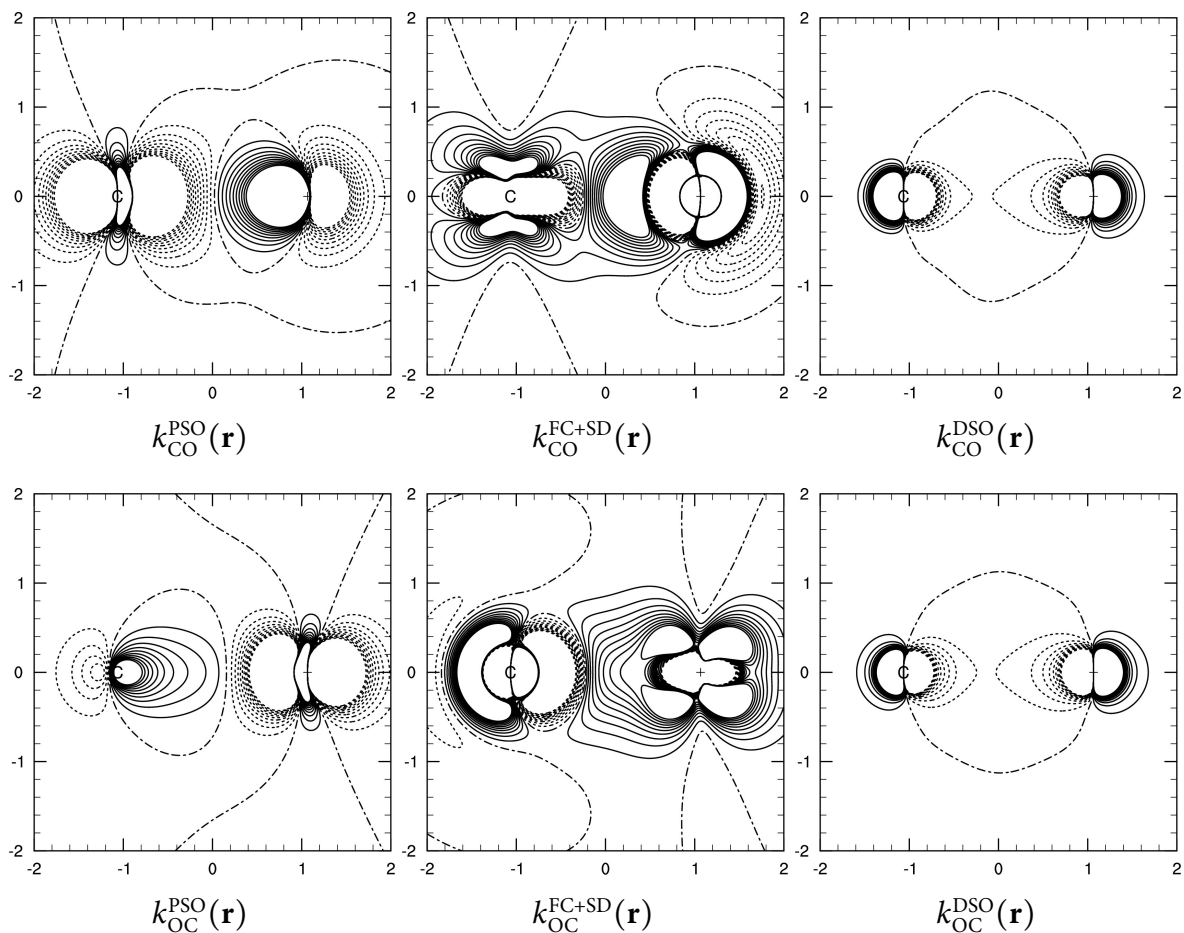
Figure 5.14: BLYP reduced isotropic indirect NSSCC densities $k_{CO}(\mathbf{r})$ (top panels; O is the perturbing nucleus) and $k_{OC}(\mathbf{r})$ (bottom panels; C is the perturbing nucleus) in CO. The position of the C nucleus is marked with "C", the position of the O nucleus is marked with a cross. Solid (dotted) contour lines are plotted in the range from +1 to +10 (−1 to −10) SI units: 10^{19} m^{-2} kg s^{-2} A^{-2}, in intervals of 1 SI unit. The dash-dotted contour line represents $k(\mathbf{r}) = 0$. The dimensions of the plots are 4×4 a_0.

Orbital contributions to $k(\mathbf{r})$ could be easily plotted separately by allowing only specific elements of the auxiliary matrix W in Eq. 5.7 to be nonzero. This is not shown in this example which has been chosen for testing purposes and as an illustration rather than to discuss the NSSCC in CO.

To sum up this short illustration, it is pertinent to underline that this real-space approach to NSSCC is not new and has been developed by other groups[158–167] under different names, with different notations and possibilities, all of them in the NR framework. The aim was to show, that it is possible to recover partly the corresponding NR densities. The advantage of the here presented approach is the possibility to address nuclear spin–spin coupling in heavy-element systems on a sound theoretical basis. One interesting application might be to visualize and study the important spin–orbit coupling effect present in the NSSCC of the TlX (X = F, Cl, Br, I) series, as observed by Autschbach and Ziegler.[206] Another interesting molecule might be PbO, the heavy homologue of CO.

5.6 Parity-violating energy shift and the γ^5 density

For an understanding of chemistry, fundamental forces other than the electromagnetic force (namely the gravitational, strong, and weak force) can usually be safely neglected. It is nevertheless very tempting, albeit extremely challenging, to try to observe the influence of the weak interaction on molecular systems directly, as this would enable low energy tests of the weak interaction.[207] This extremely weak and short-ranged interaction is of particular interest since it shows preference for particle helicity, for instance involving almost exclusively left-handed electrons.[208] As nicely shown by Wu *et al.* in the β-decay of cobalt radionuclides[209] the weak interaction breaks parity symmetry as first proposed by Lee and Yang.[210] The consequence of this parity symmetry breakdown, commonly called parity-violation (PV), makes the two "enantiomers" of a chiral molecule strictly speaking diastereomers, thus causing an energy difference between them.

The main obstacle for the observation of PV effects is its tininess. For instance, in the case of aminoacids, the theoretical PV energy difference (PVED) between the two enantiomers is on the order of 10^{-16} kJ $\cdot$ mol^{-1},[211,212] which, combined with its significant variation as a function of molecular structure, precludes any direct link between PV and biohomochirality unless a convincing amplification mechanism can be found.[213–215] The measure of such minute values furthermore calls for very accurate experiments which have to be dedicated to its observation. Only a few scientific teams in the world have performed experiments aiming at detecting PV effects in molecular systems, but with no clear-cut success so far.[216–219]

A promising new experimental setup has been proposed by Chardonnet and co-workers.[220–222] It aims at detecting PV vibrational transition frequency differences by molecular beam spectroscopy using a two-photon Ramsey-fringes experiment. A sensitivity of 0.01 Hz is expected, but the choice of the candidate molecule and the preparation of its enantiomers are crucial for a successful experiment. The ideal candidate chiral molecule for the experiment should: (i) be available in large enantiomer excess or, ideally, in enantiopure form; (ii) show a large PV frequency difference of an intense fundamental transition within the CO_2 laser operating range (850–1120 cm^{-1}); (iii) not be too bulky since the sensitivity of the experiment will be largely determined by the partition function of the molecules in a supersonic beam where the internal degrees of freedom are frozen down to about 1 K; (iv) avoid nuclei with quadrupolar moments; and (v) preferably sublimate without decomposition for injection into the Fabry-Perot cavity of the experiment, although laser ablation techniques may also be envisaged.

Prior to 2002 small organic chiral molecules such as aminoacids, chiral conformations of hydroperoxides,[223,224] or heterohalogenomethanes,[221,225–227] were extensively studied. Among

the latter, bromochlorofluoromethane (CHFClBr) has drawn particular attention due to its structural simplicity.[228] However, such a chiral molecule, although a good model, shows too low calculated PV effects[227, 229–231] (a few mHz) to be clearly observed considering today's best experimental resolution of around 1 Hz.[232] Recently, chiral halogenated adamantanes and cubanes have been synthesized, but they were found to show very low PV effects.[233] Since 2002, chiral metal transition complexes bearing heavy atoms have attracted particular interest. Considering that the PVED scales approximately as Z^5 (where Z is the atomic number),[234–237] theoretical studies clearly favor chiral compounds with a heavy atom at or near the stereochemical center for large PV effects. Indeed, chiral gold, mercury, iridium, osmium and rhenium complexes were calculated to be favorable candidates for PV observation by Schwerdtfeger and coworkers,[238–240] as well as bismuth compounds by Lazzeretti and coworkers.[241]

The aim of this section is actually to go back in time and to present already known numbers for an already disqualified candidate molecule CHFClBr, albeit from a new point of view. The molecule under study has been disqualified from being a realistic candidate molecule due to PV effects for the C–F stretching mode only in the mHz range. The here presented PV effects for the C–F stretching mode of CHFClBr within the 4-component HF theory have been published by other authors[225, 227] and this discussion will closely follow their choices of approximations. However, in contrast to previous studies the individual steps of such a calculation will be discussed using the γ^5 density

$$\gamma^5(\mathbf{r}) = \langle 0|\gamma^5(\mathbf{r})|0\rangle \tag{5.45}$$

The hope of this discussion is that the $\gamma^5(\mathbf{r})$ density may give a different and possibly helpful view on the property under study by connecting the PV energy difference to the spatial structure of the $\gamma^5(\mathbf{r})$ density and its variation upon geometry distortion.

Starting from the weak neutral-current interaction Hamiltonian between electrons and nuclei (see Note A, p. 179) in the limit of zero momentum transfer and neglecting nuclear spin-dependent terms, the PV electronic energy shift P (= half of the energy difference between two enantiomers) is given at the 4-component relativistic HF/KS level by the expectation value expression

$$P = \frac{G_F}{2\sqrt{2}} \sum_K Q_w^K \sum_i \langle \psi_i | \gamma^5 \rho_K(\mathbf{r}_i)|\psi_i\rangle = \frac{G_F}{2\sqrt{2}} \sum_K Q_w^K \int d\mathbf{r}\, \gamma^5(\mathbf{r})\rho_K(\mathbf{r}) \tag{5.46}$$

in which appears the weak nuclear charge $Q_w^K = Z_K(1 - 4\sin^2\theta_W) - N_K$ with Z_K and N_K representing the number of protons and neutrons in nucleus K, respectively, and $\sin^2\theta_W = 0.2319$ being the employed Weinberg parameter (the most recent value[242] is $\sin^2\theta_W = 0.2397(13)$). The normalized nuclear charge densities ρ_K restrict the integration over electron coordinates $\mathbf{r}_i$ to

nuclear regions, and therefore provide a natural partitioning of the operator in atomic contributions. The Fermi coupling constant $G_\mathrm{F} = 2.22254 \cdot 10^{-14}\, E_\mathrm{h} a_0^3$ demonstrates the minuteness of the effect. Finally, γ^5 is one of the Dirac matrices (see also Section 1.2, p. 31),

$$\gamma^5 = \begin{pmatrix} 0_{2\times2} & 1_{2\times2} \\ 1_{2\times2} & 0_{2\times2} \end{pmatrix}. \tag{5.47}$$

Eqs. 5.45 and 5.46 define the density $\gamma^5(\mathbf{r})$ and its evaluation is a straightforward task,

$$\gamma^5(\mathbf{r}) = \phi_\kappa^{\mathrm{L}\dagger}(\mathbf{r})\phi_\lambda^{\mathrm{S}}(\mathbf{r})D_{\lambda\kappa}^{\mathrm{o,SL}} + \phi_\kappa^{\mathrm{S}\dagger}(\mathbf{r})\phi_\lambda^{\mathrm{L}}(\mathbf{r})D_{\lambda\kappa}^{\mathrm{o,LS}}, \tag{5.48}$$

when compared with the corresponding expression for the evaluation of the charge density

$$\rho(\mathbf{r}) = -e\phi_\kappa^{\mathrm{L}\dagger}(\mathbf{r})\phi_\lambda^{\mathrm{L}}(\mathbf{r})D_{\lambda\kappa}^{\mathrm{o,LL}} - e\phi_\kappa^{\mathrm{S}\dagger}(\mathbf{r})\phi_\lambda^{\mathrm{S}}(\mathbf{r})D_{\lambda\kappa}^{\mathrm{o,SS}}. \tag{5.49}$$

Here κ, λ are indices over large (L) or small (S) component atomic orbitals ϕ and $D_{\lambda\kappa}^{\mathrm{o}}$ is the real part of corresponding quaternion atomic orbital density matrix. Having defined $\gamma^5(\mathbf{r})^*$ makes it possible to obtain P numerically on a suitably chosen grid of points by integrating $\gamma^5(\mathbf{r})$ weighted with the normalized nuclear charge densities and scaled with the appropriate factors. In the approximation of point charge nuclei, which is a very good approximation (see Tab. 5.4), P is given by

$$P \approx \frac{G_\mathrm{F}}{2\sqrt{2}} \sum_K Q_\mathrm{w}^K \int \mathrm{d}\mathbf{r}\, \gamma^5(\mathbf{r})\delta^3(\mathbf{r} - \mathbf{r}_K) = \frac{G_\mathrm{F}}{2\sqrt{2}} \sum_K Q_\mathrm{w}^K \gamma^5(\mathbf{r}_K), \tag{5.50}$$

and the integration grid turns out to be a sum of very few (in this case five) scaled densities, evaluated at the nuclear centers $\mathbf{r}_K$ (see rightmost column in Tab. 5.4). The numerical approach offers clearly zero computational advantage for the evaluation of P, but it makes it possible to visualize $\gamma^5(\mathbf{r})$ on a 3-dimensional grid. As will be shown in the following it will be useful to visualize the spatial structure of $\gamma^5(\mathbf{r})$ despite the fact that for the PV energy shift $\gamma^5(\mathbf{r})$ is sampled only at (or very close to) the nuclear centers

Before turning to the discussion of the $\gamma^5(\mathbf{r})$ density plots, it is useful to recapitulate what experimentalists and theoreticians are aiming for in studies of PV effects in vibrational spectra. The goal is to detect the PV vibrational transition frequency shift

$$P_{\mathrm{o}\to n} = P_n - P_\mathrm{o} \qquad \text{with} \qquad P_n = \langle n|P(q)|n \rangle \tag{5.51}$$

for the transition from the vibrational ground state ($n = 0$) to a vibrational excited state n, particularly the PV shift $P_{\mathrm{o}\to 1}$ that corresponds to the fundamental transition. Here q is the

---

* The matrix γ^5 and the density $\gamma^5(\mathbf{r})$ are distinguished by always specifying the coordinate argument for the latter.

Table 5.4: Atomic contributions to $P(0)$ at the CCSD(T) equilibrium geometry of R-CHFClBr (HF, $q = 0$, all values in E_h). The rightmost column contains values of the $\gamma^5(\mathbf{r})$ density evaluated at the nuclear centers $\mathbf{r}_K$, scaled with $\frac{G_\mathrm{F}}{2\sqrt{2}}Q_\mathrm{w}^K$. These values are atomic contributions to $P(0)$ in the approximation of point charge nuclei.

nucleus K	$\sum_i \langle \psi_i \vert \gamma^5 \rho_K(\mathbf{r}_i) \vert \psi_i \rangle$	$\frac{G_\mathrm{F}}{2\sqrt{2}}Q_\mathrm{w}^K$ $\times \sum_i \langle \psi_i \vert \gamma^5 \rho_K(\mathbf{r}_i) \vert \psi_i \rangle$	$\gamma^5(\mathbf{r}_K)$	$\frac{G_\mathrm{F}}{2\sqrt{2}}Q_\mathrm{w}^K$ $\times \gamma^5(\mathbf{r}_K)$
C	-1.315×10^{-06}	5.752×10^{-20}	-1.315×10^{-06}	5.752×10^{-20}
H	4.942×10^{-09}	2.812×10^{-24}	4.942×10^{-09}	2.812×10^{-24}
F	-1.198×10^{-05}	8.798×10^{-19}	-1.198×10^{-05}	8.798×10^{-19}
Cl	2.731×10^{-05}	-3.598×10^{-18}	2.731×10^{-05}	-3.598×10^{-18}
Br	-2.514×10^{-05}	8.191×10^{-18}	-2.516×10^{-05}	8.200×10^{-18}
Cl + Br		4.593×10^{-18}		4.602×10^{-18}
sum = $P(0)$		5.530×10^{-18}		5.539×10^{-18}
Ref. 225		5.530×10^{-18}		

normal mode coordinate. Inter-mode coupling is thus neglected (but not the anharmonicity). Although the weak neutral current interaction is extremely localized in space to domains of nonvanishing nuclear charge, P is quite sensitive to the chemical environment and to its changes along the normal mode coordinate q. It is a molecular property being a sum of localized atomic contributions thanks to the nature of the weak interaction.

For our HF study of the PV fundamental vibrational transition frequency shift in CFH-ClBr we have adopted the same approximations as detailed in Ref. 225. This means that we have used the same basis sets and the same coupled cluster singles and doubles including perturbative triples (CCSD(T)) equilibrium geometry and normal mode displacement vectors. We have calculated the CCSD(T) energy V and the PV shift P at eleven values of q ($q = 0, \pm 0.018897, \pm 0.037795, \pm 0.094486, \pm 0.188973, \pm 0.472431$, all a_0) and obtained the MacLaurin expansion coefficients $V^{(k)}$ and $P^{(k)}$ which appear in

$$V(q) = V(0) + \sum_{k=2} \frac{1}{k!} V^{(k)}(0) q^k \tag{5.52}$$

and

$$P(q) = P(0) + \sum_{k=1} \frac{1}{k!} P^{(k)}(0) q^k \tag{5.53}$$

by a polynomial fit of sufficiently high order (see Tab. 5.5).

Table 5.5: MacLaurin expansion coefficients $V^{(k)}$ (CCSD(T)) and $P^{(k)}$ (HF) for $V(q)$ and $P(q)$ along the CCSD(T) C–F stretch normal mode coordinate q in R-CHFClBr.

k	$V^{(k)}(0)$	$P^{(k)}(0)$
1		$-1.423223 \times 10^{-17}$
2	4.609133×10^{-1}	2.827622×10^{-17}
3	$-1.757234 \times 10^{+0}$	$-1.186713 \times 10^{-17}$
4	$5.882756 \times 10^{+0}$	$-1.564150 \times 10^{-16}$
5	$-2.000394 \times 10^{+1}$	5.541905×10^{-16}
6	$-3.049929 \times 10^{+0}$	4.750391×10^{-15}
7	$-1.480692 \times 10^{+2}$	
8	$1.684608 \times 10^{+4}$	

Within the approximation of point charge nuclei the MacLaurin expansion of $P(q)$ can be reexpressed using expansion coefficients of the $\gamma^5(\mathbf{r})$ density at the nuclear centers

$$P^{(k)}(0) = \frac{G_\mathrm{F}}{2\sqrt{2}} \sum_K Q_\mathrm{w}^K \gamma^{5(k)}(\mathbf{r}_K) \tag{5.54}$$

with

$$\gamma^5(\mathbf{r}, q) = \gamma^5(\mathbf{r}) + \sum_{k=1} \frac{1}{k!} \gamma^{5(k)}(\mathbf{r}_K) q^k \tag{5.55}$$

From second-order perturbation theory, starting from harmonic solutions, $P_{0\to1}$ is approximately given by[225]

$$P_{0\to1} = \frac{\hbar}{\mu\omega_e} \left[P^{(2)}(0) - \frac{\hbar}{\mu\omega_e^2} P^{(1)}(0) V^{(3)}(0) \right]. \tag{5.56}$$

Using $\mu = 9.7031$ amu and $\omega_e = 1120.6555$ cm^{-1} yields the $0 \to 1$ PV transition frequency shift of -1.405×10^{-19} E_h (-0.9245 mHz). There is no reason to stop at this order of perturbational treatment since the contribution from higher order $V^{(k)}(0)$ and $P^{(k)}(0)$ can be obtained by a numerical solution of the vibrational Schrödinger equation using the Numerov-Cooley method,[*] which includes all higher order anharmonicity effects[†] and comes at a cost of CPU seconds. In general, the contribution from higher orders is rather small, here: $+0.032 \times 10^{-19}$ E_h ($+0.0212$ mHz). The reason why this little exercise has been repeated here was to detail the atomic contributions to $P^{(1)}(0)$ and $P^{(2)}(0)$, and to emphasize that an understanding of $P^{(1)}(0)$ and $P^{(2)}(0)$, or equivalently $\gamma^{5(1)}(\mathbf{r}_K)$ and $\gamma^{5(2)}(\mathbf{r}_K)$, gives already a fair understanding of $P_{0\to1}$. Note that $P(0)$ (or $\gamma^5(\mathbf{r}_K)$) is not sampled in a vibrational spectrum.

The atomic contributions to $P^{(1)}(0)$ and $P^{(2)}(0)$ are listed in Tabs. 5.6 and 5.7. In both cases the contributions from Cl and Br dominate, in the case of $P^{(1)}(0)$ by at least one order of magnitude compared with the other atomic contributions. Although $\gamma^{5(1)}(\mathbf{r}_\mathrm{C})$ competes in

---

[*] We have used a grid of 5000 points in the range $q = -1.2 \cdots + 1.2$ a_0.   [†] The Numerov-Cooley solution includes only those higher order anharmonicity effects that are actually cast by the polynomial expansion or other employed interpolation.

the order of magnitude with the values from Cl and Br, the value is quenched by the relatively small weak nuclear charge of C (−5.5656 compared to −16.7692 of Cl or −41.4660 of Br). The same observation can be made for $\gamma^{5(2)}(\mathbf{r}_F)$.

Table 5.6: Atomic contributions to $P^{(1)}(0)$ at the CCSD(T) equilibrium geometry of R-CHFClBr (HF, $q = 0$, all values in E_h). The rightmost column contains values of the $\gamma^{5(1)}(\mathbf{r})$ density evaluated at the nuclear centers $\mathbf{r}_K$, scaled with $\frac{G_F}{2\sqrt{2}}Q_w^K$. These values are atomic contributions to $P^{(1)}(0)$ in the approximation of point charge nuclei.

nucleus K	$\sum_i \langle \psi_i \vert \gamma^5 \rho_K(\mathbf{r}_i) \vert \psi_i \rangle^{(1)}$	$\frac{G_F}{2\sqrt{2}}Q_w^K$ $\times \sum_i \langle \psi_i \vert \gamma^5 \rho_K(\mathbf{r}_i) \vert \psi_i \rangle^{(1)}$	$\gamma^{5(1)}(\mathbf{r}_K)$	$\frac{G_F}{2\sqrt{2}}Q_w^K$ $\times \gamma^{5(1)}(\mathbf{r}_K)$
C	-1.342×10^{-05}	5.870×10^{-19}	-1.342×10^{-05}	5.870×10^{-19}
H	6.787×10^{-08}	3.861×10^{-23}	6.787×10^{-08}	3.861×10^{-23}
F	7.377×10^{-06}	-5.419×10^{-19}	7.377×10^{-06}	-5.419×10^{-19}
Cl	-4.937×10^{-05}	6.506×10^{-18}	-4.937×10^{-05}	6.506×10^{-18}
Br	6.378×10^{-05}	-2.078×10^{-17}	6.385×10^{-05}	-2.081×10^{-17}
Cl + Br		-1.427×10^{-17}		-1.430×10^{-17}
sum = $P^{(1)}(0)$		-1.423×10^{-17}		-1.423×10^{-17}
Ref. 225		-1.424×10^{-17}		

With the exception of C and H, the atomic contributions P_K show alternating signs for the series $P_K(0), P_K^{(1)}(0), P_K^{(2)}(0)$. This can be anticipated for F from the fact that the field around F is reduced with an increasing q (= increasing C–F distance). A positive q shows however the opposite effect for C which performs a counteracting motion combined with an increasing P_K. Due to the relatively high nuclear mass, the displacement vectors of Cl and Br are small. The overall series $P(0), P^{(1)}(0), P^{(2)}(0)$ is of alternating sign.

It is now time to compare these observations with the corresponding isosurface plots of $\gamma^5(\mathbf{r})$, $\gamma^{5(1)}(\mathbf{r})$, and $\gamma^{5(2)}(\mathbf{r})$, depicted in Figs. 5.16, 5.18, and 5.20. These have been obtained by fitting a polynomial of sixth order to $\gamma^5(\mathbf{r}, q)$ for 80^3 points in space. In these plots the C–H bond points away from the reader and the correct R-configuration[243] can be verified performing a clockwise rotation around C when going from Br over Cl to F. The isosurfaces in Figs. 5.16, 5.18, and 5.20. are colored according to the sign and the coloring would exactly switch in all plots for the corresponding S-enantiomer.

At first sight, the $\gamma^5(\mathbf{r})$ density in Fig. 5.16 seems to have four lobes around each nucleus, separated by two nodal surfaces. At a closer look (see detail in Fig. 5.17), the $\gamma^5(\mathbf{r})$ density can be recognized to consist rather of two dumb-bell shaped isosurfaces around each atom,

Table 5.7: Atomic contributions to $P^{(2)}(0)$ at the CCSD(T) equilibrium geometry of R-CHFClBr (HF, $q = 0$, all values in E_h). The rightmost column contains values of the $\gamma^{5(2)}(\mathbf{r})$ density evaluated at the nuclear centers $\mathbf{r}_K$, scaled with $\frac{G_\mathrm{F}}{2\sqrt{2}}Q_\mathrm{w}^K$. These values are atomic contributions to $P^{(2)}(0)$ in the approximation of point charge nuclei.

nucleus K	$\sum_i \langle \psi_i \vert \gamma^5 \rho_K(\mathbf{r}_i) \vert \psi_i \rangle^{(2)}$	$\frac{G_\mathrm{F}}{2\sqrt{2}}Q_\mathrm{w}^K$ $\times \sum_i \langle \psi_i \vert \gamma^5 \rho_K(\mathbf{r}_i) \vert \psi_i \rangle^{(2)}$	$\gamma^{5(2)}(\mathbf{r}_K)$	$\frac{G_\mathrm{F}}{2\sqrt{2}}Q_\mathrm{w}^K$ $\times \gamma^{5(2)}(\mathbf{r}_K)$
C	8.521×10^{-06}	-3.726×10^{-19}	8.521×10^{-06}	-3.726×10^{-19}
H	-1.006×10^{-07}	-5.723×10^{-23}	-1.006×10^{-07}	-5.723×10^{-23}
F	-1.875×10^{-05}	1.378×10^{-18}	-1.875×10^{-05}	1.378×10^{-18}
Cl	3.688×10^{-05}	-4.859×10^{-18}	3.688×10^{-05}	-4.860×10^{-18}
Br	-9.861×10^{-05}	3.213×10^{-17}	-9.871×10^{-05}	3.216×10^{-17}
Cl + Br		2.727×10^{-17}		2.730×10^{-17}
sum = $P^{(2)}(0)$		2.828×10^{-17}		2.828×10^{-17}
Ref. 225		2.806×10^{-17}		

separated by one nodal surface. The $\gamma^5(\mathbf{r})$ density is nonzero at all five nuclear centers (see Tab. 5.4) but "unfortunately" for the PV energy shift, the maxima of abs($\gamma^5(\mathbf{r})$) are located at four points *outside* the nuclear centers. The largest isosurface is found around C. The nodal surfaces that separate the two $\gamma^5(\mathbf{r})$ isosurfaces of opposite sign are in all cases very close to the nuclei. As an illustration, the $\gamma^5(\mathbf{r})$ density is plotted in the vicinity of the C nucleus in Fig. 5.15. This observation has two important implications: (i) there exist many *chiral* structures where one or several, or even all nuclei lie on $\gamma^5(\mathbf{r})$ nodal surfaces and the total PV energy shift can become zero, and (ii) among different methods it is possible to obtain very different atomic contributions of even opposite sign by only a tiny displacement of the nodal surface.

As stated above, $\gamma^5(\mathbf{r})$ is not monitored in a PV vibrational spectroscopy experiment, but predominantly its first and second-order variation $\gamma^{5(1)}(\mathbf{r})$ and $\gamma^{5(2)}(\mathbf{r})$ (see Figs. 5.18 and 5.20 and details in Figs. 5.19 and 5.21). The first-order variations are large for C and F, for the second-order derivative of $\gamma^5(\mathbf{r})$ the relatively diffuse helical isosurfaces of C and F dominate the picture (see Fig. 5.20). It might come as a surprise that this observation is not reflected in the actual values at the nuclear centers (compare with Tabs. 5.6 and 5.6). Both $\gamma^{5(1)}(\mathbf{r})$ and $\gamma^{5(2)}(\mathbf{r})$ are largest for Cl and Br having very small displacement vectors, in apparent disagreement with the plots where the largest variation is found close to C and F. This can only mean we do not look close enough and that the centers C and F are again very close to nodal surfaces. Like in the case of $\gamma^5(\mathbf{r})$, this signals that it can be difficult to get agreement for $\gamma^{5(1)}(\mathbf{r})$ and $\gamma^{5(2)}(\mathbf{r})$
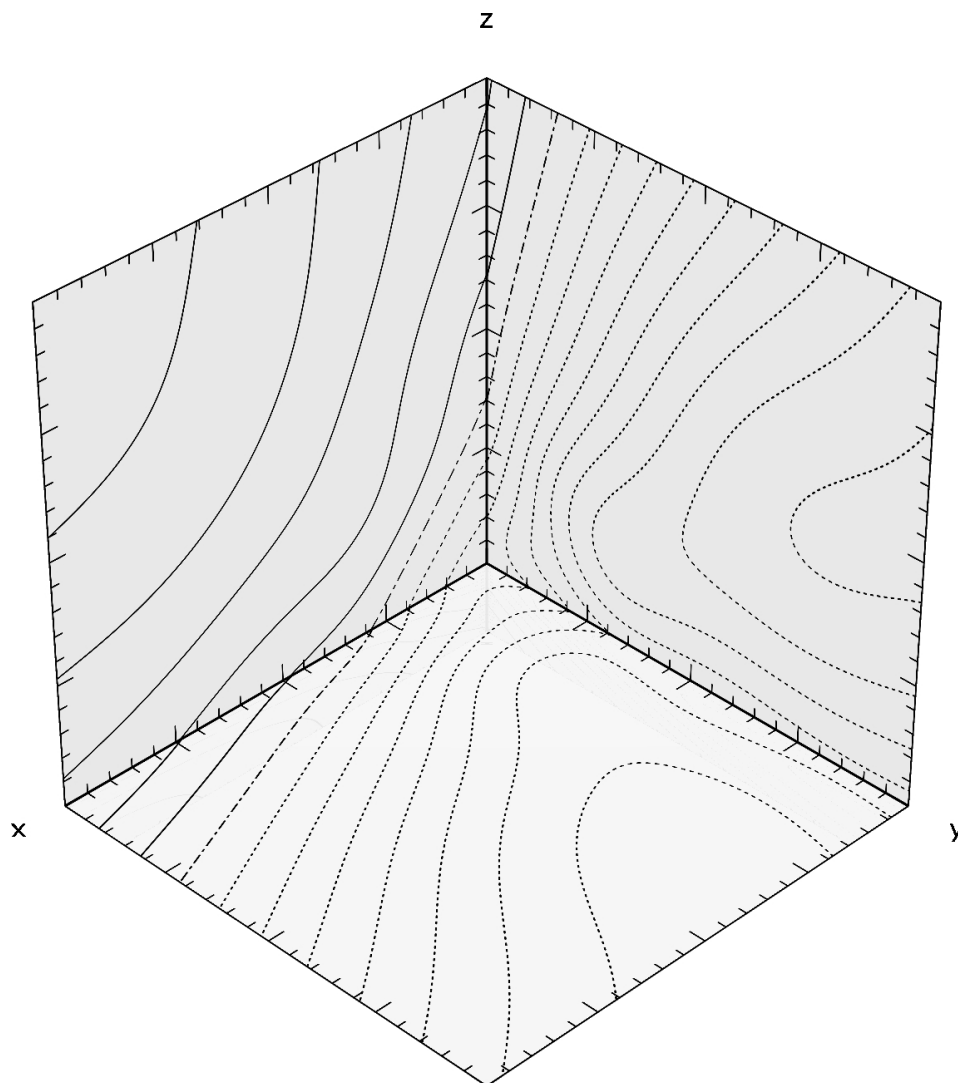
Figure 5.15: HF $\gamma^5(\mathbf{r})$ density in the vicinity of the C nucleus in R-CHFClBr. The dimensions of the box are $0.1{\times}0.1{\times}0.1\ a_{\mathrm{o}}$. The center of the C nucleus is located at the origin (far corner). Solid (dotted) contour lines are plotted following the series $+0.5 \times 10^{-6}$, $+1.0 \times 10^{-6}$, $+1.5 \times 10^{-6}$, $\cdots$ (-0.5×10^{-6}, -1.0×10^{-6}, -1.5×10^{-6}, $\cdots$) a_{o}^{-3}. The dash-dotted contour line represents the cut through the nodal surface.

among different methods, say HF and various density functionals. In a recent computational study of the $P_{0 \to 1}$ shift in chiral oxorhenium complexes we have met this difficulty.[244]

Few approaches to rationalize the magnitude and sign of $\gamma^5(\mathbf{r})$ by simple models exist.[245, 246] The challenge for the future is to rationalize $\gamma^{5(1)}(\mathbf{r})$ and $\gamma^{5(2)}(\mathbf{r})$. An understanding of these densities will make it possible to tune the candidate molecule and the experimental setup such that the tiny effect is maximized and hopefully within the reach of experimental resolution.
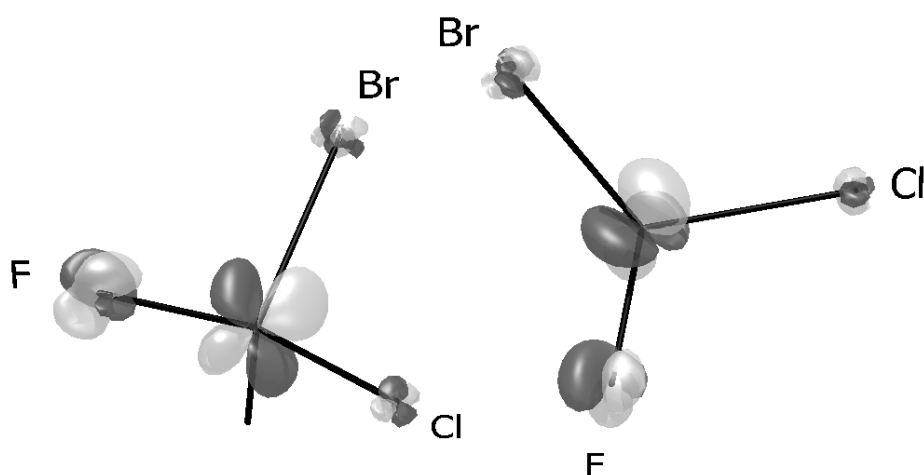
Figure 5.16: HF $\gamma^5(\mathbf{r})$ density in R-CHFClBr from two perspectives (dark isosurface: $+5 \times 10^{-7}\ a_0^{-3}$, light isosurface: $-5 \times 10^{-7}\ a_0^{-3}$).
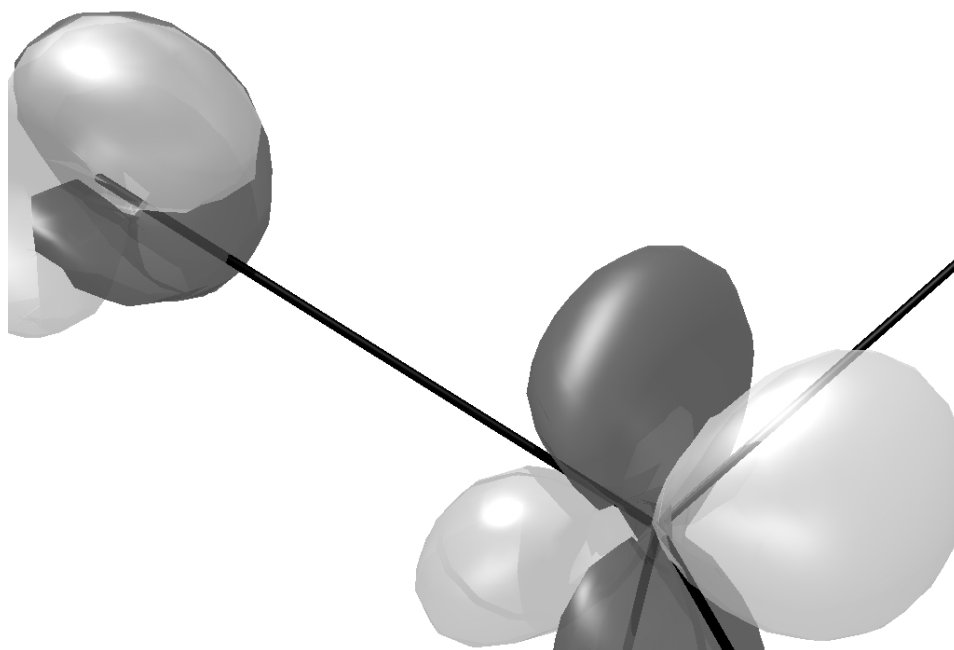
Figure 5.17: Zoom into the HF $\gamma^5(\mathbf{r})$ density along the C–F bond in R-CHFClBr (dark isosurface: $+5 \times 10^{-7}\ a_0^{-3}$, light isosurface: $-5 \times 10^{-7}\ a_0^{-3}$).
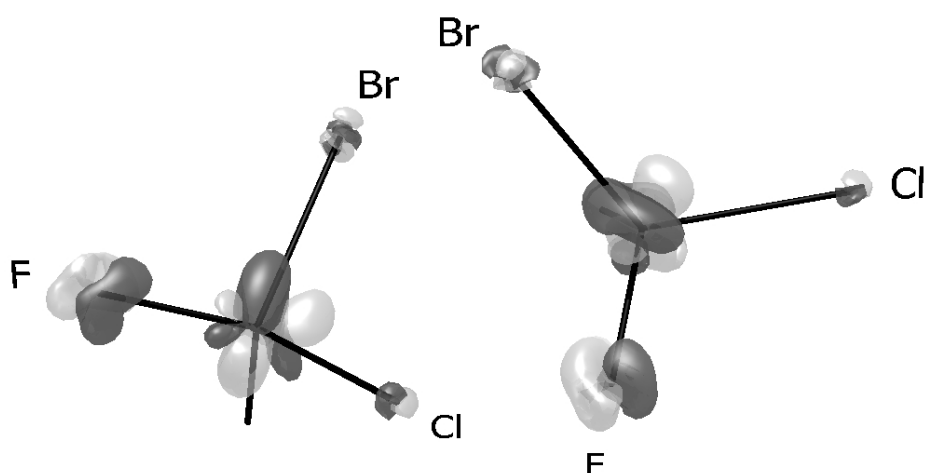
Figure 5.18: HF $\gamma^{5(1)}(\mathbf{r})$ density in R-CHFClBr from two perspectives (dark isosurface: $+1 \times 10^{-6}\ a_0^{-4}$, light isosurface: $-1 \times 10^{-6}\ a_0^{-4}$).
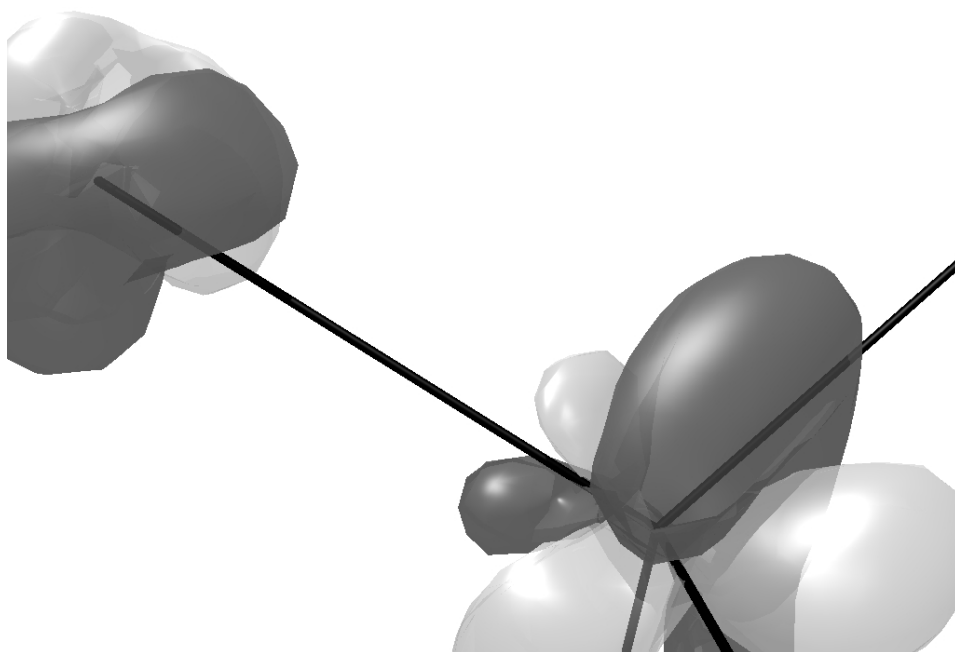
Figure 5.19: Zoom into the HF $\gamma^{5(1)}(\mathbf{r})$ density along the C–F bond in R-CHFClBr (dark isosurface: $+1 \times 10^{-6}\ a_0^{-4}$, light isosurface: $-1 \times 10^{-6}\ a_0^{-4}$).
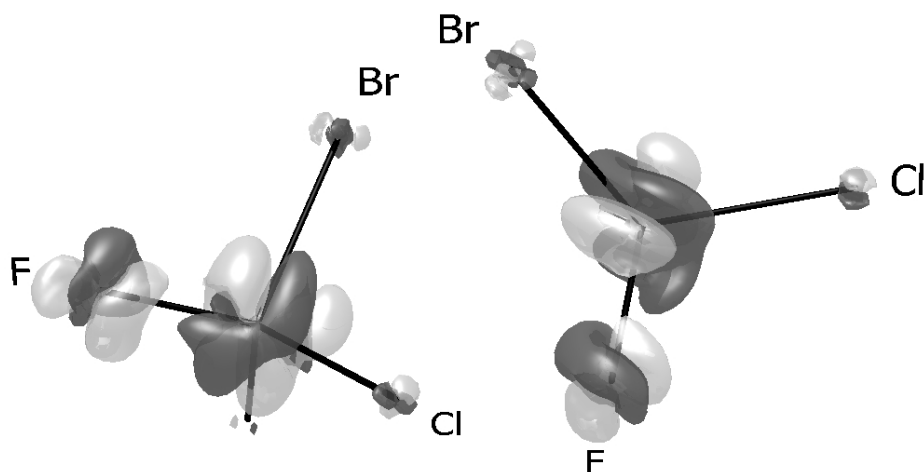
Figure 5.20: HF $\gamma^{5(2)}(\mathbf{r})$ density in R-CHFClBr from two perspectives (dark isosurface: $+1 \times 10^{-6}\ a_\mathrm{o}^{-5}$, light isosurface: $-1 \times 10^{-6}\ a_\mathrm{o}^{-5}$).
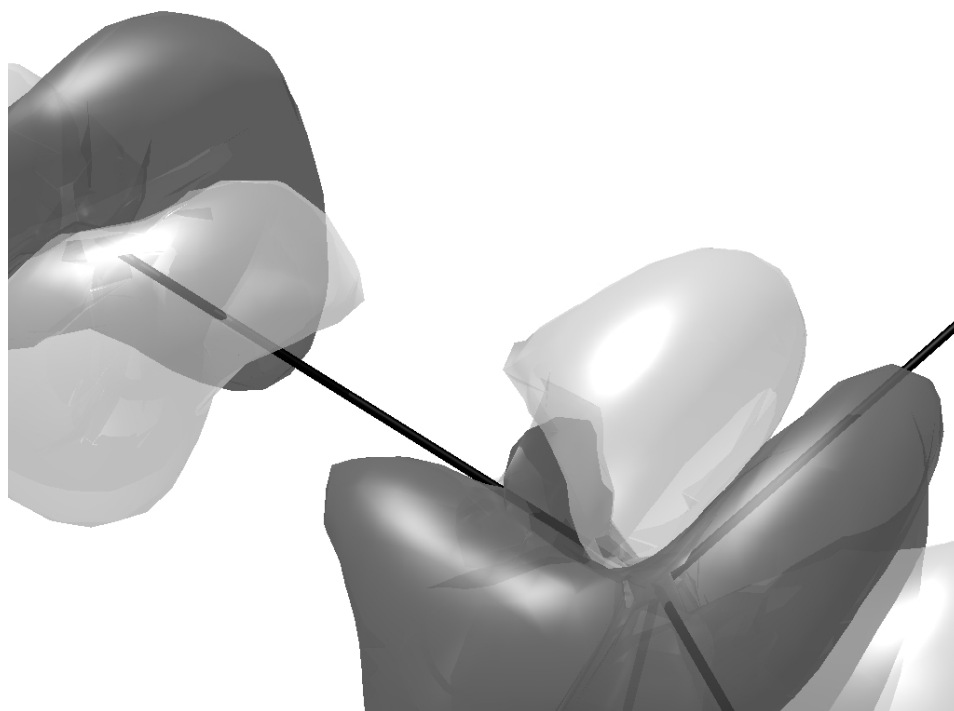
Figure 5.21: Zoom into the HF $\gamma^{5(2)}(\mathbf{r})$ density along the C–F bond in R-CHFClBr (dark isosurface: $+1 \times 10^{-6}\ a_\mathrm{o}^{-5}$, light isosurface: $-1 \times 10^{-6}\ a_\mathrm{o}^{-5}$).

Concluding remarks and perspectives

Summing up, it is clear the future holds great opportunities. It also holds pitfalls. The trick will be to avoid the pitfalls, seize the opportunities, and get back home by six o'clock.

Woody Allen, *My Speech to the Graduates* in *Side Effects*

Summing up, it has been a pleasure to watch several projects form connections with one another, which have converged towards the main theme of this thesis: quantum chemistry beyond charge density.

What has been achieved with the current project and what are the perspectives and challenges for the future?

A nice collection of tools has been presented that offer a real-space approach to frequency-dependent second-order molecular properties within the 4-component relativistic framework with the possibility to impose other static perturbations and to visualize these effects.

We have presented implementations which allow us to calculate parity-violating (PV) effects in nuclear magnetic resonance parameters at the 4-component relativistic HF and DFT level of theory.

The first tests of linear and quadratic response theory within noncollinear TD-SDFT look very promising. We have successfully implemented two interpolation schemes for asymptotically shape-corrected functionals, i.e. the gradient-regulated asymptotic connection procedure (GRAC) and the statistical averaging of (model) orbital potentials (SAOP).

Of course some problems remain to be solved. For the calculation of nuclear magnetic resonance shielding constants using SDFT, the DFT code needs to be adapted to enable gauge origin including atomic orbitals (London orbitals)—for instance, following the NR implementation of Helgaker *et al.* [247] This also holds for the visualization routines which presently employ a common gauge origin. In order to study nondivergent response functions in the resonant regions of optical frequencies, the response code needs to be adapted to take relaxation into account.[172]

We have obtained an anomalous PV contribution to the nuclear magnetic resonance shielding constant of ^{209}Po in chiral H_2Po_2 and also anomalous magnetizabilities for H_5C_5Sb, and H_5C_5Bi. These incongruous results—in both cases including spin–orbit coupling—may signal triplet instabilities. Although such instabilities can typically be avoided using nonhybrid DFT, it will be important to introduce methods to detect such instabilities reliably in the future.

Also the noncollinear TD-SDFT linear and quadratic response is only a stopover on the way to a genuine relativistic TD-CDFT. The charge and charge current density, as part of the 4-current density, are mixed through a Lorentz transformation. This strongly suggests that density and current density functionals should have the same mathematical form in the relativistic domain which strongly favors the 4-component relativistic framework for the development of new current density functionals. The very first steps toward this goal have been made. For the development of a 4-component relativistic TD-CDFT implementation we can greatly benefit from the available and well-tested TD-SDFT code structure. The necessary modifications are truly minimal. What remains of course, is the formulation and programing of the corresponding functional derivatives. A simple current density functional is the (vorticity-dependent) LDA current functional suggested by Vignale, Rasolt, and Geldart[89,90,248] (VRG). This functional has been successfully implemented in the DIRAC[16] code and the calculated Lévy-Leblond isotropic shielding constants in N_2, F_2, HF, CO, and H_2O are in excellent agreement with the results reported by Lee *et al.* [249] (see Tab. 5.8).

Up to this point, we have practiced mostly on "toy systems", i.e. when calculating the excitation energies we knew most results *a priori*. Having validated the implementations, it will be very exciting to apply the presented methodology to "real problems", i.e. where the performance of TD-SDFT and the real-space approach to molecular properties within the 4-component relativistic framework are not yet known.

Table 5.8: Isotropic shielding constants in N_2, F_2, HF, CO, and H_2O (in ppm). All calculations have been carried out at the geometries detailed in Ref. 249 using the H-IV basis set[250] and the Lévy-Leblond Hamiltonian. The common gauge origin has been placed at the nucleus under study. Results of Lee et al. [249] are given for comparison (in brackets).

		RHF	LDA	LDA+VRG	BLYP	BLYP+VRG	B3LYP	B3LYP+VRG	SAOP	SAOP+VRG	exp.
N_2	$\sigma(^{14}N)$	−109.8 (−109.8)	−91.4 (−91.4)	−96.9 (−96.9)	−84.6 (−84.6)	−90.0 (−89.9)	−91.6	−97.4	−77.0	−82.3	−61.6±0.2 [b]
F_2	$\sigma(^{19}F)$	−168.0 (−168.0)	−283.7 (−283.8)	−291.9 (−291.9)	−271.8 (−271.9)	−279.7 (−279.7)	−252.3	−260.1	−260.0	−267.5	−232.8 [c]
HF	$\sigma(^{1}H)$	29.0 (29.0)	30.1 (30.1)	30.1 (30.1)	30.8 (30.8)	30.8 (30.8)	30.3	30.3	29.1	29.1	28.5±0.2 [d]
	$\sigma(^{19}F)$	410.9 (410.9)	412.2 (412.2)	411.7 (411.7)	406.3 (406.3)	405.7 (405.7)	407.9	407.3	416.4	416.0	410.±6 [e]
CO	$\sigma(^{13}C)$	−23.1 (−23.1)	−20.3 (−20.3)	−24.6 (−24.5)	−14.8 (−14.8)	−19.0 (−18.9)	−18.4	−22.3	−2.2	−6.2	3.0±0.9 [f]
	$\sigma(^{17}O)$	−84.5 (−84.5)	−87.7 (−87.7)	−94.6 (−94.5)	−77.5 (−77.5)	−84.2 (−84.1)	−81.3	−88.5	−50.5	−56.9	−42.3±17.2 [g]
H_2O	$\sigma(^{1}H)$	30.6 (30.6)	30.9 (30.9)	30.9 (30.9)	31.5 (31.5)	31.5 (31.5)	31.3	31.3	30.8	30.8	30.052±0.015 [d]
	$\sigma(^{17}O)$	320.7 (320.7)	327.0 (327.0)	326.9 (326.9)	318.0 (318.1)	317.9 (317.9)	319.3	319.1	322.9	322.6	344.0±17.2 [g]

[a] Ref. 249. [b] Ref. 251. [c] Ref. 157. [d] Ref. 252. [e] Ref. 253. [f] Ref. 254. [g] Ref. 255.

Part II

Papers

Paper I

R. Bast, P. Schwerdtfeger, and T. Saue

Parity nonconservation contribution to the nuclear magnetic resonance shielding constants of chiral molecules: A four-component relativistic study

Parity nonconservation contribution to the nuclear magnetic resonance shielding constants of chiral molecules: A four-component relativistic study

Radovan Bast
Laboratoire de Chimie Quantique, Institut de Chimie de Strasbourg,
LC3-UMR 7177 CNRS/Université Louis Pasteur, 4 Rue Blaise Pascal, F-67000 Strasbourg, France

Peter Schwerdtfeger
Centre of Theoretical Chemistry and Physics, Building 44, Institute of Fundamental Sciences (IFS),
Massey University (Albany Campus), Private Bag 102904, North Shore MSC,
Auckland, New Zealand

Trond Saue[a]
Laboratoire de Chimie Quantique, Institut de Chimie de Strasbourg,
LC3-UMR 7177 CNRS/Université Louis Pasteur, 4 Rue Blaise Pascal, F-67000 Strasbourg, France

A systematic four-component relativistic study of the parity nonconservation (PNC) contribution to the (isotropic) NMR shielding constants of chiral molecules is presented for the P enantiomers of the series H_2X_2 ($X = {}^{17}O, {}^{33}S, {}^{77}Se, {}^{125}Te, {}^{209}Po$). The PNC contributions are obtained within a linear response approach at the Hartree-Fock level. A careful design of the basis sets is necessary. The four-component relativistic results based on the Dirac-Coulomb Hamiltonian are compared with the nonrelativistic Lévy-Leblond results and those obtained by the spin-free modified Dirac Hamiltonian. The calculations confirm the nonrelativistic scaling law $Z^{2.4}$ of the PNC contribution with respect to nuclear charge Z. However, the calculations also show that the *overall* scaling is significantly modified by relativistic effects. The scalar relativistic effect scales as $Z^{4.7}$ for the selected set of molecules, whereas the spin-orbit effect, of opposite sign, scales better than Z^6 and completely dominates the PNC contribution for the heaviest elements. This opens up the intriguing possibility of the experimental observation of PNC effects on NMR parameters of molecules containing heavy atoms. The presented formalism is expected to be valuable in assisting the search for suitable candidate molecules. © *2006 American Institute of Physics.* [DOI: 10.1063/1.2218333]

I. INTRODUCTION

Physics is not symmetric under the parity operation. The parity nonconservation (PNC) of the electroweak interaction was first postulated by Lee and Yang[1] in 1956 and is today well known in nuclear and particle physics. PNC can be observed for instance in the β decay under very low temperature in an external magnetic field (as first performed by Wu *et al.*[2]) or in the optical rotation in atomic heavy-metal vapors.[3–5]

The next logical but ambitious step has been to move the attention towards chemical systems. In the realm of molecular physics the inclusion of the electroweak neutral-current interaction leads to a minute energy difference between the two enantiomers of a chiral molecule. The possible connection between this energy difference and the homochirality in biomolecular life is subject to intensive discussion (e.g., Refs. 6–8). However, an unequivocal experimental determination of this energy difference between two enantiomers has not been achieved so far despite several claims.

While the current search for the experimental manifestation of PNC effects in molecules focuses mainly on differences in the infrared and electronic spectra of chiral molecules (see Refs. 9 and 10 for a review and references

therein), their influence on NMR parameters such as the shielding tensor or spin-spin coupling constants shows an interesting and possibly complementary alternative despite immense technical obstacles[11] which shall not be the subject of this article. Gorshkov *et al.*[12] were apparently the first to propose a search for PNC effects in magnetic-resonance experiments on chiral molecules. Barra *et al.* independently proposed and explored this possibility in the context of NMR in a series of papers.[13–15] They formulated both the theory within the relativistic (R) and the nonrelativistic (NR) framework and performed the first calculations using a relativistically parametrized extended Hückel method. Since their pioneer work only very recently have a few theoretical *ab initio* studies[16–18] been published.

A reinvestigation of this problem by an *ab initio* approach has been deemed necessary since the semiempirical extended Hückel method used by Barra *et al.*[13,14] is known to underestimate PNC energy differences by about an order of magnitude. Independently Laubender and Berger[16] and Soncini *et al.*[17] have published the first *ab initio* calculations of PNC NMR shielding constants—both of them in a NR formalism without the inclusion of spin-orbit coupling. Laubender and Berger[16] have studied the chiral series H_2X_2 ($X = {}^{17}O, {}^{33}S, {}^{77}Se$) and 2-fluorooxirane. Soncini *et al.*[17] have reported a NR formalism by calculating the PNC contribu-

[a] Electronic mail: tsaue@chimie.u-strasbg.fr

125, 064504-1

tions for $H_2{}^{33}S_2$ and m-1,2 dithiin, presenting expressions for both diamagnetic and paramagnetic contributions to the NMR shielding tensor. Recently, Weijo et al.[18] have reported a study of PNC contributions to the (isotropic) NMR shielding constants and indirect spin-spin coupling constants in chiral halomethanes at the level of Hartree-Fock and density-functional theory. They have shown significant effects of electron correlation on the PNC contributions.

The recent publications of other groups[16–18] conclude with negative results in the sense that the calculated PNC contributions are several orders of magnitude below the present resolution in NMR spectroscopy.[11] However, they suggest, as did the results of Barra et al.[13–15] that such effects may indeed be observable for molecules containing heavy elements. This has motivated us to pursue the development of this theoretical methodology by extending it to a four-component relativistic framework which offers a solid theoretical basis for the treatment of heavy-element compounds and which is found to be very successful in the calculations of PNC energy differences in the infrared spectra.[19–22] This will make it possible to verify the scaling of the PNC contribution with respect to the nuclear charge for a series of homologous molecules. This Z scaling (Z is the number of protons) is expected[16] to be much smaller for the PNC NMR shielding constants (Z^2–Z^4) compared with PNC energy differences (Z^5–Z^6). We shall see that this is not the case.

Here we present a systematic four-component relativistic study of the PNC contribution to the (isotropic) NMR shielding constants of chiral molecules for the P enantiomers of the series H_2X_2 ($X={}^{17}O, {}^{33}S, {}^{77}Se, {}^{125}Te, {}^{209}Po$) using a linear response approach at the Hartree-Fock level. We will give the Hamiltonian employed in this study as well as its nonrelativistic limit (NRL) and compare our results with the work of other authors[16] and demonstrate where a NR treatment is justified as well as its limitations. At several points we will emphasize various approximations usually introduced in the derivation of the Hamiltonian. The spin-orbit coupling is naturally included in a four-component relativistic framework—we will assess its effect by deleting the quaternion imaginary parts of matrix representations of the modified Dirac equation and property gradients as described in Refs. 23 and 24, respectively.

The chosen set of molecules is *not* suitable for the experimental search of PNC effects due to stereomutation as already pointed out in Ref. 16. However, this model set is very well studied from the theoretical point of view and is ideal for a systematic calibration of our implementation which we expect to be valuable for future search of suitable candidates for the experimental determination of PNC effects in NMR spectra.

II. FORMALISM

The Hamiltonian employed in this study (1) for the electroweak neutral-current interaction between electrons and nuclei can be derived from the V-A (vector electron minus axial vector nucleus) Fermi coupling neglecting the momentum transfer between the electrons and the nuclei and con-

sists of nuclear spin-independent ($\hat{h}_i^{\text{PNC}}$) and nuclear spin-dependent one-electron terms ($\hat{h}_{\mathbf{I},i}^{\text{PNC}}$) (1). SI-based atomic units are used throughout.

$$
\begin{aligned}
\hat{H}^{\text{PNC}} &= \sum_i \{\hat{h}_i^{\text{PNC}} + \hat{h}_{\mathbf{I},i}^{\text{PNC}}\} \\
&= \frac{G_F}{\sqrt{2}} \sum_{i,A} \left\{ \frac{1}{2} Q_{w,A} \gamma^5 \rho_A(\mathbf{r}_i) - \lambda_A \right. \\
&\quad \left. \times (1 - 4\sin^2\theta_W)\boldsymbol{\alpha}\cdot\mathbf{I}_A\rho_A(\mathbf{r}_i) \right\}.
\end{aligned}
\tag{1}
$$

Here the indices i and A run over all electrons and nuclei, respectively, $G_F = 2.222\,54\cdot10^{-14}E_h a_0^3$ is the Fermi coupling constant, $Q_{w,A} = Z_A(1-4\sin^2\theta_W) - N_A$ is the weak nuclear charge with Z_A and N_A representing the number of protons and neutrons in nucleus A, respectively, and $\sin^2\theta_W = 0.2319$ is the employed Weinberg parameter [the most recent value is $\sin^2\theta_W = 0.2397(13)$ (Ref. 25)].

γ^5 is one of the Dirac matrices (2) with $1_{2\times2}$ being the 2×2 identity matrix,

$$
\gamma^5 = \begin{pmatrix} 0_{2\times2} & 1_{2\times2} \\ 1_{2\times2} & 0_{2\times2} \end{pmatrix}, \quad \boldsymbol{\alpha} = \begin{pmatrix} 0_{2\times2} & \boldsymbol{\sigma} \\ \boldsymbol{\sigma} & 0_{2\times2} \end{pmatrix}.
\tag{2}
$$

ρ_A is the normalized nuclear charge density, and λ_A a nucleus-dependent parameter close to unity.[9,26,27] $\boldsymbol{\alpha}$ is given in Eq. (2) with $\boldsymbol{\sigma}$ being the Pauli spin matrices in the standard representation. Finally, $\mathbf{I}_A$ is the spin of nucleus A. This is only an approximation to the (unknown) nuclear spin density distribution. In the case of a positive experimental measurement the theoretical PNC contribution could be used to reveal or to verify various nuclear spin or charge density distribution models (see, e.g., Ref. 28 and references therein). A more detailed discussion of the above operator is found in Ref. 9.

In this paper we will consider only the nuclear spin-dependent terms $\hat{h}_{\mathbf{I},i}^{\text{PNC}}$ and defer the possible effect of the first term $\hat{h}_i^{\text{PNC}}$ to a later publication. We therefore set $\hat{H}^{\text{PNC}} \equiv \hat{H}_{\mathbf{I}}^{\text{PNC}}$ and obtain our final expression (3) by replacing the nuclear spin by the nuclear magnetic moment $\mathbf{M}_A = \gamma_A\mathbf{I}_A$, where γ_A is the magnetogyric ratio of nucleus A,

$$
\begin{aligned}
\hat{H}^{\text{PNC}} &\equiv \hat{H}_{\mathbf{I}}^{\text{PNC}} \\
&= -\frac{G_F(1-4\sin^2\theta_W)}{\sqrt{2}} \sum_{i,A} \left\{ \frac{1}{\gamma_A}\boldsymbol{\alpha}\cdot\mathbf{M}_A\rho_A(\mathbf{r}_i) \right\}.
\end{aligned}
\tag{3}
$$

For comparison with the work of Laubender and Berger[16] we have set the nucleus-dependent parameter $\lambda_A \equiv 1.0$. The contribution of the nuclear anapole moment[29] to the PNC shieldings has been neglected as well.

For later discussion it will be instructive to consider the NRL of Eq. (3). We employ the NRL of the small component bispinor,

$$
\lim_{c\to\infty} c|\psi^S\rangle = \frac{1}{2m}(\boldsymbol{\sigma}\cdot\mathbf{p})|\psi^L\rangle,
\tag{4}
$$

in conjunction with the Dirac identity,

$$(\boldsymbol{\sigma} \cdot \mathbf{P})(\boldsymbol{\sigma} \cdot \mathbf{Q}) = \mathbf{P} \cdot \mathbf{Q} + i\boldsymbol{\sigma} \cdot (\mathbf{P} \times \mathbf{Q}), \tag{5}$$

for arbitrary vectors $\mathbf{P}$ and $\mathbf{Q}$ to obtain

$$\langle \psi | (\boldsymbol{\alpha} \cdot \mathbf{M}_A \rho_A(\mathbf{r}_i)) | \psi \rangle$$
$$= \langle \psi^L | (\boldsymbol{\alpha} \cdot \mathbf{M}_A \rho_A(\mathbf{r}_i)) | \psi^S \rangle + \langle \psi^S | (\boldsymbol{\alpha} \cdot \mathbf{M}_A \rho_A(\mathbf{r}_i)) | \psi^L \rangle$$
$$= \frac{1}{2mc} \{ \langle \psi^L | (\boldsymbol{\alpha} \cdot \mathbf{M}_A \rho_A(\mathbf{r}_i))(\boldsymbol{\sigma} \cdot \mathbf{p}) | \psi^L \rangle + \langle \psi^L | (\boldsymbol{\sigma} \cdot \mathbf{p})$$
$$\times (\boldsymbol{\sigma} \cdot \mathbf{M}_A \rho_A(\mathbf{r}_i)) | \psi^L \rangle \}. \tag{6}$$

The NRL can then be expressed as

$$\lim_{c \to \infty} c \hat{H}^{\mathrm{PNC}} = -\frac{G_F(1 - 4\sin^2\theta_W)}{2\sqrt{2}m}$$
$$\times \sum_{i,A} \frac{1}{\gamma_A} \{ \mathbf{M}_A \cdot [\mathbf{p}_i, \delta^3(\mathbf{r}_{iA})]_+$$
$$- 2i(\mathbf{s}_i \times \mathbf{M}_A) \cdot [\mathbf{p}_i, \delta^3(\mathbf{r}_{iA})] \}. \tag{7}$$

Here we have also made the transition from a finite nucleus density $\rho_A(\mathbf{r}_i)$ to a point nucleus contact interaction described by the Dirac distribution $\delta^3(\mathbf{r}_{iA})$ with $\mathbf{r}_{iA} = \mathbf{r}_i - \mathbf{r}_A$. $\mathbf{s} = \boldsymbol{\sigma}/2$ denotes the electron spin, c the speed of light, $[\cdots]$ the commutator, and $[\cdots]_+$ the anticommutator.

The nuclear magnetic shielding is defined as the second derivative of the energy with respect to the nuclear magnetic moment $\mathbf{M}_A$ and the external uniform magnetic field $\mathbf{B}$ at zero perturbation strength:

$$\sigma_{A,\epsilon\tau} = \frac{\partial^2 E(\mathbf{M}_A, \mathbf{B})}{\partial M_{A,\epsilon} \partial B_\epsilon} \bigg|_{\mathbf{M}_A = 0, \mathbf{B} = 0}. \tag{8}$$

At the four-component relativistic level the operator associated with an external magnetic field is usually chosen as

$$\hat{h}_{\mathbf{B}} = -\frac{c}{2} \mathbf{B} \cdot \sum_i (\boldsymbol{\alpha} \times \mathbf{r}_{iG}) \quad \text{with } \mathbf{r}_{iG} = \mathbf{r}_i - \mathbf{r}_G, \tag{9}$$

where $\mathbf{r}_G$ is the gauge origin. The PNC contribution to the NMR shielding tensor is thereby given by the linear response function

$$\sigma_{A,\epsilon\tau}^{\mathrm{PNC}} = \frac{G_F(1 - 4\sin^2\theta_W)}{2\gamma_A\sqrt{2}c_0} \langle\langle c\alpha_\epsilon \rho_A(\mathbf{r}_i)); c(\boldsymbol{\alpha} \times r_{iG})_\tau \rangle\rangle_{\omega=0}. \tag{10}$$

In Eq. (10) two different c appear (c and c_0). By varying $c \to \infty$ the fixed $c_0 \approx 137.036$ a.u. guarantees the NRL employed in the literature. We will make use of this technique later in this article. Note, however, that in the strict NRL the PNC contribution (as well as the shielding itself) is zero, as discussed in Ref. 24.

The static linear response function $\langle\langle \hat{H}_A; \hat{H}_B \rangle\rangle_{\omega=0}$ is constructed from property gradients $\mathbf{E}_A^{[1]}$ and $\mathbf{E}_B^{[1]}$ according to

$$\langle\langle \hat{H}_A; \hat{H}_B \rangle\rangle_{\omega=0} = -\mathbf{E}_A^{[1]\dagger} (E_0^{[2]})^{-1} \mathbf{E}_B^{[1]}, \tag{11}$$

where $E_0^{[2]}$ is the electronic Hessian. In practice the explicit evaluation of $E_0^{[2]}$ is computationally too demanding and the linear response function is constructed by first solving the response equation

$$E_0^{[2]} \mathbf{X}_B(\omega) = -\mathbf{E}_B^{[1]} \tag{12}$$

by expanding the solution vector $\mathbf{X}_B$ (12) in trial vectors, followed by contraction of $\mathbf{X}_B$ with the property gradient $\mathbf{E}_A^{[1]}$.[30]

We will not show in detail how relativistic effects can be eliminated in a four-component formalism using the spin-free modified Dirac or the Lévy-Leblond Hamiltonian as this has been done elsewhere.[24]

III. COMPUTATIONAL DETAILS

All calculations have been carried out at the Hartree-Fock level using a development version of the DIRAC code.[31] The molecules H_2X_2 ($X = {}^{17}O, {}^{33}S, {}^{77}Se, {}^{125}Te, {}^{209}Po$) have been investigated at various dihedral angles with the bond lengths and H-X-X angles kept fixed and taken from Refs. 16 and 32 for comparison. The X_2 unit was aligned along the y axis with the dihedral angle bisected by the yz plane. We have used both (contracted) aug-cc-pV{D, T, Q}Z basis sets for H, O, S, and Se as well as the even-tempered basis sets developed by Laerdahl and Schwerdtfeger[32] for O, S, Se, Te, and Po together with uncontracted aug-cc-pVDZ for H. The even-tempered parent set consists of 26 exponents. We will denote these basis sets as "$s.p.d.f$" where s, p, d, and f represent the subsets with the respective angular momenta.

The gauge origin has been placed at the center of the nucleus under study (O, S, Se, Te, Po). A Gaussian charge distribution has been chosen as the nuclear model for the Dirac-Coulomb and the spin-free calculations using the recommended values of Ref. 33. For comparison with the NR calculations by Laubender and Berger[16] point-charge nuclei have been used for the Lévy-Leblond calculations (wave function and response) unless otherwise indicated. The small component basis set for the calculations based on the Dirac-Coulomb Hamiltonian has been generated using separately unrestricted kinetic balance (UKB) and restricted kinetic balance (RKB), respectively, for comparison with the spin-free results. In the Dirac-Coulomb and the spin-free calculations the (SS|SS) integrals have been eliminated in both the self-consistent field (SCF) and the linear response part. Their contribution to energies has been modeled by classical Coulombic repulsion of small component atomic charges.[34] The response equation (12) has been solved with respect to the property gradient associated with the external magnetic field $\mathbf{B}$. Rotations between positive and negative-energy solutions have been suppressed within the linear response module. This approximation implies neglecting the diamagnetic contribution as discussed in Ref. 35. In the nonrelativistic limit the diamagnetic contribution to the PNC shielding constant is zero, as shown by Soncini et al.[7] We find that the inclusion of these rotations alters, for instance, the PNC contribution to the NMR shielding constant of ^{77}Se only by 1.3% (at the dihedral angle of 45°). The corresponding number for ^{209}Po is 0.008%. A tight convergence of the response vector is, however, very important. We have used the value 1.0×10^{-9} as threshold for the ratio of norms between the residual and property gradient vectors.

TABLE I. PNC NMR shielding constant (in ppm) of the nuclei $X = {}^{17}O$, ${}^{33}S$, ${}^{77}Se$, ${}^{125}Te$ and ${}^{209}Po$ in the P enantiomers of H_2X_2 for the dihedral angle of 45°. DC denotes the Dirac-Coulomb Hamiltonian, UKB and RKB the application of unrestricted and restricted kinetic balance, respectively, SF the use of the spin-free modified Dirac Hamiltonian, and LL the use Lévy-Leblond Hamiltonian. PC denotes a point-charge model for the nucleus.

	Basis set	DC(UKB)	DC(RKB)	SF	LL(PC)
$H_2{}^{17}O_2$	aug-cc-pVDZ	3.832×10^{-9}	4.913×10^{-9}	3.968×10^{-9}	3.979×10^{-9}
	aug-cc-pVTZ	4.458×10^{-9}	4.466×10^{-9}	4.616×10^{-9}	4.600×10^{-9}
	aug-cc-pVQZ	4.913×10^{-9}	4.926×10^{-9}	5.090×10^{-9}	5.067×10^{-9}
	1-25.2-26.20-24.20-24	6.064×10^{-9}	6.064×10^{-9}	6.229×10^{-9}	6.121×10^{-9}
$H_2{}^{33}S_2$	aug-cc-pVDZ	-6.348×10^{-8}	-6.460×10^{-8}	-7.011×10^{-8}	-7.100×10^{-8}
	aug-cc-pVTZ	-7.187×10^{-8}	-7.351×10^{-8}	-7.948×10^{-8}	-8.036×10^{-8}
	aug-cc-pVQZ	-7.235×10^{-8}	-7.525×10^{-8}	-8.141×10^{-8}	-8.215×10^{-8}
	1-25.2-26.20-24.20-24	-9.977×10^{-8}	-9.977×10^{-8}	-1.049×10^{-7}	-9.748×10^{-8}
$H_2{}^{77}Se_2$	aug-cc-pVDZ	-2.367×10^{-8}	-2.403×10^{-8}	-1.438×10^{-7}	-1.652×10^{-7}
	aug-cc-pVTZ	-2.674×10^{-8}	-2.803×10^{-8}	-1.725×10^{-7}	-1.797×10^{-7}
	aug-cc-pVQZ	-2.172×10^{-8}	-2.573×10^{-8}	-1.883×10^{-7}	-1.866×10^{-7}
	1-25.2-26.15-25.20-24	1.255×10^{-8}	1.255×10^{-8}	-2.719×10^{-7}	-2.005×10^{-7}
$H_2{}^{125}Te_2$	1-25.2-26.15-25.19-25	-1.295×10^{-6}	-1.295×10^{-6}	6.128×10^{-7}	3.146×10^{-7}
$H_2{}^{209}Po_2$	1-25.2-26.12-25.15-24	1.277×10^{-3}	1.246×10^{-3}	-5.246×10^{-6}	-9.953×10^{-7}

IV. RESULTS AND DISCUSSION

We have tested our implementation by calculating the PNC contribution to the (isotropic) NMR shielding constants for the nuclei $X = {}^{17}O$, ${}^{33}S$, ${}^{77}Se$, ${}^{125}Te$, and ${}^{209}Po$ in the P enantiomers of H_2X_2 for the dihedral angle of 45° at the Hartree-Fock level. These results are reported in Table I. The PNC contribution is studied using the Dirac-Coulomb (DC) Hamiltonian, the spin-free modified Dirac Hamiltonian, and the Lévy-Leblond Hamiltonian.

The choice of the basis sets deserves a detailed discussion. In Table I results for two different classes of basis sets are reported. We have used aug-cc-pV{D, T, Q}Z basis sets (using their original contraction scheme) in the first instance for comparison with the work of Laubender and Berger.[16] We confirm their observation that these basis sets are not converged without the inclusion of high-exponent p functions (results not shown here). For four-component relativistic calculations of $H_2{}^{33}S_2$ and its heavier homologs these basis sets are qualitatively inappropriate. Rather than correcting these basis sets by liberating or adding high exponents to the sets, we have chosen even-tempered basis sets with a common parent set as our reference. These even-tempered basis sets are unbiased and have a greater flexibility in the core s and p regions which in practice makes them superior to aug-cc-pVNZ basis sets for this type of calculation. Somewhat to our surprise we have found that the PNC NMR shieldings are not converged with the even-tempered basis sets developed by Laerdahl and Schwerdtfeger[32] and that, in particular, the inclusion of polarizing f functions is important. A representative series of results for $H_2{}^{77}Se_2$ obtained during the basis set optimization for Se is given in Table II. The basis sets for the other elements have been obtained in a similar fashion. They can be considered very close to the basis set limit within Hartree-Fock.

For the DC calculations two values are given (UKB and RKB) for each combination of molecule and basis set. The generation of the small component basis set is usually real-

ized by RKB which is based on the nonrelativistic limit of the coupling between the large and small components (4). Introducing an external vector potential **A** alters, however, the coupling of large and small components and requires "magnetic balance"[35] such that the use of a modest basis set generated using RKB may lead to substantial errors for NMR shieldings.[36] This can be corrected by applying UKB, which considers the three components of the linear momentum **p** separately and thus provides more flexibility to ensure that the correct coupling can be attained. The difference between UKB and RKB is known to decrease with increasing quality of the basis set. We observe identical results for the best performing even-tempered basis sets for UKB and RKB.

For hydrogen going beyond uncontracted aug-cc-pVDZ is not needed. This to some extent indicates the rather atomic nature of this property. Analysis of the linear response functions contributing to the PNC NMR shielding constant for ${}^{77}Se$ in H_2Se_2 shows that they are dominated by orbital rotations between highest occupied molecular orbital (HOMO)-lowest unoccupied molecular orbital (LUMO) Kramer's partners. Following the projection analysis described in Ref. 37, the relevant molecular orbitals ψ_k^{mol} may

TABLE II. Basis-set dependence of the Dirac-Coulomb unrestricted kinetic balance PNC NMR shielding constant (in ppm) of the nucleus ${}^{77}Se$ in the P enantiomer of H_2Se_2 for the dihedral angle of 45°. The basis set 1-25.2-26.15-25.20-24 has been chosen for further calculations.

Basis set	
1-25.2-26.15-25	3.156×10^{-8}
1-25.2-26.15-25.21-23	1.224×10^{-8}
1-25.2-26.15-25.20-24	1.255×10^{-8}
1-25.2-26.15-25.19-25	1.252×10^{-8}
1-25.2-26.13-25.21-23	1.223×10^{-8}
1-25.2-26.15-26.21-23	1.221×10^{-8}

TABLE III. PNC NMR shielding constants (in ppm) of the nuclei $X = {}^{17}$O, ^{33}S, ^{77}Se, ^{125}Te, and ^{209}Po in the P enantiomers of H_2X_2 for various dihedral angles. DC denotes the Dirac-Coulomb Hamiltonian, UKB the application of unrestricted kinetic balance, and LL the use of the Lévy-Leblond Hamiltonian. PC denotes a point-charge model and GM a Gaussian model for the nucleus. The basis sets are 1-25.2-26.20-24.20-24 for O, 1-25.2-26.15-25.20-24 for S and Se, 1-25.2-26.15-25.19-25 for Te, and 1-25.2-26.12-25.15-24 for Po.

	30°	45°	60°	90°	120°	150°
			$H_2{}^{17}O_2$			
DC(UKB)	5.306×10^{-9}	6.064×10^{-9}	5.219×10^{-9}	1.634×10^{-10}	-4.812×10^{-9}	-4.888×10^{-9}
LL(PC)	5.355×10^{-9}	6.121×10^{-9}	5.272×10^{-9}	1.652×10^{-10}	-4.912×10^{-9}	-5.023×10^{-9}
			$H_2{}^{33}S_2$			
DC(UKB)	-8.336×10^{-8}	-9.977×10^{-8}	-9.532×10^{-8}	-3.977×10^{-8}	2.477×10^{-8}	3.806×10^{-8}
LL(PC)	-8.251×10^{-8}	-9.748×10^{-8}	-9.170×10^{-8}	-3.533×10^{-8}	2.884×10^{-8}	4.158×10^{-8}
			$H_2{}^{77}Se_2$			
DC(UKB)	4.690×10^{-8}	1.255×10^{-8}	-3.458×10^{-8}	-9.935×10^{-8}	-1.502×10^{-7}	-1.738×10^{-7}
LL(GM)	-1.694×10^{-7}	-1.993×10^{-7}	-1.841×10^{-7}	-5.595×10^{-8}	8.602×10^{-8}	1.091×10^{-7}
LL(PC)	-1.704×10^{-7}	-2.005×10^{-7}	-1.852×10^{-7}	-5.629×10^{-8}	8.653×10^{-8}	1.098×10^{-7}
			$H_2{}^{125}Te_2$			
DC(UKB)	-1.420×10^{-6}	-1.295×10^{-6}	-8.249×10^{-7}	3.879×10^{-7}	1.590×10^{-6}	2.008×10^{-6}
LL(PC)	2.675×10^{-7}	3.146×10^{-7}	2.915×10^{-7}	9.472×10^{-8}	-1.250×10^{-7}	-1.640×10^{-7}
			$H_2{}^{209}Po_2$			
DC(UKB)	-7.244×10^{-4}	1.277×10^{-3}	3.043×10^{-4}	-3.086×10^{-6}	-3.395×10^{-4}	5.709×10^{-4}
LL(PC)	-8.694×10^{-7}	-9.953×10^{-7}	-9.422×10^{-7}	-3.130×10^{-7}	3.932×10^{-7}	5.248×10^{-7}

be decomposed into orbitals ψ_i^A calculated for each constituent atom according to

$$|\psi_k^{\text{mol}}\rangle = \sum_{i,A} |\psi_i^A\rangle c_{ik}^A + |\psi_k^{\text{pol}}\rangle, \quad (13)$$

where ψ_k^{pol} is a polarization contribution which by definition is strictly orthogonal to the chosen reference atomic orbitals.

Individual gradient elements of a property operator $\hat{\Omega}$ may then be decomposed into intra- and interatomic contributions, e.g.,

$$\langle \psi_{\text{HOMO}} | \hat{\Omega} | \psi_{\text{LUMO}} \rangle = \sum_{i,A} \sum_{j,B} c_{iA}^* c_{jB} \langle \psi_{iA} | \hat{\Omega} | \psi_{jB} \rangle$$
$$+ \text{ polarization.} \quad (14)$$

We find that the HOMO-LUMO gradient elements of the nuclear spin-dependent PNC operator (3) are dominated by intra-atomic contributions ($A = B$ above) from the selected Se center, in particular, the Se $4p_{1/2}$ atomic orbitals coupling with Se $4s_{1/2}$ and inner Se $s_{1/2}$ atomic orbitals. The atomic character of the gradient elements can be rationalized from the presence of the nuclear charge density ρ_{Se} in the operator which restricts integration to a small volume around the selected Se center. Perhaps somewhat less intuitive is the observation that the gradient elements of the property operator (9) associated with the external magnetic field are dominated by intra-atomic contributions as well, but this is readily understood by the presence of Dirac $\boldsymbol{\alpha}$ matrices in the operator coupling large and small components. Due to the atomic and very local nature of the small components the gradient elements are almost exclusively restricted to intra-atomic contributions, but this time from all centers. We find that the property gradient elements are dominated by intra-atomic coupling of $4p_{3/2}$ orbitals on the two Se centers. Note, however, that gradient elements coupling occupied positive-energy solutions to virtual negative-energy solutions will have a completely different character since the "small" components of negative-energy solutions are in fact large and delocalized.

Analyzing the values given in Table I we state that our Lévy-Leblond results are in excellent agreement with the NR results reported by Laubender and Berger,[16] except that the latter authors have consistently the wrong sign in their results.[38] The Lévy-Leblond PNC contributions are throughout largest in magnitude for the even-tempered basis sets and larger than the best (modified 5Z) basis sets used in Ref. 16 (results not shown here). In the previous nonrelativistic studies (Refs. 16–18) the electron spin-dependent term of the nonrelativistic PNC operator [second term in Eq. (7)] was omitted. By selectively deleting the spin-dependent terms of the corresponding property operator we have been able to investigate the validity of this approximation and indeed find no PNC contribution from this term. For the NR treatment of $H_2{}^{77}Se_2$ we have furthermore examined the difference between a point-charge model and a Gaussian model for the nucleus (Table III). The difference is less than 1%.

Table III shows results for the nuclei $X = {}^{17}$O, ^{33}S, ^{77}Se, ^{125}Te, and ^{209}Po in H_2X_2 for various dihedral angles. Only the results for the even-tempered basis sets are given. The PNC NMR shielding constant is bound to be zero at the dihedral angles of 0° and 180° due to mirror symmetry. The sinusoidal trait for the dihedral angles between 0° and 180° is typical and well known also for PNC energy differences or optical rotation. The zero crossing is usually found near 90°.

A direct comparison of the DC (UKB) and the Lévy-Leblond results in Table I shows that relativistic effects are negligible for $H_2{}^{17}O_2$ (6.064×10^{-9} ppm R versus 6.121×10^{-9} ppm NR). Also for $H_2{}^{33}S_2$ the inclusion of relativity is not necessary for qualitative results. The deviation is only

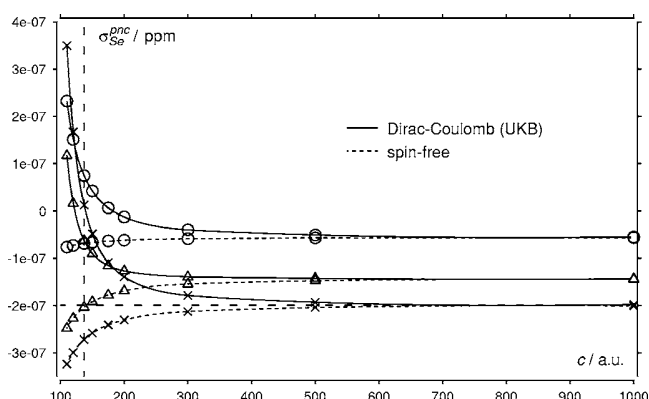TABLE IV. Components σ_{ii}^{PNC} of the PNC NMR shielding tensor (in ppm) of the nucleus ^{77}Se in the P enantiomer of H$_2$Se$_2$ for the dihedral angle of 45°. DC denotes the Dirac-Coulomb Hamiltonian, UKB the application of unrestricted kinetic balance, SF the use of the spin-free modified Dirac Hamiltonian, and LL the use of the Lévy-Leblond Hamiltonian, PC denotes a point-charge model for the nucleus.

	DC(UKB)	SF	LL(PC)
xx	-2.094×10^{-6}	-1.830×10^{-6}	-1.310×10^{-6}
zz	1.908×10^{-6}	1.220×10^{-6}	8.766×10^{-7}
$xx+zz$	-1.867×10^{-7}	-6.105×10^{-7}	-4.330×10^{-7}
yy	2.244×10^{-7}	-2.052×10^{-7}	-1.686×10^{-7}

2% (-9.977×10^{-8} ppm R versus -9.748×10^{-8} ppm NR). For H$_2$Se$_2$ and its heavier homologs on the other hand the discrepancy is evident. For these systems an appropriate inclusion of relativistic effects is substantial even for a qualitative treatment. For ^{77}Se, ^{125}Te, and ^{209}Po a relativistic treatment even changes the sign of the PNC NMR shielding constant at several dihedral angles, as seen in Table III. More insight can be gained by looking at the individual diagonal components of the PNC NMR shielding tensor, as shown for H$_2$^{77}Se$_2$ for the dihedral angle of 45° in Table IV. For all Hamiltonians the xx and zz components have opposite signs. The smaller yy component changes sign upon inclusion of spin-orbit interaction, but scalar relativistic effects are non-negligible as well.

In Fig. 1 we trace the PNC NMR shielding constant σ^{PNC}, as well as σ_{yy}^{PNC} and $(\sigma_{xx}^{PNC}+\sigma_{zz}^{PNC})/2$ of ^{77}Se in H$_2$Se$_2$ for the dihedral angle of 45°, at variable speeds of light c and with or without the inclusion of spin-orbit coupling. At large values of c the components go smoothly into the NR result. The spin-free results are negative for all values of c and decrease significantly for small values of c. However, this effect is completely quenched by a dramatic spin-orbit effect of opposite sign under ultrarelativistic conditions ($c < c_0 \approx 137.036$ a.u.). We indeed observe for ^{209}Po that whereas scalar relativistic effects alter the shielding constant from -9.953×10^{-7} to -5.246×10^{-6} ppm, spin-orbit coupling amplifies the value by three orders of magnitude to 1.277×10^{-3} ppm. This corresponds to a line splitting of about 30 mHz at a magnetic field of 1 T. This difference is larger than the maximal theoretical resolution of 6 mHz given in Ref. 11. We will in a future publication elucidate these mechanisms by means of projection analysis.

The opposing trends of scalar relativistic and spin-orbit

FIG. 1. Dependence of the PNC NMR shielding constant (in ppm) of the nucleus ^{77}Se in the P enantiomer of H$_2$Se$_2$ for the dihedral angle of 45° on the speed of light c (in a.u.). The symbols ($\times$, $\bigcirc$, and $\triangle$) represent the average trace $\sigma^{PNC}=(\sigma_{xx}^{PNC}+\sigma_{yy}^{PNC}+\sigma_{zz}^{PNC})/3$, σ_{yy}^{PNC}, and $(\sigma_{xx}^{PNC}+\sigma_{zz}^{PNC})/2$, respectively. The vertical dashed line represents the true speed of light $c_0 \approx 137$ a.u.; the horizontal dashed line shows the nonrelativistic limit (-1.993×10^{-7} ppm).

effects make it difficult to extract an overall scaling of the PNC NMR shielding constant with respect to nuclear charge Z. Table V shows the PNC contributions to the reduced (isotropic) NMR shielding constants $\gamma_A \sigma_A^{PNC}$ for the different nuclei as well as their Z scaling with respect to H$_2$O$_2$. The observed scaling may be compared with the predictions of Gorshkov et al.[12] based on atomic order of magnitude estimates. Our values confirm the predicted NR Z-scaling law 2 (here 2.4) which was also observed by Laubender and Berger.[16] Scalar relativistic effects provide significant enhancement, scaling as $Z^{4.7}$. For the heavier elements the PNC NMR shielding constants are, however, completely dominated by the large spin-orbit contribution, of opposite sign. According to Gorshkov et al.[12] the spin-orbit contribution should scale as Z^4. We indeed observe this scaling for H$_2$S$_2$, but for the heavier elements the scaling is even more important, rising to $Z^{7.1}$ for polonium. We believe that this signals the onset of second-order spin-orbit effects, not taken into account in the estimates of Gorshkov et al.[12] and known to lead to dramatic effects on bond lengths in molecules containing superheavy elements (see, for instance, Ref. 39). We will investigate this effect closer in a forthcoming study.

V. CONCLUSION

We have studied the importance of relativistic effects on the calculation of the PNC contribution to the (isotropic)

TABLE V. Reduced PNC NMR shielding constants $\gamma_A \sigma_A^{PNC}=\gamma_A(\sigma_{A,xx}^{PNC}+\sigma_{A,yy}^{PNC}+\sigma_{A,zz}^{PNC})/3$ (in 10^{-6} a.u.) of the nuclei $X=$O, S, Se, Te, and Po in the P enantiomers of H$_2$X$_2$ for the dihedral angle of 45°. Z is the number of protons, LL denotes the use of the Lévy-Leblond Hamiltonian, SR is the contribution of scalar relativity (SF-LL), and SO the effect of spin-orbit coupling (DC-SF). The numbers in parenthesis give the Z-scaling exponent with respect to H$_2$O$_2$.

Z	LL		SR		SO		SR+SO
8	-1.263×10^{-12}		-2.228×10^{-14}		3.404×10^{-14}		1.176×10^{-14}
16	-1.139×10^{-11}	(3.2)	-8.672×10^{-13}	(5.3)	5.996×10^{-13}	(4.1)	-2.677×10^{-13}
34	-5.842×10^{-11}	(2.6)	-2.081×10^{-11}	(4.7)	8.289×10^{-11}	(5.4)	6.208×10^{-11}
52	-1.522×10^{-10}	(2.6)	-1.443×10^{-10}	(4.7)	9.232×10^{-10}	(5.5)	7.789×10^{-10}
84	-4.188×10^{-10}	(2.5)	-1.788×10^{-09}	(4.8)	5.395×10^{-07}	(7.1)	5.377×10^{-07}

NMR shielding constants for the nuclei X = ^{17}O, ^{33}S, ^{77}Se, ^{125}Te, and ^{209}Po in H_2X_2 at the Hartree-Fock level. Comparing the results obtained within the Dirac-Coulomb formalism and approximate frameworks with either spin-orbit effects or all relativistic effects eliminated it has been observed that spin-orbit effects are substantial even for a qualitative treatment already for $H_2{}^{77}Se_2$, causing a sign change of the PNC contribution. This dramatic difference will be subject of a detailed analysis in a forthcoming paper where also correlation effects will be addressed. One may also consider the extension of the Dirac-Coulomb Hamiltonian by the Gaunt or Breit, thus introducing spin-other orbit coupling which may dampen the spin-orbit effect.

We have shown that the relativistic enhancement factor[40,41] scales approximately as Z^2 or higher, hence the overall Z scaling is much higher than previously anticipated. This scaling raises the hope for detecting parity violation effects in NMR properties of chiral molecules including heavy elements. Possible candidates are nuclei with nuclear spin $I=1/2$ to avoid large line-broadening effects from nuclear quadrupole coupling. Promising isotopes are therefore ^{187}Os,[42] ^{183}W, ^{117}Sn, and ^{119}Sn as chiral centers. A second possibility is to attach a heavy nucleus to a chiral center containing a light atom. Here the single center theorem of Hegstrom *et al.*[43] could enhance PNC effects in NMR properties.

We aim to apply the presented methodology for the study of more realistic systems. These are often considerably larger than the presented set of molecules which might require the use of more efficient (two-component) Hamiltonians. While the NMR technique seems to impose more experimental boundary conditions than high-resolution infrared spectroscopy experiments[11] it offers a possibly complementary approach for the first experimental verification.

ACKNOWLEDGMENTS

[1] T. Lee and C. Yang, Phys. Rev. **104**, 254 (1956).
[2] C. Wu, E. Ambler, R. Hayward, D. Hoppes, and R. Hudson, Phys. Rev. **105**, 1413 (1957).
[3] M. J. D. Macpherson, K. P. Zetie, R. B. Warrington, D. N. Stacey, and J. P. Hoare, Phys. Rev. Lett. **67**, 2784 (1991).
[4] D. M. Meekhof, P. Vetter, P. K. Majumder, S. K. Lamoreaux, and E. N. Fortson, Phys. Rev. Lett. **71**, 3442 (1993).
[5] N. H. Edwards, S. J. Phipp, P. E. G. Baird, and S. Nakayama, Phys. Rev. Lett. **74**, 2654 (1995).
[6] M. Quack, Angew. Chem., Int. Ed. **41**, 4618 (2002).
[7] R. Wesendrup, J. K. Laerdahl, R. N. Compton, and P. Schwerdtfeger, J. Phys. Chem. A **107**, 6668 (2003).
[8] R. Sullivan, M. Pyda, J. Pak, B. Wunderlich, J. R. Thompson, R. Pagni, H. Pan, C. Barnes, P. Schwerdtfeger, and R.Compton, J. Phys. Chem. A **107**, 6674 (2003).
[9] R. Berger, in *Relativistic Electronic Structure Theory*, edited by P. Schwerdtfeger (Elsevier, Amsterdam, Netherlands, 2004), Pt. 2, p. 188.
[10] J. Crassous, C. Chardonnet, T. Saue, and P. Schwerdtfeger, Org. Biomol. Chem. **3**, 13 (2005).
[11] J.-B. Robert and A. L. Barra, Chirality **13**, 699 (2001).
[12] V. G. Gorshkov, M. G. Kozlov, and L. N. Labzovskii, Sov. Phys. JETP **55**, 1042 (1982).
[13] A. L. Barra, J.-B. Robert, and L. Wiesenfeld, Phys. Lett. A **115**, 443 (1986).
[14] A. L. Barra, J.-B. Robert, and L. Wiesenfeld, Europhys. Lett. **5**, 217 (1988).
[15] A. L. Barra and J.-B. Robert, Mol. Phys. **88**, 875 (1996).
[16] G. Laubender and R. Berger, ChemPhysChem **4**, 395 (2003).
[17] A. Soncini, F. Faglioni, and P. Lazzeretti, Phys. Rev. A **68**, 033402 (2003).
[18] V. Weijo, P. Manninen, and J. Vaara, J. Chem. Phys. **123**, 054501 (2005).
[19] J. K. Laerdahl, P. Schwerdtfeger, and H. M. Quiney, Phys. Rev. Lett. **84**, 3811 (2000).
[20] P. Schwerdtfeger, J. K. Laerdahl, and C. Chardonnet, Phys. Rev. A **65**, 042508 (2002).
[21] R. Bast and P. Schwerdtfeger, Phys. Rev. Lett. **91**, 023001 (2003).
[22] P. Schwerdtfeger and R. Bast, J. Am. Chem. Soc. **126**, 1652 (2004).
[23] L. Visscher and T. Saue, J. Chem. Phys. **113**, 3996 (2000).
[24] T. Saue, Adv. Quantum Chem. **48**, 383 (2005).
[25] P. L. Anthony, R. G. Arnold, C. Arroyo *et al.* (SLAC E158 collaboration), Phys. Rev. Lett. **95**, 081601 (2005).
[26] R. N. Cahn and G. L. Kane, Phys. Lett. **71B**, 348 (1977).
[27] W. J. Marciano and A. I. Sanda, Phys. Rev. D **17**, 3055 (1978).
[28] T. N. Mukhamedjanov and O. P. Sushkov, Phys. Rev. A **73**, 032105 (2006).
[29] Ya. B. Zel'dovich, Sov. Phys. JETP **6**, 1184 (1958).
[30] T. Saue and H. J. Aa. Jensen, J. Chem. Phys. **118**, 522 (2003).
[31] H. J. Aa. Jensen, T. Saue, L. Visscher *et al.*, DIRAC, a relativistic *ab initio* electronic structure program, Release DIRAC04.0, 2004 (http://dirac.chem.sdu.dk).
[32] J. K. Laerdahl and P. Schwerdtfeger, Phys. Rev. A **60**, 4439 (1999).
[33] L. Visscher and K. G. Dyall, At. Data Nucl. Data Tables **67**, 207 (1997).
[34] L. Visscher, Theor. Chem. Acc. **96**, 68 (1997).
[35] G. A. Aucar, T. Saue, L. Visscher, and H. J. Aa. Jensen, J. Chem. Phys. **110**, 6208 (1999).
[36] M. Pecul, T. Saue, K. Ruud, and A. Rizzo, J. Chem. Phys. **121**, 3051 (2004).
[37] K. Faegri and T. Saue, J. Chem. Phys. **115**, 2456 (2001).
[38] R. Berger (private communication).
[39] T. Saue, K. Fægri, and O. Gropen, Chem. Phys. Lett. **263**, 360 (1996).
[40] M. A. Bouchiat and C. C. Bouchiat, Phys. Lett. **48B**, 111 (1974).
[41] M. A. Bouchiat and C. Bouchiat, J. Phys. (Paris) **35**, 899 (1974).
[42] R. Benn, E. Joussen, H. Lehmkuhl, F. López-Ortiz, and A. Rufinska, J. Am. Chem. Soc. **111**, 8754 (1989).
[43] R. A. Hegstrom, D. W. Rein, and P. G. H. Sandars, J. Chem. Phys. **73**, 2329 (1980).

Paper II

V. Weijo, R. Bast, P. Manninen, T. Saue, and J. Vaara

Methodological aspects in the calculation of parity-violating effects in nuclear magnetic resonance parameters

Methodological aspects in the calculation of parity-violating effects in nuclear magnetic resonance parameters

Ville Weijo
Laboratory of Physical Chemistry, Department of Chemistry, P.O. Box 55 (A.I. Virtasen aukio 1), University of Helsinki, FI-00014, Helsinki, Finland and Center for Theoretical Chemistry, Department of Chemistry, Aarhus University, DK-8000 Århus C, Denmark

Radovan Bast
Laboratoire de Chimie Quantique, Institut de Chimie de Strasbourg, LC3-UMR7177 CNRS/Université Louis Pasteur, 4 Rue Blaise Pascal, F-67000 Strasbourg, France

Pekka Manninen[a)]
Laboratory of Physical Chemistry, Department of Chemistry, P.O. Box 55 (A.I. Virtasen aukio 1), University of Helsinki, FI-00014 Helsinki, Finland

Trond Saue
Laboratoire de Chimie Quantique, Institut de Chimie de Strasbourg, LC3-UMR7177 CNRS/Université Louis Pasteur, 4 Rue Blaise Pascal, F-67000 Strasbourg, France

Juha Vaara
Laboratory of Physical Chemistry, Department of Chemistry, P.O. Box 55 (A.I. Virtasen aukio 1), University of Helsinki, FI-00014 Helsinki, Finland

We examine the quantum chemical calculation of parity-violating (PV) electroweak contributions to the spectral parameters of nuclear magnetic resonance (NMR) from a methodological point of view. Nuclear magnetic shielding and indirect spin-spin coupling constants are considered and evaluated for three chiral molecules, H_2O_2, H_2S_2, and H_2Se_2. The effects of the choice of a one-particle basis set and the treatment of electron correlation, as well as the effects of special relativity, are studied. All of them are found to be relevant. The basis-set dependence is very pronounced, especially at the electron correlated *ab initio* levels of theory. Coupled-cluster and density-functional theory (DFT) results for PV contributions differ significantly from the Hartree-Fock data. DFT overestimates the PV effects, particularly with nonhybrid exchange-correlation functionals. Beginning from third-row elements, special relativity is of importance for the PV NMR properties, shown here by comparing perturbational one-component and various four-component calculations. In contrast to what is found for nuclear magnetic shielding, the choice of the model for nuclear charge distribution—point charge or extended (Gaussian)—has a significant impact on the PV contribution to the spin-spin coupling constants. © *2007 American Institute of Physics*. [DOI: 10.1063/1.2436886]

I. INTRODUCTION

Energy differences between two enantiomers of chiral molecules caused by the parity-violating (PV) electroweak neutral current have been studied theoretically for 20 years. Since the early semiempirical studies,[1] computational methods have improved greatly. One-particle basis sets, inclusion of electron correlation, and the use of relativistic approaches have had a significant impact on the theoretical predictions. For instance, in the H_2O_2 molecule, the estimated PV energy difference has increased by almost two orders of magnitude from the first nonrelativistic (NR) *ab initio* studies[2] to modern nonrelativistic and relativistic coupled-cluster (CC) and multiconfigurational calculations.[3–6]

Parity-violating effects in nuclear magnetic resonance (NMR) spectral parameters,[7] that is, nuclear shielding and indirect spin-spin coupling, have also gained interest over the years. After the pioneering studies by Barra *et al.*[8,9] there has been a resurgence of interest.[10–12] These studies have been performed at the NR level and only the Hartree-Fock (HF) or density-functional theory (DFT) methods were used. While certain exchange-correlation functionals, such as hybrid B3LYP, reproduce quite well the CC results for PV energy differences,[6] it is not *a priori* certain whether present-day DFT is generally sufficient for treating electron correlation in PV contributions to other properties. For example, DFT and second-order perturbation theory give clearly different estimates on the contribution to the C–F stretching mode in CHFClBr.[13] A four-component relativistic study[14] found a significant difference between NR and relativistic PV NMR calculations in molecules containing third-row elements, in agreement with expectations based on PV energy differences. Very recently, a combined study of electron correlation and basis-set effects in dihedral molecules was pub-

lished by Laubender and Berger.[15] They calculated PV contributions to nuclear shielding using CC and complete active space self-consistent field (CASSCF) methods, as well as DFT for H_2O_2, H_2S_2, and H_2Se_2 molecules.

In this paper we systematically investigate all three aspects of quantum chemical calculations: the one-electron basis set, the choice of the Hamiltonian, and the N-electron model. Within the NR framework, three families of Dunning's correlation-consistent basis sets are benchmarked and the effects of electron correlation are systematically investigated using the HF method, two CC models, as well as DFT with both generalized gradient approximation and hybrid exchange-correlation functionals. Calculations are carried out for three dihedral molecules, H_2O_2, H_2S_2, and H_2Se_2. Our NR results are in line with the previous studies[10,11,15] concerning PV contributions to the nuclear shielding, although our dihedral angles are different and DFT methods are benchmarked here more extensively. The effect of special relativity is studied by performing one-component calculations based on the Breit-Pauli Hamiltonian[12] as well as four-component calculations based on the Dirac-Coulomb (DC) Hamiltonian, with and without spin-orbit (SO) coupling.[14] We further investigate the effect of the nuclear charge distribution by comparing point-charge and extended (Gaussian) models.

II. THEORY

A. Four-component relativistic parity-violating Hamiltonian

The four-component relativistic calculations are based on the Hamiltonian that describes the electroweak neutral-current interaction between electrons and nuclei,

$$H^{PV} = -\frac{G_F}{\sqrt{2}}(1-4\sin^2\theta_W)\sum_{i,K}\left[\frac{\lambda_K}{\gamma_K}\boldsymbol{\alpha}\cdot\mathbf{M}_K\rho_K(\mathbf{r}_i)\right], \quad (1)$$

where the indices i and K run over all electrons and nuclei, respectively. $G_F = 2.222\,54\times10^{-14}$ a.u. is the Fermi coupling constant, $\sin^2\theta_W = 0.2319$ is the Weinberg parameter, and $\boldsymbol{\alpha}$ are the well-known 4×4 Dirac matrices. For comparison with previous studies of PV NMR effects, we have set the nucleus-dependent parameters $\lambda_K \equiv 1.0$. For experimental predictions, these factors could be approximated and the results scaled accordingly. γ_K, $\mathbf{M}_K$, and $\rho_K(\mathbf{r}_i)$ are the magnetogyric ratio, the nuclear magnetic moment, and the normalized nuclear charge density of nucleus K, respectively.

In the formalism of response theory,[16] the elements of the PV contribution to the nuclear shielding tensor are given by the linear response function

$$\sigma_{K,\epsilon\tau}^{PV} = \frac{1}{\gamma_K}\frac{G_F\alpha}{2\sqrt{2}}(1-4\sin^2\theta_W)\langle\langle\, c\boldsymbol{\alpha}_\epsilon\rho_K(\mathbf{r}));c(\boldsymbol{\alpha}$$
$$\times\mathbf{r}_O)_\tau\rangle\rangle_{\omega=0}, \quad (2)$$

with $\mathbf{r}_O = \mathbf{r} - \mathbf{O}$. The first operator in Eq. (2) corresponds to the PV interaction and the second is the relativistic Zeeman operator. The gauge origin $\mathbf{O}$ is placed at the nucleus under study ($\mathbf{O}\equiv\mathbf{r}_K$). We have introduced the fine structure constant $\alpha=1/c_0$ such that when varying the speed of light c

$\to\infty$, the fixed $c_0\approx137.036$ a.u. guarantees the correct non-relativistic limit employed in the literature.

The PV contribution to the indirect spin-spin coupling between the nuclei K and L can be cast within the linear response theory framework in the form

$$J_{KL,\epsilon\tau}^{PV} = \frac{1}{2\pi}\frac{G_F\alpha^3}{\sqrt{2}}(1-4\sin^2\theta_W)[R_{KL,\epsilon\tau}+R_{LK,\tau\epsilon}], \quad (3)$$

with

$$R_{KL,\epsilon\tau} = \gamma_L\left\langle\!\!\left\langle\, c\boldsymbol{\alpha}_\epsilon\rho_K(\mathbf{r}));\frac{(\boldsymbol{\alpha}\times\mathbf{r}_L)_\tau}{r_L^3}\right\rangle\!\!\right\rangle_{\omega=0}. \quad (4)$$

Here, the latter operator in the linear response function is the relativistic hyperfine interaction in the approximation of pointlike distribution of the magnetic moment of nucleus L.

It is possible to eliminate either all relativistic effects[17] or, exclusively, the SO interaction within the four-component framework.[18,19] This is useful for the discussion and for making the distinction between scalar relativistic effects and SO coupling using the same basis set. Reference 20 contains a discussion on the separation of scalar relativistic and SO effects.

B. Perturbational one-component treatment

1. Leading-order contributions

At the nonrelativistic limit, the leading-order PV contributions to NMR shielding and coupling constants are obtained from the nuclear-spin-dependent part of the two-component PV Hamiltonian,[1,12,21]

$$H_K^{PV(2)} = \sum_\epsilon h_{K,\epsilon}^{PV(2)}I_{K,\epsilon},$$

$$h_{K,\epsilon}^{PV(2)} = -\frac{G_F\alpha}{2\sqrt{2}}\lambda_K(1-4\sin^2\theta_W)\sum_i[-i\nabla_{i,\epsilon},\delta(\mathbf{r}_{iK})]_+, \quad (5)$$

where the anticommutator $[A,B]_+ = AB+BA$ appears and I_K is the nuclear spin operator. The operator (5) can be combined with the relevant magnetic operators for the calculation of PV contributions to NMR parameters. The leading-order PV contribution to the isotropic nuclear shielding constant $\sigma_K^{PV} = \text{Tr}\,\boldsymbol{\sigma}_K^{PV}/3$ can be expressed as a linear response function[8,12]

$$\sigma_{K,\epsilon\tau}^{PV} = \frac{1}{\gamma_K}\langle\langle h_{K,\epsilon}^{PV(2)};h_{B_0,\tau}^{OZ}\rangle\rangle_{\omega=0}, \quad (6)$$

where

$$H_{B_0}^{OZ} = \sum_\tau h_{B_0,\tau}^{OZ}B_{0,\tau} \quad (7)$$

is the NR orbital Zeeman interaction, with

$$h_{B_0,\tau}^{OZ} = \frac{1}{2}\sum_i \ell_{iO,\tau}, \quad (8)$$

where ℓ_{iO} is the angular momentum operator of electron i with respect to the gauge origin. According to Soncini *et al.*[10] Eq. (6) covers the leading-order contribution if the gauge origin is placed at the nucleus in question.

PV contributions to the indirect spin-spin coupling constant $J_{KL}^{PV} = \mathrm{Tr}\, \mathbf{J}_{KL}^{PV}/3$ can also be written as linear response functions. The leading-order correction is a combination of the orbital hyperfine paramagnetic nuclear spin-electron orbit (PSO) operator,[8,12]

$$H_K^{PSO} = \sum_\tau I_{K,\tau} h_{K,\tau}^{PSO}, \quad h_{K,\tau}^{PSO} = \alpha^2 \gamma_K \sum_i \frac{\ell_{iK,\tau}}{r_{iK}^3}, \quad (9)$$

and the PV term in Eq. (5), giving rise to

$$J_{KL,\epsilon\tau}^{PV} = \frac{1}{2\pi} [\langle\langle h_{K,\epsilon}^{PV(2)}; h_{L,\tau}^{PSO} \rangle\rangle_{\omega=0} + \langle\langle h_{L,\tau}^{PV(2)}; h_{K,\epsilon}^{PSO} \rangle\rangle_{\omega=0}]. \quad (10)$$

Other leading-order contributions do not contribute to the isotropic part of the tensor.[12]

2. Higher-order contributions to shielding

The operator combinations that lead to beyond-leading-order relativistic PV contributions within the Breit-Pauli framework have been listed for nuclear shielding and indirect spin-spin coupling in Ref. 12. Some of the higher-order terms of indirect spin-spin coupling are explicitly divergent in the approximation of pointlike nuclear magnetic moment, and some of the contributions to both nuclear shielding and spin-spin coupling contain divergent operator contributions such as two delta functions located at the same nucleus. Strictly speaking, no well-defined values can be found for these terms at the limit of large uncontracted basis sets.[22]

Due to the inherent problems described above, the treatment of higher-order contributions by the perturbational approach cannot be complete. We presently focus on scalar relativistic corrections to the PV shielding expression of Eq. (6) as well as on the SO correction, three terms of a total of 12 in the next-to-leading-order PV contributions.[12] The presently considered scalar relativistic corrections, namely, mass-velocity (mv) and one-electron Darwin terms, contribute through the following quadratic response functions:

$$\sigma_{K,\epsilon\tau}^{PV,mv} = \frac{1}{\gamma_K} \langle\langle h_{K,\epsilon}^{PV(2)}; h_{B_0,\tau}^{OZ}, h^{mv} \rangle\rangle_{\omega_1=0,\omega_2=0} \quad (11)$$

and

$$\sigma_{K,\epsilon\tau}^{PV,Darwin} = \frac{1}{\gamma_K} \langle\langle h_{K,\epsilon}^{PV(2)}; h_{B_0,\tau}^{OZ}, h^{Darwin} \rangle\rangle_{\omega_1=0,\omega_2=0}, \quad (12)$$

where

$$h^{mv} = -\frac{1}{8} \alpha^2 \sum_i \nabla_i^2, \quad h^{Darwin} = \frac{\pi}{2} \alpha^2 \sum_{i,N} Z_N \delta(\mathbf{r}_{iN}). \quad (13)$$

It should be noted that the response functions in both Eqs. (11) and (12) are, in principle, divergent, but it will be informative to evaluate their contributions when using contracted, medium-sized basis sets that cannot fully describe this divergence. The SO effect is included by using the one-electron field-free spin-orbit operator

TABLE I. Calculated equilibrium geometries for P-H_2X_2 (X=O, S, and Se). r_{KL} denotes the K-L distance (in a.u.), α the X-X-H angle (deg), and β the dihedral angle (deg). The experimental reference data (Refs. 28 and 29) are in parentheses.

Molecule	r_{XX}	r_{XH}	α	β
H_2O_2	2.761 (2.767)	1.826 (1.824)	99.85 (99.4)	112.16 (111.8)
H_2S_2	3.938 (3.895)	2.542 (2.536)	97.66 (97.51)	90.79 (90.76)
H_2Se_2	4.447	2.781	95.770	90.254

$$h_\tau^{SO} = \frac{1}{4} \alpha^2 g_e \sum_{i,K} \frac{Z_K}{r_{iK}^3} s_{i,\tau} \ell_{iK,\tau}, \quad (14)$$

where g_e is the electron gyromagnetic ratio and s_i is the electron spin. It contributes together with the orbital Zeeman and the electron spin-dependent part of the PV operator[12]

$$H_K^{PV(3)} = \sum_{\rho\sigma\tau} \varepsilon_{\rho\sigma} h_{K,\rho\sigma}^{PV(3)} I_{K,\tau},$$

$$h_{K,\rho\sigma}^{PV(3)} = i \frac{G_F \alpha}{\sqrt{2}} \lambda_K (1 - 4 \sin^2 \theta_W) \sum_i s_{i,\sigma}[-i\nabla_{i,\rho}, \delta(\mathbf{r}_{iK})]_-, \quad (15)$$

within the quadratic response function

$$\sigma_{K,\epsilon\tau}^{PV,SO} = \frac{1}{\gamma_K} \sum_{\rho\sigma} \varepsilon_{\epsilon\rho\sigma} \langle\langle h_{K,\rho\sigma}^{PV(3)}; h_{B_0,\tau}^{OZ}, h_\sigma^{SO} \rangle\rangle_{\omega_1=0,\omega_2=0}. \quad (16)$$

In the above expressions, $\varepsilon_{\alpha\beta\gamma}$ is the Levi-Civita symbol. Some of the other nondivergent response functions resulting from beyond-leading-order PV contributions[12] were evaluated during the course of the work, but these terms were found to be insignificant.

III. COMPUTATIONAL DETAILS

A. Geometries

Geometries were optimized at the coupled-cluster singles and doubles with noniterative triples [CCSD(T)] level of theory with augmented correlation-consistent polarized valence triple-zeta (aug-cc-pVTZ) basis sets[23–25] for H, O, and S. For Se, the Stuttgart energy-adjusted pseudopotential[26] with the related aug-cc-pVTZ valence basis set[27] was used. Equilibrium geometry parameters are detailed in Table I. The available experimental equilibrium geometries (Ref. 28 for H_2O_2 and Ref. 29 for H_2S_2) are listed for comparison. The computational geometries are in good agreement with the experiments, as expected at this level of theory.

B. Perturbational one-component calculations

The isotropic part of perturbational PV contributions to nuclear shielding and indirect spin-spin coupling were evaluated using the DALTON quantum chemistry program.[30]

The correlation-consistent polarized valence (cc-pVXZ),[23,24] sets augmented with diffuse functions (aug-cc-pVXZ), and correlation-consistent polarized

TABLE II. Effects of electron correlation to the leading-order parity-violating contributions to the nuclear shielding constants (10^{-10} ppm) and indirect spin-spin couplings (nHz). The basis sets used are cc-pwCV5Z for H_2O_2 and H_2S_2, as well as cc-pV5Z for H_2Se_2, unless otherwise noted.

Molecule	Property	HF	CC2	CCSD	B3LYP	BP86	PBE0	PBE
H_2O_2	σ^{PV}_{17O}	29.12	37.37	38.08	46.84	52.11	44.02	53.26
	$^1J^{PV}_{OH}$	0.0207	0.0156	0.0181	0.0232	0.0237	0.0227	0.0243
	$^2J^{PV}_{OH}$	0.1094	0.0881	0.0781	0.0982	0.0941	0.1009	0.0947
	$^3J^{PV}_{HH}$	0.0003	−0.0002	0.0006	0.0005	0.0005	0.0005	0.0005
	$^1J^{PV}_{OO}$	−0.4157	−0.3532	−0.3432	−0.4714	−0.4734	−0.4540	−0.4786
H_2S_2	σ^{PV}_{33S}	92.03	43.11[a]	60.00[a]	35.50	13.18	42.20	16.13
	$^1J^{PV}_{SH}$	−0.0077	−0.0094[a]	−0.0073[a]	−0.0068	−0.0063	−0.0073	−0.0063
	$^2J^{PV}_{SH}$	0.0385	0.0458[a]	0.0239[a]	0.0410	0.0461	0.0453	0.0461
	$^3J^{PV}_{HH}$	−0.0000	−0.0001[a]	−0.0000[a]	−0.0000	−0.0000	−0.0000	−0.0000
	$^1J^{PV}_{SS}$	−0.2454	−0.1085[a]	−0.1370[a]	−0.1253	−0.0903	−0.1540	−0.0949
H_2Se_2	σ^{PV}_{77Se}	256.13	102.59[b]	139.86[b]	116.78	60.54	128.64	68.57
	$^1J^{PV}_{SeH}$	−0.0190	−0.0272[b]	−0.0184[b]	−0.0118	−0.0101	−0.0147	−0.0101
	$^2J^{PV}_{SeH}$	0.0778	0.0952[b]	0.0270[b]	0.0631	0.0782	0.0824	0.0803
	$^3J^{PV}_{HH}$	−0.0000	−0.0002[b]	−0.0001[b]	−0.0000	−0.0000	−0.0000	−0.0000
	$^1J^{PV}_{SeSe}$	−6.6063	−2.5581[b]	−3.1805[b]	−3.0380	−1.9430	−3.7946	−2.0805

[a]These contributions are calculated with the cc-pwCVQZ basis set due to program limitations.
[b]These contributions are calculated with the cc-pVQZ basis set due to program limitations.

weighted core-valence basis sets[31] (cc-pwCVXZ) were used. Here X=D, T, Q, 5, and 6 denote double- to hextuple-zeta basis sets.

The wave-function-based methods used were the Hartree-Fock self-consistent field method as well as the approximate coupled-cluster singles and doubles[32] (CC2) and coupled-cluster singles and doubles (CCSD) models.[33] These methods form a hierarchy in both systematically increasing accuracy and computational cost. The PV contributions were also evaluated with DFT, using the BP86 (Ref. 34 and 35) and the nonempirical PBE (Ref. 36) functionals that represent the generalized gradient approximation (GGA). In addition, two hybrid functionals were employed: PBE0, which is constructed from PBE by adding one-fourth of HF exchange,[37] and the widely used Becke three-parameter hybrid functional (B3LYP).[38–40] The gauge origin was placed at the nucleus in question (^{17}O, ^{33}S, and ^{77}Se) during the calculations of the shielding contributions.

C. Four-component calculations

All four-component computations at the relativistic Dirac-Coulomb (DC) and spin-free (SF) as well as nonrelativistic Lévy-Leblond (LL) levels were carried out using the HF self-consistent field of theory with a development version of the DIRAC code.[41]

Even-tempered basis sets were used for O, S, and Se, as detailed and discussed in Ref. 14. They are based on the even-tempered family of sets developed by Lærdahl and Schwerdtfeger.[3] For H we used the uncontracted aug-cc-pVDZ basis. The basis-set convergence of PV contributions to nuclear shielding based on the DC Hamiltonian has been discussed elsewhere,[14] and we will presently only include the basis-set converged results for the purposes of comparison. In the DC calculations, the small-component basis set was generated using unrestricted kinetic balance. In the DC and SF calculations the (SS|SS) class of two-electron integrals

was eliminated in both the wave function optimization and linear response phases. Rotations between positive and negative energy orbitals have been suppressed in the linear response module. These approximations have been discussed earlier.[14] We used the same convergence criteria as in Ref. 14. The common gauge origin in the shielding terms was placed at the nucleus under study.

A Gaussian charge distribution was chosen as the nuclear model for the relativistic DC and SF calculations,[42] both in the optimization of the reference wave function and in the PV operator. For the four-component NR LL calculations, both point-charge and Gaussian models were used. It should be noted that the used relativistic hyperfine operator corresponds to a pointlike nuclear spin distribution regardless of the nuclear model employed in the PV operator.

IV. RESULTS AND DISCUSSION

A. Effects of electron correlation

1. Nuclear shielding

The leading-order PV shielding contributions are presented at the best applicable basis-set levels in Table II. Figure 1 illustrates the results as functions of the basis set. The HF results are in line with the earlier NR studies.[10,11,15] These results deviate significantly from those obtained by correlated methods, however. For H_2O_2, CC2 and CCSD produce quite similar results, which are in turn over 25% larger in magnitude than the HF data. For H_2S_2 and H_2Se_2, the difference is even larger, although this time in the opposite direction: The results of the CC methods are about one-half of what is obtained at the HF level. There is, however, a notable difference between CC2 and CCSD; i.e., the full inclusion of singles and doubles excitations is important. Of all the methods employed here, CCSD can be considered to be the most accurate. Our results are qualitatively similar to those of the previous study,[15] although it appears that elec-
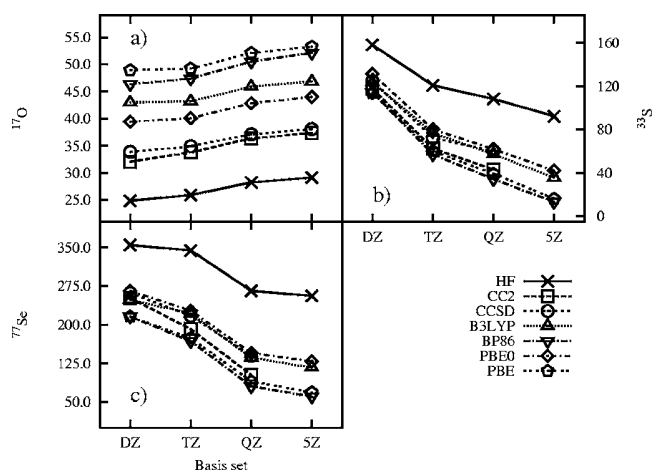
FIG. 1. Effect of basis-set quality in the parity-violating contribution to the nuclear shielding constants (in 10^{-10} ppm) of (a) ^{17}O in H_2O_2, (b) ^{33}S in H_2S_2, and (c) ^{77}Se in H_2Se_2 calculated with cc-pwCVXZ (cc-pVXZ for H_2Se_2) ($X=$D, T, Q, and 5) basis sets.

tron correlation effects are more prominent near the equilibrium geometry than at other specific values of dihedral angle.

Overall, from the DFT functionals used here, hybrid functionals are more accurate than GGAs. For H_2O_2, both hybrid functionals overestimate the magnitude of the effect by an amount almost of the size of the difference between HF and CCSD data. For H_2S_2 and H_2Se_2, however, B3LYP and PBE0 results agree rather well with CCSD, slightly underestimating and overestimating, respectively, the CCSD results. Both GGA functionals, on the other hand, clearly overestimate electron correlation effects in the present cases and cannot be considered reliable for this property. A similar inaccurate behavior has earlier been observed with the GGA BLYP functional.[15]

The dependence of the PV contribution to the isotropic ^{17}O NMR shielding constant on the dihedral angle of H_2O_2 obtained with different methods is presented in Fig. 2. The effect of electron correlation on the angular dependence is twofold. First, while the HF calculations show a symmetric sinusoidal curve with a zero crossing at 90°, electron correlation shifts this point to a smaller angle. The CC and DFT curves cross zero at almost identical values. Another effect of
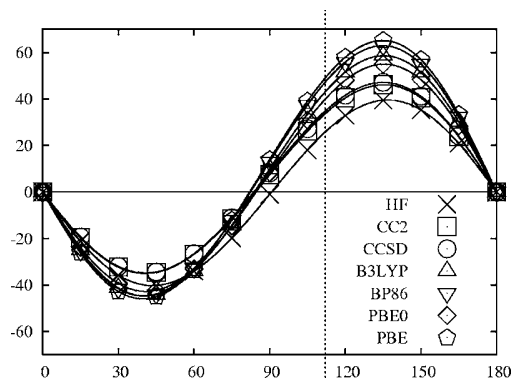
FIG. 2. Calculated dependence of the leading-order parity-violating contribution to NMR shielding constant (10^{-10} ppm) in H_2O_2 on the dihedral angle (deg) at different computational levels using the cc-pwCVTZ basis set.

electron correlation is the asymmetry of the curve. Whereas the HF results peak at almost the same height at angles 45° and 135°, the other methods produce clearly asymmetric curves. The CCSD method gives, for instance, the value of -34.4×10^{-10} ppm at 45° compared to 47.1×10^{-10} ppm at 135°. The DFT functionals produce even larger asymmetry effects. Again, the GGA functionals overestimate the effect as compared to hybrid functionals. The HF and CC data in the figure are similar to those found in previous studies.[11,15]

2. Spin-spin coupling contributions

In Table II we also investigate the effect of electron correlation to the PV contributions to indirect spin-spin coupling constants. The nuclei are ordered as $H_1-X_2-X_3-H_4$ ($X=^{17}O$, ^{33}S, and ^{77}Se), and $^1J_{XH}$, $^2J_{XH}$, $^3J_{HH}$, and $^1J_{XX}$ denote the X_2H_1, X_3H_1, H_1H_4, and X_2X_3 coupling constants, respectively. Figures 3–5 illustrate the PV contributions to spin-spin couplings in H_2O_2, H_2S_2, and H_2Se_2, respectively, as functions of the basis set.
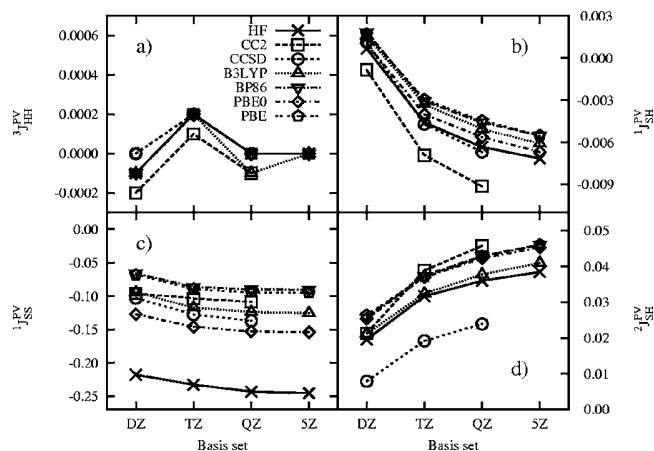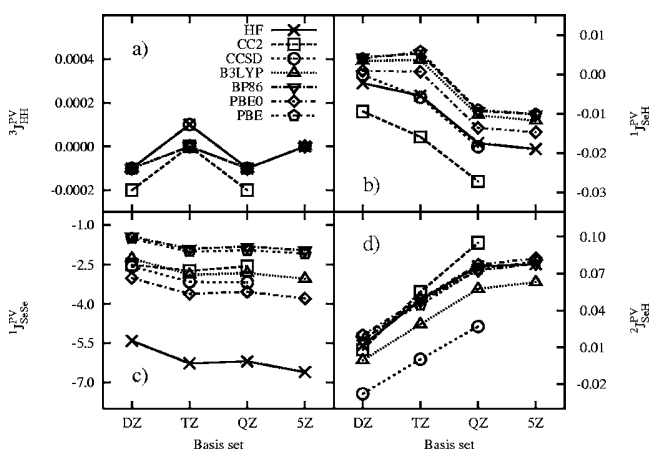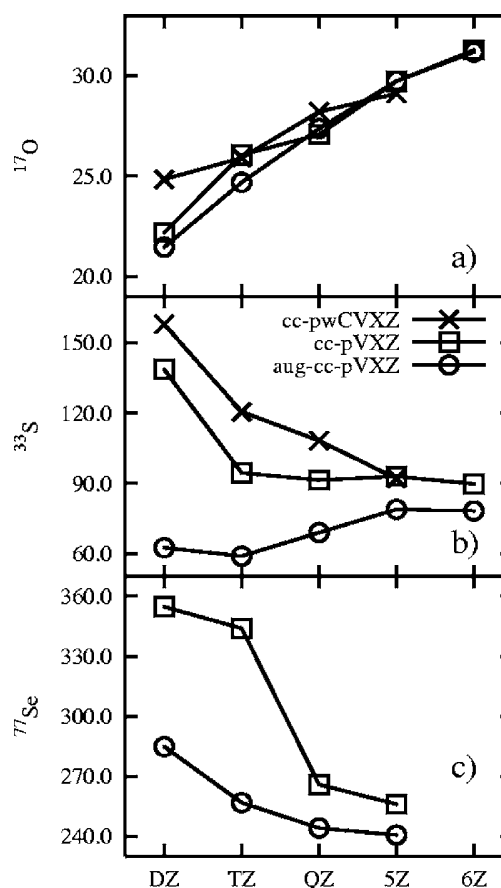

FIG. 3. Effect of basis-set quality in the parity-violating contribution to the spin-spin coupling constants (in nHz) of H_2O_2 molecule calculated with cc-pwCVXZ ($X=$D, T, Q, and 5) basis sets. (a) $^3J_{HH}$, (b) $^1J_{OH}$, (c) $^1J_{OO}$, and (d) $^2J_{OH}$.

FIG. 4. Effect of basis-set quality in the parity-violating contribution to the spin-spin coupling constants (in nHz) of H_2S_2 molecule calculated with cc-pwCVXZ ($X=$D, T, Q, and 5) basis sets. (a) $^3J_{HH}$, (b) $^1J_{SH}$, (c) $^1J_{SS}$, and (d) $^2J_{SH}$.

FIG. 5. Effect of basis-set quality in the parity-violating contribution to the spin-spin coupling constants (in nHz) of H_2Se_2 molecule calculated with cc-pVXZ (X=D, T, Q, and 5) basis sets. (a) $^3J_{HH}^{PV}$, (b) $^1J_{SeH}^{PV}$, (c) $^1J_{SeSe}^{PV}$, and (d) $^1J_{SeH}^{PV}$.

In H_2O_2 electron correlation generally decreases the magnitude of the PV spin-spin coupling contributions. The two CC methods give results similar to each other, apart from the case of the tiny $^3J_{HH}^{PV}$. Contrary to the case of PV nuclear shieldings, DFT is not able to reproduce the correlation contributions but gives results similar to the HF data. Comparing the CCSD and HF values, we find that the overall magnitude of the effect of electron correlation is 10%–30%.

For the two heavier molecules, H_2S_2 and H_2Se_2, correlation effects in the PV coupling contributions are dramatic and, in particular, the CC2 results are far from the CCSD data. For $^2J_{XH}^{PV}$ (X=S and Se), CC2 even gives correlation contributions of the opposite sign as compared to CCSD. Also in these cases, the DFT functionals fail in general, with the exceptions of $^1J_{SS}^{PV}$ and $^1J_{SeSe}^{PV}$, where B3LYP and PBE0 give results that are within 11% of the CCSD data.

B. Basis-set effects

1. Shielding contributions

The basis-set convergence in NR calculations of isotropic nuclear shielding constants is presented in Fig. 1. In the H_2O_2 molecule, the magnitude of the HF-level PV contribution increases only by a few percent when the basis set is enhanced from a QZ to a 5Z quality. Even the step from a DZ to a 5Z basis set leads maximally to an increase of 17% in magnitude (in the HF data). There are no qualitative differences between different correlation methods in their basis-set convergence behavior. The other two molecules, on the other hand, exhibit very different behaviors when moving upward in the basis-set hierarchy. In H_2S_2, practically no convergence is found in the studied range, and differences between various N-electron models are large. In addition, the GGA DFT contributions decrease in magnitude by approximately 60%, whereas the contributions by the hybrid DFT functionals decrease in magnitude by 38% (B3LYP) and 32% (PBE0). Contributions calculated with the two CC methods also show large differences between the TZ and QZ levels. The results are qualitatively similar in H_2Se_2, although the relative differences are smaller. In this case the

FIG. 6. Effect of basis-set family in the parity-violating contribution to the nuclear shielding constants (in 10^{-10} ppm) of (a) ^{17}O in H_2O_2, (b) ^{33}S in H_2S_2, and (c) ^{77}Se in H_2Se_2 calculated with cc-pVXZ, cc-pwCVXZ, and aug-cc-pVXZ (X=D, T, Q, 5, and 6) basis sets.

5Z contributions are fairly well converged at the HF level. Although the difference between TZ and QZ levels is 23%, the magnitude of the PV contribution decreases only by 4% between the QZ and 5Z quality basis sets. The DFT results are not quite as well converged when going from the QZ to the 5Z level; they decrease in magnitude by 25% and 11% with GGAs and hybrid functionals, respectively. Similar to H_2S_2, the convergence of the CCSD data follows the B3LYP results somewhat closely.

The role of the choice of the basis-set family is examined at the HF level of theory, with cc-pwCVXZ, cc-pVXZ, and aug-cc-pVXZ basis sets, as presented in Fig. 6. In H_2O_2 the differences between the basis-set families are not very large. The biggest difference occurs at the DZ level, and when the basis-set quality increases, the differences are expectedly reduced. At the 5Z level, the difference between cc-pwCV5Z and aug-cc-pV5Z basis sets is only 2%, the cc-pV5Z result being in between. At the 6Z level, the cc-pV6Z and aug-cc-pV6Z contributions are identical to within less than 1%. In H_2S_2, the differences between basis-set families are more pronounced; e.g., the aug-cc-pVDZ contribution is only 39% of the cc-pwCVDZ contribution. Again, the differences between the basis-set families become smaller with increasing X. At the 5Z level, the cc-pV5Z and cc-pwCV5Z contributions are identical to within 1% accuracy, whereas

TABLE III. Impact of the treatment of relativistic effects as well as the model used for the nuclear charge distribution to the parity-violation-induced isotropic NMR shielding constant of ^{17}O, ^{33}S, and ^{77}Se in H_2O_2, H_2S_2, and H_2Se_2, respectively, at the calculated equilibrium geometries at the Hartree-Fock level of theory. Results in 10^{-10} ppm.

	Wave function[a]	Nuclear model[b]	SR+SO[c]	SR[d]	NR
^{17}O	1-C(BP)	PC	29.17	30.13	29.12
	4-C	GM	31.67	34.05	32.90
	4-C	PC			32.86
^{33}S	1-C(BP)	PC	105.83	93.75	92.03
	4-C	GM	92.92	85.18	84.38
	4-C	PC			84.58
^{77}Se	1-C(BP)	PC	328.00	221.52	256.13
	4-C	GM	342.42	276.62	255.78
	4-C	PC			257.42

[a]Four-component (4-C) calculations using the even -tempered set detailed in Ref. 14 for O, S, and Se, as well as the uncontracted aug-cc-pVDZ set for H. Perturbational one-component (1-C) calculations with the Breit-Pauli Hamiltonian using the cc-pV5Z basis set.
[b]PC denotes point-charge and GM Gaussian charge distribution.
[c]Dirac-Coulomb (DC) calculations including scalar relativistic and spin-orbit interaction effects.
[d]Spin-free (SF) relativistic calculations including scalar relativistic effects.

the aug-cc-pV5Z contribution is only 86% of the cc-pwCV5Z contribution. The difference persists at the 6Z level, where the aug-cc-pV6Z contribution is 87% of the cc-pV6Z contribution. Hence, the augmentation with diffuse functions seems to have a larger impact than the presence of high-exponent primitives in the set. For H_2Se_2, no core-valence or 6Z sets are available. Similarly with H_2S_2, there is a notable difference between the augmented and nonaugmented sets at the 5Z level.

2. Spin-spin coupling contributions

As with the nuclear shielding contributions, a monotonic basis-set dependence in PV spin-spin coupling is found in H_2O_2, as illustrated in Fig. 3. The difference between the QZ and 5Z levels is around 10%, and thus the 5Z results cannot be considered fully converged.

A systematic trend is also found for H_2S_2, with the exception of the small $^3J_{HH}^{PV}$, as shown in Fig. 4. In both $^{33}S^1H$ coupling contributions, we observe a decreasing slope of the basis-set dependence starting from the TZ level. Convergence in $^1J_{SS}^{PV}$ is rather complete at all levels of theory, with differences of less than 8% between the TZ and QZ sets and of the order of 1% between the QZ and 5Z sets.

Finally, Fig. 5 summarizes the corresponding results for H_2Se_2. Both one- and two-bond $^{77}Se^1H$ couplings are far off at the DZ and TZ levels when compared to the larger basis sets. The combination of DFT and small basis sets can even give the wrong sign, as is the case in $^1J_{SeH}^{PV}$. While the difference between the QZ and 5Z quality basis sets in $^2J_{SeH}^{PV}$ calculated with HF is around 2%, the results with other methods differ by 7%–13% for both $^1J_{SeH}^{PV}$ and $^2J_{SeH}^{PV}$. In $^1J_{SeSe}^{PV}$, the basis-set dependence is slightly misleading with all the methods. The DZ quality basis sets somewhat underestimate the contribution, as compared to the larger basis sets. Comparison of TZ and QZ results may give a false impression of convergence, while the results at the 5Z level in fact deviate again more. Differences between QZ and 5Z quality basis sets are around 7% with all methods.

C. Relativistic effects

1. Shielding contributions

In order to discuss the effect of special relativity on the PV contribution to the NMR shielding, we have performed four-component relativistic DC and SF calculations at the HF level for H_2O_2, H_2S_2, and H_2Se_2 at the equilibrium geometries given in Table I. In addition, we have calculated the nonrelativistic Lévy-Leblond values both with an extended Gaussian and a point-charge model for the nuclei using the same even-tempered basis set, as in the DC and SF calculations for a consistent comparison. Scalar relativistic effects can then be identified as the difference between SF and NR results, and the contribution due to spin-orbit coupling as the difference between DC and SF. The results are given in Table III.

In H_2O_2 and H_2S_2, the results for the heavy-atom PV NMR shielding extrapolate the (rather slowly) convergent trend of the results obtained with the cc-pwCVXZ basis sets in one-component calculations. For the PV NMR shielding of Se, the NR results for the cc-pV5Z (256.13×10^{-10} ppm) and the even-tempered basis (257.42×10^{-10} ppm) are very close to each other. Scalar relativity increases the PV contribution in all systems, whereas spin-orbit coupling contributions are negative in H_2O_2 but positive in H_2S_2 and H_2Se_2. While the SF results are close to the NR HF contributions, spin-orbit coupling alters the contribution dramatically only in H_2Se_2 (342.42×10^{-10} ppm at the DC level compared to 255.78×10^{-10} ppm at the SF level). At the studied equilibrium geometry, spin-orbit coupling does not change the sign of the PV NMR shielding contrary to what was observed in Ref. 14.

We also evaluated selected higher-order terms in the shielding constant within the Breit-Pauli scheme at the HF level using the cc-pV5Z basis set. In Table III we have listed the combined contributions of scalar relativistic corrections [Eqs. (11) and (12)] in column scalar relativity (SR). Although divergent with large uncontracted basis sets, the divergent character of these terms is not yet visible at the cc-

TABLE IV. Effects of the relativistic treatment of parity-violation contributions to the spin-spin coupling constants of H_2O_2, H_2S_2, and H_2Se_2. Calculations were made at different levels of theory: four-component nonrelativistic with point-charge nuclear model (NR-PC), and the following levels with Gaussian nuclear charge distribution: four-component nonrelativistic, four-component spin-free, and four-component Dirac-Coulomb Hamiltonians. All values are in nHz. (See footnotes in Table III.)

Molecule	Coupling	SR+SO	SR	NR	NR-PC	1-C[a]
H_2O_2	$^1J_{OH}$	0.0258	0.0233	0.0039	0.0212	0.0207
	$^2J_{OH}$	0.1265	0.1224	0.1086	0.1140	0.1094
	$^3J_{HH}$	0.0003	0.0003	0.0003	0.0003	0.0003
	$^1J_{OO}$	−0.5037	−0.4792	−0.8882	−0.3732	−0.4157
H_2S_2	$^1J_{SH}$	−0.0028	−0.0085	−0.0226	−0.0105	−0.0077
	$^2J_{SH}$	0.0433	0.0425	0.0354	0.0402	0.0385
	$^3J_{HH}$	0.0000	0.0000	0.0001	0.0001	0.0000
	$^1J_{SS}$	−0.1565	−0.2692	−0.3068	−0.2085	−0.2454
H_2Se_2	$^1J_{SeH}$	0.1378	−0.0256	−0.0495	−0.0172	−0.0190
	$^2J_{SeH}$	0.0041	0.0882	0.0546	0.0349	0.0778
	$^3J_{HH}$	−0.0002	0.0000	0.0000	0.0000	0.0000
	$^1J_{SeSe}$	12.9293	−8.2238	−7.5414	−9.2640	−6.6063

[a]One-component Hartree-Fock calculation using the cc-pwCV5Z (cc-pV5Z for H_2Se_2) basis.

pV5Z level, and these corrections seem to be reasonable in H_2O_2 and H_2S_2. In H_2Se_2, on the other hand, these contributions have the wrong sign. The spin-orbit terms of Eq. (16) are included in the column SR+SO. Again, in H_2O_2 and H_2S_2 the corrections due to spin-orbit coupling are in relatively good agreement with four-component calculations. The spin-orbit correction is overestimated in H_2Se_2, but it seems that the combination of scalar relativistic and spin-orbit corrections coincides with the four-component results.

2. Spin-spin coupling contributions

The preceding conclusions are somewhat modified when considering the PV spin-spin coupling contributions presented in Table IV. The details of Hamiltonians are similar to those in the shielding contributions. The difference between NR and SF results is pronounced, especially in $^1J_{HX}^{PV}$ and $^1J_{XX}^{PV}$. In H_2O_2 and H_2S_2, the inclusion of SO contributions (the step from SF to DC) is in the same direction as scalar relativistic effects, smaller in magnitude in the former and larger in the latter. In H_2Se_2, spin-orbit coupling is utterly non-negligible and qualitatively changes $^1J_{SeH}^{PV}$, $^2J_{SeH}^{PV}$, and $^1J_{SeSe}^{PV}$. Relativistic effects in the $^3J_{HH}^{PV}$ contributions are totally negligible in all the studied systems.

Mainly due to the differences in the used basis sets, the four-component NR values using a pointlike nuclear model for the $^1J_{OO}^{PV}$ and $^1J_{SS}^{PV}$ are smaller and $^1J_{SeSe}^{PV}$ is considerably larger in magnitude as compared to one-component NR values.

D. Choice of the nuclear model

For PV NMR shieldings the difference between the results obtained with the Gaussian nuclear charge distribution and point-charge nuclei is negligible: the largest deviation (0.6%) appears for Se. However, the difference between the two models is significant for the PV contribution to spin-spin coupling, especially for the interchalcogen couplings (e.g., −0.888 nHz using the Gaussian model, as compared to

−0.373 nHz using point charge for $^1J_{OO}^{PV}$). In Table V we have studied the dependence of the leading-order nonrelativistic PV contribution to the $^1J_{OO}$ coupling constant on the exponent of the Gaussian nuclear charge distribution at the HF level.

The observed trend indicates that the chosen nuclear model is very important for the study of the PV contribution to spin-spin couplings. However, to observe the difference between a point-charge and a Gaussian distribution, high-exponent basis sets such as in the employed even-tempered set are needed. Without sufficiently high exponents for describing the wave function close to the nuclei, the difference between results obtained by these two nuclear models is negligible. For brevity, these test calculations are not shown here.

In passing, we note that the contribution from the finite nuclear model arises mainly from the treatment of the PV operator, while the nuclear model used in the optimization of the wave function has a minor role. For example, $^1J_{OO}^{PV} = −0.4634$ nHz is obtained for a finite nucleus in the SCF optimization but a pointlike charge model for the PV operator.

V. CONCLUSIONS

In our study all aspects of a quantum chemical calculation—the choice of the electron correlation method,

TABLE V. Effect of the exponent of the Gaussian nuclear charge distribution model on the parity-violating contribution (in nHz) to the indirect $^1J_{OO}$ spin-spin coupling constant in H_2O_2 at the calculated equilibrium geometry. A four-component Lévy-Leblond calculation.

Exponent	$^1J_{OO}$
$\alpha_0 = 5.863 \times 10^8$	−0.8882
$10\alpha_0$	−0.7920
$20\alpha_0$	−0.5796
$100\alpha_0$	−0.3733
$1000\alpha_0$	−0.3732
∞	−0.3732

the basis set, and the Hamiltonian—were found to affect the calculated PV contributions to NMR shielding and spin-spin couplings constant of H_2X_2 (X=O,S,Se) molecules. One-component nonrelativistic calculations were performed using the HF level of theory and different coupled-cluster models (CC2 and CCSD). Also DFT exchange-correlation functionals, BP86 and PBE belonging to the GGA category and B3LYP and PBE0 being hybrid functionals, were benchmarked against the CCSD results. Four-component calculations were performed at the HF level using different Hamiltonians.

The adequate treatment of electron correlation was found to be very important: the CCSD results can differ by 45% from the HF data. In the nuclear shielding calculations, all DFT functionals were found to overestimate electron correlation effects. In general, hybrid functionals perform much better than GGAs and produce accuracy approaching the CC methods. Therefore, our results are in partial disagreement with the conclusions of Laubender and Berger[15] on the performance of DFT: the hybrid DFT functionals perform well in this property. With spin-spin couplings the results show larger variation, from $^1J_{SS}^{PV}$, where the B3LYP data are within 10% from the CCSD results, to $^1J_{OO}^{PV}$, where all functionals produce an electron correlation effect with an opposite sign as compared to CCSD.

From the previous studies of PV contributions to NMR shieldings,[10–12,15] it is known that the choice of the one-particle basis set can be crucial. Our results confirm this observation. The basis-set dependence of both the PV nuclear shielding and spin-spin coupling is amplified by the use of a correlated electronic-structure method. The use of DFT and small basis set can even result in a wrong sign in the PV spin-spin coupling contributions. Also, the rate of basis-set convergence is, in general, worse with correlated methods than with HF. Our study indicates that specially tailored basis sets should be used. Their quality may be judged by studying the convergence of property matrix elements for individual atoms. Unfortunately, this may lead to the use of very large basis sets—both in the exponent range and the l values covered—for even qualitative estimates. This makes the study of these effects unfeasible for very large systems.

Relativistic effects do not appear to play a major role in the PV contribution to the nuclear shielding constant in molecules containing only light elements, here H_2O_2 and H_2S_2. For H_2Se_2, four-component relativistic HF calculations with the spin-free Hamiltonian produce results similar to those of the nonrelativistic HF calculations, but the effect of the spin-orbit interaction can be comparable in size to the effect of electron correlation. In the case of indirect spin-spin coupling, the conclusions are more varied. The most significant deviation between the four-component Dirac-Coulomb and nonrelativistic HF calculations was, not surprisingly, found for H_2Se_2, where relativity changes the magnitude of $^1J_{SeSe}^{PV}$ by 40% and, most importantly, changes its sign. Only the $^3J_{HH}^{PV}$ contributions are practically unaffected by relativistic effects in all systems.

We found the choice of the nuclear model—point-charge or extended (Gaussian) charge distribution—to have a sig-nificant impact on the parity-violating contribution to indirect spin-spin couplings. In contrast to what is found for PV contributions to nuclear magnetic shielding, the pointlike nuclear charge distribution is an oversimplified model for the calculation of PV spin-spin couplings.

ACKNOWLEDGMENTS

[1] R. A. Hegstrom, D. W. Rein, and P. G. H. Sandars, J. Chem. Phys. **73**, 2329 (1980).
[2] S. F. Mason and G. E. Tranter, Chem. Phys. Lett. **94**, 34 (1983).
[3] J. K. Lærdahl and P. Schwerdtfeger, Phys. Rev. A **60**, 4439 (1999).
[4] J. Thyssen, J. K. Lærdahl, and P. Schwerdtfeger, Phys. Rev. Lett. **85**, 3105 (2000).
[5] R. Berger and M. Quack, ChemPhysChem **1**, 57 (2000).
[6] A. C. Hennum, T. Helgaker, and W. Klopper, Chem. Phys. Lett. **354**, 274 (2002).
[7] *Calculation of NMR and EPR Parameters: Theory and Applications*, edited by M. Kaupp, M. Bühl, and V. G. Malkin (Viley-VCH, Weinheim, 2004).
[8] A. L. Barra, J. B. Robert, and L. Wiesenfeld, Phys. Lett. A **115**, 443 (1986).
[9] A. L. Barra, J. B. Robert, and L. Wiesenfeld, Europhys. Lett. **5**, 217 (1988).
[10] A. Soncini, F. Faglioni, and P. Lazzeretti, Phys. Rev. A **68**, 033402 (2003).
[11] G. Laubender and R. Berger, ChemPhysChem **4**, 395 (2003).
[12] V. Weijo, P. Manninen, and J. Vaara, J. Chem. Phys. **123**, 054501 (2005).
[13] P. Schwerdtfeger, T. Saue, J. N. P. van Stralen, and L. Visscher, Phys. Rev. A **71**, 012103 (2005).
[14] R. Bast, P. Schwerdtfeger, and T. Saue, J. Chem. Phys. **125**, 064504 (2006).
[15] G. Laubender and R. Berger, Phys. Rev. A **74**, 032105 (2006).
[16] J. Olsen and P. Jørgensen, J. Chem. Phys. **82**, 3235 (1985); in *Modern Electronic Structure Theory, Part II*, edited by D. R. Yarkony (World Scientific, Singapore, 1995).
[17] J.-M. Lévy-Leblond, Commun. Math. Phys. **6**, 286 (1967).
[18] L. Visscher and T. Saue, J. Chem. Phys. **113**, 3996 (2000).
[19] T. Saue, Adv. Quantum Chem. **48**, 383 (2005).
[20] L. Visscher and E. van Lenthe, Chem. Phys. Lett. **306**, 357 (1999).
[21] M. Bouchiat and C. Bouchiat, J. Phys. (Paris) **35**, 899 (1974).
[22] A. Velenik, T. Živković, W. H. de Jeu, and J. N. Murrel, Mol. Phys. **18**, 693 (1970).
[23] T. H. Dunning, Jr., J. Chem. Phys. **90**, 1007 (1989).
[24] D. E. Woon and T. H. Dunning, Jr., J. Chem. Phys. **98**, 1358 (1993).
[25] R. A. Kendall, T. H. Dunning, Jr., and R. J. Harrison, J. Chem. Phys. **96**, 6769 (1992).
[26] A. Bergner, M. Dolg, W. Küchle, H. Stoll, and H. Preuß, Mol. Phys. **80**, 1431 (1993).
[27] J. M. L. Martin and A. Sundermann, J. Chem. Phys. **114**, 3408 (2001).
[28] J. Koput, J. Mol. Spectrosc. **119**, 438 (1986).
[29] C. J. Marsden and B. J. Smith, J. Phys. Chem. **92**, 347 (1988).
[30] DALTON, Release 2.0, a molecular electronic structure program, 2005, see http://www.kjemi.uio.no/software/dalton/dalton.html

[31] K. A. Peterson and T. H. Dunning, Jr., J. Chem. Phys. **117**, 10548 (2002).

[32] O. Christiansen, H. Koch, and P. Jørgensen, Chem. Phys. Lett. **243**, 409 (1995).

[33] G. D. Purvis and R. J. Barlett, J. Chem. Phys. **76**, 1910 (1982).

[34] J. P. Perdew, Phys. Rev. B **33**, 8822 (1986); Phys. Rev. B **34**, 7406(E) (1986).

[35] A. D. Becke, Phys. Rev. A **38**, 3098 (1988).

[36] J. P. Perdew, K. Burke, and M. Ernzerhof, Phys. Rev. Lett. **77**, 2865 (1996).

[37] C. Adamo, G. E. Scuseria, and V. Barone, J. Chem. Phys. **111**, 2889 (1999).

[38] A. D. Becke, J. Chem. Phys. **98**, 5648 (1993).

[39] C. Lee, W. Yang, and R. G. Parr, Phys. Rev. B **37**, 785 (1988).

[40] P. J. Stephens, F. J. Devlin, C. F. Chabalowski, and M. J. Frisch, J. Phys. Chem. **98**, 11623 (1994).

[41] DIRAC Release 4.0 a relativistic *ab initio* electronic structure program, 2004, see http://dirac.chem.sdu.dk

[42] L. Visscher and K. G. Dyall, At. Data Nucl. Data Tables **67**, 207 (1997).

Paper III

R. Bast, A. Heßelmann, P. Sałek, T. Helgaker, and T. Saue

Static and frequency-dependent dipole-dipole polarizabilities of all closed-shell atoms up to radium: a four-component relativistic density functional theory study

Static and frequency-dependent dipole-dipole polarizabilities of all closed-shell atoms up to Radium: a four-component relativistic DFT study

Radovan BAST, Andreas HEßELMANN, Paweł SAŁEK, Trygve HELGAKER, Trond SAUE

Part III

Notes

Parity-violating electronic neutral weak Hamiltonian

There is no question that there is an unseen world. The problem is,
how far is it from midtown and how late is it open?

Woody Allen, *Examining Psychic Phenomena* in *Without Feathers*

The route to the effective 4-component relativistic parity-violating (PV) electronic neutral weak Hamiltonian for molecular calculations is a long journey "through the beautiful forest of particle physics, gauge theories, and quantum field theory"[256] which is far beyond the scope of this short note. A very useful guide fur such an expedition can be found in Ref. 256 together with the bibliography for more detailed excursions. Also Ref. 52 has been used for this note.

Almost the home strait of Ref. 256 is the starting point of this note: the Lagrangian density of the neutral weak electron-nucleon (e-nuc) contact interaction in the low-energy (zero momentum transfer) limit,

$$\mathcal{L}_{\text{int}}^{\text{e-nuc}} = \frac{G_{\text{F}}}{\sqrt{2}} \, j_\mu^{\text{e}} \, j^{\mu,\text{nuc}} \, , \tag{A.1}$$

with the Fermi coupling constant $G_{\text{F}} = 2.22254 \cdot 10^{-14} \, E_{\text{h}} a_{\text{o}}^3$ and an implicit sum over all nucleons (nuc), that is, all protons (p) and neutrons (n). Being a contact interaction, attention can be restricted to one atomic center, say nucleus K, with Z_K protons and N_K neutrons. At this stage, the generalized 4-currents j_μ can be regarded as linear combinations of the generalized densities $\psi^\dagger M \psi$ with M denoting the Dirac matrices (see Tabs. 1.2 and 1.3). The Dirac matrices and the associated currents can be classified according to the transformation under parity reversal as polar vectors (V) and pseudoscalars (P) which change sign, and as axial vectors (A) and scalars (S) which do not.

It can be shown[52] that only V–A (polar vector minus axial vector) Fermi coupling is of relevance and the corresponding electron and nucleon 4-currents that appear in Eq. A.1 are

given by

$$j_\mu^e = j_{\mu,V}^e - j_{\mu,A}^e \qquad (A.2)$$
$$= C_V^e \psi_e^\dagger (\boldsymbol{\alpha}, 1_{4\times4}) \psi_e - C_A^e \psi_e^\dagger (\boldsymbol{\Sigma}, \gamma^5) \psi_e$$

$$j_\mu^{nuc} = j_{\mu,V}^{nuc} - j_{\mu,A}^{nuc} \qquad (A.3)$$
$$= C_V^{nuc} \psi_{nuc}^\dagger (\mathbf{0}, 1_{2\times2}) \psi_{nuc} - C_A^{nuc} \psi_{nuc}^\dagger (\boldsymbol{\sigma}, 0) \psi_{nuc}.$$

In Eq. A.3 the so-called "nonrelativistic approximation"[52] has been invoked which means to neglect of the nucleon small component bispinors. For the Dirac matrices α, Σ, and γ^5, see Section 1.2, p. 31, for their explicit form.

Before giving the explicit coupling coefficients C of Eqs. A.2 and A.3 and actually coupling the electron and nucleon 4-currents, it is worthwhile to pause for a moment and study the transformation under the parity operation of the space-like components $(\boldsymbol{\alpha}, \boldsymbol{\Sigma}, \boldsymbol{\sigma})$ and time-like components $(1_{4\times4}, \gamma^5, 1_{2\times2})$ and their combinations: $\boldsymbol{\alpha}$ transforms as the coordinates which change sign (V), matrices $\boldsymbol{\Sigma}$ and $\boldsymbol{\sigma}$ transform as rotations (A), $1_{4\times4}$ and $1_{2\times2}$ as S, and finally γ^5 is the pseudoscalar chirality matrix (P). The four possible electron-nucleon combinations are

$$j_{\mu,V}^e j_V^{\mu,nuc} \qquad \text{which transforms as} \qquad S$$
$$-j_{\mu,V}^e j_A^{\mu,nuc} \qquad V$$
$$-j_{\mu,A}^e j_V^{\mu,nuc} \qquad P$$
$$j_{\mu,A}^e j_A^{\mu,nuc} \qquad A$$

The parity-even S and A combinations can be dropped being practically unobservable due to the minute size of the Fermi coupling constant G_F in Eq. A.1. Only the parity-odd V and P combinations shall be considered in the following. They are tiny, too. However, they distinguish themselves from all other fundamental interactions which makes them observable in a suitable experiment.

Returning to Eqs. A.2 and A.3, the electron (e), up quark (u), and down quark (d) coupling coefficients[52, 256] read as

$$C_V^e = 1 - 4\sin^2\theta_W \tag{A.4}$$

$$C_V^u = 1 - \frac{8}{3}\sin^2\theta_W \tag{A.5}$$

$$C_V^d = 1 - \frac{4}{3}\sin^2\theta_W \tag{A.6}$$

$$C_A^e = -\frac{1}{2} \tag{A.7}$$

$$C_A^u = \frac{1}{2} \tag{A.8}$$

$$C_A^d = -\frac{1}{2}, \tag{A.9}$$

with the Weinberg parameter $\sin^2\theta_W = 0.2397(13)$.[242] The p and n coupling coefficients are approximately[52] given by*

$$C_V^p = 2C_V^u + C_V^d \tag{A.10}$$

$$C_V^n = 2C_V^d + C_V^u, \tag{A.11}$$

with corresponding relations for C_A^p and C_A^p since protons consist of two u and one d and neutrons of two d and one u.

The nucleon V-currents can be combined (added up) to the weak charge Q_w^K which allows us to express the V current for nucleus K by

$$j_{\mu,V}^K = (\mathbf{0}, Q_w^K \rho_K), \tag{A.12}$$

where ρ_K is the nuclear charge distribution (typically modeled by a Gaussian distribution), and the weak charge Q_w^K is given by

$$Q_w^K = (2Z_K + N_K)C_V^u - (2N_K + Z_K)C_V^d \tag{A.13}$$
$$= Z_K(1 - 4\sin^2\theta_W) - N_K.$$

In contrast to $j_{\mu,V}^K$, the combination of nucleon A-currents to form $j_{\mu,A}^K$ is less evident.[256] Typically, $j_{\mu,A}^K$ is approximately given by

$$j_{\mu,A}^K = (\lambda_K \mathbf{I}_K \rho_K, 0) = (\frac{\lambda_K}{\gamma_K}\mathbf{M}_K\rho_K, 0), \tag{A.14}$$

with the nucleus-dependent form factor λ_K on the order of unity[256] and chosen as $\lambda_K \equiv 1$ in actual calculations. The nuclear spin distribution is approximated by the nuclear Gaussian charge

---

* Quark currents are replaced by nucleon currents, weighted by the number of valence quarks present.[52]

distribution scaled with the nuclear spin $\mathbf{I}_K$, or equivalently, scaled with the nuclear magnetic moment $\mathbf{M}_K$ and divided by the magnetogyric ratio γ_K.

We have gathered all ingredients to form the parity-odd combinations of electron and nucleon 4-currents (Eqs. A.2 and A.3) and obtain the effective one-electron Hamiltonians

$$\hat{h}_{i,A} = -\frac{G_F C_A^e}{\sqrt{2}} \gamma^5 \sum_K Q_w^K \rho_K(\mathbf{r}_i) \tag{A.15}$$

and

$$\hat{h}_{i,V} = -\frac{G_F C_V^e}{\sqrt{2}} \boldsymbol{\alpha} \cdot \sum_K \frac{\lambda_K}{\gamma_K} \mathbf{M}_K \rho_K(\mathbf{r}_i), \tag{A.16}$$

respectively, with C_A^e and C_V^e given in Eqs. A.7 and A.4. The first Hamiltonian ($\hat{h}_{i,A}$) is employed in calculations of PV energy differences between enantiomers. The second Hamiltonian ($\hat{h}_{i,A}$) is employed in calculations of PV effects on nuclear magnetic resonance parameters.

The remaining part of this note will consider the NR limit of $\hat{h}_{i,A}$ and $\hat{h}_{i,A}$ for reference. For this we employ the NR limit of the small component bispinor (see for instance Ref. 64),

$$\lim_{c \to \infty} 2mc \, |\psi^S\rangle = (\boldsymbol{\sigma} \cdot \mathbf{p}) |\psi^L\rangle, \tag{A.17}$$

and evaluate expectation values of $\hat{h}_{i,A}$ and $\hat{h}_{i,A}$ (Eqs. A.15 and A.16). To avoid a overloaded notation the expectation values are written using one-electron spinors $|\psi_i\rangle$, however without loss of generality.

For the expectation value of $\hat{h}_{i,A}$ we focus on the expectation value of $\gamma^5 \rho_K(\mathbf{r}_i)$ given by

$$\langle \psi_i | \gamma^5 \rho_K(\mathbf{r}_i) | \psi_i \rangle = \langle \psi_i^L | 1_{2\times2} \rho_K(\mathbf{r}_i) | \psi_i^S \rangle + \langle \psi_i^S | 1_{2\times2} \rho_K(\mathbf{r}_i) | \psi_i^L \rangle \tag{A.18}$$

$$= \langle \psi_i^L | [1_{2\times2}\rho_K(\mathbf{r}_i), (\boldsymbol{\sigma} \cdot \mathbf{p})]_+ | \psi_i^L \rangle$$

and the NR limit of $c\hat{h}_{i,A}$ can be identified as

$$\lim_{c \to \infty} c\hat{h}_{i,A} = -\frac{1}{2m} \frac{G_F C_A^e}{\sqrt{2}} \sum_K Q_w^K [1_{2\times2}\rho_K(\mathbf{r}_i), (\boldsymbol{\sigma} \cdot \mathbf{p})]_+. \tag{A.19}$$

Here $[\cdots]_+$ denotes the anticommutator.

For the expectation value of $\hat{h}_{i,V}$ we focus on the expectation value of $(\boldsymbol{\alpha} \cdot \mathbf{M}_K \rho_K(\mathbf{r}_i))$ given by

$$\langle \psi_i | \boldsymbol{\alpha} \cdot \mathbf{M}_K \rho_K(\mathbf{r}_i) | \psi_i \rangle = \langle \psi_i^L | [(\boldsymbol{\sigma} \cdot \mathbf{M}_K \rho_K(\mathbf{r}_i)), (\boldsymbol{\sigma} \cdot \mathbf{p})]_+ | \psi_i^L \rangle. \tag{A.20}$$

The two scalar products that constitute the anticommutator in Eq. A.20 read as

$$(\boldsymbol{\sigma} \cdot \mathbf{M}_K \rho_K(\mathbf{r}_i))(\boldsymbol{\sigma} \cdot \mathbf{p}) = \mathbf{M}_K \rho_K(\mathbf{r}_i) \cdot \mathbf{p} + i\boldsymbol{\sigma} \cdot (\mathbf{M}_K \rho_K(\mathbf{r}_i) \times \mathbf{p}) \tag{A.21}$$

$$(\boldsymbol{\sigma} \cdot \mathbf{p})(\boldsymbol{\sigma} \cdot \mathbf{M}_K \rho_K(\mathbf{r}_i)) = \mathbf{p} \cdot \mathbf{M}_K \rho_K(\mathbf{r}_i) + i\boldsymbol{\sigma} \cdot (\mathbf{p} \times \mathbf{M}_K \rho_K(\mathbf{r}_i)), \tag{A.22}$$

where the Dirac identity (Eq. 0.2) has been used. The sum of the first right-hand side terms in Eqs. A.21 and A.22 can be written as

$$\mathbf{M}_K \rho_K(\mathbf{r}_i) \cdot \mathbf{p} + \mathbf{p} \cdot \mathbf{M}_K \rho_K(\mathbf{r}_i) = \mathbf{M}_K \cdot [\mathbf{p}, \rho_K(\mathbf{r}_i)]_+. \tag{A.23}$$

The sum of the remaining right-hand side terms in Eqs. A.21 and A.22 can be simplified using the Levi-Civita antisymmetric permutation symbol ϵ_{rst}:[*]

$$\begin{aligned}
\mathrm{i}\boldsymbol{\sigma} \cdot (\mathbf{M}_K \rho_K(\mathbf{r}_i) \times \mathbf{p}) & \tag{A.24} \\
+\mathrm{i}\boldsymbol{\sigma} \cdot (\mathbf{p} \times \mathbf{M}_K \rho_K(\mathbf{r}_i)) &= \mathrm{i}\epsilon_{lmn}\sigma_l M_{K,m}\rho_K(\mathbf{r}_i)p_n + \mathrm{i}\epsilon_{lnm}\sigma_l p_n \rho_K(\mathbf{r}_i)M_{K,m} \\
&= \mathrm{i}\epsilon_{nlm}\sigma_l M_{K,m}\rho_K(\mathbf{r}_i)p_n - \mathrm{i}\epsilon_{nlm}\sigma_l p_n \rho_K(\mathbf{r}_i)M_{K,m} \\
&= -\mathrm{i}(\boldsymbol{\sigma} \times \mathbf{M}_K) \cdot [\mathbf{p}, \rho_K(\mathbf{r}_i)].
\end{aligned}$$

Consequently, the NR limit of $c\hat{h}_{i,\mathrm{V}}$ can be identified as

$$\lim_{c \to \infty} c\hat{h}_{i,\mathrm{V}} = -\frac{1}{2m} \frac{G_\mathrm{F} C_\mathrm{V}^\mathrm{e}}{\sqrt{2}} \sum_K \frac{\lambda_K}{\gamma_K} \left\{ \mathbf{M}_K \cdot [\mathbf{p}, \rho_K(\mathbf{r}_i)]_+ - \mathrm{i}(\boldsymbol{\sigma} \times \mathbf{M}_K) \cdot [\mathbf{p}, \rho_K(\mathbf{r}_i)] \right\}. \tag{A.25}$$

---

[*] $\epsilon_{rst} = 1 (= 0)$ if rst is an even (odd) permutation of lmn, $\epsilon = 0$ if any index is repeated.

Calculation of various densities in the Kramers restricted basis

I am greatly relieved that the universe is finally explainable. I was beginning to think it was me.

Woody Allen, *Strung Out* in *Mere Anarchy*

This note describes the calculation of various densities in the Kramers restricted basis. This will be done for the operator M which shall represent one of the 16 Dirac matrices (see Section 1.3, p. 30). All other densities can then be constructed by linear combination of the appropriate densities $\psi^\dagger M \psi$. The matrix M consists of two 2×2 blocks and therefore $\psi^\dagger M \psi$ contains the two contributions

$$\psi^\dagger M \psi = f \psi^{L\dagger} M^{LX} \psi^X + g \psi^{S\dagger} M^{SY} \psi^Y, \tag{B.1}$$

where L represents the large and S the small component. The pair (X, Y) is then either (L, S) or (S, L), and f and g are scalar factors (which can be complex). The explicit reference to a point in space is omitted for notational ease.

It will be sufficient to discuss only the first right-hand side term in Eq. B.1

$$f \psi^{L\dagger} M^{LX} \psi^X = f \begin{bmatrix} \psi^{L\alpha\star} & \psi^{L\beta\star} \end{bmatrix} \begin{bmatrix} M^{LX}_{\alpha\alpha} & M^{LX}_{\alpha\beta} \\ M^{LX}_{\beta\alpha} & M^{LX}_{\beta\beta} \end{bmatrix} \begin{bmatrix} \psi^{X\alpha} \\ \psi^{X\beta} \end{bmatrix}, \tag{B.2}$$

which in the basis of Kramers paired fermion basis functions (AO basis) reads

$$f \psi^{L\dagger} M^{LX} \psi^X = f \Omega^{LX}_{\kappa\lambda} \Bigg[M^{LX}_{\alpha\alpha} D^{XL}_{\lambda\kappa} + M^{LX}_{\alpha\beta} D^{XL}_{\lambda\bar{\kappa}} \tag{B.3}$$

$$+ M^{LX}_{\beta\alpha} D^{XL}_{\bar{\lambda}\kappa} + M^{LX}_{\beta\beta} D^{XL}_{\bar{\lambda}\bar{\kappa}} \Bigg].$$

Here $\Omega^{MN}_{\kappa\lambda}$ is the orbital overlap distribution $\phi^{\dagger M}_{\kappa}\phi^{N}_{\lambda}$ and $D^{NM}_{\lambda\kappa}$ the corresponding AO density matrix (see Section 1.3, p. 32, for the definition of a Kramers paired basis). From now on a time reversal symmetric density matrix is assumed:

$$D = \begin{bmatrix} D_{\lambda\kappa} & D_{\lambda\bar{\kappa}} \\ -D^{\star}_{\lambda\bar{\kappa}} & D^{\star}_{\lambda\kappa} \end{bmatrix} = \begin{bmatrix} A & B \\ -B^{\star} & A^{\star} \end{bmatrix}. \tag{B.4}$$

This is not a restriction in practice since general matrices can be separated into time reversal symmetric and antisymmetric parts and an antisymmetric matrix can be converted into a symmetric one by extracting the imaginary phase (see Section 2.5, p. 57, for more details). For this, densities corresponding to time reversal antisymmetric Dirac matrices (Tab. 1.2) will be multiplied by the imaginary i. Eq. B.3 becomes then

$$f\psi^{L\dagger}M^{LX}\psi^{X} = f\Omega^{LX}_{\kappa\lambda}\bigg[M^{LX}_{\alpha\alpha}A^{XL} + M^{LX}_{\alpha\beta}B^{XL} \tag{B.5}$$
$$-M^{LX}_{\beta\alpha}B^{XL\star} + M^{LX}_{\beta\beta}A^{XL\star}\bigg].$$

The complex terms can be expressed using real and purely imaginary matrices. Tab. B.1 lists the necessary density matrix blocks and factors for the evaluation of densities corresponding to eight Dirac matrices. A multiplication with the β matrix can be achieved by switching the sign of factor g. It is now clear that all densities can be (and are) evaluated using one single routine which samples the appropriate density matrix blocks with the appropriate prefactors. For instance to obtain the components of the current density times the imaginary ifrom the velocity densities $\psi^{\dagger}i\boldsymbol{\alpha}\psi$, f and g have to be multiplied with $-ec$. The imaginary phase is introduced because the matrices α_x, α_y, and α_z are time reversal antisymmetric (see Tab. 1.4). Same is done for the matrices Σ_x, Σ_y, and Σ_z (Tab. B.1). For the evaluation of corresponding density gradients only $\Omega^{MN}_{\kappa\lambda}$ has to be adapted.

M	D-block	f	g	X	Y
$1_{4\times4}$	$\mathrm{Re}(A)$	1	1	L	S
$i\Sigma_x$	$\mathrm{Im}(B)$	i	i	L	S
$i\Sigma_y$	$\mathrm{Re}(B)$	−1	−1	L	S
$i\Sigma_z$	$\mathrm{Im}(A)$	i	i	L	S
γ^5	$\mathrm{Re}(A)$	1	1	S	L
$i\alpha_x$	$\mathrm{Im}(B)$	i	i	S	L
$i\alpha_y$	$\mathrm{Re}(B)$	−1	−1	S	L
$i\alpha_z$	$\mathrm{Im}(A)$	i	i	S	L

Table B.1: Factors (f, g), bispinor blocks (X, Y), and density matrix blocks defined in this note for the evaluation of various densities $\psi^\dagger M\psi$.

Appendix C

Visualization of linear and nonlinear response by finite perturbation

> *Guy comes into a doctor's office.*
> *He says, 'Doc, it hurts when I do this.'*
> *The doctor says, 'Don't do it.'*
> *Think about that.*

Woody Allen in *Anything Else* (2003)

This note gives some ideas for the visualization of linear and nonlinear response to static perturbations using the finite perturbation method. These perturbations can be combined with analytically induced frequency-dependent densities which are accessible within linear response (Section 5.1).

All properties that can be calculated using the finite perturbation method, and which imply that certain densities change, can also be visualized in terms of density derivatives. Typically, very simple relationships exist between such density derivatives and energy derivatives. To see the connection consider as a simple example the (electron) charge density of Ne. In the presence of an external electric field the charge density is modified to specific values of the perturbation amplitudes (= field strengths), and can be monitored. This is done in Fig. C.1 for several field strengths F of a weak electric field, with both positive and negative values. In the limit $|F| \to 0$ these plots will approach the analytical density derivative (scaled by F). From the induced first-order charge density $\rho^{(j)}$ with respect to the field amplitude F_j at zero field, the components α_{ij} of the static electric dipole polarizability can be obtained by integration, scaled with the appropriate component of the position (see Section 5.2), e.g.

$$\alpha_{ij} = \int \mathrm{d}\mathbf{r}\, r_i \rho^{(j)} = \int \mathrm{d}\mathbf{r}\, r_j \rho^{(i)}. \tag{C.1}$$

In general, the perturbation should be chosen as large as necessary for numerical precision and as small as possible for the perturbation theory to hold. More perturbations can be added and each perturbation will increase the dimensionality of the problem by one. One way to reduce the dimensionality back to a distribution that can be visualized, is to express the variation along one or several perturbations in terms of the Taylor expansion coefficients, similarly to static molecular properties that are expressed by Taylor expansions coefficients of the energy. However, in contrast to the energy derivatives, these expansion coefficient plots are not just numbers but actually functions of Taylor expansion coefficients in space. For visualization of such derivatives in practice one needs to perform polynomial fits for typically half a million series of points instead of for just one series of energies. The advantage of real-space plots is the possibility to visualize e.g. geometric derivatives of various densities and property densities (see Section 5.6) without worries about orthonormality terms that would be needed in an analytical approach.

The possibilities and limitations have to be the same as in conventional finite perturbation approaches. We have tested the limitation imposed by the numerical precision and were able to obtain densities representing up to sixth-order variations. These operations can be performed independently of a specific quantum chemistry code as long as the density distribution is represented in some convenient format. Initially we have obtained these derivatives from a collection of files in GAUSSIAN[191] cube file format. For derivatives corresponding to diffuse properties this format is however not ideal because the precision of seven floating point digits in each point is not enough for a finite perturbation approach. We could visually see the onset of numerical noise. This can be pointed out as an advantage over the pure energy derivative approach where it is more difficult to see a possible problem from one single number.
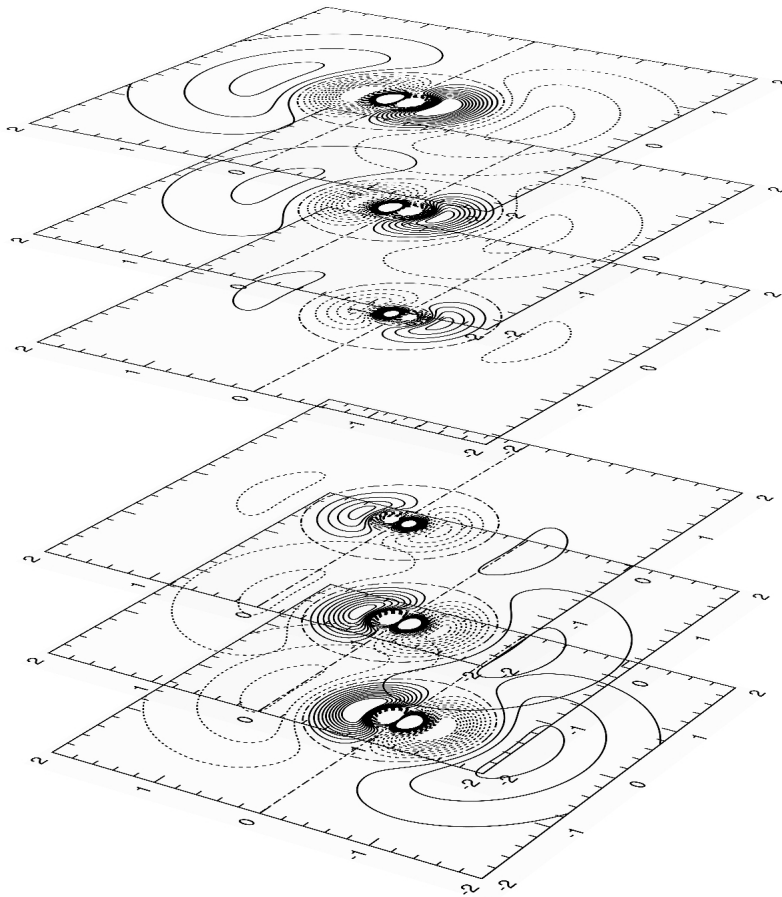
Figure C.1: Change in the charge density of Ne in the presence of a weak external electric field (LDA, uncontracted t-aug-cc-pVTZ). Solid (dotted) contour lines are plotted in the range from $+0.0001$ to $+0.001$ (-0.0001 to -0.001) e/a_o^3 in intervals of 0.0001 e/a_o^3. The dash-dotted contour line represents 0 e/a_o^3. The dimensions of the plots are 4×4 a_o. The electric field vector is oriented along the ordinates of individual plots. From bottom to top the field strength is following the series $-0.003, -0.002, -0.001, +0.001, +0.002, +0.003$ E_h/ea_o.

SDFT response: transformation between variable sets

<div style="text-align:center">

Benny:	*Where you gonna get four fourths and a third?*
	Can't you add?
Denny:	*I don't do fractions. Alright?*

Woody Allen's *Small Time Crooks* (2000)

</div>

The XC energy of a GGA-type functional can be defined in terms of the XC energy density F according to

$$E_{\text{XC}}^{\text{GGA}} = \int d\mathbf{r}\ F(n_\uparrow, n_\downarrow, |\nabla n_\uparrow|, (\nabla n_\uparrow \cdot \nabla n_\downarrow), |\nabla n_\downarrow|). \tag{D.1}$$

This variables set $\{n_\uparrow, n_\downarrow, |\nabla n_\uparrow|, (\nabla n_\uparrow \cdot \nabla n_\downarrow), |\nabla n_\downarrow|)\}$ is advantageous for the computational evaluation of derivatives of F. Another, but equivalent set of scalar variables $\{n, s, Z, Y, X\}$, with the definitions

$$n = n_\uparrow + n_\downarrow \tag{D.2}$$

$$s = n_\uparrow - n_\downarrow \tag{D.3}$$

$$Z = \nabla n \cdot \nabla n \tag{D.4}$$

$$Y = \nabla n \cdot \nabla s \tag{D.5}$$

$$X = \nabla s \cdot \nabla s \tag{D.6}$$

facilitates the derivation and an efficient implementation of the closed-shell SDFT response as discussed in Section 3.2, p. 66. This note describes how the necessary expressions can be transformed between these two sets and contains further below all necessary nonzero closed-shell derivatives of F with respect to the variable set $\{n, s, Z, Y, X\}$ expressed in terms of the derivatives with respect to $\{n_\uparrow, n_\downarrow, |\nabla n_\uparrow|, (\nabla n_\uparrow \cdot \nabla n_\downarrow), |\nabla n_\downarrow|)\}$.

Using the definitions in Eqs. D.2 and D.3, it is understood that n and s are complementary variables to $n_\uparrow$ and $n_\downarrow$. Their gradients are connected in a straightforward analogy according to

$$\nabla n = \nabla n_\uparrow + \nabla n_\downarrow \tag{D.7}$$

$$\nabla s = \nabla n_\uparrow - \nabla n_\downarrow. \tag{D.8}$$

These expressions may be inverted,

$$n_\uparrow = \frac{1}{2}(n + s) \tag{D.9}$$

$$n_\downarrow = \frac{1}{2}(n - s) \tag{D.10}$$

$$\nabla n_\uparrow = \frac{1}{2}(\nabla n + \nabla s) \tag{D.11}$$

$$\nabla n_\downarrow = \frac{1}{2}(\nabla n - \nabla s). \tag{D.12}$$

Also the interconversion between $\{(\nabla n_\uparrow \cdot \nabla n_\uparrow), (\nabla n_\uparrow \cdot \nabla n_\downarrow), (\nabla n_\downarrow \cdot \nabla n_\downarrow)\}$ and $\{(\nabla n \cdot \nabla n), (\nabla n \cdot \nabla s), (\nabla s \cdot \nabla s)\}$ is rather straightforward,

$$Z = (\nabla n \cdot \nabla n) = (\nabla n_\uparrow \cdot \nabla n_\uparrow) + 2(\nabla n_\uparrow \cdot \nabla n_\downarrow) + (\nabla n_\downarrow \cdot \nabla n_\downarrow) \tag{D.13}$$

$$Y = (\nabla n \cdot \nabla s) = (\nabla n_\uparrow \cdot \nabla n_\uparrow) - (\nabla n_\downarrow \cdot \nabla n_\downarrow) \tag{D.14}$$

$$X = (\nabla s \cdot \nabla s) = (\nabla n_\uparrow \cdot \nabla n_\uparrow) - 2(\nabla n_\uparrow \cdot \nabla n_\downarrow) + (\nabla n_\downarrow \cdot \nabla n_\downarrow), \tag{D.15}$$

and accordingly

$$(\nabla n_\uparrow \cdot \nabla n_\uparrow) = \frac{1}{4}(Z + 2Y + X) \tag{D.16}$$

$$(\nabla n_\uparrow \cdot \nabla n_\downarrow) = \frac{1}{4}(Z - X) \tag{D.17}$$

$$(\nabla n_\downarrow \cdot \nabla n_\downarrow) = \frac{1}{4}(Z - 2Y + X). \tag{D.18}$$

In order to apply the chain rule and transform derivatives of F with respect to $\{n_\uparrow, n_\downarrow, |\nabla n_\uparrow|, (\nabla n_\uparrow \cdot \nabla n_\downarrow), |\nabla n_\downarrow|)\}$, which are delivered by the DFT evaluator modules of the DIRAC code,[16, 113] to derivatives of F with respect to $\{n, s, Z, Y, X\}$, which are required for the response module, partial derivatives between these sets will be needed. The first-order derivatives are summarized in Tab. D.1. Using Tab. D.1, for instance $\frac{\partial F}{\partial n}$ is given by

$$\begin{aligned}
\frac{\partial F}{\partial n} &= \frac{\partial F}{\partial n_\uparrow}\frac{\partial n_\uparrow}{\partial n} + \frac{\partial F}{\partial n_\downarrow}\frac{\partial n_\downarrow}{\partial n} \\
&= \frac{1}{2}\frac{\partial F}{\partial n_\uparrow} + \frac{1}{2}\frac{\partial F}{\partial n_\downarrow},
\end{aligned} \tag{D.19}$$

Table D.1: Partial derivatives between the variable sets $\{n_\uparrow,\ n_\downarrow,\ |\nabla n_\uparrow|,\ (\nabla n_\uparrow \cdot \nabla n_\downarrow),\ |\nabla n_\downarrow|\}$ and $\{n, s, Z, Y, X\}$.

	$n_\uparrow$	$n_\downarrow$	$|\nabla n_\uparrow|$	$(\nabla n_\uparrow \cdot \nabla n_\downarrow)$	$|\nabla n_\downarrow|$
n	$\frac{\partial n_\uparrow}{\partial n}$	$\frac{\partial n_\downarrow}{\partial n}$			
s	$\frac{\partial n_\uparrow}{\partial s}$	$\frac{\partial n_\downarrow}{\partial s}$			
Z			$\frac{\partial |\nabla n_\uparrow|}{\partial Z}$	$\frac{\partial (\nabla n_\uparrow \cdot \nabla n_\downarrow)}{\partial Z}$	$\frac{\partial |\nabla n_\downarrow|}{\partial Z}$
Y			$\frac{\partial |\nabla n_\uparrow|}{\partial Y}$	$\frac{\partial (\nabla n_\uparrow \cdot \nabla n_\downarrow)}{\partial Y}$	$\frac{\partial |\nabla n_\downarrow|}{\partial Y}$
X			$\frac{\partial |\nabla n_\uparrow|}{\partial X}$	$\frac{\partial (\nabla n_\uparrow \cdot \nabla n_\downarrow)}{\partial X}$	$\frac{\partial |\nabla n_\downarrow|}{\partial X}$

	$n_\uparrow$	$n_\downarrow$	$|\nabla n_\uparrow|$	$(\nabla n_\uparrow \cdot \nabla n_\downarrow)$	$|\nabla n_\downarrow|$
n	$\frac{1}{2}$	$\frac{1}{2}$			
s	$\frac{1}{2}$	$-\frac{1}{2}$			
Z			$\frac{1}{4}\frac{1}{2|\nabla n_\uparrow|}$	$\frac{1}{4}$	$\frac{1}{4}\frac{1}{2|\nabla n_\downarrow|}$
Y			$\frac{1}{2}\frac{1}{2|\nabla n_\uparrow|}$	0	$-\frac{1}{2}\frac{1}{2|\nabla n_\downarrow|}$
X			$\frac{1}{4}\frac{1}{2|\nabla n_\uparrow|}$	$-\frac{1}{4}$	$\frac{1}{4}\frac{1}{2|\nabla n_\downarrow|}$

which for a closed-shell reference simplifies to

$$\frac{\partial F}{\partial n} = \frac{\partial F}{\partial n_\uparrow}. \tag{D.20}$$

As a second example, the derivative of F with respect to X, given by

$$\frac{\partial F}{\partial X} = \frac{\partial F}{\partial |\nabla n_\uparrow|}\frac{\partial |\nabla n_\uparrow|}{\partial X} + \frac{\partial F}{\partial (\nabla n_\uparrow \cdot \nabla n_\downarrow)}\frac{\partial (\nabla n_\uparrow \cdot \nabla n_\downarrow)}{\partial X} + \frac{\partial F}{\partial |\nabla n_\downarrow|}\frac{\partial |\nabla n_\downarrow|}{\partial X} \tag{D.21}$$

$$= \frac{1}{4}\frac{1}{2|\nabla n_\uparrow|}\frac{\partial F}{\partial |\nabla n_\uparrow|} - \frac{1}{4}\frac{\partial F}{\partial (\nabla n_\uparrow \cdot \nabla n_\downarrow)} + \frac{1}{4}\frac{1}{2|\nabla n_\downarrow|}\frac{\partial F}{\partial |\nabla n_\downarrow|},$$

simplifies to

$$\frac{\partial F}{\partial X} = \frac{1}{4}\frac{1}{|\nabla n_\uparrow|}\frac{\partial F}{\partial |\nabla n_\uparrow|} - \frac{1}{4}\frac{\partial F}{\partial (\nabla n_\uparrow \cdot \nabla n_\downarrow)} \tag{D.22}$$

for a closed-shell reference.

This exercise is trivial for the first-order partial derivatives. For higher order derivatives this can rapidly become cumbersome since the restriction to closed-shell may only be imposed at the end. Therefore, all other partial derivatives have been derived automatically. As a result of this derivation, all 69 nonzero closed-shell derivatives of F with respect to the variable set $\{n, s, Z, Y, X\}$ up to fourth-order (up to cubic response), expressed in terms of the derivatives with respect to $\{n_\uparrow, n_\downarrow, |\nabla n_\uparrow|, (\nabla n_\uparrow \cdot \nabla n_\downarrow), |\nabla n_\downarrow|)\}$ are listed below. Remember however, that

only derivatives up to second (third) order are needed for linear (quadratic) response. For notational ease derivatives with respect to $\{n_\uparrow, n_\downarrow, |\nabla n_\uparrow|, (\nabla n_\uparrow \cdot \nabla n_\downarrow), |\nabla n_\downarrow|\}$ are abbreviated by F_{PQRST}, which is defined as

$$F_{PQRST} = \left[\frac{\partial}{\partial n_\uparrow}\right]^P \left[\frac{\partial}{\partial n_\downarrow}\right]^Q \left[\frac{\partial}{\partial |\nabla n_\uparrow|}\right]^R \left[\frac{\partial}{\partial |\nabla n_\downarrow|}\right]^S \left[\frac{\partial}{\partial (\nabla n_\uparrow \cdot \nabla n_\downarrow)}\right]^T F.$$

$$\frac{\partial^4 F}{\partial n^4} = \frac{F_{40000}}{8} + \frac{F_{31000}}{2} + \frac{3\,F_{22000}}{8} \tag{D.23}$$

$$\frac{\partial^4 F}{\partial s^4} = \frac{F_{40000}}{8} - \frac{F_{31000}}{2} + \frac{3\,F_{22000}}{8} \tag{D.24}$$

$$\begin{aligned}
\frac{\partial^4 F}{\partial Z^4} = {}& \frac{F_{00103}}{64\,|\nabla n_\uparrow|} + \frac{3\,F_{00202}}{256\,|\nabla n_\uparrow|^2} + \frac{3\,F_{00112}}{256\,|\nabla n_\uparrow|^2} + \frac{F_{00301}}{256\,|\nabla n_\uparrow|^3} \\
& + \frac{3\,F_{00211}}{256\,|\nabla n_\uparrow|^3} - \frac{3\,F_{00102}}{256\,|\nabla n_\uparrow|^3} + \frac{F_{00400}}{2048\,|\nabla n_\uparrow|^4} + \frac{F_{00310}}{512\,|\nabla n_\uparrow|^4} \\
& + \frac{3\,F_{00220}}{2048\,|\nabla n_\uparrow|^4} - \frac{3\,F_{00201}}{256\,|\nabla n_\uparrow|^4} - \frac{3\,F_{00111}}{256\,|\nabla n_\uparrow|^4} - \frac{3\,F_{00300}}{1024\,|\nabla n_\uparrow|^5} \\
& - \frac{9\,F_{00210}}{1024\,|\nabla n_\uparrow|^5} + \frac{3\,F_{00101}}{256\,|\nabla n_\uparrow|^5} + \frac{15\,F_{00200}}{2048\,|\nabla n_\uparrow|^6} + \frac{15\,F_{00110}}{2048\,|\nabla n_\uparrow|^6} \\
& - \frac{15\,F_{00100}}{2048\,|\nabla n_\uparrow|^7} + \frac{F_{00004}}{256}
\end{aligned} \tag{D.25}$$

$$\begin{aligned}
\frac{\partial^4 F}{\partial Y^4} = {}& \frac{F_{00400}}{128\,|\nabla n_\uparrow|^4} - \frac{F_{00310}}{32\,|\nabla n_\uparrow|^4} + \frac{3\,F_{00220}}{128\,|\nabla n_\uparrow|^4} - \frac{3\,F_{00300}}{64\,|\nabla n_\uparrow|^5} \\
& + \frac{3\,F_{00210}}{64\,|\nabla n_\uparrow|^5} + \frac{15\,F_{00200}}{128\,|\nabla n_\uparrow|^6} - \frac{9\,F_{00110}}{128\,|\nabla n_\uparrow|^6} - \frac{15\,F_{00100}}{128\,|\nabla n_\uparrow|^7}
\end{aligned} \tag{D.26}$$

$$\begin{aligned}
\frac{\partial^4 F}{\partial X^4} = {}& -\frac{F_{00103}}{64\,|\nabla n_\uparrow|} + \frac{3\,F_{00202}}{256\,|\nabla n_\uparrow|^2} + \frac{3\,F_{00112}}{256\,|\nabla n_\uparrow|^2} \\
& - \frac{F_{00301}}{256\,|\nabla n_\uparrow|^3} - \frac{3\,F_{00211}}{256\,|\nabla n_\uparrow|^3} - \frac{3\,F_{00102}}{256\,|\nabla n_\uparrow|^3} + \frac{F_{00400}}{2048\,|\nabla n_\uparrow|^4} \\
& + \frac{F_{00310}}{512\,|\nabla n_\uparrow|^4} + \frac{3\,F_{00220}}{2048\,|\nabla n_\uparrow|^4} + \frac{3\,F_{00201}}{256\,|\nabla n_\uparrow|^4} + \frac{3\,F_{00111}}{256\,|\nabla n_\uparrow|^4} \\
& - \frac{3\,F_{00300}}{1024\,|\nabla n_\uparrow|^5} - \frac{9\,F_{00210}}{1024\,|\nabla n_\uparrow|^5} - \frac{3\,F_{00101}}{256\,|\nabla n_\uparrow|^5} + \frac{15\,F_{00200}}{2048\,|\nabla n_\uparrow|^6} \\
& + \frac{15\,F_{00110}}{2048\,|\nabla n_\uparrow|^6} - \frac{15\,F_{00100}}{2048\,|\nabla n_\uparrow|^7} + \frac{F_{00004}}{256}
\end{aligned} \tag{D.27}$$

$$\frac{\partial^4 F}{\partial n^3 \partial Z} = \frac{F_{30100}}{32 \left|\nabla n_\uparrow\right|} + \frac{F_{30010}}{32 \left|\nabla n_\uparrow\right|} + \frac{3 F_{21100}}{32 \left|\nabla n_\uparrow\right|} + \frac{3 F_{21010}}{32 \left|\nabla n_\uparrow\right|}$$
$$+ \frac{F_{30001}}{16} + \frac{3 F_{21001}}{16} \tag{D.28}$$

$$\frac{\partial^4 F}{\partial n^3 \partial X} = \frac{F_{30100}}{32 \left|\nabla n_\uparrow\right|} + \frac{F_{30010}}{32 \left|\nabla n_\uparrow\right|} + \frac{3 F_{21100}}{32 \left|\nabla n_\uparrow\right|} + \frac{3 F_{21010}}{32 \left|\nabla n_\uparrow\right|}$$
$$- \frac{F_{30001}}{16} - \frac{3 F_{21001}}{16} \tag{D.29}$$

$$\frac{\partial^4 F}{\partial n \partial Z^3} = \frac{3 F_{10102}}{128 \left|\nabla n_\uparrow\right|} + \frac{3 F_{10012}}{128 \left|\nabla n_\uparrow\right|} + \frac{3 F_{10201}}{256 \left|\nabla n_\uparrow\right|^2} + \frac{3 F_{10111}}{128 \left|\nabla n_\uparrow\right|^2}$$
$$+ \frac{3 F_{10021}}{256 \left|\nabla n_\uparrow\right|^2} + \frac{F_{10300}}{512 \left|\nabla n_\uparrow\right|^3} + \frac{3 F_{10210}}{512 \left|\nabla n_\uparrow\right|^3} + \frac{3 F_{10120}}{512 \left|\nabla n_\uparrow\right|^3}$$
$$- \frac{3 F_{10101}}{256 \left|\nabla n_\uparrow\right|^3} + \frac{F_{10030}}{512 \left|\nabla n_\uparrow\right|^3} - \frac{3 F_{10011}}{256 \left|\nabla n_\uparrow\right|^3} - \frac{3 F_{10200}}{512 \left|\nabla n_\uparrow\right|^4}$$
$$- \frac{3 F_{10110}}{256 \left|\nabla n_\uparrow\right|^4} - \frac{3 F_{10020}}{512 \left|\nabla n_\uparrow\right|^4} + \frac{3 F_{10100}}{512 \left|\nabla n_\uparrow\right|^5} + \frac{3 F_{10010}}{512 \left|\nabla n_\uparrow\right|^5}$$
$$+ \frac{F_{10003}}{64} \tag{D.30}$$

$$\frac{\partial^4 F}{\partial n \partial X^3} = \frac{3 F_{10102}}{128 \left|\nabla n_\uparrow\right|} + \frac{3 F_{10012}}{128 \left|\nabla n_\uparrow\right|} - \frac{3 F_{10201}}{256 \left|\nabla n_\uparrow\right|^2} - \frac{3 F_{10111}}{128 \left|\nabla n_\uparrow\right|^2}$$
$$- \frac{3 F_{10021}}{256 \left|\nabla n_\uparrow\right|^2} + \frac{F_{10300}}{512 \left|\nabla n_\uparrow\right|^3} + \frac{3 F_{10210}}{512 \left|\nabla n_\uparrow\right|^3} + \frac{3 F_{10120}}{512 \left|\nabla n_\uparrow\right|^3}$$
$$+ \frac{3 F_{10101}}{256 \left|\nabla n_\uparrow\right|^3} + \frac{F_{10030}}{512 \left|\nabla n_\uparrow\right|^3} + \frac{3 F_{10011}}{256 \left|\nabla n_\uparrow\right|^3} - \frac{3 F_{10200}}{512 \left|\nabla n_\uparrow\right|^4}$$
$$- \frac{3 F_{10110}}{256 \left|\nabla n_\uparrow\right|^4} - \frac{3 F_{10020}}{512 \left|\nabla n_\uparrow\right|^4} + \frac{3 F_{10100}}{512 \left|\nabla n_\uparrow\right|^5} + \frac{3 F_{10010}}{512 \left|\nabla n_\uparrow\right|^5}$$
$$- \frac{F_{10003}}{64} \tag{D.31}$$

$$\frac{\partial^4 F}{\partial s^3 \partial Y} = \frac{F_{30100}}{16 \left|\nabla n_\uparrow\right|} - \frac{F_{30010}}{16 \left|\nabla n_\uparrow\right|} - \frac{3 F_{21100}}{16 \left|\nabla n_\uparrow\right|} + \frac{3 F_{21010}}{16 \left|\nabla n_\uparrow\right|} \tag{D.32}$$

$$\frac{\partial^4 F}{\partial s \partial Y^3} = \frac{F_{10300}}{64 \left|\nabla n_\uparrow\right|^3} - \frac{3 F_{10210}}{64 \left|\nabla n_\uparrow\right|^3} + \frac{3 F_{10120}}{64 \left|\nabla n_\uparrow\right|^3} - \frac{F_{10030}}{64 \left|\nabla n_\uparrow\right|^3}$$
$$- \frac{3 F_{10200}}{64 \left|\nabla n_\uparrow\right|^4} + \frac{3 F_{10020}}{64 \left|\nabla n_\uparrow\right|^4} + \frac{3 F_{10100}}{64 \left|\nabla n_\uparrow\right|^5} - \frac{3 F_{10010}}{64 \left|\nabla n_\uparrow\right|^5} \tag{D.33}$$

$$\frac{\partial^4 F}{\partial Z^3 \partial X} = -\frac{F_{00103}}{128 \left|\nabla n_\uparrow\right|} + \frac{F_{00301}}{512 \left|\nabla n_\uparrow\right|^3} + \frac{3 F_{00211}}{512 \left|\nabla n_\uparrow\right|^3}$$
$$+ \frac{F_{00400}}{2048 \left|\nabla n_\uparrow\right|^4} + \frac{F_{00310}}{512 \left|\nabla n_\uparrow\right|^4} + \frac{3 F_{00220}}{2048 \left|\nabla n_\uparrow\right|^4} - \frac{3 F_{00201}}{512 \left|\nabla n_\uparrow\right|^4}$$
$$- \frac{3 F_{00111}}{512 \left|\nabla n_\uparrow\right|^4} - \frac{3 F_{00300}}{1024 \left|\nabla n_\uparrow\right|^5} - \frac{9 F_{00210}}{1024 \left|\nabla n_\uparrow\right|^5} + \frac{3 F_{00101}}{512 \left|\nabla n_\uparrow\right|^5} \tag{D.34}$$

$$+ \frac{15\, F_{00200}}{2048\, |\nabla n_\uparrow|^6} + \frac{15\, F_{00110}}{2048\, |\nabla n_\uparrow|^6} - \frac{15\, F_{00100}}{2048\, |\nabla n_\uparrow|^7} - \frac{F_{00004}}{256}$$

$$\frac{\partial^4 F}{\partial Z \partial X^3} = \frac{F_{00103}}{128\, |\nabla n_\uparrow|} - \frac{F_{00301}}{512\, |\nabla n_\uparrow|^3} - \frac{3\, F_{00211}}{512\, |\nabla n_\uparrow|^3} + \frac{F_{00400}}{2048\, |\nabla n_\uparrow|^4}$$
$$+ \frac{F_{00310}}{512\, |\nabla n_\uparrow|^4} + \frac{3\, F_{00220}}{2048\, |\nabla n_\uparrow|^4} + \frac{3\, F_{00201}}{512\, |\nabla n_\uparrow|^4} + \frac{3\, F_{00111}}{512\, |\nabla n_\uparrow|^4}$$
$$- \frac{3\, F_{00300}}{1024\, |\nabla n_\uparrow|^5} - \frac{9\, F_{00210}}{1024\, |\nabla n_\uparrow|^5} - \frac{3\, F_{00101}}{512\, |\nabla n_\uparrow|^5} + \frac{15\, F_{00200}}{2048\, |\nabla n_\uparrow|^6}$$
$$+ \frac{15\, F_{00110}}{2048\, |\nabla n_\uparrow|^6} - \frac{15\, F_{00100}}{2048\, |\nabla n_\uparrow|^7} - \frac{F_{00004}}{256} \tag{D.35}$$

$$\frac{\partial^3 F}{\partial n^3} = \frac{F_{30000}}{4} + \frac{3\, F_{21000}}{4} \tag{D.36}$$

$$\frac{\partial^3 F}{\partial Z^3} = \frac{3\, F_{00102}}{64\, |\nabla n_\uparrow|} + \frac{3\, F_{00201}}{128\, |\nabla n_\uparrow|^2} + \frac{3\, F_{00111}}{128\, |\nabla n_\uparrow|^2} + \frac{F_{00300}}{256\, |\nabla n_\uparrow|^3}$$
$$+ \frac{3\, F_{00210}}{256\, |\nabla n_\uparrow|^3} - \frac{3\, F_{00101}}{128\, |\nabla n_\uparrow|^3} - \frac{3\, F_{00200}}{256\, |\nabla n_\uparrow|^4} - \frac{3\, F_{00110}}{256\, |\nabla n_\uparrow|^4}$$
$$+ \frac{3\, F_{00100}}{256\, |\nabla n_\uparrow|^5} + \frac{F_{00003}}{64} \tag{D.37}$$

$$\frac{\partial^3 F}{\partial X^3} = \frac{3\, F_{00102}}{64\, |\nabla n_\uparrow|} - \frac{3\, F_{00201}}{128\, |\nabla n_\uparrow|^2} - \frac{3\, F_{00111}}{128\, |\nabla n_\uparrow|^2} + \frac{F_{00300}}{256\, |\nabla n_\uparrow|^3}$$
$$+ \frac{3\, F_{00210}}{256\, |\nabla n_\uparrow|^3} + \frac{3\, F_{00101}}{128\, |\nabla n_\uparrow|^3} - \frac{3\, F_{00200}}{256\, |\nabla n_\uparrow|^4} - \frac{3\, F_{00110}}{256\, |\nabla n_\uparrow|^4}$$
$$+ \frac{3\, F_{00100}}{256\, |\nabla n_\uparrow|^5} - \frac{F_{00003}}{64} \tag{D.38}$$

$$\frac{\partial^4 F}{\partial n^2 \partial s^2} = \frac{F_{40000}}{8} - \frac{F_{22000}}{8} \tag{D.39}$$

$$\frac{\partial^4 F}{\partial n^2 \partial Z^2} = \frac{F_{20101}}{32\, |\nabla n_\uparrow|} + \frac{F_{20011}}{32\, |\nabla n_\uparrow|} + \frac{F_{11101}}{16\, |\nabla n_\uparrow|} + \frac{F_{20200}}{128\, |\nabla n_\uparrow|^2}$$
$$+ \frac{F_{20110}}{64\, |\nabla n_\uparrow|^2} + \frac{F_{20020}}{128\, |\nabla n_\uparrow|^2} + \frac{F_{11200}}{64\, |\nabla n_\uparrow|^2} + \frac{F_{11110}}{64\, |\nabla n_\uparrow|^2}$$
$$- \frac{F_{20100}}{128\, |\nabla n_\uparrow|^3} - \frac{F_{20010}}{128\, |\nabla n_\uparrow|^3} - \frac{F_{11100}}{64\, |\nabla n_\uparrow|^3} + \frac{F_{20002}}{32}$$
$$+ \frac{F_{11002}}{32} \tag{D.40}$$

$$\frac{\partial^4 F}{\partial n^2 \partial Y^2} = \frac{F_{20200}}{32\, |\nabla n_\uparrow|^2} - \frac{F_{20110}}{16\, |\nabla n_\uparrow|^2} + \frac{F_{20020}}{32\, |\nabla n_\uparrow|^2} + \frac{F_{11200}}{16\, |\nabla n_\uparrow|^2}$$
$$- \frac{F_{11110}}{16\, |\nabla n_\uparrow|^2} - \frac{F_{20100}}{32\, |\nabla n_\uparrow|^3} - \frac{F_{20010}}{32\, |\nabla n_\uparrow|^3} - \frac{F_{11100}}{16\, |\nabla n_\uparrow|^3} \tag{D.41}$$

$$\frac{\partial^4 F}{\partial n^2 \partial X^2} = -\frac{F_{20101}}{32\,|\nabla n_\uparrow|} - \frac{F_{20011}}{32\,|\nabla n_\uparrow|} - \frac{F_{11101}}{16\,|\nabla n_\uparrow|}$$
$$+ \frac{F_{20200}}{128\,|\nabla n_\uparrow|^2} + \frac{F_{20110}}{64\,|\nabla n_\uparrow|^2} + \frac{F_{20020}}{128\,|\nabla n_\uparrow|^2} + \frac{F_{11200}}{64\,|\nabla n_\uparrow|^2}$$
$$+ \frac{F_{11110}}{64\,|\nabla n_\uparrow|^2} - \frac{F_{20100}}{128\,|\nabla n_\uparrow|^3} - \frac{F_{20010}}{128\,|\nabla n_\uparrow|^3} - \frac{F_{11100}}{64\,|\nabla n_\uparrow|^3}$$
$$+ \frac{F_{20002}}{32} + \frac{F_{11002}}{32} \tag{D.42}$$

$$\frac{\partial^4 F}{\partial s^2 \partial Z^2} = \frac{F_{20101}}{32\,|\nabla n_\uparrow|} + \frac{F_{20011}}{32\,|\nabla n_\uparrow|} - \frac{F_{11101}}{16\,|\nabla n_\uparrow|} + \frac{F_{20200}}{128\,|\nabla n_\uparrow|^2}$$
$$+ \frac{F_{20110}}{64\,|\nabla n_\uparrow|^2} + \frac{F_{20020}}{128\,|\nabla n_\uparrow|^2} - \frac{F_{11200}}{64\,|\nabla n_\uparrow|^2} - \frac{F_{11110}}{64\,|\nabla n_\uparrow|^2}$$
$$- \frac{F_{20100}}{128\,|\nabla n_\uparrow|^3} - \frac{F_{20010}}{128\,|\nabla n_\uparrow|^3} + \frac{F_{11100}}{64\,|\nabla n_\uparrow|^3} + \frac{F_{20002}}{32}$$
$$- \frac{F_{11002}}{32} \tag{D.43}$$

$$\frac{\partial^4 F}{\partial s^2 \partial Y^2} = \frac{F_{20200}}{32\,|\nabla n_\uparrow|^2} - \frac{F_{20110}}{16\,|\nabla n_\uparrow|^2} + \frac{F_{20020}}{32\,|\nabla n_\uparrow|^2} - \frac{F_{11200}}{16\,|\nabla n_\uparrow|^2}$$
$$+ \frac{F_{11110}}{16\,|\nabla n_\uparrow|^2} - \frac{F_{20100}}{32\,|\nabla n_\uparrow|^3} - \frac{F_{20010}}{32\,|\nabla n_\uparrow|^3} + \frac{F_{11100}}{16\,|\nabla n_\uparrow|^3} \tag{D.44}$$

$$\frac{\partial^4 F}{\partial s^2 \partial X^2} = -\frac{F_{20101}}{32\,|\nabla n_\uparrow|} - \frac{F_{20011}}{32\,|\nabla n_\uparrow|} + \frac{F_{11101}}{16\,|\nabla n_\uparrow|}$$
$$+ \frac{F_{20200}}{128\,|\nabla n_\uparrow|^2} + \frac{F_{20110}}{64\,|\nabla n_\uparrow|^2} + \frac{F_{20020}}{128\,|\nabla n_\uparrow|^2} - \frac{F_{11200}}{64\,|\nabla n_\uparrow|^2}$$
$$- \frac{F_{11110}}{64\,|\nabla n_\uparrow|^2} - \frac{F_{20100}}{128\,|\nabla n_\uparrow|^3} - \frac{F_{20010}}{128\,|\nabla n_\uparrow|^3} + \frac{F_{11100}}{64\,|\nabla n_\uparrow|^3}$$
$$+ \frac{F_{20002}}{32} - \frac{F_{11002}}{32} \tag{D.45}$$

$$\frac{\partial^4 F}{\partial Z^2 \partial Y^2} = \frac{F_{00202}}{128\,|\nabla n_\uparrow|^2} - \frac{F_{00112}}{128\,|\nabla n_\uparrow|^2} + \frac{F_{00301}}{128\,|\nabla n_\uparrow|^3} - \frac{F_{00211}}{128\,|\nabla n_\uparrow|^3}$$
$$- \frac{F_{00102}}{128\,|\nabla n_\uparrow|^3} + \frac{F_{00400}}{512\,|\nabla n_\uparrow|^4} - \frac{F_{00220}}{512\,|\nabla n_\uparrow|^4} - \frac{3\,F_{00201}}{128\,|\nabla n_\uparrow|^4}$$
$$+ \frac{F_{00111}}{128\,|\nabla n_\uparrow|^4} - \frac{3\,F_{00300}}{256\,|\nabla n_\uparrow|^5} + \frac{F_{00210}}{256\,|\nabla n_\uparrow|^5} + \frac{3\,F_{00101}}{128\,|\nabla n_\uparrow|^5}$$
$$+ \frac{15\,F_{00200}}{512\,|\nabla n_\uparrow|^6} - \frac{F_{00110}}{512\,|\nabla n_\uparrow|^6} - \frac{15\,F_{00100}}{512\,|\nabla n_\uparrow|^7} \tag{D.46}$$

$$\frac{\partial^4 F}{\partial Z^2 \partial X^2} = -\frac{F_{00202}}{256\,|\nabla n_\uparrow|^2} - \frac{F_{00112}}{256\,|\nabla n_\uparrow|^2} + \frac{F_{00102}}{256\,|\nabla n_\uparrow|^3} \tag{D.47}$$

$$+ \frac{F_{00400}}{2048\,|\nabla n_\uparrow|^4} + \frac{F_{00310}}{512\,|\nabla n_\uparrow|^4} + \frac{3\,F_{00220}}{2048\,|\nabla n_\uparrow|^4} - \frac{3\,F_{00300}}{1024\,|\nabla n_\uparrow|^5}$$

$$- \frac{9\,F_{00210}}{1024\,|\nabla n_\uparrow|^5} + \frac{15\,F_{00200}}{2048\,|\nabla n_\uparrow|^6} + \frac{15\,F_{00110}}{2048\,|\nabla n_\uparrow|^6} - \frac{15\,F_{00100}}{2048\,|\nabla n_\uparrow|^7}$$

$$+ \frac{F_{00004}}{256}$$

$$\frac{\partial^4 F}{\partial Y^2 \partial X^2} = \frac{F_{00202}}{128\,|\nabla n_\uparrow|^2} - \frac{F_{00112}}{128\,|\nabla n_\uparrow|^2} - \frac{F_{00301}}{128\,|\nabla n_\uparrow|^3} + \frac{F_{00211}}{128\,|\nabla n_\uparrow|^3}$$

$$- \frac{F_{00102}}{128\,|\nabla n_\uparrow|^3} + \frac{F_{00400}}{512\,|\nabla n_\uparrow|^4} - \frac{F_{00220}}{512\,|\nabla n_\uparrow|^4} + \frac{3\,F_{00201}}{128\,|\nabla n_\uparrow|^4}$$

$$- \frac{F_{00111}}{128\,|\nabla n_\uparrow|^4} - \frac{3\,F_{00300}}{256\,|\nabla n_\uparrow|^5} + \frac{F_{00210}}{256\,|\nabla n_\uparrow|^5} - \frac{3\,F_{00101}}{128\,|\nabla n_\uparrow|^5}$$

$$+ \frac{15\,F_{00200}}{512\,|\nabla n_\uparrow|^6} - \frac{F_{00110}}{512\,|\nabla n_\uparrow|^6} - \frac{15\,F_{00100}}{512\,|\nabla n_\uparrow|^7} \tag{D.48}$$

$$\frac{\partial^4 F}{\partial n^2 \partial s \partial Y} = \frac{F_{30100}}{16\,|\nabla n_\uparrow|} - \frac{F_{30010}}{16\,|\nabla n_\uparrow|} + \frac{F_{21100}}{16\,|\nabla n_\uparrow|} - \frac{F_{21010}}{16\,|\nabla n_\uparrow|} \tag{D.49}$$

$$\frac{\partial^4 F}{\partial n^2 \partial Z \partial X} = \frac{F_{20200}}{128\,|\nabla n_\uparrow|^2} + \frac{F_{20110}}{64\,|\nabla n_\uparrow|^2} + \frac{F_{20020}}{128\,|\nabla n_\uparrow|^2} + \frac{F_{11200}}{64\,|\nabla n_\uparrow|^2}$$

$$+ \frac{F_{11110}}{64\,|\nabla n_\uparrow|^2} - \frac{F_{20100}}{128\,|\nabla n_\uparrow|^3} - \frac{F_{20010}}{128\,|\nabla n_\uparrow|^3} - \frac{F_{11100}}{64\,|\nabla n_\uparrow|^3}$$

$$- \frac{F_{20002}}{32} - \frac{F_{11002}}{32} \tag{D.50}$$

$$\frac{\partial^4 F}{\partial n \partial s^2 \partial Z} = \frac{F_{30100}}{32\,|\nabla n_\uparrow|} + \frac{F_{30010}}{32\,|\nabla n_\uparrow|} - \frac{F_{21100}}{32\,|\nabla n_\uparrow|} - \frac{F_{21010}}{32\,|\nabla n_\uparrow|}$$

$$+ \frac{F_{30001}}{16} - \frac{F_{21001}}{16} \tag{D.51}$$

$$\frac{\partial^4 F}{\partial n \partial s^2 \partial X} = \frac{F_{30100}}{32\,|\nabla n_\uparrow|} + \frac{F_{30010}}{32\,|\nabla n_\uparrow|} - \frac{F_{21100}}{32\,|\nabla n_\uparrow|} - \frac{F_{21010}}{32\,|\nabla n_\uparrow|}$$

$$- \frac{F_{30001}}{16} + \frac{F_{21001}}{16} \tag{D.52}$$

$$\frac{\partial^4 F}{\partial n \partial Z^2 \partial X} = - \frac{F_{10102}}{128\,|\nabla n_\uparrow|} - \frac{F_{10012}}{128\,|\nabla n_\uparrow|} + \frac{F_{10201}}{256\,|\nabla n_\uparrow|^2}$$

$$+ \frac{F_{10111}}{128\,|\nabla n_\uparrow|^2} + \frac{F_{10021}}{256\,|\nabla n_\uparrow|^2} + \frac{F_{10300}}{512\,|\nabla n_\uparrow|^3} + \frac{3\,F_{10210}}{512\,|\nabla n_\uparrow|^3}$$

$$+ \frac{3\,F_{10120}}{512\,|\nabla n_\uparrow|^3} - \frac{F_{10101}}{256\,|\nabla n_\uparrow|^3} + \frac{F_{10030}}{512\,|\nabla n_\uparrow|^3} - \frac{F_{10011}}{256\,|\nabla n_\uparrow|^3}$$

$$- \frac{3\,F_{10200}}{512\,|\nabla n_\uparrow|^4} - \frac{3\,F_{10110}}{256\,|\nabla n_\uparrow|^4} - \frac{3\,F_{10020}}{512\,|\nabla n_\uparrow|^4} + \frac{3\,F_{10100}}{512\,|\nabla n_\uparrow|^5}$$

$$+ \frac{3\,F_{10010}}{512\,|\nabla n_\uparrow|^5} - \frac{F_{10003}}{64} \tag{D.53}$$

$$\frac{\partial^4 F}{\partial n \partial Z \partial Y^2} = \frac{F_{10201}}{64\,|\nabla n_\uparrow|^2} - \frac{F_{10111}}{32\,|\nabla n_\uparrow|^2} + \frac{F_{10021}}{64\,|\nabla n_\uparrow|^2} + \frac{F_{10300}}{128\,|\nabla n_\uparrow|^3}$$
$$- \frac{F_{10210}}{128\,|\nabla n_\uparrow|^3} - \frac{F_{10120}}{128\,|\nabla n_\uparrow|^3} - \frac{F_{10101}}{64\,|\nabla n_\uparrow|^3} + \frac{F_{10030}}{128\,|\nabla n_\uparrow|^3}$$
$$- \frac{F_{10011}}{64\,|\nabla n_\uparrow|^3} - \frac{3\,F_{10200}}{128\,|\nabla n_\uparrow|^4} + \frac{F_{10110}}{64\,|\nabla n_\uparrow|^4} - \frac{3\,F_{10020}}{128\,|\nabla n_\uparrow|^4}$$
$$+ \frac{3\,F_{10100}}{128\,|\nabla n_\uparrow|^5} + \frac{3\,F_{10010}}{128\,|\nabla n_\uparrow|^5} \tag{D.54}$$

$$\frac{\partial^4 F}{\partial n \partial Z \partial X^2} = - \frac{F_{10102}}{128\,|\nabla n_\uparrow|} - \frac{F_{10012}}{128\,|\nabla n_\uparrow|} - \frac{F_{10201}}{256\,|\nabla n_\uparrow|^2}$$
$$- \frac{F_{10111}}{128\,|\nabla n_\uparrow|^2} - \frac{F_{10021}}{256\,|\nabla n_\uparrow|^2} + \frac{F_{10300}}{512\,|\nabla n_\uparrow|^3} + \frac{3\,F_{10210}}{512\,|\nabla n_\uparrow|^3}$$
$$+ \frac{3\,F_{10120}}{512\,|\nabla n_\uparrow|^3} + \frac{F_{10101}}{256\,|\nabla n_\uparrow|^3} + \frac{F_{10030}}{512\,|\nabla n_\uparrow|^3} + \frac{F_{10011}}{256\,|\nabla n_\uparrow|^3}$$
$$- \frac{3\,F_{10200}}{512\,|\nabla n_\uparrow|^4} - \frac{3\,F_{10110}}{256\,|\nabla n_\uparrow|^4} - \frac{3\,F_{10020}}{512\,|\nabla n_\uparrow|^4} + \frac{3\,F_{10100}}{512\,|\nabla n_\uparrow|^5}$$
$$+ \frac{3\,F_{10010}}{512\,|\nabla n_\uparrow|^5} + \frac{F_{10003}}{64} \tag{D.55}$$

$$\frac{\partial^4 F}{\partial n \partial Y^2 \partial X} = - \frac{F_{10201}}{64\,|\nabla n_\uparrow|^2} + \frac{F_{10111}}{32\,|\nabla n_\uparrow|^2} - \frac{F_{10021}}{64\,|\nabla n_\uparrow|^2}$$
$$+ \frac{F_{10300}}{128\,|\nabla n_\uparrow|^3} - \frac{F_{10210}}{128\,|\nabla n_\uparrow|^3} - \frac{F_{10120}}{128\,|\nabla n_\uparrow|^3} + \frac{F_{10101}}{64\,|\nabla n_\uparrow|^3}$$
$$+ \frac{F_{10030}}{128\,|\nabla n_\uparrow|^3} + \frac{F_{10011}}{64\,|\nabla n_\uparrow|^3} - \frac{3\,F_{10200}}{128\,|\nabla n_\uparrow|^4} + \frac{F_{10110}}{64\,|\nabla n_\uparrow|^4}$$
$$- \frac{3\,F_{10020}}{128\,|\nabla n_\uparrow|^4} + \frac{3\,F_{10100}}{128\,|\nabla n_\uparrow|^5} + \frac{3\,F_{10010}}{128\,|\nabla n_\uparrow|^5} \tag{D.56}$$

$$\frac{\partial^4 F}{\partial s^2 \partial Z \partial X} = \frac{F_{20200}}{128\,|\nabla n_\uparrow|^2} + \frac{F_{20110}}{64\,|\nabla n_\uparrow|^2} + \frac{F_{20020}}{128\,|\nabla n_\uparrow|^2} - \frac{F_{11200}}{64\,|\nabla n_\uparrow|^2}$$
$$- \frac{F_{11110}}{64\,|\nabla n_\uparrow|^2} - \frac{F_{20100}}{128\,|\nabla n_\uparrow|^3} - \frac{F_{20010}}{128\,|\nabla n_\uparrow|^3} + \frac{F_{11100}}{64\,|\nabla n_\uparrow|^3}$$
$$- \frac{F_{20002}}{32} + \frac{F_{11002}}{32} \tag{D.57}$$

$$\frac{\partial^4 F}{\partial s \partial Z^2 \partial Y} = \frac{F_{10102}}{64\,|\nabla n_\uparrow|} - \frac{F_{10012}}{64\,|\nabla n_\uparrow|} + \frac{F_{10201}}{64\,|\nabla n_\uparrow|^2} - \frac{F_{10021}}{64\,|\nabla n_\uparrow|^2}$$
$$+ \frac{F_{10300}}{256\,|\nabla n_\uparrow|^3} + \frac{F_{10210}}{256\,|\nabla n_\uparrow|^3} - \frac{F_{10120}}{256\,|\nabla n_\uparrow|^3} - \frac{F_{10101}}{64\,|\nabla n_\uparrow|^3}$$
$$- \frac{F_{10030}}{256\,|\nabla n_\uparrow|^3} + \frac{F_{10011}}{64\,|\nabla n_\uparrow|^3} - \frac{3\,F_{10200}}{256\,|\nabla n_\uparrow|^4} + \frac{3\,F_{10020}}{256\,|\nabla n_\uparrow|^4}$$
$$+ \frac{3\,F_{10100}}{256\,|\nabla n_\uparrow|^5} - \frac{3\,F_{10010}}{256\,|\nabla n_\uparrow|^5} \tag{D.58}$$

$$\frac{\partial^4 F}{\partial s \partial Y \partial X^2} = \frac{F_{10102}}{64\,|\nabla n_\uparrow|} - \frac{F_{10012}}{64\,|\nabla n_\uparrow|} - \frac{F_{10201}}{64\,|\nabla n_\uparrow|^2} + \frac{F_{10021}}{64\,|\nabla n_\uparrow|^2} \tag{D.59}$$

$$+ \frac{F_{10300}}{256\,|\nabla n_\uparrow|^3} + \frac{F_{10210}}{256\,|\nabla n_\uparrow|^3} - \frac{F_{10120}}{256\,|\nabla n_\uparrow|^3} + \frac{F_{10101}}{64\,|\nabla n_\uparrow|^3}$$

$$- \frac{F_{10030}}{256\,|\nabla n_\uparrow|^3} - \frac{F_{10011}}{64\,|\nabla n_\uparrow|^3} - \frac{3\,F_{10200}}{256\,|\nabla n_\uparrow|^4} + \frac{3\,F_{10020}}{256\,|\nabla n_\uparrow|^4}$$

$$+ \frac{3\,F_{10100}}{256\,|\nabla n_\uparrow|^5} - \frac{3\,F_{10010}}{256\,|\nabla n_\uparrow|^5}$$

$$\frac{\partial^4 F}{\partial Z \partial Y^2 \partial X} = -\frac{F_{00202}}{128\,|\nabla n_\uparrow|^2} + \frac{F_{00112}}{128\,|\nabla n_\uparrow|^2} + \frac{F_{00102}}{128\,|\nabla n_\uparrow|^3} \tag{D.60}$$

$$+ \frac{F_{00400}}{512\,|\nabla n_\uparrow|^4} - \frac{F_{00220}}{512\,|\nabla n_\uparrow|^4} - \frac{3\,F_{00300}}{256\,|\nabla n_\uparrow|^5} + \frac{F_{00210}}{256\,|\nabla n_\uparrow|^5}$$

$$+ \frac{15\,F_{00200}}{512\,|\nabla n_\uparrow|^6} - \frac{F_{00110}}{512\,|\nabla n_\uparrow|^6} - \frac{15\,F_{00100}}{512\,|\nabla n_\uparrow|^7}$$

$$\frac{\partial^3 F}{\partial n^2 \partial Z} = \frac{F_{20100}}{16\,|\nabla n_\uparrow|} + \frac{F_{20010}}{16\,|\nabla n_\uparrow|} + \frac{F_{11100}}{8\,|\nabla n_\uparrow|} + \frac{F_{20001}}{8} \tag{D.61}$$

$$+ \frac{F_{11001}}{8}$$

$$\frac{\partial^3 F}{\partial n^2 \partial X} = \frac{F_{20100}}{16\,|\nabla n_\uparrow|} + \frac{F_{20010}}{16\,|\nabla n_\uparrow|} + \frac{F_{11100}}{8\,|\nabla n_\uparrow|} - \frac{F_{20001}}{8} \tag{D.62}$$

$$- \frac{F_{11001}}{8}$$

$$\frac{\partial^3 F}{\partial n \partial s^2} = \frac{F_{30000}}{4} - \frac{F_{21000}}{4} \tag{D.63}$$

$$\frac{\partial^3 F}{\partial n \partial Z^2} = \frac{F_{10101}}{16\,|\nabla n_\uparrow|} + \frac{F_{10011}}{16\,|\nabla n_\uparrow|} + \frac{F_{10200}}{64\,|\nabla n_\uparrow|^2} + \frac{F_{10110}}{32\,|\nabla n_\uparrow|^2} \tag{D.64}$$

$$+ \frac{F_{10020}}{64\,|\nabla n_\uparrow|^2} - \frac{F_{10100}}{64\,|\nabla n_\uparrow|^3} - \frac{F_{10010}}{64\,|\nabla n_\uparrow|^3} + \frac{F_{10002}}{16}$$

$$\frac{\partial^3 F}{\partial n \partial Y^2} = \frac{F_{10200}}{16\,|\nabla n_\uparrow|^2} - \frac{F_{10110}}{8\,|\nabla n_\uparrow|^2} + \frac{F_{10020}}{16\,|\nabla n_\uparrow|^2} - \frac{F_{10100}}{16\,|\nabla n_\uparrow|^3} \tag{D.65}$$

$$- \frac{F_{10010}}{16\,|\nabla n_\uparrow|^3}$$

$$\frac{\partial^3 F}{\partial n \partial X^2} = -\frac{F_{10101}}{16\,|\nabla n_\uparrow|} - \frac{F_{10011}}{16\,|\nabla n_\uparrow|} + \frac{F_{10200}}{64\,|\nabla n_\uparrow|^2} \tag{D.66}$$

$$+ \frac{F_{10110}}{32\,|\nabla n_\uparrow|^2} + \frac{F_{10020}}{64\,|\nabla n_\uparrow|^2} - \frac{F_{10100}}{64\,|\nabla n_\uparrow|^3} - \frac{F_{10010}}{64\,|\nabla n_\uparrow|^3}$$

$$+ \frac{F_{10002}}{16}$$

$$\frac{\partial^3 F}{\partial s^2 \partial Z} = \frac{F_{20100}}{16 \left| \nabla n_\uparrow \right|} + \frac{F_{20010}}{16 \left| \nabla n_\uparrow \right|} - \frac{F_{11100}}{8 \left| \nabla n_\uparrow \right|} + \frac{F_{20001}}{8}$$
$$- \frac{F_{11001}}{8} \tag{D.67}$$

$$\frac{\partial^3 F}{\partial s^2 \partial X} = \frac{F_{20100}}{16 \left| \nabla n_\uparrow \right|} + \frac{F_{20010}}{16 \left| \nabla n_\uparrow \right|} - \frac{F_{11100}}{8 \left| \nabla n_\uparrow \right|} - \frac{F_{20001}}{8}$$
$$+ \frac{F_{11001}}{8} \tag{D.68}$$

$$\frac{\partial^3 F}{\partial Z^2 \partial X} = -\frac{F_{00102}}{64 \left| \nabla n_\uparrow \right|} + \frac{F_{00201}}{128 \left| \nabla n_\uparrow \right|^2} + \frac{F_{00111}}{128 \left| \nabla n_\uparrow \right|^2}$$
$$+ \frac{F_{00300}}{256 \left| \nabla n_\uparrow \right|^3} + \frac{3 F_{00210}}{256 \left| \nabla n_\uparrow \right|^3} - \frac{F_{00101}}{128 \left| \nabla n_\uparrow \right|^3} - \frac{3 F_{00200}}{256 \left| \nabla n_\uparrow \right|^4}$$
$$- \frac{3 F_{00110}}{256 \left| \nabla n_\uparrow \right|^4} + \frac{3 F_{00100}}{256 \left| \nabla n_\uparrow \right|^5} - \frac{F_{00003}}{64} \tag{D.69}$$

$$\frac{\partial^3 F}{\partial Z \partial Y^2} = \frac{F_{00201}}{32 \left| \nabla n_\uparrow \right|^2} - \frac{F_{00111}}{32 \left| \nabla n_\uparrow \right|^2} + \frac{F_{00300}}{64 \left| \nabla n_\uparrow \right|^3} - \frac{F_{00210}}{64 \left| \nabla n_\uparrow \right|^3}$$
$$- \frac{F_{00101}}{32 \left| \nabla n_\uparrow \right|^3} - \frac{3 F_{00200}}{64 \left| \nabla n_\uparrow \right|^4} + \frac{F_{00110}}{64 \left| \nabla n_\uparrow \right|^4} + \frac{3 F_{00100}}{64 \left| \nabla n_\uparrow \right|^5} \tag{D.70}$$

$$\frac{\partial^3 F}{\partial Z \partial X^2} = -\frac{F_{00102}}{64 \left| \nabla n_\uparrow \right|} - \frac{F_{00201}}{128 \left| \nabla n_\uparrow \right|^2} - \frac{F_{00111}}{128 \left| \nabla n_\uparrow \right|^2}$$
$$+ \frac{F_{00300}}{256 \left| \nabla n_\uparrow \right|^3} + \frac{3 F_{00210}}{256 \left| \nabla n_\uparrow \right|^3} + \frac{F_{00101}}{128 \left| \nabla n_\uparrow \right|^3} - \frac{3 F_{00200}}{256 \left| \nabla n_\uparrow \right|^4}$$
$$- \frac{3 F_{00110}}{256 \left| \nabla n_\uparrow \right|^4} + \frac{3 F_{00100}}{256 \left| \nabla n_\uparrow \right|^5} + \frac{F_{00003}}{64} \tag{D.71}$$

$$\frac{\partial^3 F}{\partial Y^2 \partial X} = -\frac{F_{00201}}{32 \left| \nabla n_\uparrow \right|^2} + \frac{F_{00111}}{32 \left| \nabla n_\uparrow \right|^2} + \frac{F_{00300}}{64 \left| \nabla n_\uparrow \right|^3}$$
$$- \frac{F_{00210}}{64 \left| \nabla n_\uparrow \right|^3} + \frac{F_{00101}}{32 \left| \nabla n_\uparrow \right|^3} - \frac{3 F_{00200}}{64 \left| \nabla n_\uparrow \right|^4} + \frac{F_{00110}}{64 \left| \nabla n_\uparrow \right|^4}$$
$$+ \frac{3 F_{00100}}{64 \left| \nabla n_\uparrow \right|^5} \tag{D.72}$$

$$\frac{\partial^2 F}{\partial n^2} = \frac{F_{20000}}{2} + \frac{F_{11000}}{2} \tag{D.73}$$

$$\frac{\partial^2 F}{\partial s^2} = \frac{F_{20000}}{2} - \frac{F_{11000}}{2} \tag{D.74}$$

$$\frac{\partial^2 F}{\partial Z^2} = \frac{F_{00101}}{8\,|\nabla n_\uparrow|} + \frac{F_{00200}}{32\,|\nabla n_\uparrow|^2} + \frac{F_{00110}}{32\,|\nabla n_\uparrow|^2} - \frac{F_{00100}}{32\,|\nabla n_\uparrow|^3}$$
$$+ \frac{F_{00002}}{16} \tag{D.75}$$

$$\frac{\partial^2 F}{\partial Y^2} = \frac{F_{00200}}{8\,|\nabla n_\uparrow|^2} - \frac{F_{00110}}{8\,|\nabla n_\uparrow|^2} - \frac{F_{00100}}{8\,|\nabla n_\uparrow|^3} \tag{D.76}$$

$$\frac{\partial^2 F}{\partial X^2} = -\frac{F_{00101}}{8\,|\nabla n_\uparrow|} + \frac{F_{00200}}{32\,|\nabla n_\uparrow|^2} + \frac{F_{00110}}{32\,|\nabla n_\uparrow|^2}$$
$$- \frac{F_{00100}}{32\,|\nabla n_\uparrow|^3} + \frac{F_{00002}}{16} \tag{D.77}$$

$$\frac{\partial^4 F}{\partial n\partial s\partial Z\partial Y} = \frac{F_{20101}}{32\,|\nabla n_\uparrow|} - \frac{F_{20011}}{32\,|\nabla n_\uparrow|} + \frac{F_{20200}}{64\,|\nabla n_\uparrow|^2} - \frac{F_{20020}}{64\,|\nabla n_\uparrow|^2}$$
$$- \frac{F_{20100}}{64\,|\nabla n_\uparrow|^3} + \frac{F_{20010}}{64\,|\nabla n_\uparrow|^3} \tag{D.78}$$

$$\frac{\partial^4 F}{\partial n\partial s\partial Y\partial X} = -\frac{F_{20101}}{32\,|\nabla n_\uparrow|} + \frac{F_{20011}}{32\,|\nabla n_\uparrow|} + \frac{F_{20200}}{64\,|\nabla n_\uparrow|^2}$$
$$- \frac{F_{20020}}{64\,|\nabla n_\uparrow|^2} - \frac{F_{20100}}{64\,|\nabla n_\uparrow|^3} + \frac{F_{20010}}{64\,|\nabla n_\uparrow|^3} \tag{D.79}$$

$$\frac{\partial^4 F}{\partial s\partial Z\partial Y\partial X} = -\frac{F_{10102}}{64\,|\nabla n_\uparrow|} + \frac{F_{10012}}{64\,|\nabla n_\uparrow|} + \frac{F_{10300}}{256\,|\nabla n_\uparrow|^3}$$
$$+ \frac{F_{10210}}{256\,|\nabla n_\uparrow|^3} - \frac{F_{10120}}{256\,|\nabla n_\uparrow|^3} - \frac{F_{10030}}{256\,|\nabla n_\uparrow|^3} - \frac{3\,F_{10200}}{256\,|\nabla n_\uparrow|^4}$$
$$+ \frac{3\,F_{10020}}{256\,|\nabla n_\uparrow|^4} + \frac{3\,F_{10100}}{256\,|\nabla n_\uparrow|^5} - \frac{3\,F_{10010}}{256\,|\nabla n_\uparrow|^5} \tag{D.80}$$

$$\frac{\partial^3 F}{\partial n\partial s\partial Y} = \frac{F_{20100}}{8\,|\nabla n_\uparrow|} - \frac{F_{20010}}{8\,|\nabla n_\uparrow|} \tag{D.81}$$

$$\frac{\partial^3 F}{\partial n\partial Z\partial X} = \frac{F_{10200}}{64\,|\nabla n_\uparrow|^2} + \frac{F_{10110}}{32\,|\nabla n_\uparrow|^2} + \frac{F_{10020}}{64\,|\nabla n_\uparrow|^2} - \frac{F_{10100}}{64\,|\nabla n_\uparrow|^3}$$
$$- \frac{F_{10010}}{64\,|\nabla n_\uparrow|^3} - \frac{F_{10002}}{16} \tag{D.82}$$

$$\frac{\partial^3 F}{\partial s\partial Z\partial Y} = \frac{F_{10101}}{16\,|\nabla n_\uparrow|} - \frac{F_{10011}}{16\,|\nabla n_\uparrow|} + \frac{F_{10200}}{32\,|\nabla n_\uparrow|^2} - \frac{F_{10020}}{32\,|\nabla n_\uparrow|^2}$$
$$- \frac{F_{10100}}{32\,|\nabla n_\uparrow|^3} + \frac{F_{10010}}{32\,|\nabla n_\uparrow|^3} \tag{D.83}$$

$$\frac{\partial^3 F}{\partial s \partial Y \partial X} = -\frac{F_{10101}}{16 \left| \nabla n_\uparrow \right|} + \frac{F_{10011}}{16 \left| \nabla n_\uparrow \right|} + \frac{F_{10200}}{32 \left| \nabla n_\uparrow \right|^2}$$
$$- \frac{F_{10020}}{32 \left| \nabla n_\uparrow \right|^2} - \frac{F_{10100}}{32 \left| \nabla n_\uparrow \right|^3} + \frac{F_{10010}}{32 \left| \nabla n_\uparrow \right|^3} \tag{D.84}$$

$$\frac{\partial^2 F}{\partial n \partial Z} = \frac{F_{10100}}{8 \left| \nabla n_\uparrow \right|} + \frac{F_{10010}}{8 \left| \nabla n_\uparrow \right|} + \frac{F_{10001}}{4} \tag{D.85}$$

$$\frac{\partial^2 F}{\partial n \partial X} = \frac{F_{10100}}{8 \left| \nabla n_\uparrow \right|} + \frac{F_{10010}}{8 \left| \nabla n_\uparrow \right|} - \frac{F_{10001}}{4} \tag{D.86}$$

$$\frac{\partial^2 F}{\partial s \partial Y} = \frac{F_{10100}}{4 \left| \nabla n_\uparrow \right|} - \frac{F_{10010}}{4 \left| \nabla n_\uparrow \right|} \tag{D.87}$$

$$\frac{\partial^2 F}{\partial Z \partial X} = \frac{F_{00200}}{32 \left| \nabla n_\uparrow \right|^2} + \frac{F_{00110}}{32 \left| \nabla n_\uparrow \right|^2} - \frac{F_{00100}}{32 \left| \nabla n_\uparrow \right|^3} - \frac{F_{00002}}{16} \tag{D.88}$$

$$\frac{\partial F}{\partial n} = F_{10000} \tag{D.89}$$

$$\frac{\partial F}{\partial Z} = \frac{F_{00100}}{4 \left| \nabla n_\uparrow \right|} + \frac{F_{00001}}{4} \tag{D.90}$$

$$\frac{\partial F}{\partial X} = \frac{F_{00100}}{4 \left| \nabla n_\uparrow \right|} - \frac{F_{00001}}{4} \tag{D.91}$$

Bibliography

[1] CAS Science Spotlight Most Cited—Chemistry (see http://www.cas.org/spotlight/bchem.html).

[2] F. Wang, T. Ziegler, E. van Lenthe, S. van Gisbergen, and E. J. Baerends, J. Chem. Phys. **122**, 204103 (2005).

[3] D. Peng, W. Zou, and W. Liu, J. Chem. Phys. **123**, 144101 (2005).

[4] J. Gao et al., J. Chem. Phys. **123**, 054102 (2005).

[5] J. Jusélius, D. Sundholm, and J. Gauss, J. Chem. Phys. **121**, 3952 (2004).

[6] P. Pyykkö, Adv. Quantum Chem. **11**, 353 (1978).

[7] P. Pyykkö and J.-P. Desclaux, Acc. Chem. Res. **12**, 276 (1979).

[8] K. S. Pitzer, Acc. Chem. Res. **12**, 271 (1979).

[9] P. Pyykkö, Chem. Rev. **88**, 563 (1988).

[10] H. Schwarz, Angew. Chem. Int. Ed. **42**, 4442 (2003).

[11] W. Liu, G. Hong, D. Dai, L. Li, and M. Dolg, Theor. Chem. Acc. **96**, 75 (1997).

[12] W. Liu, F. Wang, and L. Li, J. Theor. Comput. Chem. **2**, 257 (2003).

[13] H. M. Quiney, H. Skaane, and I. P. Grant, Chem. Phys. Lett. **290**, 473 (1998).

[14] H. M. Quiney, H. Skaane, and I. P. Grant, Adv. Quantum Chem. **32**, 1 (1999).

[15] I. P. Grant and H. M. Quiney, Int. J Quant. Chem. **80**, 283 (2000).

[16] Development version of DIRAC—a relativistic ab initio electronic structure program—written by H. J. Aa. Jensen, T. Saue, and L. Visscher with contributions from V. Bakken, E. Eliav, T. Enevoldsen, T. Fleig, O. Fossgaard, T. Helgaker, J. Lærdahl, C. V. Larsen, P.

Norman, J. Olsen, M. Pernpointner, J. K. Pedersen, K. Ruud, P. Sałek, J. N. P. van Stralen, J. Thyssen, O. Visser, and T. Winther (see http://dirac.chem.sdu.dk).

[17] K. G. Dyall, in *NATO ASI Series, Vol. 318*, edited by G. L. Malli, Plenum, New York, 1991.

[18] K. G. Dyall, Chem. Phys. Lett. **224**, 186 (1994).

[19] L. Visscher, O. Visser, P. J. C. Aerts, H. Merenga, and W. C. Nieuwpoort, Comp. Phys. Comm. **81**, 120 (1994).

[20] T. Yanai, T. Nakajima, Y. Ishikawa, and K. Hirao, J. Chem. Phys. **114**, 6526 (2001).

[21] T. Yanai, H. Iikura, T. Nakajima, Y. Ishikawa, and K. Hirao, J. Chem. Phys. **115**, 8267 (2001).

[22] T. Yanai, T. Nakajima, Y. Ishikawa, and K. Hirao, J. Chem. Phys. **116**, 10122 (2002).

[23] T. Helgaker, in his lecture at the International Karlsruhe Nanoscience Workshop, Karlsruhe, 2005.

[24] T. Saue, Adv. Quantum Chem. **48**, 383 (2005).

[25] M. E. Rose, *Relativistic Electron Theory*, Wiley, New York, 1961.

[26] R. E. Moss, *Advanced Molecular Quantum Mechanics: An Introduction to Relativistic Quantum Mechanics and the Quantum Theory of Radiation*, Chapman and Hall, London, 1973.

[27] P. Strange, *Relativistic Quantum Mechanics: with applications in condensed matter and atomic physics*, Cambridge University Press, Cambridge, 1998.

[28] K. G. Dyall and K. Fægri jr., *Introduction to Relativistic Quantum Chemistry*, Oxford University Press, New York, 2007.

[29] M. Reiher and A. Wolf, *Relativistic Quantum Chemistry: The Fundamental Theory of Molecular Science*, Wiley-VCH, Weinheim, 2007.

[30] B. A. Hess (ed.), *Relativistic Effects in Heavy-Element Chemistry and Physics*, John Wiley & Sons, New York, 2002.

[31] P. Schwerdtfeger (ed.), *Relativistic Electronic Structure Theory, Part 1: Fundamentals*, Elsevier, Amsterdam, 2002.

[32] P. Schwerdtfeger (ed.), *Relativistic Electronic Structure Theory, Part 2: Applications*, Elsevier, Amsterdam, 2004.

[33] U. Kaldor and S. Wilson (eds.), *Theoretical Chemistry and Physics of Heavy and Superheavy Elements*, Kluwer Academic, Dordrecht, 2003.

[34] K. Hirao and Y. Ishikawa (eds.), *Recent Advances in Relativistic Molecular Theory*, World Scientific, Singapore, 2004.

[35] P. Hohenberg and W. Kohn, Phys. Rev. B **136**, 864 (1964).

[36] W. Kohn and L. J. Sham, Phys. Rev. A **140**, 1133 (1965).

[37] J. P. Perdew et al., J. Chem. Phys. **123**, 062201 (2005).

[38] A. K. Rajagopal and J. Callaway, Phys. Rev. B **7**, 1912 (1973).

[39] E. Runge and E. K. U. Gross, Phys. Rev. Lett. **52**, 997 (1984).

[40] G. Vignale, Lect. notes Phys. **706**, 75 (2006).

[41] N. T. Maitra, Lect. notes Phys. **706**, 61 (2006).

[42] D. H. Whiffen, Pure Appl. Chem. **50**, 75 (1978).

[43] W. Kutzelnigg, Fundamentals of nonrelativistic and relativistic theory of NMR and ESR parameters, in *Calculation of NMR and EPR Parameters: Theory and Applications*, edited by M. Kaupp, M. Bühl, and V. G. Malkin, Wiley-VCH, Weinheim, 2004.

[44] P. A. M. Dirac, Proc. Roy. Soc. London, Ser. A **123**, 714 (1929).

[45] S. J. Vosko, L. Wilk, and M. Nusair, Can. J. Phys. **58**, 1200 (1980).

[46] V. N. Ostrovsky, HYLE—International Journal for Philosophy of Chemistry **11**, 101 (2005).

[47] T. Helgaker, P. Jørgensen, and J. Olsen, *Molecular Electronic Structure Theory*, John Wiley & Sons, Chichester, 2000.

[48] M. Gell-Mann, Nuovo Cimento Suppl. **4**, 848 (1956).

[49] H. J. Aa. Jensen, K. G. Dyall, T. Saue, and K. Fægri jr., J. Chem. Phys. **104**, 4083 (1996).

[50] Footnote 2 on p. 607 in: W. Pauli, Z. Phys. **43**, 601 (1927).

[51] G. Arfken, *Mathematical Methods for Physicists, 3rd ed.*, Academic Press, Orlando, 1985.

[52] W. Greiner and B. Müller, *Gauge Theory of Weak Interactions, 3rd ed.*, Springer, Berlin, 2000.

[53] T. Saue and H. J. Aa. Jensen, J. Chem. Phys. **118**, 522 (2003).

[54] M. Dolg, Relativistic effective core potentials, in *Relativistic Electronic Structure Theory, Part 1: Fundamentals*, edited by P. Schwerdtfeger, Elsevier, Amsterdam, 2002.

[55] M. Douglas and N. M. Kroll, Ann. Phys. **82**, 89 (1974).

[56] B. A. Hess, Phys. Rev. A **32**, 756 (1985).

[57] B. A. Hess, Phys. Rev. A **33**, 3742 (1986).

[58] E. van Lenthe, E. J. Baerends, and J. G. Snijders, J. Chem. Phys. **99**, 4597 (1993).

[59] E. van Lenthe, J. G. Snijders, and E. J. Baerends, J. Chem. Phys. **105**, 6505 (1996).

[60] L. Visscher and T. Saue, J. Chem. Phys. **113**, 3996 (2000).

[61] K. G. Dyall, J. Chem. Phys. **100**, 2118 (1994).

[62] W. Kutzelnigg, Int. J Quant. Chem. **25**, 107 (1984).

[63] W. Kutzelnigg, Perturbation theory of relativistic effects, in *Relativistic Electronic Structure Theory, Part 1: Fundamentals*, edited by P. Schwerdtfeger, Elsevier, Amsterdam, 2002.

[64] T. Saue and L. Visscher, Four-component electronic structure methods for molecules, in *Theoretical Chemistry and Physics of Heavy and Superheavy Elements*, edited by U. Kaldor and S. Wilson, Kluwer Academic, Dordrecht, 2003.

[65] J.-M. Lévy-Leblond, Commun. Math. Phys. **6**, 286 (1967).

[66] T. Saue, Post dirac-fock-methods—properties, in *Relativistic Electronic Structure Theory, Part 1: Fundamentals*, edited by P. Schwerdtfeger, Elsevier, Amsterdam, 2002.

[67] K. Schwarzschild, Gött. Nach., Math.-Phys. Kl., 126 (1903).

[68] W. Gordon, Z. Phys. **50**, 630 (1928).

[69] M. Barysz, A. J. Sadlej, and J. G. Snijders, Int. J Quant. Chem. **65**, 225 (1997).

[70] M. Barysz and A. J. Sadlej, J. Mol. Struct. (Theochem) **573**, 181 (2001).

[71] H. J. Aa. Jensen and M. Iliaš, unpublished.

[72] M. Iliaš and T. Saue, J. Chem. Phys. **126**, 064102 (2007).

[73] W. Liu and D. Peng, J. Chem. Phys. **125**, 044102 (2006).

[74] W. Kutzelnigg and W. Liu, J. Chem. Phys. **123**, 241102 (2005).

[75] W. Kutzelnigg and W. Liu, Mol. Phys. **104**, 2225 (2006).

[76] L. L. Foldy and S. A. Wouthuysen, Phys. Rev. **78**, 29 (1950).

[77] J.-L. Heully, I. Lindgren, E. Lindroth, S. Lundqvist, and A.-M. Mårtensson-Pendrill, J. Phys. B **78**, 29 (1986).

[78] B. A. Hess, C. M. Marian, U. Wahlgren, and O. Gropen, Chem. Phys. Lett. **251**, 365 (1996).

[79] B. Schimmelpfennig, program AMFI, Stockholm, Sweden.

[80] J. P. Perdew and K. Schmidt, Jacob's ladder of density functional approximations for the exchange-correlation energy, in *Density Functional Theory and Its Applications to Materials*, edited by V. E. Van Doren, K. Van Alsenoy, and P. Geerlings, American Institute of Physics, Melville, 2001.

[81] D. C. Langreth and J. P. Perdew, Phys. Rev. B **21**, 5469 (1980).

[82] J. P. Perdew, Phys. Rev. Lett. **55**, 1655 (1985); Phys. Rev. Lett. **55**, 2370(E) (1985).

[83] P. J. Stephens, F. J. Devlin, C. F. Chabalowski, and M. J. Frisch, J. Phys. Chem. **98**, 11623 (1994).

[84] A. D. Becke, J. Chem. Phys. **98**, 5648 (1993).

[85] C. Adamo and V. Barone, J. Chem. Phys. **100**, 6158 (1999).

[86] U. von Barth and L. Hedin, J. Phys. C **5**, 1629 (1972).

[87] O. Gunnarsson and B. I. Lundqvist, Phys. Rev. B **13**, 4274 (1976); Phys. Rev. B **15**, 6006(E) (1977).

[88] G. F. Giuliani and G. Vignale, *Quantum Theory of the Electron Liquid*, Cambridge University Press, Cambridge, 2005.

[89] G. Vignale and M. Rasolt, Phys. Rev. Lett. **59**, 2360 (1987).

[90] G. Vignale and M. Rasolt, Phys. Rev. B **37**, 10685 (1988).

[91] L. N. Oliveira, E. K. U. Gross, and W. Kohn, Phys. Rev. Lett. **60**, 2430 (1988).

[92] H. Eschrig, *The Fundamentals of Density Functional Theory*, Edition am Gutenbergplatz, Leipzig, 2003.

[93] M. Levy, Proc. Natl. Acad. Sci. USA **76**, 6062 (1979).

[94] K. Capelle and G. Vignale, Phys. Rev. Lett. **24**, 5546 (2001).

[95] K. Capelle, C. A. Ullrich, and G. Vignale, Phys. Rev. A **76**, 012508 (2007).

[96] A. Savin, On degeneracy, near-degeneracy and density functional theory, in *Recent Developments and Applications of Modern Density Functional Theory*, edited by J. M. Seminario, Elsevier, Amsterdam, 1996.

[97] A. D. Becke, Can. J. Phys. **74**, 995 (1996).

[98] A. D. Becke, J. Chem. Phys. **117**, 6935 (2002).

[99] E. R. Johnson, R. M. Dickson, and A. D. Becke, J. Chem. Phys. **126**, 184104 (2007).

[100] G. Vignale and W. Kohn, Phys. Rev. Lett. **77**, 2037 (1996).

[101] M. van Faassen, Int. J. Mod. Phys. B **20**, 3419 (2006).

[102] P. Jørgensen and J. Simons, *Second Quantization Based Methods in Quantum Chemistry*, Academic Press, New York, 1981.

[103] G. A. Aucar, T. Saue, L. Visscher, and H. J. Aa. Jensen, J. Chem. Phys. **110**, 6208 (1999).

[104] W. Kutzelnigg, Phys. Rev. A **67**, 032109 (2003).

[105] O. Christiansen, P. Jørgensen, and C. Hättig, Int. J Quant. Chem. **68**, 1 (1998).

[106] J. H. Shirley, Phys. Rev. B **138**, 979 (1965).

[107] W. Kutzelnigg, Theor. Chim. Acta **83**, 263 (1992).

[108] R. Kubo, J. Phys. Soc. Japan **12**, 570 (1959).

[109] P. W. Langhoff, S. T. Epstein, and M. Karplus, Rev. Mod. Phys. **44**, 602 (1972).

[110] J. Olsen and P. Jørgensen, J. Chem. Phys. **82**, 3235 (1985).

[111] H. Hettema, H. J. Aa. Jensen, P. Jørgensen, and J. Olsen, J. Chem. Phys. **97**, 1174 (1992).

[112] P. Sałek, O. Vahtras, T. Helgaker, and H. Ågren, J. Chem. Phys. **117**, 9630 (2002).

[113] P. Sałek, T. Helgaker, and T. Saue, Chem. Phys. **311**, 187 (2005).

[114] T. Saue and T. Helgaker, J. Comput. Chem. **23**, 814 (2002).

[115] P. Norman and H. J. Aa. Jensen, J. Chem. Phys. **121**, 6145 (2004).

[116] J. Henriksson, T. Saue, and P. Norman, J. Chem. Phys. **128**, 024105 (2008).

[117] I. Tunell et al., J. Chem. Phys. **119**, 11024 (2003).

[118] B. Jansik, P. Sałek, D. Jonsson, O. Vahtras, and H. Ågren, J. Chem. Phys. **122**, 054107 (2005).

[119] Python, a dynamic object-oriented programming language (see http://www.python.org).

[120] Maxima, a computer algebra system (see http://maxima.sourceforge.net).

[121] N. T. Maitra and K. Burke, Chem. Phys. Lett. **359**, 237 (2002).

[122] N. T. Maitra and K. Burke, Chem. Phys. Lett. **441**, 167 (2007).

[123] S. Varga, E. Engel, W.-D. Sepp, and B. Fricke, Phys. Rev. A **59**, 4288 (1999).

[124] S. Varga et al., J. Chem. Phys. **112**, 3499 (2000).

[125] M. Mayer, O. D. Häberlen, and N. Rösch, Phys. Rev. A **54**, 4775 (1996).

[126] J. Anton, B. Fricke, and E. Engel, Phys. Rev. A **69**, 012505 (2004).

[127] J. Anton, B. Fricke, and P. Schwerdtfeger, Chem. Phys. **311**, 97 (2005).

[128] C. van Wüllen, J. Comput. Chem. **23**, 779 (2002).

[129] J. E. Sansonetti, W. C. Martin, and S. L. Young, *Handbook of Basic Atomic Spectroscopic Data, version 1.1*, NIST, Gaithersburg, 2004, (http://physics.nist.gov/Handbook).

[130] L. L. Hirst, Rev. Mod. Phys. **69**, 607 (1997).

[131] P. F. de Châtel and K. Ayuel, Physica D **266**, 256 (1999).

[132] L. D. Landau and E. M. Lifshitz, *Course of Theoretical Physics 8: Electrodynamics of Continuous Media*, Pergamon, London, 1960.

[133] K. Capelle and E. K. U. Gross, Phys. Rev. Lett. **78**, 1872 (1997).

[134] C. Lee, W. Yang, and R. G. Parr, Phys. Rev. B **37**, 785 (1988).

[135] B. Miehlich, A. Savin, H. Stoll, and H. Preuss, Chem. Phys. Lett. **157**, 200 (1989).

[136] R. Bauernschmitt and R. Ahlrichs, Chem. Phys. Lett. **256**, 454 (1996).

[137] R. A. Kendall, T. H. Dunning jr., and R. J. Harrison, J. Chem. Phys. **96**, 6796 (1992), to d-aug-cc-pVTZ we have added *1s1p1d* diffuse exponents using the outermost quotient of each angular momentum.

[138] D. E. Woon and T. H. Dunning jr., J. Chem. Phys. **98**, 1358 (1993), to aug-cc-pVTZ we have added *2s2p2d2f* diffuse exponents using the outermost quotient of each angular momentum.

[139] J. C. Slater, Phys. Rev. **81**, 385 (1951).

[140] A. D. Becke, Phys. Rev. A **38**, 3098 (1988).

[141] K. Pierloot, E. van Besien, E. van Lenthe, and E. J. Baerends, J. Chem. Phys. **126**, 194311 (2007).

[142] J. Oddershede, Adv. Chem. Phys. **67**, 201 (1987).

[143] P. R. T. Schipper, O. V. Gritsenko, S. J. A. van Gisbergen, and E. J. Baerends, J. Chem. Phys. **112**, 1344 (2000).

[144] R. van Leeuwen and E. J. Baerends, Phys. Rev. A **49**, 2421 (1994).

[145] T. Yanai, D. P. Tew, and N. C. Handy, Chem. Phys. Lett. **393**, 51 (2004).

[146] J. P. Perdew, K. Burke, and M. Ernzerhof, Phys. Rev. Lett. **77**, 3865 (1996).

[147] J. P. Perdew, Phys. Rev. B **33**, 8822 (1986); Phys. Rev. B **34**, 7406(E) (1986).

[148] L. Visscher and K. G. Dyall, At. Data Nucl. Data Tables **67**, 207 (1997).

[149] N. B. Balabanov and K. A. Peterson, J. Chem. Phys. **123**, 064107 (2005).

[150] K. G. Dyall, Theor. Chem. Acc. **112**, 403 (2004); Theor. Chem. Acc. **117**, 483 (2007); Theor. Chem. Acc. **117**, 491 (2007); basis sets available from the DIRAC web site (http://dirac.chem.sdu.dk).

[151] R. A. Kendall, T. H. Dunning jr., and R. J. Harrison, J. Chem. Phys. **96**, 6796 (1992).

[152] T. H. Dunning jr., J. Chem. Phys. **90**, 1007 (1989).

[153] G. Jansen and B. A. Hess, Z. Phys. D **13**, 363 (1989).

[154] H. A. Witek, T. Nakajima, and K. Hirao, J. Chem. Phys. **113**, 8015 (2000).

[155] K. Pierloot and E. van Besien, J. Chem. Phys. **123**, 204309 (2005).

[156] C. J. Jameson and A. D. Buckingham, J. Phys. Chem. **83**, 3366 (1979).

[157] C. J. Jameson and A. D. Buckingham, J. Chem. Phys. **73**, 5684 (1980).

[158] P. Lazzeretti, M. Maglioni, and R. Zanasi, J. Mol. Struct. (Theochem) **313**, 299 (1994).

[159] A. Soncini and P. Lazzeretti, J. Chem. Phys. **118**, 7165 (2003).

[160] A. Soncini and P. Lazzeretti, J. Chem. Phys. **119**, 1343 (2003).

[161] O. L. Malkina and V. G. Malkin, Angew. Chem. Int. Ed. **42**, 4335 (2003).

[162] O. Malkina, Interpretation of indirect nuclear spin–spin coupling constants, in *Calculation of NMR and EPR Parameters: Theory and Applications*, edited by M. Kaupp, M. Bühl, and V. G. Malkin, Wiley-VCH, Weinheim, 2004.

[163] J. Gräfenstein and D. Cremer, Chem. Phys. Lett. **383**, 332 (2004).

[164] J. Gräfenstein and D. Cremer, Chem. Phys. Lett. **387**, 415 (2004).

[165] A. Soncini, P. W. Fowler, P. Lazzeretti, and R. Zanasi, Chem. Phys. Lett. **401**, 164 (2005).

[166] A. Soncini and P. Lazzeretti, ChemPhysChem **7**, 679 (2006).

[167] D. Cremer and J. Gräfenstein, Phys. Chem. Chem. Phys. **9**, 2791 (2007).

[168] R. A. Kendall, T. H. Dunning jr., and R. J. Harrison, J. Chem. Phys. **96**, 6796 (1992), to d-aug-cc-pVTZ we have added *1s1p1d1f* diffuse exponents using the outermost quotient of each angular momentum.

[169] K. P. Huber and G. Herzberg, *Molecular Spectra and Molecular Structure—Constants of Diatomic Molecules*, Van Norstrand Reinhold, New York, 1979.

[170] D. E. Woon and T. H. Dunning jr., J. Chem. Phys. **100**, 2975 (1994).

[171] T. van Mourik, A. K. Wilson, and T. H. Dunning jr., Mol. Phys. **99**, 529 (1999).

[172] P. Norman, D. M. Bishop, H. J. Aa. Jensen, and J. Oddershede, J. Chem. Phys. **123**, 194103 (2005).

[173] M. Faraday, Philos. Trans. R. London, 440 (1825).

[174] I. Fernández and G. Frenking, Chem. Eur. J. **13**, 5873 (2007).

[175] G. Frenking and A. Krapp, J. Comput. Chem. **28**, 15 (2007).

[176] Z. Chen, C. S. Wannere, C. Corminboeuf, R. Puchta, and P. von Ragué Schleyer, Chem. Rev. **105**, 3842 (2005).

[177] P. Lazzeretti, Prog. Nucl. Magn. Reson. Spectrosc. **36**, 1 (2000).

[178] P. Lazzeretti and R. Zanasi, J. Chem. Phys. **75**, 5019 (1981).

[179] P. Lazzeretti and R. Zanasi, Chem. Phys. Lett. **80**, 533 (1981).

[180] J. A. N. F. Gomes and R. B. Mallion, Chem. Rev. **101**, 1349 (2001).

[181] R. Herges, Chem. Rev. **105**, 3758 (2005).

[182] A. Soncini, J. Chem. Theor. Comput. (2007), ASAP.

[183] J. Jusélius, D. Sundholm, and J. Gauss, manuscript in preparation.

[184] D. Cappel, S. Tüllmann, A. Krapp, and G. Frenking, Angew. Chem. Int. Ed. **117**, 3683 (2005).

[185] I. Fernández and G. Frenking, Chem. Eur. J. **12**, 3617 (2006).

[186] I. Fernández and G. Frenking, J. Org. Chem. **71**, 2251 (2006).

[187] I. Fernández and G. Frenking, Chem. Commun. , 5030 (2006).

[188] I. Fernández and G. Frenking, Faraday Discuss. **135**, 403 (2007).

[189] D. S. Shobe, J. Phys. Chem. A **109**, 9118 (2005).

[190] R. Salcedo, J. Mol. Struct. (Theochem) **674**, 125 (2004).

[191] M. J. Frisch et al., Gaussian 03, Revision C.02, Gaussian, Inc., Wallingford, CT, 2004.

[192] D. E. Woon and T. H. Dunning jr., J. Chem. Phys. **98**, 1358 (1993).

[193] A. K. Wilson, D. E. Woon, K. A. Peterson, and T. H. Dunning jr., J. Chem. Phys. **110**, 7667 (1999).

[194] K. A. Peterson, J. Chem. Phys. **119**, 11099 (2003).

[195] B. Metz, H. Stoll, and M. Dolg, J. Chem. Phys. **113**, 2563 (2000).

[196] K. G. Dyall, Theor. Chem. Acc. **99**, 366 (1998); addendum Theor. Chem. Acc. **108**, 365 (2002); revision Theor. Chem. Acc. **115**, 441 (2006); basis sets available from the DIRAC web site (http://dirac.chem.sdu.dk).

[197] M. M. Sternheim, Phys. Rev. **128**, 676 (1962).

[198] V. Sychrovský, J. Gräfenstein, and D. Cremer, J. Chem. Phys. **113**, 3530 (2000).

[199] T. Helgaker, M. Watson, and N. C. Handy, J. Chem. Phys. **113**, 9402 (2000).

[200] T. Enevoldsen, L. Visscher, T. Saue, H. J. Aa. Jensen, and J. Oddershede, J. Chem. Phys. **112**, 3493 (2000).

[201] S. Huzinaga, *Approximate Atomic Functions*, University of Alberta, Edmonton, 1971.

[202] W. Kutzelnigg, U. Fleischer, and M. Schindler, in *NMR Basic Principles and Progress, Vol. 23*, edited by P. Diehl, E. Fluck, H. Günther, R. Kosfeld, and J. Seelig, Springer, Berlin, 1990.

[203] W. S. Lee and J. M. Schulman, J. Chem. Phys. **70**, 1530 (1979).

[204] J. E. Pérez, F. S. Ortiz, R. H. Contreras, C. G. Giribet, and M. C. Ruiz De Azúa, J. Mol. Struct. (Theochem) **210**, 193 (1990).

[205] P. Bouř and M. Boudĕšínský, J. Chem. Phys. **110**, 2836 (1999).

[206] J. Autschbach and T. Ziegler, J. Chem. Phys. **113**, 9410 (2000).

[207] J. Erler and M. J. Ramsey-Musolf, Prog. Part. Nucl. Phys. **54**, 351 (2005).

[208] F. Wilczek, Nature **433**, 239 (2005).

[209] C. Wu, E. Ambler, R. Hayward, D. Hoppes, and R. Hudson, Phys. Rev. **105**, 1413 (1957).

[210] T. Lee and C. Yang, Phys. Rev. **104**, 254 (1956).

[211] R. Berger and M. Quack, ChemPhysChem **1**, 57 (2000).

[212] J. K. Lærdahl, R. Wesendrup, and P. Schwerdtfeger, ChemPhysChem **1**, 60 (2000).

[213] P. Cintas, ChemPhysChem **2**, 409 (2001).

[214] F. Faglioni, A. Passalacqua, and P. Lazzeretti, Origins Life Evol. B **35**, 461 (2005).

[215] G. Lente, J. Phys. Chem. A **110**, 12711 (2006).

[216] A. S. Lahamer et al., Phys. Rev. Lett. **85**, 4470 (2000).

[217] A. Szabo-Nagy and L. Keszthelyi, Proc. Natl. Acad. Sci. **96**, 4252 (1999).

[218] C. Daussy et al., Phys. Rev. Lett. **83**, 1554 (1999).

[219] A. Salam, The origin of chirality, the role of phase transitions and their inductions in amino acids, in *Chemical Evolution: Origin of Life*, edited by C. Ponnamperuma and J. Chela-Flores, A. Deepak Publishing, Hampton, 1993.

[220] C. Daussy et al., Phys. Rev. Lett. **94**, 203904 (2005).

[221] J. Crassous et al., ChemPhysChem **4**, 541 (2003).

[222] J. Crassous, C. Chardonnet, T. Saue, and P. Schwerdtfeger, Org. Biomol. Chem. **3**, 13 (2005).

[223] M. Quack and M. Willeke, J. Phys. Chem. A **110**, 3338 (2006).

[224] R. Berger, M. Gottselig, M. Quack, and M. Willeke, Angew. Chem. Int. Ed. **40**, 4195 (2001).

[225] P. Schwerdtfeger, T. Saue, J. N. P. van Stralen, and L. Visscher, Phys. Rev. A **71**, 012103 (2005).

[226] M. Quack and J. Stohner, Phys. Rev. Lett. **84**, 3807 (2000).

[227] J. K. Lærdahl, P. Schwerdtfeger, and H. M. Quiney, Phys. Rev. Lett. **84**, 3811 (2000).

[228] V. S. Letokhov, Phys. Lett. A **54**, 275 (1975).

[229] P. Schwerdtfeger, J. K. Lærdahl, and C. Chardonnet, Phys. Rev. A **65**, 042508 (2002).

[230] M. Quack and J. Stohner, Zeit. Phys. Chem. **214**, 675 (2000).

[231] R. G. Viglione, R. Zanasi, P. Lazzeretti, and A. Ligabue, Phys. Rev. A **62**, 052516 (2000).

[232] M. Ziskind, T. Marrel, C. Daussy, and C. Chardonnet, Eur. Phys. J. D **20**, 219 (2002).

[233] A. A. Fokin et al., J. Am. Chem. Soc. **128**, 5332 (2006).

[234] B. Y. Zel'dovich, D. B. Saakyan, and I. I. Sobel'man, JETP Lett. **25**, 94 (1977).

[235] R. A. Harris and L. Stodolsky, Phys. Lett. B **78**, 313 (1978).

[236] D. W. Rein, R. A. Hegstrom, and P. G. H. Sandars, Phys. Lett. A **71**, 499 (1979).

[237] J. K. Lærdahl and P. Schwerdtfeger, Phys. Rev. A **60**, 4439 (1999).

[238] R. Bast and P. Schwerdtfeger, Phys. Rev. Lett. **91**, 023001 (2003).

[239] P. Schwerdtfeger, J. Gierlich, and T. Bollwein, Angew. Chem. Int. Ed. **42**, 1293 (2003).

[240] P. Schwerdtfeger and R. Bast, J. Am. Chem. Soc. **126**, 1652 (2004).

[241] F. Faglioni and P. Lazzeretti, Phys. Rev. A **67**, 32101 (2003).

[242] P. L. Anthony et al. (SLAC E158 collaboration), Phys. Rev. Lett. **95**, 081601 (2005).

[243] R. S. Cahn, C. K. Ingold, and V. Prelog, Angew. Chem. Int. Ed. **5**, 385 (1966).

[244] F. De Montigny, R. Bast, A. S. P. Gomes, G. Pilet, N. Vanthuyne, C. Roussel, L. Guy, T. Saue, and J. Crassous, unpublished.

[245] F. Faglioni and P. Lazzeretti, Phys. Rev. E **65**, 011904 (2001).

[246] T. Saue, unpublished.

[247] T. Helgaker, P. J. Wilson, R. D. Amos, and N. C. Handy, J. Chem. Phys. **113**, 2983 (2000).

[248] G. Vignale, M. Rasolt, and D. J. W. Geldart, Phys. Rev. B **37**, 2502 (1988).

[249] A. M. Lee, N. C. Handy, and S. M. Colwell, J. Chem. Phys. **103**, 10097 (1995).

[250] K. Ruud et al., J. Chem. Phys. **100**, 8178 (1994).

[251] C. J. Jameson et al., J. Chem. Phys. **74**, 81 (1981).

[252] W. T. Raynes, Nucl. Magn. Reson. **7**, 1 (1978).

[253] D. K. Hindermann and C. D. Cornwell, J. Chem. Phys. **48**, 4148 (1968).

[254] A. K. Jameson and C. J. Jameson, Chem. Phys. Lett. **134**, 461 (1987).

[255] R. E. Wasylishen, S. Mooibroek, and J. B. Macdonald, J. Chem. Phys. **81**, 1057 (1984).

[256] R. Berger, Parity-violation effects in molecules, in *Relativistic Electronic Structure Theory, Part 2: Applications*, edited by P. Schwerdtfeger, Elsevier, Amsterdam, 2004.